



Mohammad-Sadegh Salehi, M.Sc.

Numerical Study of Reactive Two-Phase Flows

DOCTORAL THESIS

to achieve the university degree of
Doktor der technischen Wissenschaften
submitted to

Graz University of Technology

Supervisor

Assoc.Prof. Dipl.-Ing. Dr.techn. Stefan Radl

Institute of Process and Particle Engineering
Graz University of Technology

Graz, Austria, October 2019

Mohammad-Sadegh Salehi

Numerical Study of Reactive Two-Phase Flows

Doctoral Thesis

Graz University of Technology, Graz, Austria

October 2019



Copyright ©2019 by Mohammad-Sadegh Salehi

All rights reserved. Except where otherwise noted, this thesis is licensed under CC BY-NC 4.0 (<https://creativecommons.org>). For the parts of this thesis that are owned by a different copyright holder (e.g., the publishers of journal articles included in this thesis), other licenses may apply, and other organizations may hold the copyright.

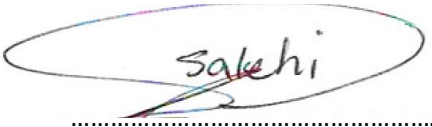


LIGGGHTS® and CFDEM® are registered trademarks of DCS Computing GmbH, the producer of the LIGGGHTS® software and the CFDEM®coupling software. See <http://www.cfdem.com/terms-trademark-policy> for details.

OpenFOAM® is the name given to software produced by OpenCFD Ltd. and released free and open source to the general public. OpenFOAM® is a registered trade mark of OpenCFD Limited, producer and distributor of the OpenFOAM software.

AFFIDAVIT

I declare that I have authored this thesis independently, that I have not used other than the declared sources/resources, and that I have explicitly marked all material which has been quoted either literally or by content from the sources used. The text document uploaded to TUGRAZonline is identical to the present doctoral thesis.



September 2019, Mohammad-Sadegh Salehi

*My prayer and my worship, and my life and my death,
are devoted to God, the Lord of the Worlds*

Acknowledgements

The present Ph.D. thesis is the outcome of my serious endeavor to boost my knowledge and skills in my professional life. Despite the faced difficulties, it was a delightful time. Specifically, I learned how to rise to the challenges independently; I had the opportunity to develop my expertise in the research field in which I was interested. I would like to express my gratitude to all people trying to help and support me during these years.

First and foremost, my sincere appreciation is given to my supervisor, Prof. Stefan Radl, who enormously helped me to broaden my experience in simulation tools and supported me to develop my skills in carrying out a research work. He taught me how to deal with challenging problems, and his profound influence in my engineering vision is incontrovertible. Thank you for being so patient, and helping me improve! Supervisors like you are hard to find, and I'm eternally grateful for everything you've taught me.

I would also like to thank Dr. Hamidreza Godini, who his guidance and support tremendously helped me to broaden my experience in reaction engineering. Your support helped me a lot to develop my skills in carrying out research work independently. You were there for me every step of the way, and I wholeheartedly appreciate everything you've done for me.

Special gratitude is given to my friends at simulation science group: Federico Municchi, Jakob D. Redlinger-Pohn, Benedict Benque, Florian Färber, Stefan Scheer and Thomas Schmid. They were all good friends and they helped me a lot during these three years.

I must acknowledge the help of the IPPT team: Michaela Cibulka, Silvia Houben, Christoph Neubauer, Adela Roller, and Stefan Scheer. They supported me with administrative stuff so that I could focus only on my scientific work.

Most of all, I would like to thank my mother, my father and my wife. Especially, I would like to express my gratitude to my wife (actually my coworker), Dr. Maryam Askarishahi, who always tries to support me to develop myself in my professional and private life. I would like to thank you for your great ideas and contribution to my Ph.D. I feel a tremendous change in my life since we work and live together. I sincerely appreciate you for your

dedication and patience. Your encouragement is always of significant help for me in difficult situations.

Finally, I would like to thank God, who let me complete this work. I genuinely feel your support and guidance in every moment of my life. Trusting in you is the only thing which I cannot live without, so I ask you to keep me on your way for the rest of my life.

Kurzfassung

Mehrphasenprozesse werden häufig in der chemischen und petrochemischen Industrie, in der Energie- und Pharmaindustrie, sowie in der biomedizinischen Industrie eingesetzt. Die Auslegung und Optimierung solcher Prozesse ist insbesondere bei reaktiven mehrphasigen Strömungen mit mehreren Herausforderungen konfrontiert. Diese Herausforderungen ergeben sich aus dem Mangel an ausreichendem Wissen aufgrund der Komplexität in Bezug auf die Strömung und das Mischen von Feststoffen, sowie der Interaktion von Stoff- und Wärmeübertragung in Mehrphasenreaktoren. Diese Probleme verschärfen sich bei der Entwicklung eines neuartigen Verfahrens, beispielsweise zur oxidativen Kopplung von Methan (OCM). Computational Fluid Dynamics (CFD) wird es Forschern ermöglichen, einen besseren Einblick in diese neue Technologie zu erhalten, da ein Zugang zu orts aufgelösten Informationen bezüglich verschiedenster Phänomene im OCM Reaktor geboten werden kann.

Die vorliegende Arbeit befasst sich mit CFD-basierten Untersuchungen eines anspruchsvollen reaktiven Mehrphasenprozesses, d.h., der oxidativen Kopplung von Methan. Dieses Verfahren ist mit einigen Herausforderungen in Bezug auf die Reaktionsführung und den Katalysator konfrontiert. In der vorliegenden Arbeit konzentrieren wir uns auf den reaktionstechnischen Aspekt des OCM-Prozesses. Es werden vier Ziele verfolgt: Das erste Ziel ist die Überprüfung des Fluid-Feststoff-Wärmeübertragungsmodells in Gegenwart einer Wärmequelle auf der Partikeloberfläche in einem Euler-Lagrange (EL)-Code. Dies wird erreicht, indem eine analytische Lösung für die Wärmeübertragungsleistung von Festbetten mit einer konstanten Wärmequelle vorgeschlagen wird. Das zweite Ziel ist die Quantifizierung der Feststoffmischrate in einer Wirbelschicht für einen weiten Bereich von Betriebsparametern und Geldart-B-Partikeleigenschaften. Zu diesem Zweck wurde eine Reihe von Metriken für das Mischen von Feststoffen in einer blasenbildenden Wirbelschicht unter Verwendung eines Zwei-Fluid-Modell-Ansatzes (TFM) untersucht. Anschließend wurde ein Satz von Korrelationen für Feststoffdispersionskoeffizienten,

dem Feststoffdiffusionsvermögen, und die charakteristische Mischzeit vorgeschlagen. Das dritte Ziel ist die Analyse des Betriebsverhalten eines OCM-Wirbelschichtreaktors. Zu diesem Zweck wurden die Auswirkungen von Eintrittstemperatur, Druck, Gasgeschwindigkeit und Methan-zu-Sauerstoff-Verhältnis im Eduktstrom auf das Betriebsverhalten des OCM-Wirbelbettreaktors sorgfältig untersucht. Um die Methanumwandlung und die Selektivität von C_2 -Produkten zu maximieren, wurde eine Sensitivitätsanalyse durchgeführt. Das vierte Ziel befasst sich mit der Untersuchung des Betriebsverhaltens von Festbettmembranreaktoren (PBMR) für OCM-Anwendungen durch Reaktionsweganalyse. Insbesondere wurde der Einfluss der Reaktandendosierung auf die Methanumwandlung und die C_2 -Selektivität mithilfe einer CFD-basierten Simulation untersucht.

Abstract

Multiphase contactors are widely used in chemical and petrochemical, energy, pharmaceutical, and biomedical industries. Design and optimization of such contactors are confronted with several challenges, especially in reactive multiphase flows. These challenges arise from the lack of knowledge due to the complexity regarding the flow and solid-fluid mixing, and the competitive nature of mass and heat transfer in multiphase reactors. These problems become more severe during developing a new and novel process such as oxidative coupling of methane (OCM). Computational Fluid Dynamics (CFD) will enable researchers to obtain a better insight into this new technology since it provides spatially-resolved information of phenomena occurring inside of the reactor.

The present thesis deals with CFD-based investigation of a challenging reactive multiphase process, i.e., oxidative coupling of methane. This process faces reaction engineering and catalyst-related challenges. The present thesis focusses on reaction engineering aspects of OCM processes. Four goals are followed: The first goal is the verification of a fluid-solid heat transfer model in the presence of a heat source on the particle surface in an Euler-Lagrange (EL) code. This is achieved by proposing an analytical solution for the thermal performance of packed beds including a constant heat source. The second goal is the quantification of solid mixing in a fluidized bed for a wide range of operating parameters and Geldart B particles. To this end, a set of metrics for solid mixing has been investigated in a bubbling fluidized bed by employing the two-fluid-model approach (TFM), and a set of correlations has been proposed for solid dispersion coefficients, solid diffusivity, and characteristic mixing time. The third goal is to analyze the performance of an OCM fluidized bed reactor. To do so, the effect of feed temperature, pressure, gas velocity, and methane-to-oxygen ratio in the feed on the performance of an OCM fluidized bed reactor have been investigated. In detail, a sensitivity analysis was conducted to maximize the methane conversion and the selectivity towards C_2 -products. The fourth goal deals with the study of packed bed membrane reactor (PBMR) performance through a reaction pathway analysis for an

OCM application. Specifically, the effect of reactant dosing on methane conversion and C_2 -selectivity has been investigated using CFD.

Table of Content

1	Goals and Content Overview	1
1.1	Experimental and Numerical Approach to Reactive Two-Phase Flows	2
1.2	Ethylene Production Processes	3
1.2.1	Oxidative Coupling of Methane	6
1.2.2	Key Parameters Influencing OCM Reactor Performance	9
1.2.3	The Need for Numerical Simulation	9
1.3	Computational Methods for Investigation of Catalytic Reactors	10
1.3.1	Euler-Lagrange Approach	11
1.3.2	Euler-Euler Approach	12
1.3.3	Heat and Mass Transport	13
1.3.4	Goal I: Verification of Simulation Platform	13
1.4	The Need for Evaluation of Solid Mixing in FBs	14
1.4.1	Key Parameters Influencing Mixing in Fluidized Beds	15
1.4.2	Goal II: Importance of Solid Mixing and the Degree of Uniformity	15
1.5	The Need for CFD-based Simulation of OCM Reactors	17
1.5.1	Challenges in Optimization of Reactor Performance	17
1.5.2	Goal III: Validated CFD Platform to Analyze OCM Fluidized Bed Reactors	18
1.5.3	Goal IV: Performance Analysis of a Packed Bed Membrane Reactor	19
1.6	Concept of the Thesis	20
1.7	Abbreviations	22
1.8	Nomenclature	22
1.9	The Author's Contribution to Publications	24
1.10	References	25
2	Analytical Solution for Thermal Transport in Packed Beds with Volumetric Heat Source	29
3	Quantification of solids mixing in bubbling fluidized beds via TFM simulations	49
3.1.	Introduction	51
3.1.1.	Goals of the Present Study	53

3.2.	Mathematical Model.....	53
3.2.1.	Flow	53
3.2.2.	Scalar Transport	57
3.3.	Results and Discussion	57
3.3.1.	Setup and Parameter Range	57
3.3.2.	Grid Dependency and Time to Pseudo Steady-State.....	59
3.3.3.	Qualitative Analysis	62
3.3.4.	Quantification of Solids Mixing	65
3.3.5.	Mixing Time Correlation.....	72
3.3.6.	Vortex-Specific Mixing Rates	76
3.4.	Conclusion	78
3.5.	Nomenclature.....	80
3.6.	References	83
3.7.	Appendix A. Model Validation and Mesh Dependency.....	90
3.7.1.	A.1 Validation.....	90
3.7.2.	A.2 Grid Sensitivity Analysis:	92
3.7.3.	References	94
3.8.	Appendix B. Solid Mean Velocity Fluctuation.....	95
4	CFD Simulation of Oxidative Coupling of Methane in Fluidized-Bed Reactors: A Detailed Analysis of Flow-Reaction Characteristics and Operating Conditions.....	98
5	Sustainable Process Design for Oxidative Coupling of Methane (OCM): Comprehensive Reactor Engineering via Computational Fluid Dynamics (CFD) Analysis of OCM Packed-Bed Membrane Reactors.....	114
6	Conclusion and Outlook.....	132
6.1	Conclusion	133
6.1.1	Goal I: Verification of Simulation Platform.....	134
6.1.2	Goal II: Importance of solid mixing and the degree of uniformity	135
6.1.3	Goal III: Validated CFD Platform to Analyze OCM Process in Fluidized-Bed Reactors ..	138
6.1.4	Goal IV: performance analysis of a packed bed membrane reactor for an OCM Process and the kinetic model.....	140
6.2	Outlook	141
6.3	Abbreviations.....	143

6.4	References.....	144
-----	-----------------	-----

“To raise new questions, new possibilities, to regard old problems from a new angle, requires creative imagination and marks real advance in science.”

(Albert Einstein)

1

Goals and Content Overview

This chapter delineates the main concept and the goals of the thesis. It also provides a declaration of the contribution of thesis author (M-S.S.) to the individual publication provided in this thesis.

1.1 Experimental and Numerical Approach to Reactive Two-Phase Flows

Catalytic reactors have been widely used in various industries. For instance, in petrochemical and chemical industries, natural gas and oil are converted to valuable products by chemical reactions. One example of this application is the process of ethylene production as one of the most valuable chemical products in these industries. Typically, the reactions involved in these processes can generate/demand a great deal of heat which can be utilized for or provided from other units. Therefore, design and optimization of such processes can reduce the capital and operating cost of the process. Consequently, obtaining a better understanding of such a process can benefit industrial sectors. Typically, these processes can be studied in two different ways: i) experimentation; ii) numerical simulation.

Experimental investigation of catalytic reactors can provide valuable information about the overall performance of the reactors, such as reactant conversion and selectivity towards desired products. However, detailed information about the contribution of the desired and undesired reactions to the reactor performance cannot be gained via experimentation. Besides, in case various mechanisms contribute to the rate of heat and mass transfer in the reactor, experimental approaches do not allow to investigate the effect each mechanism individually. Therefore, failure in isolating each phenomenon hinders us to deeply understand the contribution of specific mechanism and reactions to reactor performance. On the other hand, numerical approaches offer us such a significant advantage.

Furthermore, in experimental approaches, the concentration and temperature distributions cannot be readily measured in radial and axial directions. However, numerical methods (e.g., computational fluid dynamic) can provide point information, which can be of advantage in evaluating hotspot formation for exothermic systems. This can be also of great benefit in interpreting the collected data through experimentation.

What is more, optimizing the reactor performance requires a set of experimental runs to perform a sensitivity analysis. Nonetheless, such studies can cost a fortune due to

the cost associated with material handling, time, and the required energy, especially in large scales. However, application of numerical approaches can facilitate optimizing such processes even in the stage of conceptual design.

As a result, the present thesis deals with numerical simulation of catalytic, reactive processes with a focus on ethylene production via oxidative coupling of methane (OCM).

In the following sections, the processes utilized to produce ethylene with focus on OCM will be briefly described. Afterwards, the necessity to employ numerical approaches for catalytic reactors will be explained in more detail. Subsequently, we will set our goals based on the importance of the phenomena involved in the catalytic reactors for OCM processes. More precisely, the importance of heat exchange and solid mixing in reactive systems will be evaluated. In the next step, the thermal and chemical performance of different reactor configurations will be assessed for OCM processes.

1.2 Ethylene Production Processes

Ethylene is one of the essential building blocks for various industries such as petrochemical, packaging, transportation, electronics, textile, agriculture, and construction. Notably, its production has been continuously increasing over the recent decades (production more than 175 million tonnes only in 2019^{1,2}). Such a big market for ethylene has drawn the attention of researchers to develop new technologies with alternative feedstocks. These technologies should be more sustainable and efficient in terms of thermal and chemical performance³ as well as an environmental point of view. So far, five different methods have been proposed for ethylene production²: i) steam cracking (SC); ii) methanol to olefins (MTO); iii) Fischer-Tropsch synthesis (FTS); iv) Catalytic dehydrogenation of light alkanes; and v) Oxidative coupling of methane (OCM).

As shown in Figure 1, steam cracking, catalytic dehydrogenation, and OCM have the advantage of direct conversion of raw materials to olefins, e.g., ethylene. In contrast, FTS and MTO feature a degree of complexity in the process design due to the indirect process stemming from the generation of the intermediate product. In detail, methane needs first to be converted to syngas via reforming process, and then, FTS can be

adopted to produce olefins from syngas. Moreover, the MTO process is faced with more complexity due to the production of methanol as the second intermediate. Such complexity results in higher fixed costs because of the need for additional separation units.

OCM can be a low-cost alternative for steam cracking because of the abundance and low price of natural gas⁴. Interestingly, shale gas or biogas can also be used instead of oil as feedstock (e.g., naphtha)⁵ for ethylene production. Apart from this, an OCM process needs lower fixed costs compared with FTS and MTO processes because of providing a direct route for olefin production⁴. More interestingly, due to the high exothermicity of the involved reactions in OCM, this process requires a smaller amount of energy. Thus, CO_2 emission from the required energy will be lower². Moreover, the energy and heat generated in the OCM process can be utilized in other processes. Such features make this process worth investigating as a possible alternative to produce ethylene. In the following chapter, OCM process features will be explained in greater detail.

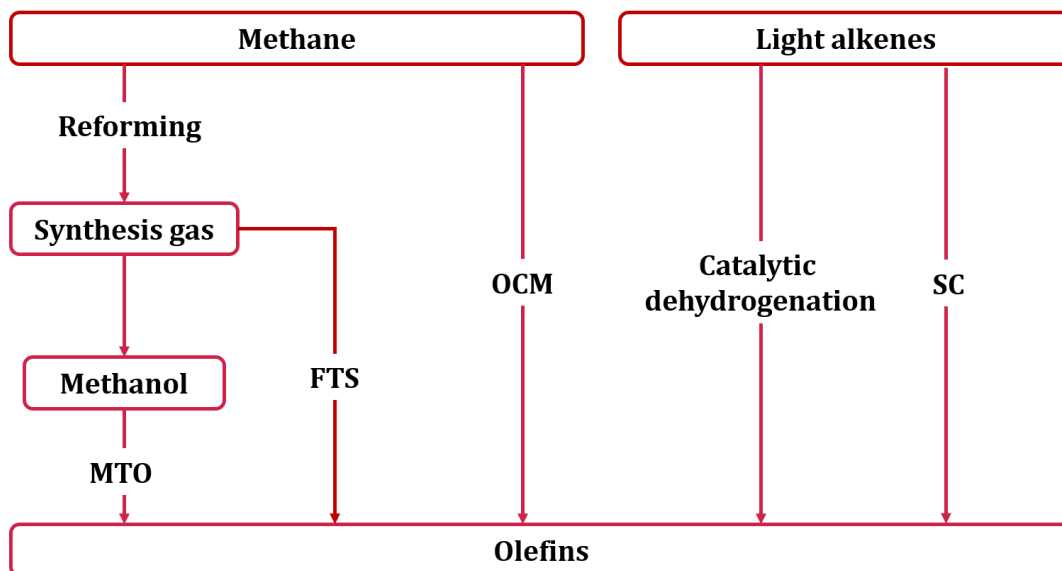


Figure 1. Schematic representation of various processes for olefin production²

Table 1. Features of various processes for the production of ethylene^{2,6-11}

Process	Catalyst	Feedstock	Reactors	Challenges
SC	–	Naphtha Ethane	Tubular reactors	Energy-intensive process; declining crude oil reserves
MTO	Zeolite-based	Methane	Fluidized bed; Fixed bed; Micro-reactors;	Coke deposition and its effect on Reaction rates; Deactivation of catalysts;
FTS	<i>Fe/Co</i> -based	Methane	Circulating fluidized bed; Fluidized bed; multi-tubular fixed bed; slurry phase reactors;	Low selectivity; A broad range of products; Catalyst design;
Catalytic dehydrogenation	Alumina-based	Light alkenes	Fixed bed reactors; Fluidized bed reactors;	Limited equilibrium conversion; Side reactions at high temperature; Catalyst design;
OCM	<i>La₂O₃/Mg, Ca</i> <i>Mn/Na₂WO₄</i> <i>Mn/SiO₂</i>	Methane	Microchannel; Membrane reactors; Staged-reactors; Fluidized bed reactors;	Need for novel reactors technology to increase C ₂ -yield; Catalyst stability and selectivity;

1.2.1 Oxidative Coupling of Methane

OCM process has attracted considerable attention of industrial sectors and academia after being developed for the first time by Keller and Bhasin¹². Specifically, researchers focus on the thermal and chemical performance of OCM reactors by exploring catalyst design and reactor development (see Table 1).

Concerning catalyst design, as reported by several researches¹³⁻¹⁶, catalysts for OCM reactors should be C_2 -selective and stable at elevated temperature. Two examples of such catalysts are La_2O_3 supported with alkaline-earth metals and $Mn/Na_2WO_4/SiO_2$. Tokovich et al.¹⁷ also investigated the effect of various catalysts on OCM performance. In a more comprehensive study, Zavyalova et al.¹⁴ proposed a map for catalyst selection based on C_2 -selectivity and methane conversion for the OCM process.

According to Kee et al.¹³, the catalyst design is governed by the catalyst metal composition as well as its particle size and morphology. However, according to Schwach et al.¹⁸, the complex relations between heterogeneous and homogeneous reaction networks must be considered in the development of selective catalysts. Accordingly, it can be concluded that the performance of new catalysts should be investigated through reaction pathway analysis. Notably, such an analysis becomes more critical in examining the total system performance of a novel reactor configuration.

Another aspect of OCM process which should be scrutinized is the reactor configuration. Typically, suitable reactor configuration should be selected considering the ease of solid processing and heat control as well as conversion and selectivity. Table 2 shows a comparison between the performance of the packed bed and fluidized bed in terms of chemical and thermal performances. Specifically, thermal control of the fluidized bed (FB) and efficient heat and mass transfer can make this type of contactors (i.e., FB) more desirable. Nonetheless, bypassing the gas through the bubble and side reactions can influence the reactant conversion and selectivity, respectively. Accurately, as the main target of OCM process is converting methane to C_2 -products (e.g., ethane and ethylene), the rate of involved side reactions should be minimized (see Table 3 for more detail). Therefore, it is of high importance to opt the bed configuration and operating conditions in such a way that the C_2 -selectivity can be maximized.

Table 2. Comparison of fluidized and packed bed features and their applications^{19,20}

Applications/features	Packed bed	Fluidized bed
Solid-catalyzed gas-phase reaction	<p>very slow or non-deactivating catalyst.</p> <p>serious temperature control problem limits the size of the unit</p>	<p>For small granular and powdery nonfriable catalyst.</p> <p>Rapid deactivation of Solids can be handled. Efficient control of temperature allows largescale operations.</p>
Gas-solid reaction	<p>unsuitable for continuous operating</p> <p>batch operation results in a non-uniform product</p>	<p>Wide range of solid particles with a fine particle can be used.</p> <p>Operation of large-scale equipment at a uniform temperature.</p> <p>Excellent performance at large scale with uniform temperature.</p>
Temperature distribution in the bed	<p>Where a great deal of heat is involved, large temperature gradients occur.</p>	<p>The almost constant temperature throughout the process due to efficient heat exchange and continuous solid feeding and removal</p>
Particle size	<p>Fairly large and uniform.</p> <p>Upon poor temperature control, sintering and reactor clogging can occur.</p>	<p>Wide size distribution with fines. Vessel and pipelines erosion, particles attrition and entrainment may be serious.</p>
Pressure drop	<p>Due to large particles, pressure drop is not a serious problem</p>	<p>High pressure drop in deep beds results in consumption of large powders</p>
Heat exchange/transport	<p>Inefficient heat exchange necessitates the application of large exchanger surface.</p> <p>Limiting factor in scale-up</p>	<p>Circulating solids provides efficient heat exchange and large heat transport.</p> <p>Heat problems are rarely limiting in scaleup.</p>
conversion	<p>In the case of gas plug flow and temperature control, conversion of close to 100% of the theoretical value is possible</p>	<p>In the case of continuous operations, the mixing of solids and gas bypassing can result in poor performance.</p> <p>High conversion requires staging or different distinctive design.</p>

So far, researches^{2,3,11,21-23} proposed different types of reactors for OCM process, the most important of which are i) packed bed reactor (PBR); ii) fluidized bed reactor (FBR); iii) packed-bed membrane reactor (PBMR). These configurations have their own pros and cons. For instance, in PBRs, due to poor mixing and high exothermicity of OCM reactions, hotspot formation characterized by a local overheating in the order of 100 K is expected. Particularly, formation of hotspots can influence the chemical performance of the bed in terms of C_2 -selectivity¹¹.

On the other hand, due to the efficient mixing of solid particles in FBRs, the reactor is claimed to be isothermal²⁴, i.e., hotspot formation is prevented. However, considering the reaction chain for OCM, a high rate of heat and mass transfer in FBs may result in a rapid consumption of oxygen. In Table 3, the kinetic model developed by Stansch et al.²⁵ has been presented for heterogeneous reactions occurring in OCM reactors. It should be mentioned that various kinetic models have been developed for OCM process. However, it is generally accepted that similar reaction pathways are predicted for different kinetics models as reported by Kee et al.¹³.

Table 3. Heterogeneous reactions: Kinetic Model reported by Stansch et al.²⁵

Reaction	Equation	Reaction heat [kJ/mol]
Total oxidation of methane	$CH_4 + 2O_2 \rightarrow CO_2 + 2H_2O$	-802.2
Oxidative coupling of methane to ethane	$2CH_4 + 0.5O_2 \rightarrow C_2H_6 + H_2O$	-176.8
Partial oxidation of methane	$CH_4 + O_2 \rightarrow CO + H_2O + H_2$	-227.5
Oxidation of carbon monoxide	$CO + 0.5O_2 \rightarrow CO_2$	-282.98
Oxidative dehydrogenation of ethane	$C_2H_6 + 0.5O_2 \rightarrow C_2H_4 + H_2O$	-104.86
Oxidation of ethylene	$C_2H_4 + 2O_2 \rightarrow 2CO + 2H_2O$	-755.92
Thermal dehydrogenation of ethane	$C_2H_6 \rightarrow C_2H_4 + H_2$	+136.96
Steam reforming of ethylene	$C_2H_4 + 2H_2O \rightarrow 2CO + 4H_2$	+210.31
Water-gas shift reaction	$CO + H_2O \rightleftharpoons CO_2 + H_2$	-41.17

1.2.2 Key Parameters Influencing OCM Reactor Performance

Chemical and thermal performances of OCM reactors are mainly governed by the parameters influencing the contribution of reactions involved in the process. It is generally accepted that many factors should be addressed during reactor analysis, such as feeding policy, feed composition, inlet feed temperature, operating pressure, and temperature. The effect of these parameters on the reactor performance will be thoroughly discussed in Chapter 1.5.1. Moreover, catalyst characteristics can influence the performance of OCM reactors in various ways.

Most importantly, the metal composition of catalyst can influence the reaction rates as reported by Kee et al.¹³. However, the reaction pathway remains almost unchanged for the developed catalysts. Secondly, the particle size and morphology of catalyst can influence the surface area available for heterogeneous reaction, and consequently methane conversion. In the case of using FBs, the size and density of the catalyst employed in reactive system figure predominantly in the fluidization regime and therefore the bed performance. Specifically, the application of smaller particles with lower density at constant fluidization velocity results in more efficient solid mixing. This can also improve the rate of heat and mass transfer as long as gas bypassing is not dominant.

In addition to the catalyst composition and geometry, thermal resistance and long-term stability of catalyst at high temperature are of high importance in the selectivity of catalyst. This can influence the overall performance of the OCM reactors. It should be noted that researchers¹³ are putting an effort to develop new catalysts for OCM reactors, which can be operated at a lower temperature, e.g., operating temperature < 600°C¹³. In addition, the configuration of the reactors, reactant residence time, and the way heat is supplied can have an enormous impact on the reactor performance.

1.2.3 The Need for Numerical Simulation

In catalytic reactors with a set of chemical reactions, the rates of the surface and gas-phase reactions are governed by the bed temperature and species partial pressure. Similarly, in OCM case, the local reactant pressure (e.g., O_2) and local temperature characterize the contribution of the desired reactions and undesired reactions.

Likewise, the net generated heat can influence the distribution of temperature in the catalytic bed. Therefore, strong coupling between heat and mass transfer cannot be neglected in the analysis of the multiphase reactive systems as in the OCM process.

This outcome motivates researchers to evaluate the bed performance via reaction pathway analysis to examine the contribution of each reaction. Evaluation of the OCM reactor performance is often accomplished through experimental and numerical studies. Due to the intense competition between reactions in the consumption of reactants, the contribution of each reaction cannot be quantified experimentally²⁶. As a result, application of numerical tools enables us potentially to analyze the reaction in such systems much more precisely.

Furthermore, the complex flow of particles in FBs and spatio-temporal fluctuations of flow properties, induced by bubble motion, cannot be easily captured through experimental measurements. In contrast, numerical approaches such as the Euler-Lagrange (EL) and Euler-Euler (EE) can provide point information on the distribution of compositions, reaction rates, and temperature. This enables us to evaluate the formation of, e.g., hotspots in a packed bed reactor and counteract unwanted effects through sensitivity analysis.

Design and optimization of the catalytic reactors necessitate to understand deeply the effect of operating parameters on reactor performance. Experiments on the large scale are associated with a great deal of material, energy, and time. Therefore, developing computational tools can significantly facilitate design and optimization of such process and minimize the number of required experiments. Furthermore, researchers can take advantage of the numerical approach to test the reactor performance in the stage of conceptual design.

1.3 Computational Methods for Investigation of Catalytic Reactors

Simulation of gas-particle flow is generally carried out using two approaches: Euler-Lagrange (EL) and Euler-Euler (EE) approaches. In the first approach, EL, the fluid is considered as a continuum, and the flow is solved using the well-known (volume-averaged) Navier-Stokes equation. On the other hand, the particles in this approach are

considered as discrete entities, and their motion is solved considering Newton's second law.

In the second approach, i.e., EE, both fluid and particles are treated as continua so that Navier-Stokes-like equations will be solved for both phases. In what follows, a brief description of EL and EE approaches will be presented.

1.3.1 Euler-Lagrange Approach

In the EL approach, to simulate fluid flow, the Navier-Stokes momentum equation is solved:

$$\partial_t(\varepsilon_g \rho_g \mathbf{u}_g) + \nabla \cdot (\varepsilon_g \rho_g \mathbf{u}_g \otimes \mathbf{u}_g) = \varepsilon_g \nabla \cdot \boldsymbol{\tau}_g - \varepsilon_g \nabla P_g + \boldsymbol{\Phi}_d + \varepsilon_g \rho_g \mathbf{g} \quad (1)$$

The first and second terms on the left-hand side of the equation represent the accumulation and the convection forces, respectively. The first and second terms on the right-hand side of the equation (1) stand for the viscous and the pressure forces, in the same order. $\boldsymbol{\Phi}_d$ denotes the fluid-particle interphase drag force. This force is commonly considered as the main force contributing to momentum exchange between the fluid and the particle in a gas-solid fluidized bed and packed bed. Finally, the term $\varepsilon_g \rho_g \mathbf{g}$ expresses the gravitational force.

Individual particle motion is simulated through Newton's second law for both the translational and the rotational motion as

$$\rho_s V_s \partial_t \mathbf{u}_s = \mathbf{f}_{\text{cont}} + \beta_{gs} V_s (\mathbf{u}_g - \mathbf{u}_s) - V_s \nabla P_g + \mathbf{f}_g \quad (2)$$

$$d_t(I_s \cdot \boldsymbol{\omega}_{p,i}) = \mathbf{t}_i \quad (3)$$

In Equation (1), the term \mathbf{f}_{cont} denotes the particle-particle contact force, and $\beta_{gs} V_s (\mathbf{u}_g - \mathbf{u}_s)$ represents the drag force exerted on the particle surface by the fluid. Finally, the terms $V_s \nabla P_g$ and \mathbf{f}_g stand for the far field pressure force, and the gravity force, respectively. The force due to particle collision can be described using a soft-sphere model based on the spring-dashpot model, which was adopted by Tsuji et al.²⁷ for studying fluidized beds for the first time.

1.3.2 Euler-Euler Approach

In the EE approach, known as the two-fluid model (TFM) in case of having one solid phase, both solid and fluid phases are treated as interpenetrating continua²⁸. Therefore, Navier-Stokes-like equations are employed to predict the solid flow and the volume fraction.

This approach is much more affordable than the EL approach as the governing equations for each particle is not solved. Therefore, researchers can take advantage of the EE approach in simulating a larger scale gas-particle flow compared to the EL approach. However, application of EL approach is more reasonable in case particle-particle interaction matter, e.g., in case of cohesive particles with liquid bridge formation.

Since the solid phase is considered as a fluid in the EE approach, we need to define the fluid-like properties of the solid phase such as solid pressure, viscosity, and granular temperature. Therefore, the kinetic theory of granular flow²⁸ (KTGF), as an extension of the kinetic theory of gases, is adopted to compute these properties through a set of constitutive equations. Together with other closures (e.g., so-called frictional stress models for dense regions), KTGF can then be used to close the set of governing equations. Eventually, the momentum balance equations for gas and solid phases can be derived respectively as follows

$$\partial_t(\varepsilon_g \rho_g \mathbf{u}_g) + \nabla \cdot (\varepsilon_g \rho_g \mathbf{u}_g \otimes \mathbf{u}_g) = -\varepsilon_g \nabla P_g + \nabla \cdot (\varepsilon_g \boldsymbol{\tau}_g) - \mathbf{I}_{gs} + \varepsilon_g \rho_g \mathbf{g} \quad (4)$$

$$\partial_t(\varepsilon_s \rho_s \mathbf{u}_s) + \nabla \cdot (\varepsilon_s \rho_s \mathbf{u}_s \otimes \mathbf{u}_s) = -\varepsilon_s \nabla P_g - \nabla \cdot (\mathbf{S}_s^{kc} + \mathbf{S}_s^{fr}) + \mathbf{I}_{gs} + \varepsilon_s \rho_s \mathbf{g} \quad (5)$$

The first term appearing on the right-hand side of Eqn. (5) denotes the static pressure force. \mathbf{S}_s^{kc} and \mathbf{S}_s^{fr} represent the solid stress tensor due to kinetic-collisional and frictional contributions, respectively. The third term (i.e., \mathbf{I}_{gs}) stands for momentum exchange force, and the last term represents the contribution of gravitational forces.

Apart from the hydrodynamics, the performance of the reactive gas-solid flow is driven by the heat and mass transfer through the exchange phenomena involved, which is briefly described in the following section.

1.3.3 Heat and Mass Transport

As discussed above, in addition to gas and solid flow, the performance of catalytic reactors (e.g., packed and fluidized bed reactors) is also influenced by reaction rates through heat and mass transfer. Consequently, it is essential to solve the governing equations for heat and species transport. Considering the rate of reactions, the species transport equation for phase q , as well as the heat balance equations for gas and solid phases can be respectively derived as

$$\partial_t(\varepsilon_q \rho_q x_{q_i}) + \nabla \cdot (\varepsilon_q \rho_q x_{q_i} \mathbf{u}_q) = \nabla \cdot (D_{q,x_i} \nabla(\varepsilon_q \rho_q x_{q_i})) + R_{q_i} \quad (6)$$

$$\begin{aligned} \partial_t(\varepsilon_g \rho_g C_{Pg} T_g) + \nabla \cdot (\varepsilon_g \rho_g C_{Pg} T_g \mathbf{u}_g) \\ = -\nabla \cdot \mathbf{q}_g - h(T_s - T_g) - \Delta H_{rg} + \gamma_R(T_R^4 - T_s^4) \end{aligned} \quad (7)$$

$$\partial_t(\varepsilon_s \rho_s C_{Ps} T_s) + \nabla \cdot (\varepsilon_s \rho_s C_{Ps} T_s \mathbf{u}_s) = -\nabla \cdot \mathbf{q}_s + h(T_s - T_g) + \gamma_R(T_R^4 - T_s^4) \quad (8)$$

In Eqn. (6), R_{q_i} is the generation rate of component i in phase q due to reactions. The terms on the left-hand side of Eqns. (7)-(8) denote the accumulation of thermal energy and convective heat transfer rate in gas and solid phases, respectively. The first term in the right-hand side of these two equations represents the heat transfer due to conduction in the corresponding phase and is given by

$$\mathbf{q}_g = -\varepsilon_g k_g \nabla T_g \quad (9)$$

$$\mathbf{q}_s = -\varepsilon_s k_s \nabla T_s \quad (10)$$

The rate of heat exchange between gas and solid phases are given by $h(T_s - T_g)$. It should be noted that due to the elevated temperature applied in OCM reactors, the heat transfer due to radiation must be included in the heat balance equation (see the last term in the right-hand side of Eqns. (7)-(8)). The reader is referred to chapters 4 and 5 for more detailed information on the corresponding governing and constitutive equations.

1.3.4 Goal I: Verification of Simulation Platform

It is generally accepted that the accuracy of the numerical approach should be demonstrated for reliable use. This analysis is typically performed through validation against experimental data or verification based on analytical solutions. It will be

preferred more to take advantages of both approaches to examine the reliability of the model implementation in the adopted numerical platform²⁹. For instance, the accuracy of the heat transfer implementation (see Eqns. (7)-(8)) needs to be evaluated for heterogeneous reactive systems.

Experimental validation of the heat transfer implementation is faced with several challenges. Most importantly, the contribution of various mechanisms of heat transfer hinders the accurate evaluation of the targeted mechanism of heat transfer. For instance, heat loss from the wall cannot be completely avoided upon temperature measurement in a bed. Patil et al.^{30,31} reported that the measurement of particle temperature in fluidized beds via infrared camera obstructs insulation of the reactor wall. In detail, they claimed that the wall heat transfer coefficient needs to be adjusted to fit the solid temperature predicted by CFD-DEM with the measured values.

Turning to analytical solutions, most of verifications have been carried out based on the solution proposed by Schumann³². However, only the heat exchange rate between the two phases was considered in this solution, which means no reaction or phase change occurs in the systems. Nonetheless, reaction or phase change are inseparable features of most applications of gas-solid contactors (e.g., catalytic reactors and wet fluidized beds^{24,33}). Hence, derivation of an analytical solution for such systems seems to be crucial. In summary, the following research goal is set as:

An analytical solution is presented to verify reactive gas-particle flow simulations, and the correctness of the predicted temperature profiles from CFD-DEM based simulations are compared with the corresponding analytical values.

1.4 The Need for Evaluation of Solid Mixing in FBs

As briefly mentioned in section 1.2.2, bubbling fluidized beds (BFBs) are claimed to provide fast solid and gas mixing, as well as a high rate of heat and mass transfer³⁴. Accordingly, in most simplified models, fluidized bed reactors are assumed to be well-mixed contactors (see Table 2 for more details). However, if releasing thermal energy is faster than the solids mixing rate, FBs will deviate from the well-mixed state. Moreover, segregation and/or inefficient solid and gas mixing amplify this

consequence. Askarishahi et al.^{24,33} showed that adding liquid via spraying causes a high degree of non-uniformity in the solid and gas temperatures in wet fluidized beds. Similarly, several researchers reported that fluidized beds operate non-uniformly in some chemical applications such as biomass process³⁵, particle coaters³⁶, bitumen crackers,³⁷ or in case of highly reactive particles in chemical looping reforming reactors (CLR)³⁸. Thus, quantification of solid and gas mixing is a requisite for process assessment, optimization, and design. To do so, the effect of key parameters influencing mixing in FBs should be qualitatively and quantitatively investigated.

1.4.1 Key Parameters Influencing Mixing in Fluidized Beds

Solids mixing in gas-solid BFBs occurs at two levels, namely, i) gross circulation of particles; and ii) local mixing. The first mixing level is also known as solids dispersion, which is induced by wake shedding, upward drifting of the emulsion phase, and the gas bubble breakup at the bed surface. The second level of mixing is also known as solids diffusivity, which is governed by various phenomena: i) particle interaction in the gas bubble wake, ii) particle exchange between emulsion phase and wake, and iii) the random movement of solid particles in the emulsion phase. Therefore, it can be claimed that solid mixing is influenced by various parameters including fluidization velocity; bed aspect ratio; solid-phase properties; and gas distribution type.

1.4.2 Goal II: Importance of Solid Mixing and the Degree of Uniformity

In FBRs, the efficiency of reactant conversion and the selectivity of desired products depend on the motion of solid particles in the dense bed and freeboard. For instance, in OCM reactors, deficient particle mixing in the dense bed can intensify gas-phase reactions.^{39,40} Consequently, an undesired conversion of methane to CO_x in the freeboard and in the bubble phase can occur. This conversion can occur to the extent that C_2 -selectivity is seriously undermined. Therefore, the utilization of a numerical approach to simulate solid and gas mixing can help us to identify optimal scenarios for design and operation of OCM reactors. Various researchers⁴¹⁻⁴⁶ studied the solid mixing through the analysis of time-averaged solid velocity fields, i.e., solid flow pattern. They evaluate the effect of operating conditions (fluidization velocity, static bed height) and particle diameter on the number and size of the vortices formed in the

bed. Such an analysis can be employed to correctly design and locate fuel feeding ports in fluidized bed reactors⁴⁷⁻⁴⁹ and consequently to improve the feeding policy.

What is more, connecting solid flow pattern to solid mixing rate can be advantageous in the evaluation of mixing quality. Mixing in a fluidized bed can be connected to the bubble-induced motion of solid particles in the bed. In detail, formation of persistent small vortices in the bed can be an indicator of pseudo dead zones in which the particle cannot easily mixed in entire bed. Such a phenomenon may typically occur at fluidization velocity very close to minimum fluidization velocity. Previous studies on solid flow pattern did not address such issues⁵⁰⁻⁵². Therefore, it is worthwhile to quantify the degree of mixing in the fluidized beds by evaluating uniformity of scalar quantity in the fluidized bed^{24,53}. In detail, developing affordable tools to simulate transport phenomena in fluidized beds may facilitate optimization and design of FBRs. However, extension of simplified models such as the two-phase model^{20,54} and dispersion model requires evaluation of dominant mechanism in the FBR. These mechanisms include solid dispersion in both lateral and axial direction,⁵⁵ as well as at the particle level (diffusivity). In other words, a set of correlations should be developed by connecting dispersion and diffusion coefficients to the operating condition and particle properties. Such correlations can notably improve the accuracy of simplified models predicting thermal and chemical performance of FBR. To be more specific, the ratio of chemical reaction rate to the rate of dispersive/diffusive solid mixing can determine the dominant mechanism of mass transfer in the bed. This ratio can be quantified based on a Damköhler number defined as the ratio of a flow time scale to a chemical time scale. To put it differently, if solid dispersion can be accurately quantified in an FBR, the optimum operating condition in favor of desired reaction can be estimated. This requires correlating the mixing time to relevant quantities (e.g., dispersion coefficient, particle properties, and fluid velocity).

In summary, correlating solid dispersion and diffusivity to the operating parameter can be of great advantage for the improvement of FBR performance. Experimental approaches are faced with several challenges due to the inherently transient nature of flow in fluidized beds. As a result, a numerical approach can be a promising tool to

develop such correlations, as adopted in the present work. Based on this analysis, the second goal of the present contribution is set to

Quantification of solid mixing in a fluidized bed reactor for a wide range of operating parameters and Geldart B particle by developing a set of correlations for solid dispersion and diffusion coefficients, as well as solid mixing time.

1.5 The Need for CFD-based Simulation of OCM Reactors

As mentioned in Section 1.2.1, in OCM reactors, desired and undesired reactions intensively compete against each other in consuming O_2 . Therefore, it is essential to design a reactor in such a way that the rates of total and partial oxidation of methane are minimized. In detail, optimization of the reactor performance requires a deep understanding of the contribution of critical parameters on distribution of reactants and temperature in the bed.

1.5.1 Challenges in Optimization of Reactor Performance

As mentioned earlier, the thermal and chemical performance of OCM reactors is governed by various factors. In summary, these factors can be categorized as follows:

i) Feed flow rate

Increasing the inlet gas flow rate (also known as gas hourly space velocity, GHSV) in fluidized bed results in more efficient mixing of particles. However, the formation of larger bubbles may induce bypassing the gas. Therefore, the overall rate of heat transfer may not necessarily increase with the gas velocity. Besides, gas bypassing undermines the contribution of catalytic reactions as the reactant (e.g., methane) can leave the bed as bubbles without contacting the catalytic particles. Hence, methane conversion may drop at higher feed flow rates. Besides, conversion of ethylene to CO can be accelerated in ethylene oxidation reaction. Investigation of such contributions in C_2 -selectivity is possible via an analysis of reaction pathways and reaction rates in the fluidized bed reactor.

Therefore, the effect of GHSV needs to be investigated carefully, such an analysis can be of great advantage in optimization of reactor length especially in fluidized beds.

ii) Temperature and pressure

Temperature influences the rate of reactions due to the inherent nature of exothermic and endothermic reactions involved in OCM process. Therefore, the temperature can impact the rate of reactions in a different manner. For instance, partial and total oxidation of methane release more thermal energy compared to the oxidative coupling of methane. Hence, operating the bed at an elevated temperature may increase the contribution of oxidative coupling in methane conversion. On the other hand, a rise in operating temperature induces steam reforming of ethylene and thermal dehydrogenation of ethane due to the endothermic nature of these reactions (see Table 3). Since the acceleration of ethylene steam reforming decreases the C_2 -selectivity, such a rise in temperature may not be in favor of OCM performance. Consequently, the influence of temperature on the overall performance of the bed in terms of C_2 -selectivity and CH_4 -conversion cannot be readily evaluated. Accordingly, a detailed analysis of the reaction pathways and sensitivity of the bed performance to the temperature is essential.

The same analysis can be applied to the pressure effect. In detail, the concentration of involved compounds in reactions depends on the local partial pressure of the reactants and products. It should be noted that the reaction rates in the OCM process are based on the adsorption of CO_2 and O_2 on the catalyst surface, which is accounted through partial pressure of these components. Therefore, the effect of pressure on the chemical and thermal performance of the bed must be evaluated by employing a comprehensive reaction pathway analysis.

1.5.2 Goal III: Validated CFD Platform to Analyze OCM Fluidized Bed Reactors

Based on the above discussion, the effect of operating conditions on the thermal and chemical performance of an OCM reactor need to be scrutinized. However, due to intense competition of desired and undesired reactions, experimental evaluation of reaction pathway seems to be impossible. Therefore, utilization of numerical approaches to study OCM reactor performance can offer a great advantage to find the optimum operating conditions leading to the highest C_2 -yield and C_2 -selectivity. As a result, third goal of the present work is set to:

Developing a CFD-based platform to analyze the effect of key operating parameters including feed temperature, pressure, GHSV, and methane to oxygen ratio on the performance of OCM fluidized bed reactor in terms of methane conversion and C₂-selectivity

1.5.3 Goal IV: Performance Analysis of a Packed Bed Membrane Reactor

As reported in Table 3, the desired reaction of OCM has a lower stoichiometric coefficient for O_2 compared to the one in total and partial oxidation of methane (as undesired reactions). Therefore, more efficient mixing in FBs may induce the consumption of O_2 in undesired reactions, followed by a drop in the C_2 -selectivity. As reported by Godini et al.¹¹, reduction of the methane-to-oxygen ratio gives rise in the methane conversion at the cost of a drop in the selectivity of C_2 -products. Hence, the way that oxygen is brought into contact with methane figures prominently in the relative contribution of these desired and undesired reactions of methane conversion.

This fact motivates reactor designers to take the feeding policy and reactant dosing more seriously as an essential factor affecting the performance of the OCM reactor. In detail, partial and total oxidation of methane compete against OCM reaction in the consumption of O_2 . Therefore, fine-dosing of oxygen can be in favor of OCM reactions. This way of feeding can be realized by utilizing a packed bed membrane reactor (PBMR) as proposed by Godini et al.^{10,56}. Their experimental results demonstrated that this configuration can improve the performance of the bed in terms of C_2 -selectivity and hotspot formation avoidance. Comprehensive investigation of reactor performance requires point information to evaluate reactant and product distribution in PBMR reactor radially and axially especially near membrane module. Besides, the contribution of each reaction should also be addressed in the reactor performance analysis, which cannot be readily measured by experimental methods. CFD-based simulations can provide these pieces of information, and thus, the fourth goal of the present dissertation is defined as:

Study of the performance of a PBMR reactor through reaction pathway analysis for OCM application and investigation of reactant dosing on methane conversion and C₂-selectivity using CFD-based simulation

1.6 Concept of the Thesis

Figure 2 encapsulates the goals presented in the current thesis as follows:

First, an analytical solution was derived for thermal performance of packed beds under constant volumetric heat source assumption (see chapter 2). More accurately, the set of heat transfer equations for gas and solid phases was analytically solved by applying Laplace transformation. Afterwards, the accuracy of implemented heat transfer equations for a phase change test case in CFDEM^{®57} code was verified. Eventually, a map was presented to show in which situation Schumann's solution³² is valid.

Subsequently, in Chapter 3, a TFM-based platform was extended to include more rigorous closures for wall boundary conditions (e.g., see Schneiderbauer⁵⁸). Afterward, a set of correlations was developed to quantify the solid mixing in bubbling fluidized beds for a wide range of Geldart B particles based on simulation results.

Thereafter, a TFM-based platform was applied to analyze a challenging multiphase reactive flow problem, i.e., OCM process. In detail, the effect of operating condition and feed compositions is investigated in a reactive bubbling fluidized bed. Finally, the effect of feed dosing on oxidative coupling of methane reactor is investigated through reaction pathways using computational fluid dynamics in a PBMR. The last two goals are presented in Chapter 4 and 5, respectively.

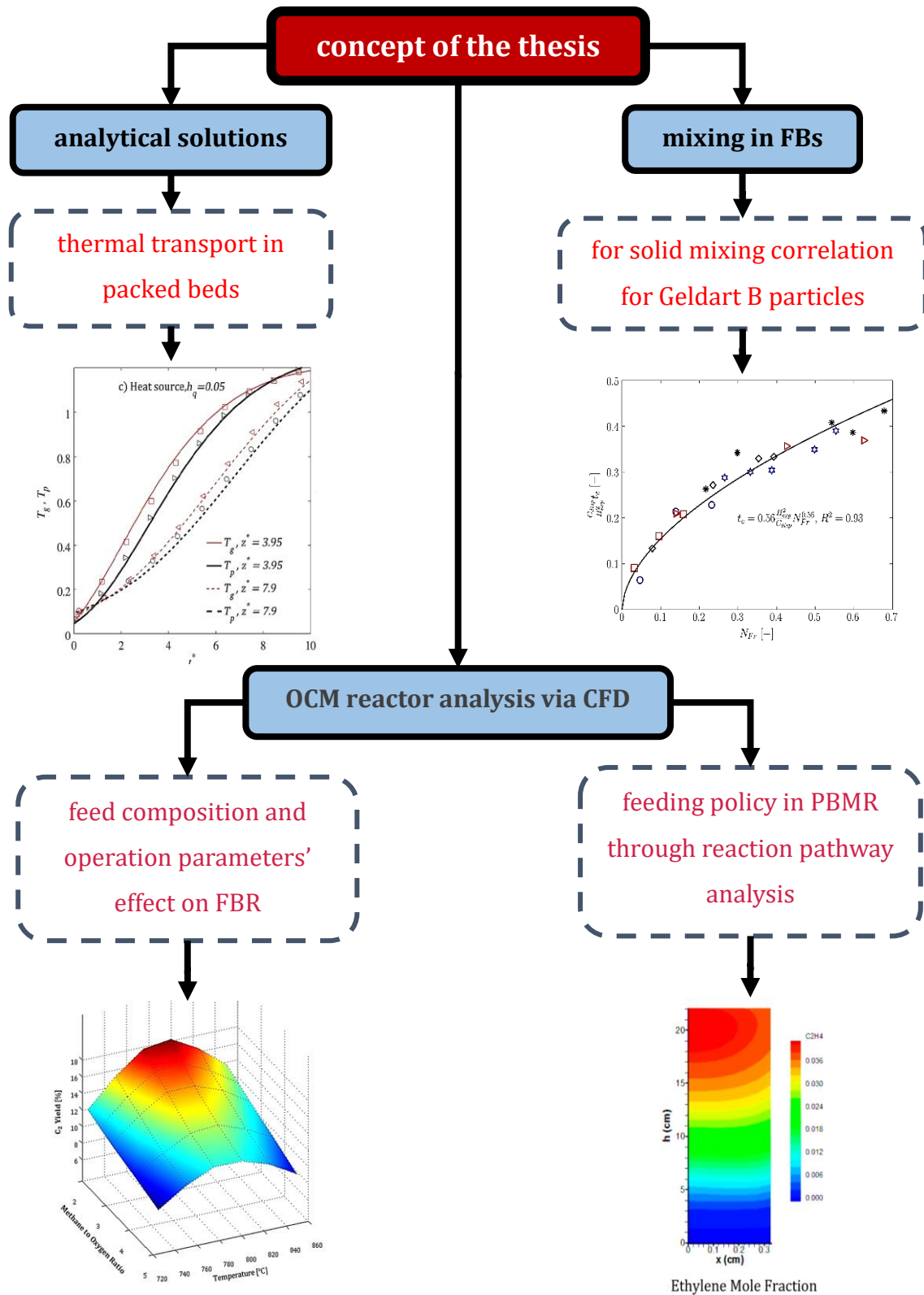


Figure 2. Overview of the topics addressed in the current thesis.

1.7 Abbreviations

CFD	Computational Fluid Dynamics
CLR	Chemical Looping Reforming Reactor
DEM	Discrete Element Method
EL	Euler-Lagrange (method)
EL	Euler-Euler (method)
FBR	Fluidized Bed Reactor
FTS	Fischer Tropsch Synthesis
GHSV	Gas Hourly Space velocity
KTGF	Kinetic Theory of Granular Flow
MFIX	Multiphase Flow with Interphase eXchange
MTO	Methanol to Olefins
OCM	Oxidative Coupling of Methane
PBR	Packed Bed Reactor
PBMR	Packed Bed Membrane Reactor
TFM	Two-Fluid Model
SC	Steam Cracking

1.8 Nomenclature

Latin Symbols

D_{q,x_i}	Diffusion coefficient of species x_i in phase q ; [m^2/s]
\mathbf{f}_{cont}	The particle-particle contact force; [N]
\mathbf{f}_g	The gravitational force; [N]
\mathbf{g}	Gravitational acceleration [m/s^2]
\mathbf{I}_{gs}	Interphase momentum exchange force; [N/m^3]

I_s	Moment of Inertia; [$kg\ m^2$]
P_g	Pressure in the fluid phase; [Pa]
P_s	Solid pressure; [Pa]
q	Fluid or solid phase
R_{qi}	Generation rate of component i in phase q due to reaction; [kg/m^3s]
\mathbf{S}_s^{fr}	Frictional solid stress tensor; [Pa]
\mathbf{S}_s^{kc}	Kinetic and collisional solid stress tensor; [Pa]
\mathbf{t}_i	Total Torque; [Nm]
T_g	Gas-phase temperature; [K]
T_s	Solid-phase temperature; [K]
\mathbf{u}_g	Fluid-phase velocity vector; [m/s]
\mathbf{u}_s	Solid-phase velocity vector; [m/s]
V_s	Solid particle volume; [m^3]
x_{qi}	Mass fraction of scalar quantity in the solid particle

Greek Letters

β_{gs}	Interphase force coefficient; [kg/m^3s]
ε_g	Volume fraction of the fluid phase (void fraction)
ε_s	Volume fraction of solids phase
ρ_g	Microscopic (material) density of the fluid phase; [kg/m^3]
ρ_s	Microscopic (material) density of solids phase; [kg/m^3]
Φ_d	volumetric interaction force; [N/m^3]
$\boldsymbol{\tau}_g$	Gas stress tensor; [Pa]
$\boldsymbol{\omega}_{p,i}$	Rotational speed of a particle [rad/s]; vorticity [$1/s$]

1.9 The Author's Contribution to Publications

The contributions of the author (M-S.S.) to the publications that constitute the present thesis are detailed in Table 4.

Table 4. Contributions of the author of the presented thesis in each publication

No.	Publication	Contribution
1	Salehi, M., Askarishahi, M., & Radl, S. (2017). <i>Analytical Solution for Thermal Transport in Packed Beds with Volumetric Heat Source</i> . Chemical Engineering Journal, 316, 131–136.	M-S.S. has contributed the original idea for this publication, running simulations, and in writing the manuscript. He also derived the analytical solution.
2	Salehi, M., Askarishahi, M., & Radl, S. (2019). <i>Quantification of solids mixing in bubbling fluidized beds via TFM simulations</i> . Submitted to Powder Technology.	M-S.S. has contributed the original idea, has contributed to writing the manuscript and post-processing the simulations. He ran all the simulations.
3	Salehi, M., Askarishahi, M., Godini, HR., & Wozny, G. (2016). <i>CFD Simulation of Oxidative Coupling of Methane in Fluidized-Bed Reactors: A Detailed Analysis of Flow-Reaction Characteristics and Operating Conditions</i> . Industrial & Engineering Chemistry Research, 55, 1149-1163.	M-S.S. has contributed the original idea for this publication, has contributed to writing the manuscript and in running the simulation, as well as post-processing the simulations.
4	Salehi, M., Askarishahi, M., Godini, HR., Görke, O., & Wozny, <i>Sustainable Process Design for Oxidative Coupling of Methane (OCM): Comprehensive Reactor Engineering via Computational Fluid Dynamics (CFD) Analysis of OCM Packed-Bed Membrane Reactors</i> . Industrial &	M-S.S. has contributed the original idea for this publication, has contributed to writing the manuscript and in running the simulations, as well as post-processing the simulations.

Engineering Chemistry Research, 55, 12,
3287-3299.

1.10 References

1. Lewandowski, S. Ethylene–Global. in *Asia Chem. Conf* (2016).
2. Amghizar, I., Vandewalle, L. A., Van Geem, K. M. & Marin, G. B. New Trends in Olefin Production. *Engineering* **3**, 171–178 (2017).
3. Kondratenko, E. V & Baerns, M. *Handbook of Heterogeneous Catalysis*. (Wiley-VCH, Weinheim, 2008).
4. San Su, Y., Ying, J. Y. & Green Jr, W. H. Upper bound on the yield for oxidative coupling of methane. *J. Catal.* **218**, 321–333 (2003).
5. Penteado, A., Esche, E. & Wozny, G. Implementation of a Customized Gas-Separation Membrane Model into Commercial Flowsheeting Software to Simulate a Hybrid CO₂ Removal Process for Oxidative Coupling of Methane. in *AIChE Annual Meeting* (2015).
6. Stöcker, M. Methanol-to-hydrocarbons: catalytic materials and their behavior. *Microporous Mesoporous Mater.* **29**, 3–48 (1999).
7. Tian, P., Wei, Y., Ye, M. & Liu, Z. Methanol to Olefins (MTO): From Fundamentals to Commercialization. *ACS Catal.* **5**, 1922–1938 (2015).
8. Galadima, A. & Muraza, O. Revisiting the oxidative coupling of methane to ethylene in the golden period of shale gas: A review. *J. Ind. Eng. Chem.* **37**, 1–13 (2016).
9. Sattler, J. J. H. B., Ruiz-Martinez, J., Santillan-Jimenez, E. & Weckhuysen, B. M. Catalytic Dehydrogenation of Light Alkanes on Metals and Metal Oxides. *Chem. Rev.* **114**, 10613–10653 (2014).
10. Godini, H. R., Arellano-Garcia, H., M. Omidkhah, R. Karimzadeh & G. Wozny. Model-based analysis of reactor feeding policies for methane oxidative coupling. *Ind. Eng. Chem. Res.* **49**, 3544–3552 (2010).
11. Godini, H. R. *et al.* Techno-economic analysis of integrating the methane oxidative coupling and methane reforming processes. *Fuel Process. Technol.* **106**, 684–694 (2013).
12. Keller, G. E. & Bhasin, M. M. Synthesis of ethylene via oxidative coupling of methane: I. Determination of active catalysts. *J. Catal.* **73**, 9–19 (1982).
13. Kee, R. J., Karakaya, C. & Zhu, H. Process intensification in the catalytic conversion of natural gas to fuels and chemicals. *Proc. Combust. Inst.* **36**, 51–76 (2017).
14. Zavyalova, U., Holena, M., Schlögl, R. & Baerns, M. Statistical analysis of past catalytic data on oxidative methane coupling for new insights into the composition of high-performance catalysts. *ChemCatChem* **3**, 1935–1947 (2011).
15. Lacombe, S., Zanthoff, H. & Mirodatos, C. Oxidative coupling of methane over

- lanthana catalysts: II. A mechanistic study using isotope transient kinetics. *J. Catal.* **155**, 106–116 (1995).
16. Otsuka, K., Jinno, K. & Morikawa, A. Active and selective catalysts for the synthesis of C₂H₄ and C₂H₆ via oxidative coupling of methane. *J. Catal.* **100**, 353–359 (1986).
 17. Tonkovich, A. L., Carr, R. W. & Aris, R. Enhanced C₂ yields from methane oxidative coupling by means of a separative chemical reactor. *Science (80-.)*. **262**, 221–223 (1993).
 18. Schwach, P., Pan, X. & Bao, X. Direct conversion of methane to value-added chemicals over heterogeneous catalysts: challenges and prospects. *Chem. Rev.* **117**, 8497–8520 (2017).
 19. Basu, P. *Combustion and gasification in fluidized beds*. (CRC press, 2006).
 20. Kunii, D., Levenspiel, O. & Brenner, H. *Fluidization Engineering*. (Elsevier Science, 1991).
 21. Jašo, S., Arellano-Garcia, H. & Wozny, G. Oxidative coupling of methane in a fluidized bed reactor: Influence of feeding policy, hydrodynamics, and reactor geometry. *Chem. Eng. J.* **171**, 255–271 (2011).
 22. Lafarga, D., Santamaria, J. & Menendez, M. Methane oxidative coupling using porous ceramic membrane reactors—I. reactor development. *Chem. Eng. Sci.* **49**, 2005–2013 (1994).
 23. ten Elshof, J. E., Bouwmeester, H. J. M. & Verweij, H. Oxidative coupling of methane in a mixed-conducting perovskite membrane reactor. *Appl. Catal. A Gen.* **130**, 195–212 (1995).
 24. Askarishahi, M., Salehi, M. & Radl, S. Two-Fluid-Model-based Full Physics Simulations of Mixing in Non-Cohesive Wet Fluidized Beds. *Ind. Eng. Chem. Res.* **58**, 12323–12346 (2019).
 25. Stansch, Z., Mleczko, L. & Baerns, M. Comprehensive kinetics of oxidative coupling of methane over the La₂O₃/CaO catalyst. *Ind. Eng. Chem. Res.* **36**, 2568–2579 (1997).
 26. Yang, L., Nieves-Remacha, M. J. & Jensen, K. F. Simulations and analysis of multiphase transport and reaction in segmented flow microreactors. *Chem. Eng. Sci.* **169**, 106–116 (2017).
 27. Tsuji, Y., Kawaguchi, T. & Tanaka, T. Discrete particle simulation of two-dimensional fluidized bed. *Powder Technol.* **77**, 79–87 (1993).
 28. Gidaspow, D. *Multiphase Flow and Fluidization: Continuum and Kinetic Theory Descriptions*. (Elsevier Science, 2012).
 29. Radl, S. *Micro-and Mesoscopic Models for Flow and Mixing of Suspensions*. (TU Graz, 2017).
 30. Patil, A. V., Peters, E., Sutkar, V. S., Deen, N. G. & Kuipers, J. A. M. A study of heat transfer in fluidized beds using an integrated DIA/PIV/IR technique. *Chem. Eng. J.* **259**, 90–106 (2015).

31. Patil, A. V, Peters, E. & Kuipers, J. A. M. Comparison of CFD–DEM heat transfer simulations with infrared/visual measurements. *Chem. Eng. J.* **277**, 388–401 (2015).
32. Schumann, T. E. W. Heat transfer: A liquid flowing through a porous prism. *J. Franklin Inst.* **208**, 405–416 (1929).
33. Askarishahi, M., Salehi, M.-S. & Radl, S. Full-physics simulations of spray-particle interaction in a bubbling fluidized bed. *AIChE J.* **63**, 2569–2587 (2017).
34. Yang, W. C. *Handbook of Fluidization and Fluid-Particle Systems*. (Taylor & Francis, 2003).
35. Salatino, P. & Solimene, R. Mixing and segregation in fluidized bed thermochemical conversion of biomass. *Powder Technol.* **316**, 29–40 (2017).
36. Hemati, M., Cherif, R., Saleh, K. & Pont, V. Fluidized bed coating and granulation: influence of process-related variables and physicochemical properties on the growth kinetics. *Powder Technol.* **130**, 18–34 (2003).
37. Cui, H. P. *et al.* Gas and solids mixing in a dynamically scaled fluid coker stripper. *Chem. Eng. Sci.* **61**, 388–396 (2006).
38. Andersson, S. *et al.* Towards rigorous multiscale flow models of nanoparticle reactivity in chemical looping applications. *Catal. Today* **338**, 152–163 (2019).
39. Zanthoff, H. & Baerns, M. Oxidative coupling of methane in the gas phase. Kinetic simulation and experimental verification. *Ind. Eng. Chem. Res.* **29**, 2–10 (1990).
40. Lane, G. S. & Wolf, E. E. Methane utilization by oxidative coupling: I. A study of reactions in the gas phase during the cofeeding of methane and oxygen. *J. Catal.* **113**, 144–163 (1988).
41. Askarishahi, M., Salehi, M.-S. & Molaei Dehkordi, A. Numerical investigation on the solid flow pattern in bubbling gas-solid fluidized beds: Effects of particle size and time averaging. *Powder Technol.* **264**, 466–476 (2014).
42. Askarishahi, M., Salehi, M.-S., Godini, H. R. & Wozny, G. CFD study on solids flow pattern and solids mixing characteristics in bubbling fluidized bed: Effect of fluidization velocity and bed aspect ratio. *Powder Technol.* **274**, 379–392 (2015).
43. Laverman, J. A. *et al.* Experimental study on the influence of bed material on the scaling of solids circulation patterns in 3D bubbling gas-solid fluidized beds of glass and polyethylene using positron emission particle tracking. *Powder Technol.* **224**, 297–305 (2012).
44. Laverman, J. A., Roghair, I., Van Sint Annaland, M. & Kuipers, H. Investigation into the hydrodynamics of gas-solid fluidized beds using particle image velocimetry coupled with digital image analysis. *Can. J. Chem. Eng.* **86**, 523–535 (2008).
45. Luo, K., Wu, F., Yang, S. & Fan, J. CFD-DEM study of mixing and dispersion behaviors of solid phase in a bubbling fluidized bed. *Powder Technol.* **274**, 482–493 (2015).
46. Li, Y., Fan, H. & Fan, X. Identify of flow patterns in bubbling fluidization. *Chem. Eng. Sci.* **117**, 455–464 (2014).

47. Liu, D. & Chen, X. Lateral solids dispersion coefficient in large-scale fluidized beds. *Combust. Flame* **157**, 2116–2124 (2010).
48. Garcia-Gutierrez, L. M., Soria-Verdugo, A. & Ruiz-Rivas, U. Optimization of the feeding ports location in a fluidized bed combustor based on Monte Carlo simulations of fuel particles motion. *Fuel* **141**, 82–92 (2015).
49. Shen, L., Zhang, M. & Xu, Y. Solids mixing in fluidized beds. *Powder Technology* **84**, 207–212 (1995).
50. Banaei, M., Deen, N. G., van Sint Annaland, M. & Kuipers, J. A. M. Particle mixing rates using the two-fluid model. *Particuology* **36**, 13–26 (2018).
51. Gorji-Kandi, S., Alavi-Amleshi, S. M. & Mostoufi, N. A solids mixing rate correlation for small scale fluidized beds. *Particuology* **21**, 55–64 (2015).
52. Mostoufi, N. & Chaouki, J. Local solid mixing in gas-solid fluidized beds. *Powder Technol.* **114**, 23–31 (2001).
53. Askarishahi, M. Towards Full-Physics Simulation of Wet Fluidized Beds. (TU Graz, 2018).
54. Kunii, D. & Levenspiel, O. Bubbling bed model. Model for flow of gas through a fluidized bed. *Ind. Eng. Chem. Fundam.* **7**, 446–452 (1968).
55. Luo, K., Wu, F., Yang, S. & Fan, J. CFD-DEM study of mixing and dispersion behaviors of solid phase in a bubbling fluidized bed. *Powder Technol.* **274**, 482–493 (2015).
56. Godini, H. R. *et al.* Design and demonstration of an experimental membrane reactor set-up for oxidative coupling of methane. *Chem. Eng. Res. Des.* **91**, 2671–2681 (2013).
57. Goniva, C., Kloss, C., Deen, N. G., Kuipers, J. A. M. & Pirker, S. Influence of rolling friction on single spout fluidized bed simulation. *Particuology* **10**, 582–591 (2012).
58. Schneiderbauer, S., Schellander, D., Löderer, A. & Pirker, S. Non-steady state boundary conditions for collisional granular flows at flat frictional moving walls. *Int. J. Multiph. Flow* **43**, 149–156 (2012).

“An expert is someone who knows some of the worst mistakes that can be made in his subject, and how to avoid them.”

(Werner Heisenberg)

2

Analytical Solution for Thermal Transport in Packed Beds with Volumetric Heat Source

In this section, an analytical solution is derived for packed bed thermal performance under the assumption of a constant volumetric heat source. This solution can be helpful to guide researchers working on packed bed modeling and to verify numerical codes for gas-solid flows.

This article was published in *Chemical Engineering Journal* 316, 2017, 131-136, <http://dx.doi.org/10.1016/j.cej.2017.01.076>

Copyright is held by Elsevier Ltd., and all rights are reserved by this organization. Permission has been granted by Elsevier Ltd. for including the following publication and its appendices into the present thesis.



Short communication

Analytical solution for thermal transport in packed beds with volumetric heat source


 Mohammad-Sadegh Salehi^a, Maryam Askarishahi^b, Stefan Radl^{a,*}
^a Institute of Process and Particle Engineering, Graz University of Technology, Inffeldgasse 13/III, 8010 Graz, Austria

^b Research Center Pharmaceutical Engineering GmbH, Inffeldgasse 13/III, 8010 Graz, Austria

HIGHLIGHTS

- An analytical solution considering a fixed heat source in a packed bed is derived.
- The solution is compared to numerical calculations and CFD-DEM simulations.
- A map that identifies the relative importance of the heat source is proposed.

ARTICLE INFO

Article history:

Received 25 August 2016

Received in revised form 20 November 2016

Accepted 18 January 2017

Available online 20 January 2017

ABSTRACT

We present an analytical solution for the thermal transport in fluid-particle systems that include a spatially and temporally constant volumetric heat source. Our solution enables the rapid calculation of temperature profiles in systems undergoing chemical reactions or phase change phenomena. Also, we propose a map that helps in deciding in which situations the simple solution of Schumann (1929) [15] is enough to calculate fluid and particle temperatures.

© 2017 Elsevier B.V. All rights reserved.

1. Introduction

The thermal design of process equipment in various industrial applications, such as solar power plants [4], thermal energy storage [20], and reactive systems [10] is an essential engineering task. Often, heat exchange between the fluid (often a gas) and the particles in the presence of a heat source has to be considered. This makes the solution of the set of equations challenging, often calling for a numerical solution. An analytical solution to predict the behaviour of such systems can be useful when (i) verifying the correctness of such numerical solutions, as well as (ii) when developing advanced control strategies that require an extremely fast evaluation of model equations [14]. A number of attempts to derive analytical solutions were successful for certain simplified situations: Schumann [15] presented such a solution for transient heat transfer in a one-dimensional packed bed. Even though his solution is valid only for perfectly insulated systems without heat source, it has been extensively used by various researchers [2,5,9,19,20,23,24]. White and Korpela [22] obtained an exact solution for the temperature distribution in a perfectly insulated packed bed (for various initial and boundary conditions) using a Laplace transformation and the method of characteristics. Murata

[11,12] calculated the temperature distribution based on Schumann's method considering heat conduction within the solid particles. Similarly, Villatoro et al. [21] provided an approximate analytical solution for such systems.

Another route was followed in the work of Amundson [1]; he attempted to predict the temperature distribution in moving and fixed beds including a volumetric heat source. Although a heat source was already considered in his work, he assumed that the heat transfer coefficient is so high that the particle and the fluid share the same temperature. Later, Sundaresan et al. [17] somewhat refined this work, however still failing to derive a solution for systems involving a heat source. Later, Sözen and Vafai [16] claimed that the derivation of analytical solutions for predicting temperatures in the packed beds with evaporation (i.e., a negative heat source) is impossible.

We will demonstrate in our present contribution that the above statement of Sözen and Vafai [16] is not accurate in case of a spatially and temporally fixed evaporation rate. Thus, we present an analytical solution that is indeed useful for a wide number of systems in which the volumetric heat source is constant. In detail, we extend the analytical solution presented by Schumann [15] to consider a constant heat source in the solid phase. This will be realized via solving the set of heat transfer equations for the gas and solid phase in the packed bed using Laplace transformation.

* Corresponding author.

E-mail address: radl@tugraz.at (S. Radl).

Another key effort in the recent past was to develop numerical strategies to tackle heat transfer problems in chemical reaction engineering applications. Among the plethora of numerical strategies that have been developed, the so-called “Computational Fluid Dynamics-Discrete Element Method” (CFD-DEM) is one of the most attractive strategies. This method allows (i) studies of packed or fluidized beds, as well as (ii) a direct modelling of the particle phase [3,6,8,10,13,18]. However, a simulation based on the CFD-DEM still requires comparison of methods relying on a continuum versus a discrete representation of the particles to avoid unwanted artefacts caused by the discrete representation of the system. Thus, considering the intrinsic limitations of a numerical solution, it appears that an analytical solution for heat exchange in the fluid-particle system with a heat source would be helpful.

2. Theoretical development

2.1. Packed bed heat transfer model

We consider the transient heat up of gas and particles (with diameter d_p) in a packed bed with a fixed voidage ε_g subject to a fixed volumetric heating rate \dot{q} . All physical properties (i.e., the density ρ and the heat capacity C_p) of the gas and particles are assumed to be constant and independent of the temperature. After neglecting gas dispersion and heat conduction in the particle bed, the following differential heat balance equations for the gas and the particle phase are considered:

$$\varepsilon_g \rho_g C_{p,g} \frac{\partial T'_g}{\partial t} = -\varepsilon_g \rho_g C_{p,g} u_g \frac{\partial T'_g}{\partial z} - ha(T'_g - T'_p) \quad (1)$$

$$(1 - \varepsilon_g) \rho_p C_{p,p} \frac{\partial T'_p}{\partial t} = ha(T'_g - T'_p) + \dot{q} \quad (2)$$

The above equations state that the rate of enthalpy change per unit total volume (for each phase) equals the volumetric heat transfer rate, and the heat inflow due to convection. In the above equations, the specific surface area a in [$\text{m}^2/\text{m}^3_{\text{tot}}$] is defined as:

$$a = (1 - \varepsilon_g) 6/d_p \quad (3)$$

h is the heat transfer coefficient in Eqs. (1) and (2), which is allowed to depend on the flow conditions, but is assumed to be constant throughout the bed. The dimensionless temperatures are defined as

$$T_g = \frac{T'_g - T'_{g,0}}{\Delta T'} = \frac{T'_g - T'_{g,0}}{T'_{g,i} - T'_{g,0}} \quad (4)$$

$$T_p = \frac{T'_p - T'_{p,0}}{\Delta T'} = \frac{T'_p - T'_{p,0}}{T'_{g,i} - T'_{g,0}} \quad (5)$$

The inlet boundary and initial conditions are respectively defined as:

$$T_g(t, 0) = 1 \quad (6)$$

$$T_g(0, z) = 0 \quad (7)$$

$$T_p(0, z) = 0 \quad (8)$$

For simplification, we next define

$$h_g = \frac{ha}{\varepsilon_g \rho_g C_{p,g}} = \frac{6h(1 - \varepsilon_g)}{\varepsilon_g \rho_g C_{p,g} d_p} \quad (9)$$

$$h_p = \frac{ha}{(1 - \varepsilon_g) \rho_p C_{p,p}} = \frac{6h}{\rho_p C_{p,p} d_p} \quad (10)$$

$$h_q = \frac{\dot{q}}{(1 - \varepsilon_g) \rho_p C_{p,p} \Delta T'} \quad (11)$$

We then re-write the transport equations to arrive at

$$\frac{\partial T_g}{\partial t} = -u_g \frac{\partial T_g}{\partial z} - h_g(T_g - T_p) \quad (12)$$

$$\frac{\partial T_p}{\partial t} = h_p(T_g - T_p) + h_q \quad (13)$$

Note that the constants h_g , h_p and h_q have the units [1/s]. It is now natural to identify dimensionless time and space coordinates as $t^* = h_p(t - z/u_g)$ and $z^* = h_g z/u_g$, respectively. Thus, u_g/h_g is a characteristic thermal length. Also, Eqs. (12) and (13) reveal the key dimensionless influence parameters which are (i) a volumetric heat capacity ratio $h^* = \frac{h_g}{h_p} = \frac{(1 - \varepsilon_g) \rho_p C_{p,p}}{\varepsilon_g \rho_g C_{p,g}}$, and (ii) a dimensionless heating rate $h_q^* = \frac{h_q}{h_p}$. In what follows, however, we will first avoid introducing these dimensionless quantities, and analyse the problem given by Eqs. (12) and (13) in its original form. We will return to the dimensionless representation when presenting our results in Chapter 3.

2.2. Solution via Laplace transformation

In order to solve the above set of partial differential equations, Laplace transformation can be used. The Laplace transform of the unknown function $T_g(t, z)$ (and similarly for T_p), as well as its time derivative, are given by

$$\ell\{T_g(t, z)\} = \bar{T}_g(s, z) = \int_0^\infty e^{-st} T_g(t, z) dt \quad (14)$$

$$\ell\left\{\frac{\partial T_g(t, z)}{\partial t}\right\} = s\bar{T}_g(s, z) - T_g(0, z) \quad (15)$$

Hence, Laplace transformation of Eqs. (12) and (13) leads to:

$$s\bar{T}_g - T_g(0, z) = -u_g \frac{\partial \bar{T}_g}{\partial z} - h_g(\bar{T}_g - \bar{T}_p) \quad (16)$$

$$s\bar{T}_p - T_p(0, z) = h_p(\bar{T}_g - \bar{T}_p) + \frac{h_q}{s} \quad (17)$$

Since $T_g(0, z)$ and $T_p(0, z)$ are zero, Eq. (17) can be simplified as:

$$\bar{T}_p = \frac{h_p \bar{T}_g + \frac{h_q}{s}}{s + h_p} \quad (18)$$

By substituting Eq. (18) in Eq. (16), we arrive at

$$\frac{s}{u_g} \left(1 + \frac{h_g}{s + h_p}\right) \bar{T}_g + \frac{\partial \bar{T}_g}{\partial z} = \frac{h_g}{(s + h_p) u_g} \frac{h_q}{s} \quad (19)$$

For simplification we now define

$$\alpha = \frac{s}{u_g} \left(1 + \frac{h_g}{s + h_p}\right) \quad (20)$$

Using the integration factor $e^{\alpha z}$, Eq. (19) is rewritten as

$$\frac{\partial}{\partial z} [e^{\alpha z} \bar{T}_g] = e^{\alpha z} \frac{h_g}{(s + h_p) u_g} \frac{h_q}{s} \quad (21)$$

The solution of this ODE is straight forward and, after considering the boundary condition $T_{g,i}$ for T_g at $z = 0$, leads to

$$\bar{T}_g = \frac{T_{g,i}}{s} e^{-\alpha z} - \frac{h_g h_q}{s(s + h_p) u_g} \frac{1}{\alpha} e^{-\alpha z} + \frac{h_q h_g}{s(s + h_p) u_g} \frac{1}{\alpha} \quad (22)$$

After some substitutions and replacements, the introduction of a scaled bed position $t_c = z/u_g$, and an inverse Laplace transformation, we arrive at:

$$T_g(t, t_c) = T_{g,i} e^{-t_c h_g} e^{-h_p(t-t_c)} J_0(2\sqrt{-a_0(t-t_c)}) + a_q [(h_g + h_p)t - 1 + e^{-(h_g+h_p)t}] + e^{-t_c h_g} [T_{g,i} h_p - a'_q (h_p(t-t_c) + 1) + a_q h_p] I_1 + e^{-t_c h_g} [a'_q h_p I_2 + a_q h_g e^{-(h_p+h_g)(t-t_c)} I_3] \tag{23}$$

$$T_p(t, t_c) = -a''_q \left[\frac{1 - e^{-h_p t}}{h_p} - (h_p + h_g) \left(-\frac{1}{h_p^2} + \frac{1}{h_p} t + \frac{1}{h_p^2} e^{-h_p t} \right) - \frac{\{e^{-h_p t} - e^{-(h_p+h_g)t}\}}{h_g} \right] + \frac{h_q}{h_p} (1 - e^{-h_p t}) + e^{-t_c h_g} [T_{g,i} h_p - a''_q ((h_p + h_g)(t - t_c) - 1)] I_1 + e^{-t_c h_g} [a''_q (h_p + h_g) I_2 - a''_q e^{-(h_p+h_g)(t-t_c)} I_3] \tag{24}$$

Where we have used the following definitions:

$$a_0 = t_c h_g h_p; \quad a_q = \frac{h_g h_q}{(h_g + h_p)^2}; \quad a'_q = \frac{h_g h_q}{h_g + h_p}; \quad a''_q = \frac{h_p h_g h_q}{(h_p + h_g)^2}$$

$$I_1 = \int_0^{t-t_c} e^{-h_p u} J_0(2\sqrt{-a_0 u}) du; \quad I_2 = \int_0^{t-t_c} u e^{-h_p u} J_0(2\sqrt{-a_0 u}) du;$$

$$I_3 = \int_0^{t-t_c} e^{h_g u} J_0(2\sqrt{-a_0 u}) du \tag{25}$$

Details related to the above derivation are comprehensively presented in Appendix A. We note in passing that a simple quadrature method was applied to approximate the integrals in Eq. (25).

3. Result and discussion

3.1. Benchmarking the analytical solution

After successful calculation of the gas and particle temperatures in the packed bed, their time profiles were studied for different heating rates. First, the heating rate was set to zero to investigate pure heat exchange between the gas and the particles. This

situation is identical to that considered by Schumann [15], and a comparison with the Schumann result proved the correct limiting behaviour of our solution. Second, a scenario involving a negative heat source (e.g., due to an endothermic reaction, or evaporation of a liquid from the particle surface) was considered. For this situation, the set of governing equations was discretized and solved using MATLAB® (specifically, the function “pdepe” was used). The temperatures obtained from this numerical calculation and our analytical solution were then compared. This study revealed that the deviation between these two solutions for the particle temperatures was larger than that for the gas temperatures. Hence, only results for particle temperature are depicted in Fig. 1, which shows the time evolution of the error for this temperature. In this figure, we have also included a line for a relative accuracy of 0.1% (i.e.,

$$E_{T_p} = \left| \frac{T_p^{numerical} - T_p^{analytical}}{T_p^{analytical}} \right| = 10^{-3}$$

which acts as the acceptance criterion for the comparison of the numerical and analytical solution. As expected, grid refinement decreases the deviation from the analytical solution at the cost of computation time: in case we use between 10 and 200 discretization points it takes between 10 s and 650 s to evaluate the discretized set of governing equations in MATLAB®, respectively. In contrast, the evaluation of Eqs. (23) and (24) takes less than 5 s in any situation studied here. Clearly, and as it can be seen in Fig. 1, only the solution using more 200 grid cells yields acceptable results (i.e., for which the relative deviation is less than 10^{-3}). Thus, our analytical solution is by at least a factor of 100 faster than a numerical approach, even though we have to numerically approximate the integrals in Eqs. (23) and (24).

3.2. Comparison with predictions from CFD-DEM simulations

After successful calculation of the temperatures, a CFD-DEM code was developed to take a heat source located on the particles' surface into account. Specifically, we implemented all relevant models into the tool CFDEM® [7]. Several simulations were performed using the developed CFDEM® tool considering various heating rates, and the results were compared with that obtained from our analytical solution (see Fig. 2). Clearly, the gas and particle temperatures are in good agreement in most regions of the bed, and systematic deviations are primarily observed near the inlet region. After a careful analysis of these deviations (see Appendix

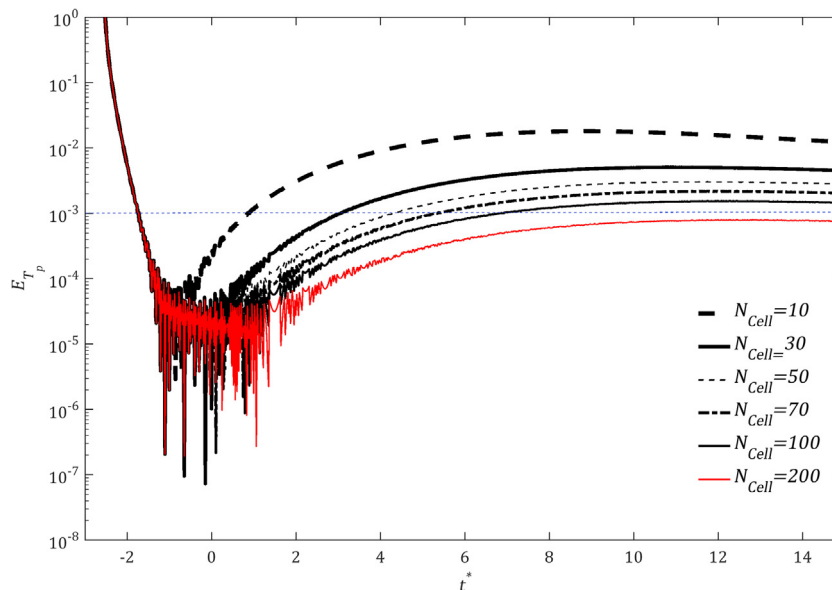


Fig. 1. Error associated with the numerical solution for the particle temperature for a variety of grid resolutions and as a function of the dimensionless time.

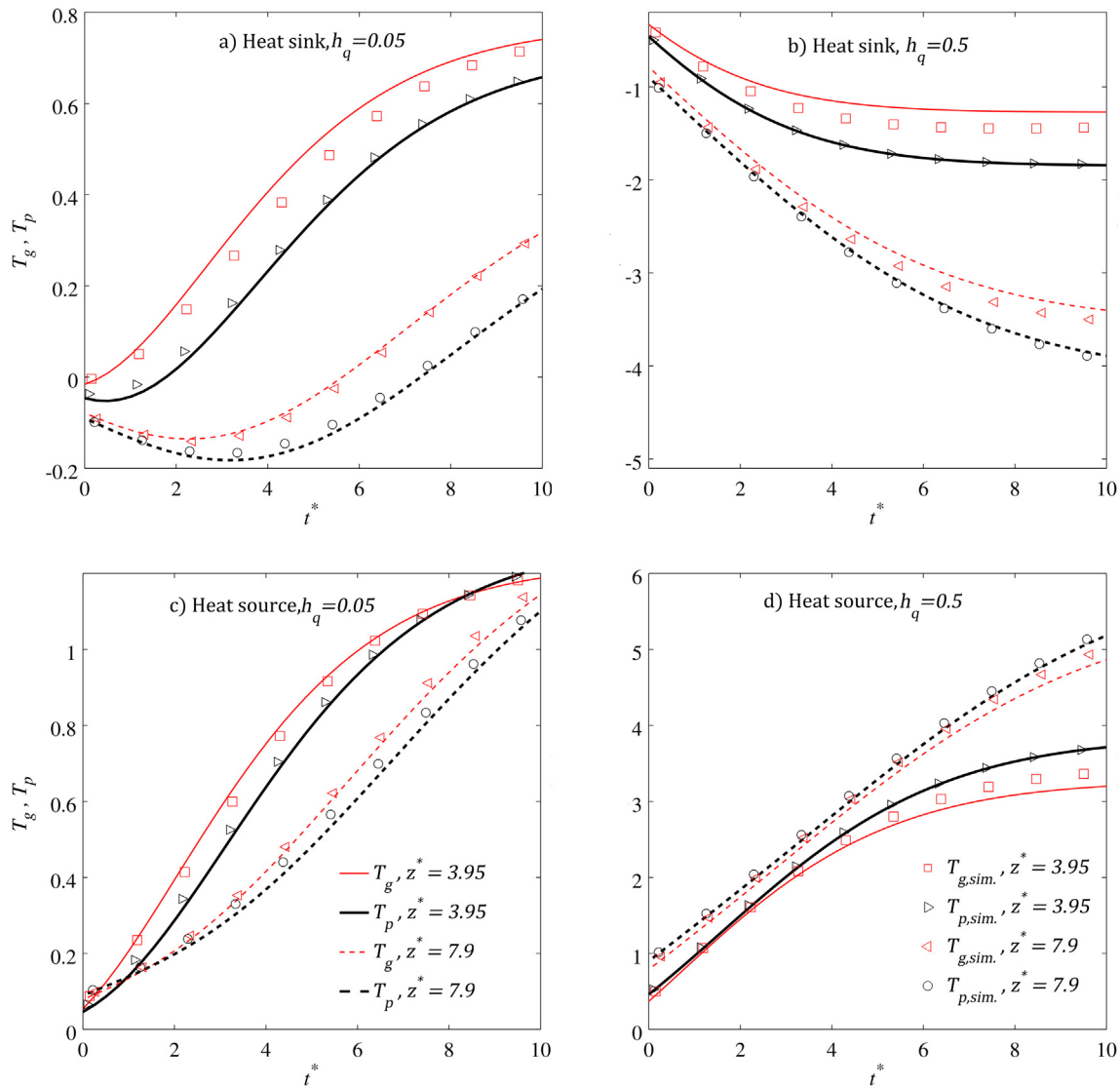


Fig. 2. Comparison of the predicted gas and particle temperatures using CFD-DEM with the corresponding analytical values as a function of time and the cooling rate (panel a: weak heat sink with $h_q^* = -0.05$; panel b: strong heat sink with $h_q^* = -0.5$), as well as the heating rate (panel c: weak heat source with $h_q^* = 0.05$, panel d: strong heat source with $h_q^* = 0.5$). The lines correspond to the analytical solution, whereas the symbols indicate results produced with CFD-DEM[®].

C for details), we conclude that they are due to the Lagrangian-to-Eulerian mapping of the particle volumes: this mapping leads to tiny fluctuation of the local voidage in the particle bed, which are then amplified by the strong dependency of the local heat transfer coefficient on the voidage. Also, it can be observed from Fig. 2 that the deviations for the gas temperature are more pronounced compared to that for the particle temperature. Moreover, an increase in the rate of heat exchange causes a larger deviation between our analytical solution and predictions by CFD-DEM simulations. This is expected, since the main error introduced in a CFD-DEM simulation is due to the above discussed mapping, and hence the predicted local heat transfer coefficient.

We next consider a map spanned by all relevant dimensionless system parameters that indicates solutions close to that of Schumann, i.e., situations with very weak heat sources. Such a map is especially helpful when deciding whether the heat release rate should be considered in a model or not.

3.3. A map to quantify effects due to a heat source

Particle and gas temperatures were calculated using the analytical solution for a large array of combinations of the dimensionless

heating rate $h_q^* = \frac{h_q}{h_p}$ and the volumetric heat capacity ratio $h^* = \frac{h_g}{h_p} = \frac{c_p \rho_p c_{p,p}}{c_g \rho_g c_{p,g}}$. The calculation was performed for a variety of dimensionless times t^* in a packed bed with total length $z^* = h_g z_{bed} / u_g$. We have then determined the critical dimensionless heating rate which leads to a maximum relative error of 20% of the predicted gas or particle temperature when using the Schumann solution. This maximum error occurs at the outlet of the bed, i.e., at $z = z_{bed}$, and hence it is essential to consider the bed length in what follows.

As depicted in Fig. 3 (panel a), for a fixed volumetric heat capacity ratio and bed length, the critical dimensionless heating rate is smaller for the particle temperature compared to the gas temperature. Thus, the error in the particle temperature limits the applicability of Schumann's solution when applying his result to a system with volumetric heat source. Therefore, in what follows we only consider the particle temperature, and results of these calculations are depicted in Fig. 3 (panel b). It can be easily seen from this figure that at identical dimensionless heating rates the volumetric heat capacities ratio only mildly affects the limiting curve of 20% deviation from the Schumann solution. Specifically, an increase in the heat capacity ratio leads to only a weak increase

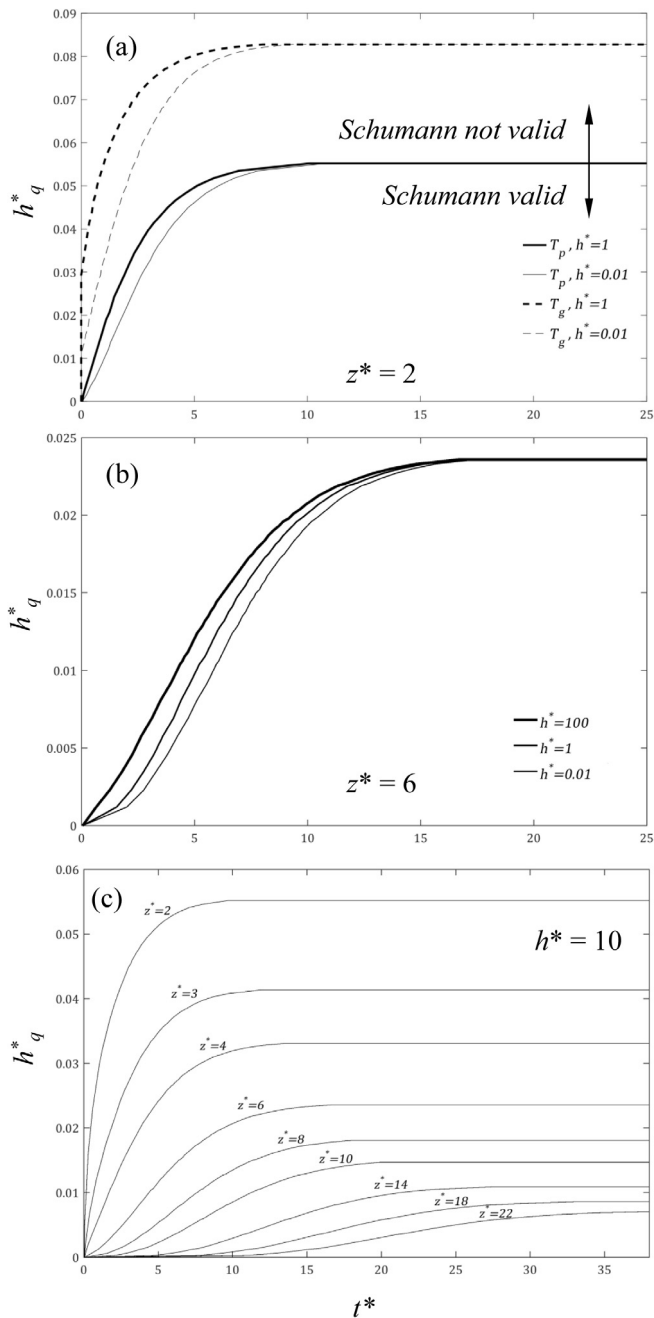


Fig. 3. Map to quantify the validity of Schumann's solution. Panel a: comparison of the map for the gas and particle temperatures at $z^* = 2$. Panel b: the effect of the heat capacity ratio on the particle temperature map for $z^* = 6$. Panel c: the effect of the dimensionless bed height for $h^* = 10$.

in the critical dimensionless heating rate. This is due to the fact that higher volumetric heat capacity ratios reflect a system in which particles have a higher capacity to store the heat. Thus, the thermal inertia of the system is simply greater.

Another point discerned from Fig. 3 (panel b) is that the critical dimensionless heating rate saturates with time, and that all curves for different h^* collapse for long times. Thus, as we approach the steady-state solution, only the dimensionless heating rate (for a fixed bed length) determines the particle temperature in the bed. In other words, and after recalling the definition of $h_q^* = \frac{\dot{q}_p}{6h(1-\epsilon_g)\Delta T}$, this means that the competition of heat release and heat transfer determines the particle temperature for long times. This is also

expected from a simple steady-state analysis considering the particles only. Interestingly, the critical heating rate is always smaller for early times, i.e., before the steady state solution is reached. This simply means that relative errors during the heat up phase of the bed are larger than that when seeking a steady-state solution.

As can be anticipated from our arguments in the last paragraph, the range of h_q^* in which Schumann's solution is valid is strongly affected by the dimensionless height of the bed. In Fig. 3 (panel c) the corresponding map for h_q^* is depicted for $h^* = 10$. We note that for larger values of h^* the results change only marginally, such that the data shown in Fig. 3c represents the limit of infinitely high heat capacity ratios. As shown in this figure, at higher dimensionless height, z^* , the domain of validity for both t^* and h_q^* is narrower. Again, this can be easily explained by the increase of the bed temperature along the flow direction at steady-state conditions.

4. Conclusion

The set of heat transfer equations was analytically solved, utilizing Laplace transformation, for a one-dimensional packed bed with constant volumetric heat source. The correctness of the calculated temperature profiles was proved via a comparison with numerical predictions based on MATLAB[®]. The calculated temperature profiles were then also compared to CFD-DEM-based simulations. This study illustrated the need to improve CFD-DEM mapping schemes, since already minute errors in the predicted local void fraction result in considerable errors when estimating the heat transfer coefficient, and hence the local temperatures.

Since Schumann's solution (i.e., a solution that does not consider a heat source) is extensively used in the literature, we also made an attempt to generate a map of situation in which Schumann's solution is acceptable for heated systems. It was demonstrated that at a constant dimensionless heating rate, an increase in the thermal capacity ratio h^* makes Schumann's solution valid for a wider range of non-dimensional times. However, this effect levels off at $h^* = 10$, and vanishes for long times. Most important, the bed length critically affects the applicability of Schumann's solution.

Acknowledgement

SR acknowledges partial funding for the present research from EC's FP7 Grant agreement no. 604656 (NanoSim). CFDEM[®] is a registered trade mark of DCS Computing GmbH, the producer of the CFDEM[®] coupling software. MA acknowledges Boehringer Ingelheim pharmaceutical company for funding this research project.

Appendix A. Supplementary material

Supplementary data associated with this article can be found, in the online version, at <http://dx.doi.org/10.1016/j.cej.2017.01.076>.

References

- [1] N.R. Amundson, Solid-fluid interactions in fixed and moving beds fixed beds with small particles, *Ind. Eng. Chem.* 48 (1956) 26–35.
- [2] R. Anderson, L. Bates, E. Johnson, J.F. Morris, Packed bed thermal energy storage: a simplified experimentally validated model, *J. Energy Storage* 4 (2015) 14–23.
- [3] M. Askarishahi, M.-S. Salehi, S. Radl, Full-physics simulations of spray-particle interaction in a bubbling fluidized bed, *AIChE J.* (2016), <http://dx.doi.org/10.1002/aic.15616>, Accepted Author Manuscript.
- [4] O. Behar, A. Khellaf, K. Mohammadi, A review of studies on central receiver solar thermal power plants, *Renew. Sustain. Energy Rev.* 23 (2013) 12–39.
- [5] M. Cascetta, G. Cau, P. Puddu, F. Serra, Numerical investigation of a packed bed thermal energy storage system with different heat transfer fluids, *Energy Procedia* 45 (2014) 598–607.

- [6] N. Deen, J. Kuipers, Direct Numerical Simulation (DNS) of mass, momentum and heat transfer in dense fluid-particle systems, *Curr. Opin. Chem. Eng.* 5 (2014) 84–89.
- [7] C. Goniva, C. Kloss, N.G. Deen, J.A. Kuipers, S. Pirker, Influence of rolling friction on single spout fluidized bed simulation, *Particuology* 10 (2012) 582–591.
- [8] A.M. Lattanzi, C.M. Hrenya, A coupled, multiphase heat flux boundary condition for the discrete element method, *Chem. Eng. J.* 304 (2016) 766–773.
- [9] P. Li, B. Xu, J. Han, Y. Yang, Verification of a model of thermal storage incorporated with an extended lumped capacitance method for various solid-fluid structural combinations, *Sol. Energy* 105 (2014) 71–81.
- [10] Z. Li, M. van Sint Annaland, J. Kuipers, N. Deen, Effect of superficial gas velocity on the particle temperature distribution in a fluidized bed with heat production, *Chem. Eng. Sci.* 140 (2016) 279–290.
- [11] S. Murata, Extension of schumann's theory to the case of low thermal diffusivity of solid particles, *J. Chem. Eng. Jpn.* 4 (1971) 140–146.
- [12] S. Murata, Exact analytical solutions to the extension of Schumann's theory on the heat transfer in packed bed, *J. Faculty Agric., Kyushu Univ.* 27 (1983) 151–158.
- [13] A. Patil, E. Peters, J. Kuipers, Comparison of CFD-DEM heat transfer simulations with infrared/visual measurements, *Chem. Eng. J.* 277 (2015) 388–401.
- [14] J. Rehr, J. Kruisz, S. Sacher, J. Khinast, M. Horn, Optimized continuous pharmaceutical manufacturing via model-predictive control, *Int. J. Pharm.* 510 (2016) 100–115.
- [15] T.E. Schumann, Heat transfer: a liquid flowing through a porous prism, *J. Franklin Inst.* 208 (1929) 405–416.
- [16] M. Sözen, K. Vafai, Analysis of the non-thermal equilibrium condensing flow of a gas through a packed bed, *Int. J. Heat Mass Transf.* 33 (1990) 1247–1261.
- [17] S. Sundaresan, N.R. Amundson, R. Aris, Observations on fixed-bed dispersion models: the role of the interstitial fluid, *AIChE J.* 26 (1980) 529–536.
- [18] V.S. Sutkar, N.G. Deen, A.V. Patil, V. Salikov, S. Antonyuk, S. Heinrich, J. Kuipers, CFD-DEM model for coupled heat and mass transfer in a spout fluidized bed with liquid injection, *Chem. Eng. J.* 288 (2016) 185–197.
- [19] M. Valmiki, W. Karaki, P. Li, J. Van Lew, C. Chan, J. Stephens, Experimental investigation of thermal storage processes in a thermocline tank, *J. Sol. Energy Eng.* 134 (2012) 041003.
- [20] J.T. Van Lew, P. Li, C.L. Chan, W. Karaki, J. Stephens, Analysis of heat storage and delivery of a thermocline tank having solid filler material, *J. Sol. Energy Eng.* 133 (2011) 021003.
- [21] F. Villatoro, J. Pérez, F. Domínguez-Muñoz, J. Cejudo-López, Approximate analytical solution for the heat transfer in packed beds for solar thermal storage in building simulators, in: Eleventh International IBPSA Conference, July 2009, pp. 709–715.
- [22] H.C. White, S.A. Korpela, On the calculation of the temperature distribution in a packed bed for solar energy applications, *Sol. Energy* 23 (1979) 141–144.
- [23] B. Xu, P.-W. Li, C.L. Chan, Extending the validity of lumped capacitance method for large Biot number in thermal storage application, *Sol. Energy* 86 (2012) 1709–1724.
- [24] B. Xu, P. Li, C. Chan, Application of phase change materials for thermal energy storage in concentrated solar thermal power plants: a review to recent developments, *Appl. Energy* 160 (2015) 286–307.

Appendix A – Inverse Laplace Transformation

A1. Gas Temperature

The inverse Laplace transform of the first term in right hand side of equation 22, denoted as \bar{T}_{g1} , can be calculated considering that

$$\bar{T}_{g1} = e^{-t_c s (1 + \frac{h_g}{s+h_p})} \frac{T_{g,i}}{s} = \frac{T_{g,i}}{s} e^{-t_c s} e^{-t_c h_g} e^{t_c h_g (\frac{h_p}{s+h_p})} \quad (A1)$$

Note, that we used the scaled bed position $t_c = z/u_g$ in the above equation as described in the manuscript.

By defining $a_0 = t_c h_g h_p$, T_{g1} is given by

$$T_{g1} = T_{g,i} e^{-t_c h_g} \ell^{-1} \left\{ e^{-t_c s} \left[\frac{1}{s} e^{\left(\frac{a_0}{s+h_p} \right)} \right] \right\} \quad (A2)$$

Considering

$$\ell^{-1} \{ e^{-as} \bar{F}(s) \} = \begin{cases} F(t-a) & t > a \\ 0 & t < a \end{cases} \quad (A3)$$

$$\ell^{-1} \{ \bar{F}(s-a) \} = e^{at} F(t) \quad (A4)$$

This equation can be rewritten as

$$T_{g1} = T_{g,i} e^{-t_c h_g} F_1(t-t_c) \quad (A5)$$

Where the function F is represented by

$$\begin{aligned}
F_1(t) &= \ell^{-1} \left\{ \left[\frac{1}{s} e^{\left(\frac{a_0}{s+h_p}\right)} \right] \right\} = \ell^{-1} \left\{ \left[\frac{s+h_p}{s} \frac{1}{s+h_p} e^{\left(\frac{a_0}{s+h_p}\right)} \right] \right\} \\
&= \int_0^t H_1(t-u) G_1(u) du
\end{aligned} \tag{A6}$$

$$G_1(u) = \ell^{-1} \left\{ \left[\frac{1}{s+h_p} e^{\left(\frac{a_0}{s+h_p}\right)} \right] \right\} = e^{-h_p u} \ell^{-1} \left\{ \frac{1}{s} e^{\frac{a_0}{s}} \right\} = e^{-h_p u} J_0(2\sqrt{-a_0 u}) \tag{A7}$$

$$H_1(u) = \ell^{-1} \left\{ \left[\frac{s+h_p}{s} \right] \right\} = \ell^{-1} \left\{ \left[1 + \frac{h_p}{s} \right] \right\} = \delta(u) + h_p \tag{A8}$$

$$F_1(t-t_c) = \int_0^{t-t_c} [\delta(t-t_c-u) + h_p] e^{-h_p u} J_0(2\sqrt{-a_0 u}) du \tag{A9}$$

Here J_0 denotes the Bessel function of order zero. Therefore, the inverse Laplace transform for first term in right hand side is calculated as

$$T_{g1} = T_{g,i} e^{-t_c h_g} \int_0^{t-t_c} [\delta(t-t_c-u) + h_p] e^{-h_p u} J_0(2\sqrt{-a_0 u}) du \tag{A10}$$

For the calculation of the second term in right hand side of Equation 22 we first rewrite this expression as the sum of three sub-terms:

$$\begin{aligned}
\bar{T}_{g2} &= -e^{-t_c s \left(1 + \frac{h_g}{s+h_p}\right)} \left[h_q h_g \frac{1}{s^2} \frac{1}{s+h_g+h_p} \right] \\
&= -e^{-t_c s} e^{-t_c h_g} e^{\left(\frac{a_0}{s+h_p}\right)} \frac{h_q h_g}{(h_g+h_p)^2} \left[\frac{h_g+h_p}{s^2} - \frac{1}{s} + \frac{1}{s+h_g+h_p} \right] \\
&= \bar{T}_{g21} + \bar{T}_{g22} + \bar{T}_{g23}
\end{aligned} \tag{A11}$$

By defining $a_q = \frac{h_q h_g}{(h_g + h_p)^2}$, and $a'_q = \frac{h_q h_g}{h_g + h_p}$, the inverse Laplace transform of \bar{T}_{g21} is given

by

$$\begin{aligned} T_{g21} &= -a'_q \ell^{-1} \left\{ \frac{1}{s^2} e^{-t_c s} e^{-t_c h_g} e^{\left(\frac{a_0}{s+h_p}\right)} \right\} = -a'_q e^{-t_c h_g} \ell^{-1} \left\{ e^{-t_c s} \left[\frac{1}{s^2} e^{\left(\frac{a_0}{s+h_p}\right)} \right] \right\} \\ &= -a'_q e^{-t_c h_g} F_{21}(t - t_c) \end{aligned} \quad (\text{A12})$$

Where the function F_{21} is

$$\begin{aligned} F_{21}(t) &= \ell^{-1} \left\{ \left[\frac{1}{s^2} e^{\left(\frac{a_0}{s+h_p}\right)} \right] \right\} = \ell^{-1} \left\{ \left[\frac{s+h_p}{s^2} \frac{1}{s+h_p} e^{\left(\frac{a_0}{s+h_p}\right)} \right] \right\} \\ &= \int_0^t H_{21}(t-u) G_{21}(u) du \end{aligned} \quad (\text{A13})$$

and the functions $G_{21}(u)$ and $H_{21}(u)$ are given by

$$G_{21}(u) = \ell^{-1} \left\{ \left[\frac{1}{s+h_p} e^{\left(\frac{a_0}{s+h_p}\right)} \right] \right\} = e^{-h_p u} \ell^{-1} \left\{ \frac{1}{s} e^{\frac{a_0}{s}} \right\} = e^{-h_p u} J_0(2\sqrt{-a_0 u}) \quad (\text{A14})$$

$$H_{21}(u) = \ell^{-1} \left\{ \left[\frac{s+h_p}{s^2} \right] \right\} = \ell^{-1} \left\{ \left[\frac{1}{s} + \frac{h_p}{s^2} \right] \right\} = 1 + h_p u \quad (\text{A15})$$

Therefore, T_{g21} is given by

$$T_{g21} = -a'_q e^{-t_c h_g} \int_0^{t-t_c} [h_p(t-t_c-u) + 1] e^{-h_p u} J_0(2\sqrt{-a_0 u}) du \quad (\text{A16})$$

The inverse Laplace transform of \bar{T}_{g22} is, similar to \bar{T}_{g1} , calculated by

$$\begin{aligned}
T_{g22} &= a_q \ell^{-1} \left\{ \frac{1}{s} e^{-t_c s} e^{-t_c h_g} e^{\left(\frac{a_0}{s+h_p}\right)} \right\} = a_q e^{-t_c h_g} \ell^{-1} \left\{ e^{-t_c s} \left[\frac{1}{s} e^{\left(\frac{a_0}{s+h_p}\right)} \right] \right\} \\
&= a_q e^{-t_c h_g} F_1(t - t_c)
\end{aligned} \tag{A17}$$

Thus, the inverse Laplace transform of \bar{T}_{g22} is given by

$$T_{g22} = a_q e^{-t_c h_g} \int_0^{t-t_c} [\delta(t - t_c - u) + h_p] e^{-h_p u} J_0(2\sqrt{-a_0 u}) du \tag{A18}$$

Considering the last term in Equation A11, we can write

$$\begin{aligned}
T_{g23} &= -a_q \ell^{-1} \left\{ \frac{1}{s + h_g + h_p} e^{-t_c s} e^{-t_c h_g} e^{\left(\frac{a_0}{s+h_p}\right)} \right\} \\
&= -a_q e^{-t_c h_g} \ell^{-1} \left\{ e^{-t_c s} \left[\frac{s + h_p}{(s + h_g + h_p)(s + h_p)} e^{\left(\frac{a_0}{s+h_p}\right)} \right] \right\} \\
&= -a_q e^{-t_c h_g} F_{23}(t - t_c)
\end{aligned} \tag{A19}$$

Where $F_{23}(t)$ is

$$F_{23}(t) = \int_0^t H_{23}(t - u) G_{23}(u) du \tag{A20}$$

$$G_{23}(u) = \ell^{-1} \left\{ \frac{1}{s + h_p} e^{\left(\frac{a_0}{s+h_p}\right)} \right\} = e^{-h_p t} \ell^{-1} \left\{ \frac{1}{s} e^{\frac{a_0}{s}} \right\} = e^{-h_p u} J_0(2\sqrt{-a_0 u}) \tag{A21}$$

$$H_{23}(u) = \ell^{-1} \left\{ \frac{s + h_p}{s + h_g + h_p} \right\} = \ell^{-1} \left\{ 1 - \frac{h_g}{s + h_g + h_p} \right\} = \delta(u) - h_g e^{-(h_p+h_g)u} \tag{A22}$$

Therefore, T_{g23} is given by

$$T_{g23} = -a_q e^{-t_c h_g} \int_0^{t-t_c} [\delta(t-t_c-u) - h_g e^{-(h_p+h_g)(t-t_c-u)}] e^{-h_p u} J_0(2\sqrt{-a_0 u}) du \quad (A23)$$

Finally, the inverse Laplace transform of the third term in Eqn. 22, denoted here as \bar{T}_{g3} , is calculated as

$$T_{g3} = a_q \ell^{-1} \left\{ \frac{h_g + h_p}{s^2} - \frac{1}{s} + \frac{1}{s + h_g + h_p} \right\} = a_q [(h_g + h_p)t - 1 + e^{-(h_g+h_p)t}] \quad (A24)$$

After summation of all terms, $T_g(t, t_c)$ is written as:

$$T_g(t, t_c) = T_{g1} + (T_{g21} + T_{g22} + T_{g23}) + T_{g23} = \quad (A25)$$

$$T_{g,i} e^{-t_c h_g} \int_0^{t-t_c} [\delta(t-t_c-u) + h_p] e^{-h_p u} J_0(2\sqrt{-a_0 u}) du \quad \{T_{g1}\}$$

$$-a'_q e^{-t_c h_g} \int_0^{t-t_c} [h_p(t-t_c-u) + 1] e^{-h_p u} J_0(2\sqrt{-a_0 u}) du \quad \{T_{g21}\}$$

$$+a_q e^{-t_c h_g} \int_0^{t-t_c} [\delta(t-t_c-u) + h_p] e^{-h_p u} J_0(2\sqrt{-a_0 u}) du \quad \{T_{g22}\}$$

$$-a_q e^{-t_c h_g} \int_0^{t-t_c} [\delta(t-t_c-u) - h_g e^{-(h_p+h_g)(t-t_c-u)}] e^{-h_p u} J_0(2\sqrt{-a_0 u}) du \quad \{T_{g23}\}$$

$$+a_q [(h_g + h_p)t - 1 + e^{-(h_g+h_p)t}] \quad \{T_{g3}\}$$

After rearranging Eqn. A25, as well as considering that the integrals involving a product with the delta function yield the function value itself, $T_g(t, t_c)$ is calculated as (see also Eqn. 23 in the manuscript):

$$T_g(t, t_c) = T_{g,i} e^{-t_c h_g} e^{-h_p(t-t_c)} J_0(2\sqrt{-a_0(t-t_c)}) \quad (A26)$$

$$\begin{aligned}
& + a_q [(h_g + h_p)t - 1 + e^{-(h_g+h_p)t}] \\
& + e^{-t_c h_g} [T_{g,i} h_p - a'_q (h_p(t - t_c) + 1) + a_q h_p] I_1 \\
& + e^{-t_c h_g} [a'_q h_p I_2 + a_q h_g e^{-(h_p+h_g)(t-t_c)} I_3]
\end{aligned}$$

Where we have used the following definitions:

$$I_1 = \int_0^{t-t_c} e^{-h_p u} J_0(2\sqrt{-a_0 u}) du; \quad I_2 = \int_0^{t-t_c} u e^{-h_p u} J_0(2\sqrt{-a_0 u}) du; \quad (A27)$$

$$I_3 = \int_0^{t-t_c} e^{h_g u} J_0(2\sqrt{-a_0 u}) du$$

A2. Particle Temperature Calculation

We now recall the Laplace transform of the particle temperature given by Eqn. 18, and the solution for the gas temperature available in Eqn. 22:

$$\begin{aligned}
\bar{T}_p = & \frac{T_{g,i}}{s(s+h_p)} e^{-t_c s (1+\frac{h_g}{s+h_p})} - h_q h_g h_p \frac{1}{s^2(s+h_p)(s+h_g+h_p)} e^{-t_c s (1+\frac{h_g}{s+h_p})} \\
& + h_q h_g h_p \frac{1}{s^2(s+h_p)(s+h_g+h_p)} + \frac{h_q}{s(s+h_p)}
\end{aligned} \quad (A27)$$

To obtain the inverse Laplace transform of \bar{T}_p , we split the above expression into four terms

$$\bar{T}_p = \bar{T}_{p_1} + \bar{T}_{p_2} + \bar{T}_{p_3} + \bar{T}_{p_4} \quad (A28)$$

By rewriting the first term in right hand side of Equation A28, \bar{T}_{p_1} is given by

$$\bar{T}_{p_1} = T_{g,i} e^{-t_c s} e^{-t_c h_g} e^{t_c h_g (\frac{h_p}{s+h_p})} \left[\frac{1}{s} - \frac{1}{(s+h_p)} \right] \quad (A29)$$

Considering the time shifting property of a Laplace transformation, the above equation can be rewritten as

$$\bar{T}_{p_1} = T_{g,i} e^{-t_c h_g} F_1(t - t_c) \quad (\text{A30})$$

Where

$$F_1(t) = \ell^{-1} \left\{ e^{\left(\frac{a_0}{s+h_p}\right)} \left[\frac{1}{s} - \frac{1}{(s+h_p)} \right] \right\} \quad (\text{A31})$$

By implementing the convolution theorem on the above equation, we obtain

$$F_1(t) = \int_0^t H_1(t-u) G_1(u) du - e^{-h_p t} J_0(2\sqrt{-a_0 t}) \quad (\text{A32})$$

where

$$G_1(u) = \ell^{-1} \left\{ \left[\frac{1}{s+h_p} e^{\left(\frac{a_0}{s+h_p}\right)} \right] \right\} = e^{-h_p u} \ell^{-1} \left\{ \frac{1}{s} e^{\frac{a_0}{s}} \right\} = e^{-h_p u} J_0(2\sqrt{-a_0 u}) \quad (\text{A33})$$

$$H_1(u) = \ell^{-1} \left\{ \left[\frac{s+h_p}{s} \right] \right\} = \ell^{-1} \left\{ \left[1 + \frac{h_p}{s} \right] \right\} = \delta(u) + h_p \quad (\text{A34})$$

By substituting H_1 and G_1 in Equation A31, T_{p_1} can be calculated as

$$T_{p_1}(t) = T_{g,i} e^{-t_c h_g} \left[\int_0^{t-t_c} (\delta(t-t_c-u) + h_p) e^{-h_p u} J_0(2\sqrt{-a_0 u}) du - e^{-h_p(t-t_c)} J_0(2\sqrt{-a_0(t-t_c)}) \right] \quad (\text{A35})$$

Using the same methodology and partial fractional decomposition, \bar{T}_{p_2} is given by

$$\bar{T}_{p_2} = -a''_q e^{-t_c s} e^{-t_c h_g} e^{\left(\frac{a_0}{s+h_p}\right)} \frac{1}{s+h_p} \left[\frac{h_p+h_g}{s^2} - \frac{1}{s} + \frac{1}{s+h_p+h_g} \right] \quad (\text{A36})$$

Where $a''_q = \frac{h_p h_g h_q}{(h_p+h_g)^2}$. Hence, we arrive at:

$$T_{p_2}(t) = -a''_q e^{-t_c h_g} \int_0^{t-t_c} [(h_p+h_g)(t-t_c-u) - 1 + e^{-(h_p+h_g)(t-t_c-u)}] e^{-h_p u} J_0(2\sqrt{-a_0 u}) du \quad (\text{A37})$$

Finally the inverse Laplace transform of \bar{T}_{p_3} and \bar{T}_{p_4} is given by

$$T_{p_3}(t) = -a''_q \left[\frac{1 - e^{-h_p t}}{h_p} - (h_p+h_g) \left\{ -\frac{1}{h_p^2} + \frac{1}{h_p} t + \frac{1}{h_p^2} e^{-h_p t} \right\} - \frac{\{e^{-h_p t} - e^{-(h_p+h_g)t}\}}{h_g} \right] \quad (\text{A38})$$

$$T_{p_4}(t) = \frac{h_q}{h_p} (1 - e^{-h_p t}) \quad (\text{A39})$$

After summation of all terms, the particle temperature is calculated as

$$T_p(t, t_c) = T_{p_1} + T_{p_2} + T_{p_3} + T_{p_4} \quad (\text{A40})$$

$$T_p(t, t_c) = \quad (\text{A41})$$

$$T_{g,i} e^{-t_c h_g} \left[\int_0^{t-t_c} (\delta(t-t_c-u) + h_p) e^{-h_p u} J_0(2\sqrt{-a_0 u}) du - e^{-h_p(t-t_c)} J_0(2\sqrt{-a_0(t-t_c)}) \right] \quad \{T_{p_1}\}$$

$$\begin{aligned}
& -a''_q e^{-t_c h_g} \int_0^{t-t_c} [(h_p + h_g)(t - t_c - u) - 1 \\
& \quad + e^{-(h_p + h_g)(t - t_c - u)}] e^{-h_p u} J_0(2\sqrt{-a_0 u}) du \quad \{T_{p_2}\}
\end{aligned}$$

$$\begin{aligned}
& -a''_q \left[\frac{1 - e^{-h_p t}}{h_p} - (h_p + h_g) \left\{ -\frac{1}{h_p^2} + \frac{1}{h_p} t + \frac{1}{h_p^2} e^{-h_p t} \right\} \right. \\
& \quad \left. - \frac{\{e^{-h_p t} - e^{-(h_p + h_g)t}\}}{h_g} \right] \quad \{T_{p_3}\}
\end{aligned}$$

$$+ \frac{h_q}{h_p} (1 - e^{-h_p t}) \quad \{T_{p_4}\}$$

After rearranging Eqn. A41, as well as simplifying the integrals involving the delta function as explained above, $T_p(t, t_c)$ is calculated as (see also Eqn. 24 in the manuscript):

$$T_p(t, t_c) =$$

$$\begin{aligned}
& -a''_q \left[\frac{1 - e^{-h_p t}}{h_p} - (h_p + h_g) \left(-\frac{1}{h_p^2} + \frac{1}{h_p} t + \frac{1}{h_p^2} e^{-h_p t} \right) \right. \\
& \quad \left. - \frac{\{e^{-h_p t} - e^{-(h_p + h_g)t}\}}{h_g} \right] + \frac{h_q}{h_p} (1 - e^{-h_p t}) \quad (A42)
\end{aligned}$$

$$+ e^{-t_c h_g} [T_{g,i} h_p - a''_q ((h_p + h_g)(t - t_c) - 1)] I_1$$

$$+ e^{-t_c h_g} [a''_q (h_p + h_g) I_2 - a''_q e^{-(h_p + h_g)(t - t_c)} I_3]$$

Note that we have used the definitions in Eqn. A27 for the integral terms I_1 , I_2 , and I_3 .

Appendix B - Octave Scripts for Evaluation of the Solution

In order to make the presented analytical solution easy to use, a computer code (using Matlab®-compatible scripts for the open-source tool “Octave”, <https://www.gnu.org/software/octave>) for the evaluation of the temperature profiles is provided. To calculate the temperatures, one needs to run the script “plotScript_packedBed.m” in Octave (all functions detailed below must be added to the path using the “addpath” command). Note that all input parameters required to calculate the temperatures have been described via comments in this script. The result plots will be saved in a file entitled “temperature_xxx_hEvap_yyy.png” in which “xxx” represents the methodology to calculate the profile (i.e. Laplace transformation or the Schumann solution), and “yyy” represents the value of the heating rate.

The computer code consists of the following octave scripts:

1. The main script entitled “plotScript_packedBed.m”, which is used to input all input parameters, call all relevant functions, and plot the results.
2. A set of functions that performs the calculations:
 - a. Function “NusseltDeenEtAl.m” for calculation of the heat transfer coefficient using the correlation developed by Deen et al [1].
 - b. Function “packedBedTemperatureLT.m” for calculation of temperatures using the presented method in the current study, i.e., a Laplace transformation.
 - c. Function “packedBedIntegral.m” to calculate the integral terms using a numerical approximation.
 - d. Function “packedBedTrnsTemperatures.m” to calculate the temperatures using the classical method presented by Schumann [2]. This function uses the sub-functions “packedBedTrnsM0.m”, “packedBedTrnsMn.m” and “packedBedTrnsMnSum.m”.

References

1. Deen, N.G., et al., *Direct numerical simulation of flow and heat transfer in dense fluid-particle systems*. Chemical Engineering Science, 2012. **81**: p. 329-344.
2. Schumann, T.E., *Heat transfer: a liquid flowing through a porous prism*. Journal of the Franklin Institute, 1929. **208**(3): p. 405-416.

Appendix C - CFD-DEM Simulation Details and Benchmark against the Schumann Solution

The simulation setup, as well as physical properties and simulation conditions for the studied system are summarized in Table C.1. A 3D CFD-DEM simulation was performed using CFDEM® code (Kloss et al., 2012). The cell size in each direction was considered as $2d_p$. It should be mentioned that in case of enforced simulation, the width, length, and height of the bed was $6 \times 6 \times 28 d_p$ (i.e., somewhat larger than in Table C.1), and the cell size in each direction was set to $1d_p$. Also, particles were placed on a hexahedral lattice into the simulation box such that every particle was perfectly centered in each cell. This was done to enforce a uniform particle volume fraction in each cell, i.e., $\varphi_p = \pi/6$.

Table C.1 - Simulation and physical properties for the CFD-DEM simulations.

In order to address the deviation of the temperature predicted when using a CFD-DEM simulation from the analytical solution, two additional simulation scenarios were considered: i) a simulation using the above-described lattice initialization of the particles in the bed, which enforces a perfectly uniform distribution of voidage in the bed; as well as ii) a voidage calculation based on a simplified mapping method (for randomly-arranged particles), in which the volume fraction of solid particles in each cell was calculated based on the particle whose centres reside inside that cell. The latter differs from the standard method used in the CFDEM® code, which uses a more advanced “divided” mapping method.

The predicted temporal evolution of the gas and particle temperature for both scenarios is depicted in Figure C1 showing data at two different positions in the bed. We note in passing that the dimensionless bed position in this figure is slightly different due to the differences in the bed voidage (causing different fluid speed and heat transfer coefficient). It can be easily discerned that when using the lattice distribution (see panel a in Figure C1), the predicted temperature is in excellent agreement with the corresponding analytical value. This demonstrates that the heat exchange between gas and particle, as well as heat source/sink for the particles have been accurately implemented in the CFDEM® code. The small deviation observed in Figure C1a can be attributed to (i) numerical diffusion inherent when using a finite computational grid, and (ii) the fluctuation of the velocity experienced by the first row of particles. The latter causes a small error in the particle Reynolds Number of these particles, and consequently the Nusselt number.

In contrast, application of the simplified mapping method makes the deviation even larger (see panel b in Figure C1). This is due to that fact that the local particle volume fraction fluctuates strongly, and consequently the local Reynolds Number and heat transfer coefficient cannot be captured accurately.

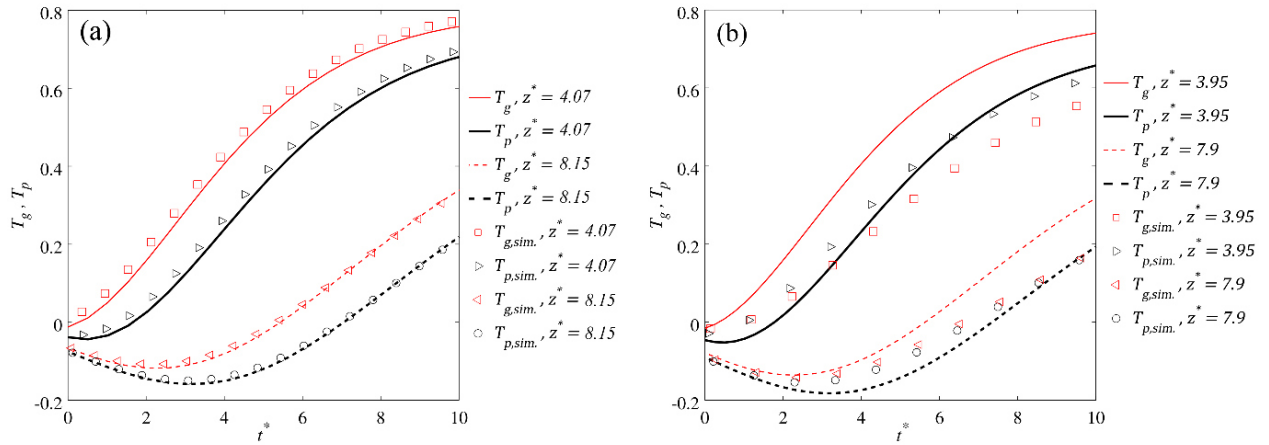


Figure C1 - Comparison of the predicted temperatures (using CFDEM®) with the analytical solution for $h_q = 0.05$ using a) a perfect lattice arrangement of the particles, as well as b) a simplified mapping method for local voidage calculation.

In order to be assured that the temperature is accurately calculated using the Laplace transformation, a scenario with zero heat source was considered. The result of this scenario was then compared with the temperature profile from the Schumann solution. As shown in Figure C2, the temperatures obtained using both methodologies are identical.

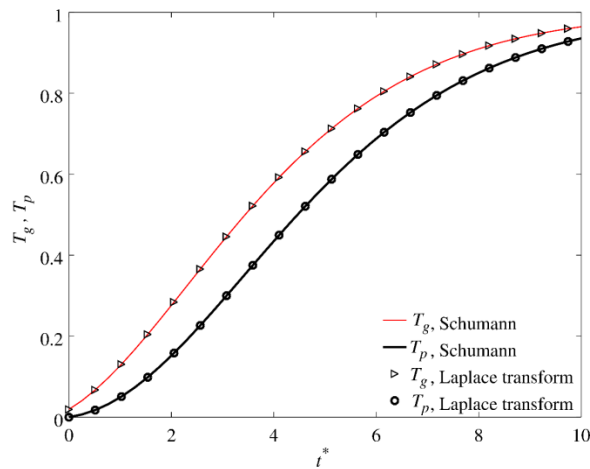


Figure C2 - Comparison of the calculated temperature using Laplace transform and Schumann's solution for a scenario without heat source.

Table C.1– Simulation conditions for the CFD-DEM simulations and benchmark.

Catalytic Bed Dimensions			Solid Phase Properties		
Height	m	0.6	d_p	m	0.022
Length	m	0.1	λ_p	W/Km	0.1
Width	m	0.1	$C_{p,p}$	J/kgK	5
			ρ_p	kg/m^3	1000
Gas Phase Properties			Initial Condition		
$C_{p,f}$	J/kgK	1007	T_{g0}	K	300
ρ_f	kg/m^3	1.188	T_{p0}	K	300
ν_f	m^2/s	$1.5 \cdot 10^{-5}$	Boundary Condition		
λ_f	W/Km	0.0256	T_{gi}	K	330
Prandtl number	–	0.70097	U	m/s	0.1
Contact Model Parameters for DEM			Numerical Simulation Parameters		
Y	N/m^2	$2 \cdot 10^5$	Δt_{CFD}	s	0.025
ν	–	0.45	Δt_{DEM}	s	$1.25 \cdot 10^{-4}$
$\mu_{c,p}$	–	1	t_{sim}	s	20
e_{pp}	–	1	Δx_{cell}	m	0.044
$\mu_{c,w}$	–	0.5	<i>time discretization scheme</i>		implicit-explicit
e_{wp}	–	0.3	<i>spatial discretization scheme</i>		2 nd order

References

Kloss, C., Goniva, C., Hager, A., Amberger, S., Pirker, S., 2012. Models, algorithms and validation for opensource DEM and CFD-DEM. Progress in Computational Fluid Dynamics, an International Journal 12, 140-152.

“Science is beautiful when it makes simple explanations of phenomena or connections between different observations.”

(Stephen Hawking)

3

Quantification of solids mixing in bubbling fluidized beds via TFM simulations

In this section, a set of correlations is presented to quantify mixing in bubbling fluidized beds. These correlations are supposed to be helpful during design and optimization of bubbling fluidized beds.

Quantification of solids mixing in bubbling fluidized beds via TFM simulations

Mohammad-Sadegh Salehi ^a, Maryam Askarishahi ^b, Stefan Radl ^a

^a *Institute for Process and Particle Engineering, Graz University of Technology, Austria*

^b *Research Center Pharmaceutical Engineering (RCPE) GmbH, 8010 Graz, Austria*

Corresponding author: E-mail: radl@tugraz.at; Tel.: +43 316 873 30412; Fax: +43 316 873 1030412

Abstract

The influence of particle density and fluidization velocity on mixing behavior of Geldart B particles was investigated in bubbling fluidized beds for various operating conditions using two-fluid model approach. The simulation results proved that the predicted solid flow pattern for a wide range of Geldart B particles differs from particles of Geldart B/D classification at identical fluidization number.

Quantitative analysis of the predicted solid velocity fluctuation revealed that the solids axial dispersion rate is higher than the lateral one. In detail, a Peclet number of 1.54 and 3.92 was predicted for axial and lateral mixing, respectively. Also, the solid dispersion and diffusion coefficients were linearly correlated with the excess gas velocity for a range of particle properties.

Finally, the characteristic global particle mixing times were computed. Thereby, the characteristic mixing time can be correlated with the particle Froude number, expanded bed height, and solid dispersion coefficient with high accuracy.

Keywords: Bubbling fluidized bed, Two-fluid model, solid mixing, dispersion, Solid flow pattern

3.1. Introduction

Bubbling fluidized beds (BFBs) are widely used in chemical and petrochemical, pharmaceutical, energy, and power industries because of their excellent heat and mass transfer characteristics, as well as fast solid and gas mixing [1]. The mixing efficiency and the rate of heat and mass transfer depend on solid/gas flow pattern and bubble-induced motion of particles in BFBs [1–4].

Despite the claim that fluidized beds (FBs) are well-mixed and easily-controllable for heterogeneous and gas-phase reactions, there are remaining challenges related to (i) the optimum design and (ii) operation in some applications. Such challenges stem from segregation and/or poor mixing of solids and gas phases, e.g., when fluidized beds are applied to process biomass [5], to coat particles [6], to crack bitumen [7], or to chemical looping reforming (CLR) reactors involving extremely reactive particles [8]. The reason is that in these fluid bed applications, the release of energy due to chemical reactions or evaporation, as well as the addition of gases or liquids (e.g., via a spray) can be faster than the global mixing of solids. It is, hence, essential to quantify the rate of mixing in fluidized beds, as it can provide valuable information, e.g., to correctly design and locate fuel feeding ports in fluidized bed reactors [9–11]. Moreover, a large enough mixing rate of solid particles is required for homogenous heating or drying in some processes. Finally, avoiding hot-spot formation in highly exothermic reactive systems [12] necessitates extremely fast mixing in an FB.

Obtaining a better insight into the parameters dominating solid flow pattern and solid mixing rates can be of significant advantage to improve the design and to optimize the operation of BFBs. It has been demonstrated that the solid flow pattern and the solid mixing rate are affected by various parameters, most important (i) geometrical bed configuration, (ii) operating conditions, and (iii) particle properties [4,13–16]. To be more specific, the distributor configuration plays a role in solid circulation pattern via influencing bubble formation as reported by various researchers [4,14–19]. Additionally, according to several studies [13,15–17,20–22], it has been proven that fluidization velocity is key for the solid flow pattern in terms of the size and the number of vortices formed in the bed. Moreover, Fan et al. [21,22] and Askarishahi, et al. [23] demonstrated that at low excess gas velocities (i.e., the difference between the actual

and minimum fluidization velocity), the predicted solid flow pattern changes with solid particle size. In contrast, at the high excess gas velocity, the solid flow pattern is not significantly affected by particle size. Moreover, the marginal effect of bed aspect ratio on the solid flow pattern was reported for bed aspect ratios close to and above one [13,15,16]. It should be noted that the effect of particle density on solid flow pattern and mixing behavior has not been thoroughly evaluated in these studies.

Apart from solid flow pattern studies, solids mixing has been commonly quantified in terms of (i) solid dispersion coefficients, (ii) granular diffusion coefficients [4,13,14,23–26], or (iii) mixing indices [27–29]. For instance, Luo et al. [25] investigated solids mixing and dispersion behavior in BFBs numerically. They showed that - what is also expected - solids mixing is faster in case of higher gas inlet velocity. Their results also demonstrated that particles are mixed more efficiently in the axial direction than in the lateral one. In another study, Medrano et al. [30] claimed that the solids fluxes depend on the excess gas velocity. This observation combines the effect of fluidization velocity and particle properties since the latter influence the minimum fluidization speed. We note in passing that in most mixing-related studies [20,25,26,31], a group of particles is colored upon initializing the process, i.e., when particles are at rest, and the fluidization speed is zero. However, it is questionable if such an approach is useful to study solid mixing rates in BFBs because of possible initialization and transition effect [32].

Recently, Li et al. [4] analyzed the effect of various parameters including solid flow pattern, bed geometry, distributor shape, and operating condition on solids mixing in the BFBs through an experimental investigation. They demonstrated that solids mixing behavior can be associated with the number and shape of vortices. In their study, the solid mixing was quantified based on a solid dispersion coefficient, a mixing index, and particle residence time. They claimed that solid flow pattern influences the uniformity and magnitude of solids dispersion coefficient along the bed. This highlights the importance of linking solids mixing with solids flow pattern.

According to our review of recent literature, it can be concluded that the role of certain parameters affecting solids flow pattern, as well as solids mixing still has not been well investigated. Furthermore, the effect of each parameter has been often considered in

an isolated fashion, which might hide the effect of certain parameter combination on flow pattern and mixing. In summary, we have identified the following gaps in knowledge:

- The influence of particle density was not thoroughly investigated.
- The effect of the initialization and startup procedure of the fluidized bed on mixing behavior was not considered in most of the studies. This was already reported by Rhodes et al. [33] and Banaei et al. [32], however, the effect of these procedures was never quantified.
- In the majority of the studies on solid flow behavior, the solid dispersion and/or mixing time were analyzed without connection to the solid flow pattern [20,26,32].
- Optimizing feeding policy and feed location concerning achieving a maximum solid mixing rate was not addressed in the literature.

3.1.1. Goals of the Present Study

Based on the described gaps, the primary objective of the current study is the quantification of solids mixing for Geldart's group B and BD powders using the Two-Fluid Model (TFM). In detail, the main goals of our study can be summarized as follows:

- examination of the effect of particle size and particle density, as well as the fluidization velocity on solid flow pattern and solids mixing behavior;
- quantifying the degree of mixing based on particles' fluctuation velocity; and
- associating the solid dispersion and mixing time to particle properties and fluidization velocity via dimensionless numbers

3.2. Mathematical Model

3.2.1. Flow

The Eulerian-Eulerian approach was applied in the present study to simulate a gas-particle flow system in a two-dimensional Cartesian frame to represent the 3D setup in MFiX [34]. It should be noted that Xie et al. [35] and Reuge, et al. [36] have shown the capability of the 2D Cartesian coordinate system to simulate the cylindrical fluidized bed in the bubbling regime.

Two-Fluid Model (TFM) is termed Eulerian-Eulerian approach since different phases are treated mathematically as interpenetrating continua [37]. In this approach, conservation equations are solved for each phase, and these equations are linked by an interphase momentum transfer coefficient and the gas pressure. It should be mentioned that in the present study, the drag law of Wen and Yu [38] has been considered for interphase momentum transfer coefficient since this drag law can well predict the rising bubbles and bed expansion as reported by Schneiderbauer et al. [39] and van Wachem et al.[40]. Besides, the kinetic theory of granular flow, as well as a frictional model, was adopted to close the solid-phase stress tensor. Finally, the no-slip boundary condition was considered for the gas phase, and Schneiderbauer's boundary condition [41] was implemented in MFIX to close the solid phase transport equations at the walls (see Appendix A for more information). The governing and constitutive equations have been listed in Table 1.

Table 1. Governing and constitutive equations for TFM simulations of gas-solid flow

Continuity equation, momentum equation and transport equation for pseudo-thermal energy (PTE) [42]	
$\frac{\partial(\varepsilon_g \rho_g)}{\partial t} + \nabla \cdot (\varepsilon_g \rho_g \mathbf{u}_g) = 0$	(1)
$\frac{\partial(\varepsilon_s \rho_s)}{\partial t} + \nabla \cdot (\varepsilon_s \rho_s \mathbf{u}_s) = 0 \quad \text{where } \varepsilon_s = 1 - \varepsilon_g$	(2)
$\frac{\partial(\varepsilon_g \rho_g \mathbf{u}_g)}{\partial t} + \nabla \cdot (\varepsilon_g \rho_g \mathbf{u}_g \mathbf{u}_g) = -\varepsilon_g \nabla P_g + \nabla \cdot (\varepsilon_g \mathbf{T}_g) - \mathbf{I}_{gs} + \varepsilon_g \rho_g \mathbf{g}$	(3)
$\frac{\partial(\varepsilon_s \rho_s \mathbf{u}_s)}{\partial t} + \nabla \cdot (\varepsilon_s \rho_s \mathbf{u}_s \mathbf{u}_s) = -\varepsilon_s \nabla P_g - \nabla \cdot (\mathbf{S}_s^{\text{kc}} + \mathbf{S}_s^{\text{fr}}) + \mathbf{I}_{gs} + \varepsilon_s \rho_s \mathbf{g}$	(4)
$\frac{3}{2} \left(\frac{\partial(\varepsilon_s \rho_s \theta)}{\partial t} + \nabla \cdot (\varepsilon_s \rho_s \mathbf{u}_s \theta) \right) = -\mathbf{S}_s^{\text{kc}} : \nabla \mathbf{u}_s - \nabla \cdot \mathbf{q} + \Pi_s - \varepsilon_s \rho_s J_s$	(5)
Interphase momentum exchange [38]	
$\mathbf{I}_{gs} = \beta_{gs} (\mathbf{u}_g - \mathbf{u}_s)$	(6)
$\beta_{gs} = \frac{3}{4} C_d \frac{\varepsilon_g \varepsilon_s \rho_g \ \mathbf{u}_g - \mathbf{u}_s\ }{d_s} \varepsilon_g^{-2.65}$	(7)

$$C_d = \begin{cases} \frac{24}{Re_s} \left[1 + 0.15(\varepsilon_g Re_s)^{0.687} \right] & \text{for } Re_s < 1000 \\ 0.44 & \text{for } Re_s \geq 1000 \end{cases} \quad (8)$$

$$Re_s = \frac{\varepsilon_g \rho_g \|\mathbf{u}_g - \mathbf{u}_s\| d_s}{\mu_g} \quad (9)$$

Gas-phase and solids phase stress tensor

$$\mathbf{T}_g = 2\mu_g \mathbf{D}_g, \mathbf{D}_g = \frac{1}{2} (\nabla \mathbf{u}_g + (\nabla \mathbf{u}_g)^T) \quad (10)$$

$$\mathbf{S}_s^{kc} = (P_s^{kc} - \lambda_s^{kc} \text{tr}(\mathbf{D}_s)) \mathbf{I} - 2\mu_s^{kc} \text{dev} \mathbf{D}_s, \mathbf{D}_s = \frac{1}{2} (\nabla \mathbf{u}_s + (\nabla \mathbf{u}_s)^T), \text{dev} \mathbf{D}_s = \mathbf{D}_s - \frac{1}{3} \text{tr}(\mathbf{D}_s) \mathbf{I} \quad (11)$$

Solids and gas viscosity [43,44]

$$\mu_s^{kc} = \left(\frac{2 + \alpha}{3} \right) \left[\frac{\mu_s^*}{g_0 \eta_s (2 - \eta_s)} \left(1 + \frac{8}{5} g_0 \eta_s \varepsilon_s \right) \left(1 + \frac{8}{5} \eta_s (3\eta_s - 2) g_0 \varepsilon_s \right) + \frac{8}{5} \eta_s \mu_b \right], \alpha = \frac{8}{5} \quad (12)$$

$$\mu_s^* = \frac{\varepsilon_s \rho_s \theta g_0 \mu}{\varepsilon_s \rho_s \theta g_0 + \frac{2\beta_{gs} \mu}{\varepsilon_s \rho_s}} \quad (13)$$

$$\mu_b = \frac{256}{5\pi} \mu \varepsilon_s \varepsilon_s g_0; \quad \mu = \frac{5}{96} \rho_s d_s \sqrt{\pi \theta} \quad (14)$$

$$\lambda_s^{kc} = \frac{8}{3} \varepsilon_s^2 \rho_s d_s g_0 \eta_s \sqrt{\frac{\theta}{\pi}} \quad (15)$$

$$\eta_s = \frac{1}{2} (1 + e_s) \quad (16)$$

Pseudo-thermal energy (PTE) flux vector \mathbf{q} [43–45], rate of dissipation of PTE J_s [45], and the exchange of fluctuation energy Π_s [46]

$$\mathbf{q} = \left(\frac{\kappa_s^*}{g_0} \right) \left[\left(1 + \frac{12}{5} \eta_s \varepsilon_s g_0 \right) \left(1 + \frac{12}{5} \eta_s^2 (4\eta_s - 3) \varepsilon_s g_0 \right) + \frac{64}{25\pi} (41 - 33\eta_s) \eta_s^2 (\varepsilon_s g_0)^2 \right] \nabla \theta \quad (17)$$

$$\kappa_s^* = \frac{\kappa}{1 + \frac{6\beta_{gs} \kappa}{5(\varepsilon_s \rho_s)^2 g_0 \theta}} \quad (18)$$

$$\kappa = \frac{75\rho_s d_s \sqrt{\pi\theta}}{48\eta_s(41 - 33\eta_s)} \quad (19)$$

$$J_s = \frac{48}{\sqrt{\pi}} \eta_s (1 - \eta_s) \frac{\varepsilon_s g_0}{d_s} \theta^{3/2} \quad (20)$$

$$\Pi_s = -3\beta_{gs}\theta + \frac{81\varepsilon_s \mu_g^2 \|\mathbf{u}_g - \mathbf{u}_s\|^2}{g_0 \rho_s d_s^3 \sqrt{\pi\theta}} \quad (21)$$

Radial Distribution Function [42]

$$g_0 = \frac{1}{\varepsilon_g} + \frac{3\varepsilon_s}{2\varepsilon_g^2} \quad (22)$$

Frictional Stress [42]

$$\mathbf{S}_s^{\text{fr}} = P_s^{\text{fr}} \mathbf{I} - 2\mu_s^{\text{fr}} \text{dev } \mathbf{D}_s \quad (23)$$

$$\mu_s^{\text{fr}} = \begin{cases} \min\left(\frac{P_s^{\text{fr}} \sin(\varphi)}{2\|\text{dev } \mathbf{D}_s\|}, \mu_m^{\text{max}}\right), & \text{for } \varepsilon_s > \varepsilon_s^* \\ 0, & \text{for } \varepsilon_s^* \leq \varepsilon_s \end{cases} \quad (24)$$

$$\mu_m^{\text{max}} = 1000 [P] \quad (25)$$

$$P_s^{\text{fr}} = 10^{25} (\varepsilon_s - \varepsilon_s^*)^{10}, \quad \varepsilon_s^* = \varepsilon_s^{\text{mf}} \quad (26)$$

Boundary Conditions [47]

$$\begin{aligned} \boldsymbol{\tau}_s^{\text{kc}} &= -\eta_w \mu_w \varepsilon_s \rho_s g_0 \theta \text{erf}(\bar{u}_s) \frac{\mathbf{u}_s^{\text{sl}}}{\|\mathbf{u}_s^{\text{sl}}\|}, \quad \mu_0 = \frac{7}{2} \frac{1 + e_w}{1 + \beta_0} \mu_w, \eta_w \\ &= \frac{1}{2} (1 + e_w), \bar{u}_s = \frac{\|\mathbf{u}_s^{\text{sl}}\|}{\sqrt{2\theta\mu_0}} \end{aligned} \quad (27)$$

$$\begin{aligned} \mathbf{n} \cdot \mathbf{q} &= \boldsymbol{\tau}_s^{\text{kc}} \cdot \mathbf{u}_s^{\text{sl}} \\ &- \frac{\rho_s \varepsilon_s g_0 \eta_w \sqrt{\theta}}{\sqrt{2\pi\mu_0^2}} \exp(-\bar{u}_s^2) \{ \mu_w [2\mu_w \|\mathbf{u}_s^{\text{sl}}\|^2 (2\eta_w - \mu_0) \\ &+ \theta (14\mu_w \eta_w - 4\mu_0 (1 + \mu_w) - 6\mu_w \mu_0^2 \eta_w)] \\ &+ \mu_0^2 \sqrt{\theta} \exp(\bar{u}_s^2) [\sqrt{\theta} (4(\eta_w - 1) + 6\mu_w^2 \eta_w) \\ &- \sqrt{2\pi\mu_w} \|\mathbf{u}_s^{\text{sl}}\| \text{erf}(\bar{u}_s)] \end{aligned} \quad (28)$$

3.2.2. Scalar Transport

The species conservation equation can be derived for a tracer in the solids phase as:

$$\frac{\partial}{\partial t}(\varepsilon_s \rho_s x_s) + \nabla \cdot (\varepsilon_s \rho_s x_s \mathbf{u}_s) = \nabla \cdot (D_{s,x} \nabla(\varepsilon_s \rho_s x_s)) \quad (29)$$

In which x_s is the mass fraction of tracer in the solid phase. The first and second terms on the left-hand side of Equation (29) represent the transport due to the accumulation, and convection transport [42], and the right-hand side term represents the contribution of diffusive solid mixing due to the random motion of particles. Hsiao and Hunt [48] used kinetic theory-based arguments to arrive at the following expression for the self-diffusion coefficient:

$$D_{s,x} = \frac{d_s \sqrt{\pi \theta}}{8(1 + e_s) \varepsilon_s g_0(\varepsilon_s)} \quad (30)$$

It should be noted that MFIX source code [34] was modified to consider the contribution of solid self-diffusivity in the species transport equation in the solid phase.

3.3. Results and Discussion

In this section, the results of simulations performed for various operating conditions and particle properties are presented. After analyzing the predicted mixing behavior in the BFB, correlations are developed to quantify the mixing quality in the bubbling fluidized beds.

3.3.1. Setup and Parameter Range

The bed set-up used for the simulations has been schematically shown in Figure 1. The summary of the studied operating conditions and particle properties have been reported in Table 2. It is worth noting that the range of particle diameter and density have been selected in such a way that the entire range of Geldart's B can be covered according to Grace's chart [2].

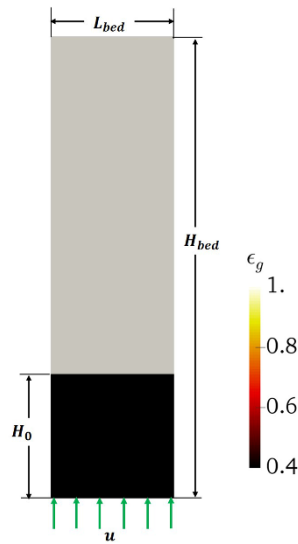


Figure 1. The schematic view of the simulated fluidized bed

Table 2. simulation parameters and physical properties of the studied fluidized bed

Property	Value
D_{Bed}	0.20 [m]
H_{bed}	0.75 [m]
H_0	0.20 [m]
ρ_s	800, 1300, 2500 and 3500 [kg/m^3]
d_s	485, 550, and 700 [μm]
ϵ_g^*	0.42
ϵ_s^{max}	0.6
φ	28.5°
e_s	0.9
e_w	0.9
β_0	0.4
μ_w	0.5
ρ_g	1.225 [kg/m^3]
μ_g	1.78×10^{-5} [$kg/(m.s)$]
u/u_{mf}	1.5 – 3.5

3.3.2. Grid Dependency and Time to Pseudo Steady-State

To find the optimum mesh size, the grid sensitivity study was performed for various operating conditions and particle properties (see Table 3). In this table, the fluidization number (i.e., u/u_{mf}) is defined as the ratio of the gas inlet velocity to the minimum fluidization velocity. Besides, the minimum fluidization velocity for the associated particle properties has been calculated based on the Ergun equation [2]. According to our grid dependency results shown in Table 3, a finer mesh is needed for lighter particles to capture the fluidized bed characteristics i.e., the time- and laterally-averaged voidage distribution (see Appendix A for more information).

Table 3. Adopted grid size for different cases based on particle properties and fluidization velocity

ρ_s [$\frac{\text{kg}}{\text{m}^3}$]	d_s [μm]	u_{mf} [$\frac{\text{m}}{\text{s}}$]	fluidization number [-]	cell size
800	485	0.089	1.5 – 3.5	$4d_p$
1300	485	0.13	1.5 – 3.5	$5d_p$
2500	485	0.22	1.5 – 3.5	$7d_p$
2500	700	0.40	1.5 – 3.5	$7d_p$
3500	485	0.31	1.5 – 3.5	$7d_p$
3500	550	0.38	1.5 – 3.5	$7d_p$

It was found that the required simulation time to reach a pseudo-steady state solids flow varies depending on the particle properties and fluidization velocity. To be more specific, the solid flow pattern needs much longer time to reach a pseudo-steady state for light particles and low fluidization velocities. For instance, for the bed of particles with a density of $1300 \text{ [kg/m}^3\text{]}$, and a fluidization velocity of $1.5u_{mf}$, a simulation time of 500 [s] is required, whereas 120 [s] is needed at the fluidization velocity of $3.5u_{mf}$. To analyze this difference, the dense bed below 0.1 [m] in height was divided into two regions with identical size as shown in Figure 2:

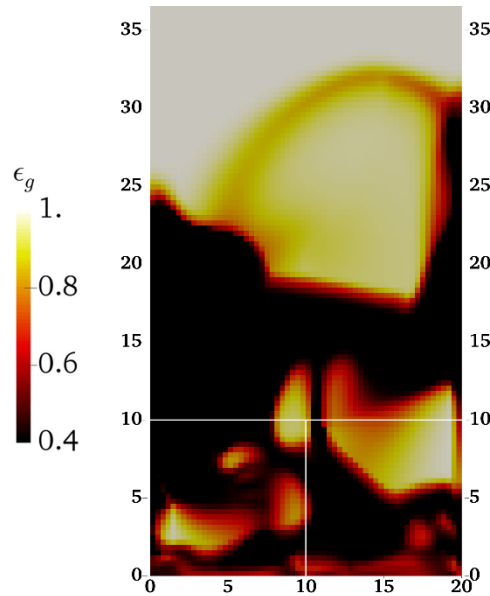


Figure 2. Illustration of the regions which are used for voidage frequency analysis

Subsequently, the temporal evolution of the average gas volume fraction was obtained in the left and right region. As depicted in Figure 3, these region-averaged voidage values are oscillating around an average value. Consequently, the power spectral magnitudes of these voidage signals were obtained and are plotted in Figure 4 for two fluidization velocities. In this figure, the dominant frequency represents how frequent the maximum region-averaged voidage appears in the left or right region. As depicted in Figure 4, the dominant frequency at the fluidization velocity of $1.5u_{mf}$ (i.e., $0.05 [Hz]$) is much lower than the corresponding values for the higher fluidization number of 3.5 (i.e., $1.85 [Hz]$). A low frequency of the region-averaged voidage means that an asymmetric flow pattern forms, which persists for a longer time, and only slowly dissolves. This leads to the requirement of a long simulation time for low gas velocities to reach the steady-state solid flow pattern.

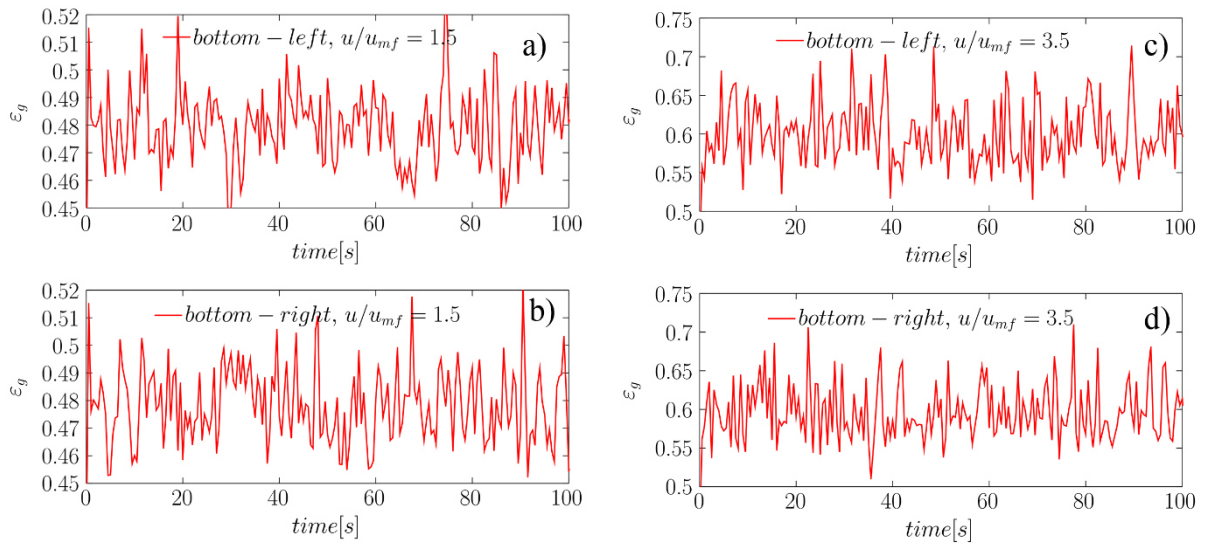


Figure 3. Temporal evolution of the voidage in the fluidized bed filled with the particle with $\rho_s = 1300[kg/m^3]$, for the left region at different fluidization velocities of a) $1.5u_{mf}$ and b) $3.5u_{mf}$ and the right region at c) $1.5u_{mf}$ and d) $3.5u_{mf}$

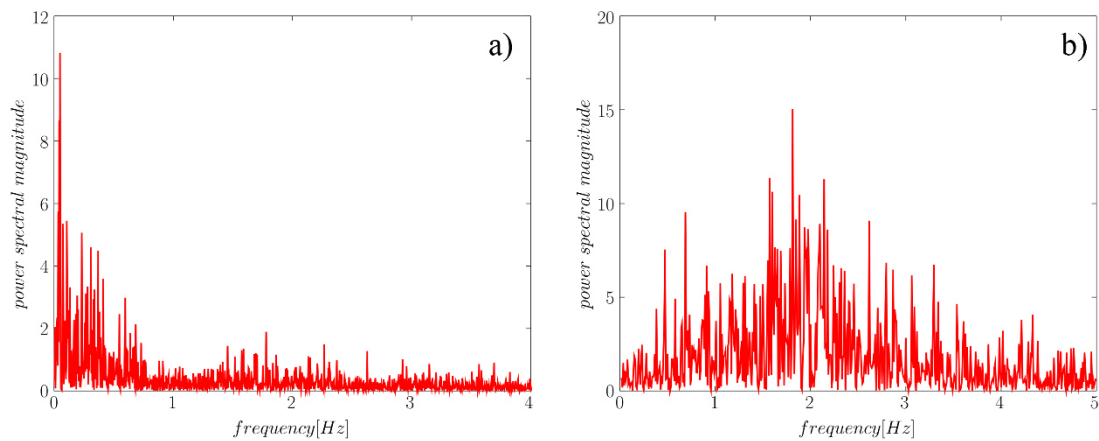


Figure 4. The power spectrum of the voidage fluctuation in the left-bottom region of the FB filled with particles with $\rho_s = 1300[kg/m^3]$ at fluidization velocities of a) $1.5u_{mf}$ and b) $3.5u_{mf}$.

The simulation results also revealed that the voidage frequency is governed by particle properties in addition to the fluidization velocity. To lump the effect of particle properties (e.g., density and diameter), as well as the fluidization velocity, the dominant frequency of voidage fluctuations was correlated with the excess gas velocity. As discerned from Figure 5, a higher excess gas velocity results in a higher voidage fluctuation frequency, meaning that the simulation time required to reach a pseudo-steady state solid flow pattern decreases.

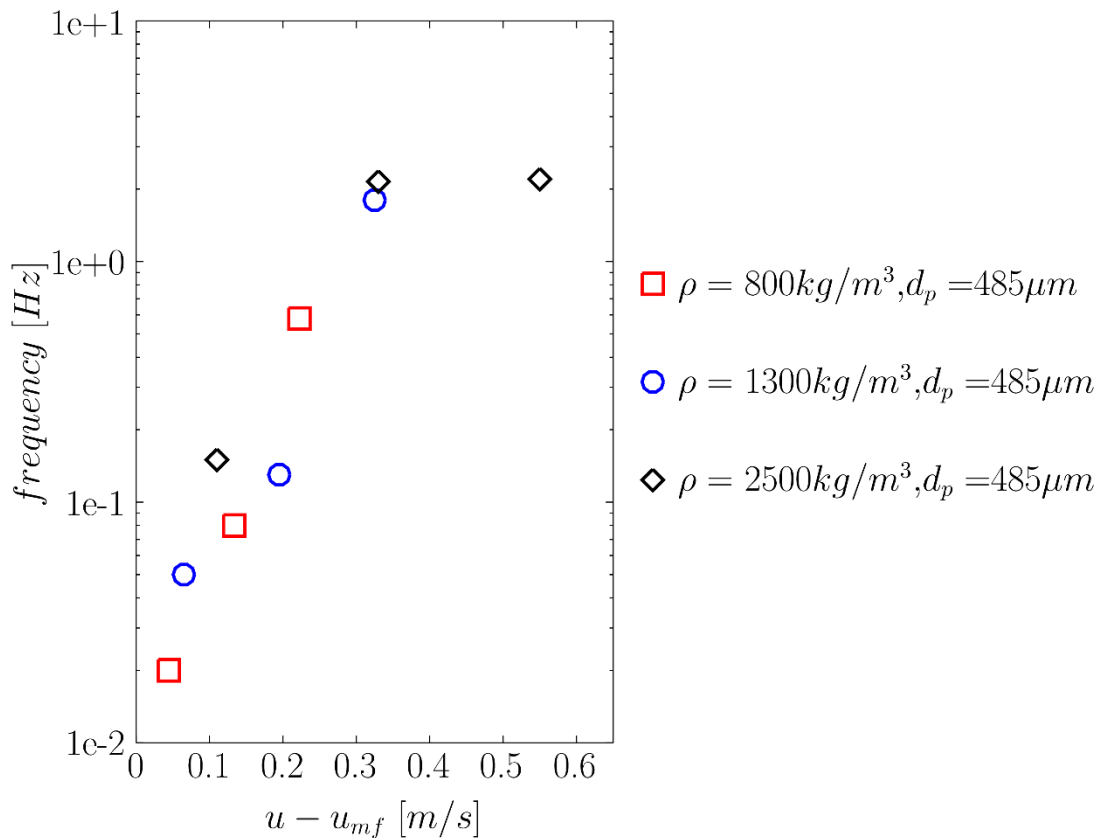


Figure 5. The dependency of the frequency of voidage fluctuations in the left bottom region versus the excess gas velocity for different particle densities

3.3.3. Qualitative Analysis

In this section, the effect of operating conditions and particle properties on gas and solid flow behavior will be qualitatively examined.

As presented in Figure 6a, at a very low fluidization number (i.e., 1.5), four vortices are formed in the bed. The solid flow is downward in the entire central region of the bed, while upward in the region close to the walls in the bottom vortices. The observed flow pattern can be explained through averaged solid volume fraction and solid pressure contour plots. As the simulation results of Bakshi et al. [49–53] demonstrated, bubbles are formed close to the wall on the distributor surface and move upward while approaching the central region in BFBs. According to Bakshi et al. [53], a voidage value of 0.7 should be used to define bubbles. This means that at the positions where the time-average voidage is higher than this threshold value, the probability of bubble existence is higher. Hence, we consider such positions as “preferred bubble paths”.

Therefore, as shown in Figure 7a, it can be said that at the fluidization number of 1.5, two distinct bubble paths can be observed in the time-averaged voidage contour-plot, which can also be seen in the predicted time-averaged solid pressure field. Notably, by comparing Figure 7 and Figure 8, it can be deduced that at the positions where the solid volume fraction is higher, also the solids pressure is higher. Accordingly, bubbles prefer to flow in the direction of lower solids pressure, which ultimately results in the formation of four vortices. As the fluidization velocity increases to $2.5u_{mf}$ and $3.5u_{mf}$, the solids pressure field becomes stronger at the regions close to the walls (in comparison with the central regions). Consequently, the gas prefers to flow towards the bed's central region. Thereby, the top vortices are enlarged at the cost of shrinking the bottom vortices, as seen in Figure 6 b-c.

The simulation results for various particle densities demonstrated that as long as the particles can be categorized as Geldart B particles [54], a qualitatively similar pattern can be predicted at identical fluidization number. Also, the flow pattern seems not to be dependent on the particle density. On the other hand, as the particle properties approach Geldart D classification, the solid flow pattern at low fluidization numbers (e.g. 1.5) slightly differs from the corresponding pattern predicted for Geldart B particles (See Figure 9a). It should be mentioned that for Geldart D particles, two vortices can be predicted at the fluidization number higher than 2.5, whereas at the fluidization number of 3.5, four vortices can still be seen in the bed filled with Geldart B particles.

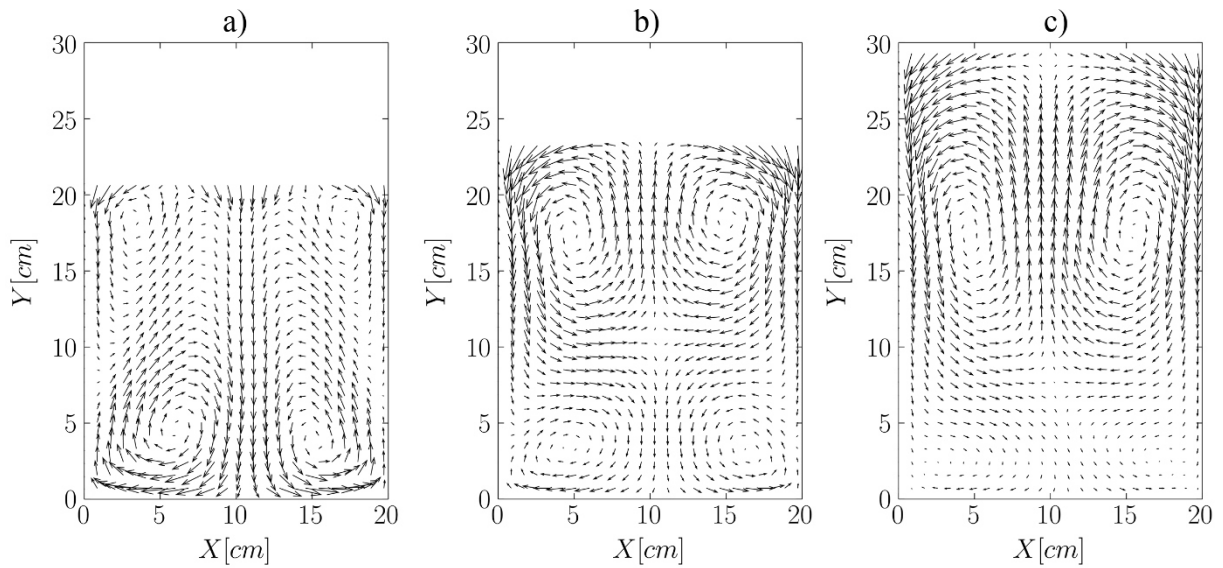


Figure 6. Time-averaged solid flow pattern for particles with a diameter of $485 \text{ } [\mu\text{m}]$ and a density of $2500 \text{ } [\text{kg}/\text{m}^3]$ at different fluidization velocities of a) $1.5 u_{mf}$, b) $2.5 u_{mf}$ and c) $3.5 u_{mf}$.

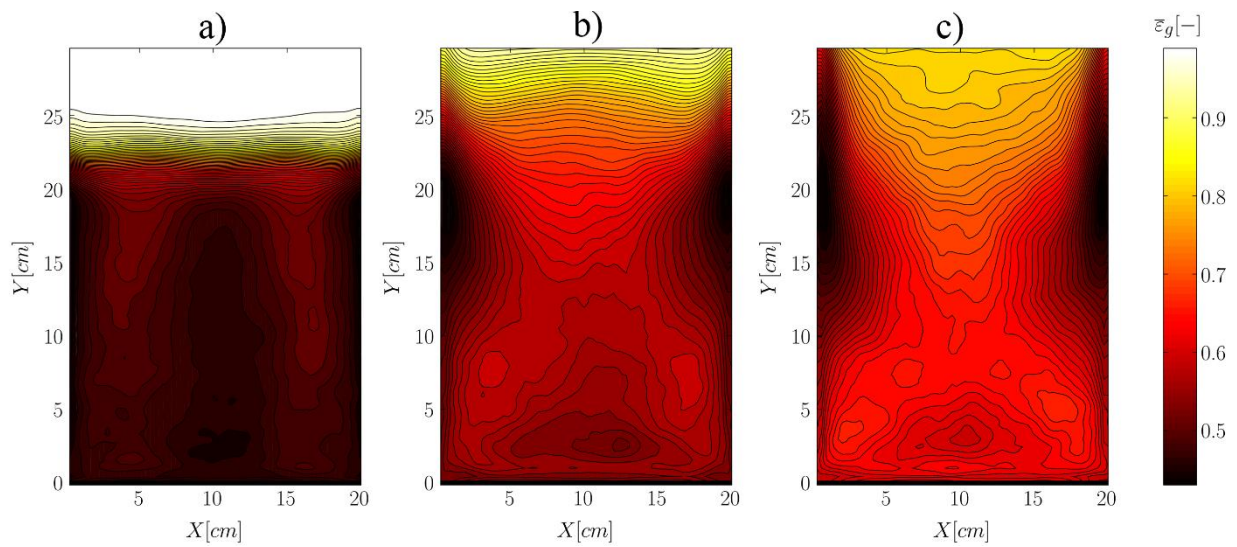


Figure 7. Time-averaged voidage distribution for particles with a diameter of $485 \text{ } [\mu\text{m}]$ and a density of $2500 \text{ } [\text{kg}/\text{m}^3]$ for a fluidization velocity of a) $1.5 u_{mf}$, b) $2.5 u_{mf}$, c) $3.5 u_{mf}$

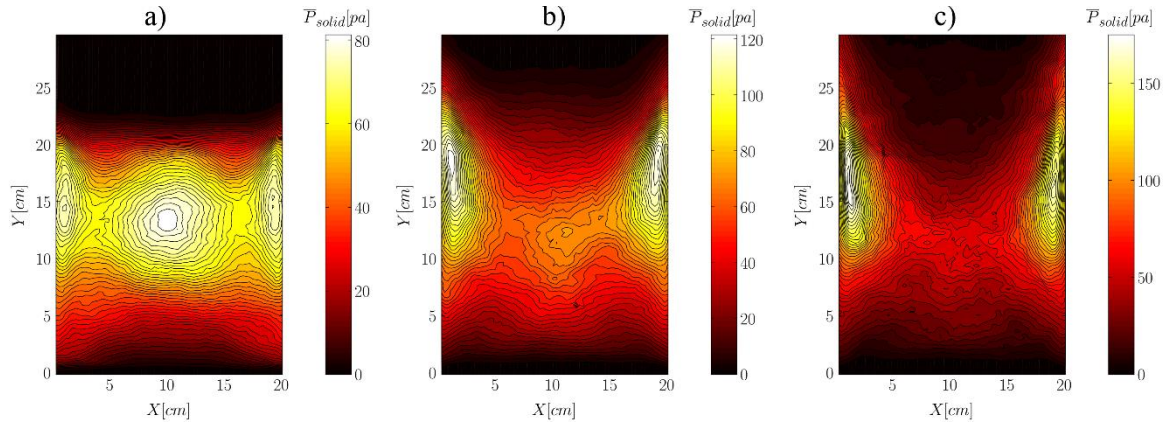


Figure 8. Time-averaged solid pressure distribution for particles with a diameter of $485 \text{ } [\mu\text{m}]$ and density of $2500 \text{ } [\text{kg}/\text{m}^3]$ for a fluidization velocity of a) $1.5 u_{mf}$, b) $2.5 u_{mf}$, c) $3.5 u_{mf}$

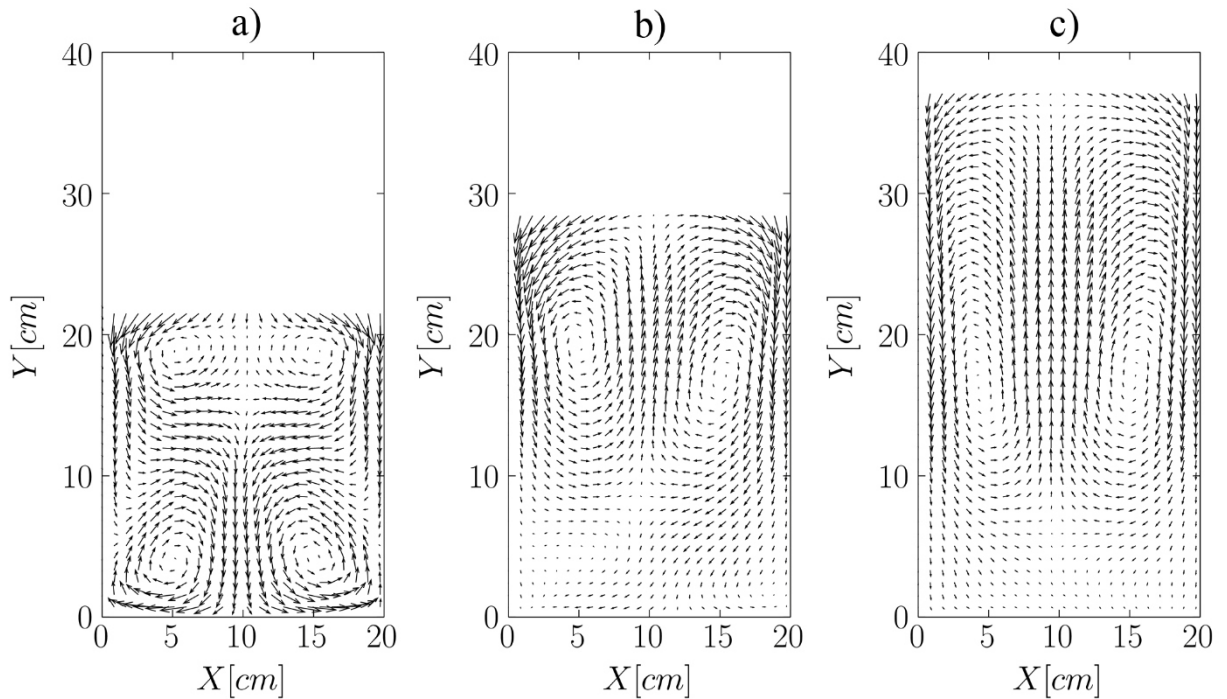


Figure 9. Solid flow pattern for particles with a diameter of $700 \text{ } [\mu\text{m}]$ and a density of $2500 \text{ } [\text{kg}/\text{m}^3]$, at different fluidization velocity: a) $1.5 u_{mf}$, b) $2.5 u_{mf}$, and c) $3.5 u_{mf}$

3.3.4. Quantification of Solids Mixing

As the solids flow pattern cannot represent the quality of mixing on its own, an attempt was made to quantify the solids mixing rate through dispersion and diffusion metrics. To quantify dispersion, the tensor characterizing fluctuations of the locally-average

particle velocity was computed based on a volume fraction-weighted (i.e., solid mass-weighted) velocity variance [55]:

$$\mathbf{v}_{ij}^{\prime 2} = \frac{1}{\sum_{k=1}^{N_{\Delta t}} \varepsilon_{s_{ij}}(t_k)} \sum_{k=1}^{N_{\Delta t}} \varepsilon_{s_{ij}}(t_k) [\mathbf{v}_{ij}(t_k) - \bar{\mathbf{v}}_{ij}] \otimes [\mathbf{v}_{ij}(t_k) - \bar{\mathbf{v}}_{ij}] \quad (31)$$

Where $\bar{\mathbf{v}}_{ij}$ and $\mathbf{v}_{ij}(t_k)$ denote the time-averaged and instantaneous solid velocity in cell ij , respectively. \otimes denotes the dyadic product.

$$\bar{\mathbf{v}}_{ij} = \frac{1}{\sum_{k=1}^{N_{\Delta t}} \varepsilon_{s_{ij}}(t_k)} \sum_{k=1}^{N_{\Delta t}} \varepsilon_{s_{ij}}(t_k) \mathbf{v}_{ij}(t_k) \quad (32)$$

$N_{\Delta t}$ stands for the total number of time steps. In our present work, only the axial and lateral component of the averaged solid velocity variances were investigated and used to quantify the solid dispersion rate and its dependence on the solids flow pattern.

As discerned from Figure 10a-b, for a specific particle density, an increase in the fluidization velocity results in a more heterogeneous distribution of the velocity variance in both lateral and axial directions. Furthermore, a rise in u / u_{mf} results in a higher velocity variance, which can be attributed to the higher bubble rise velocity at larger fluidization number.

What is more, at low fluidization velocity, i.e., $1.5u_{mf}$, the lowest axial and lateral solid velocity variances are predicted near the vertical walls. In addition, the velocity variance increases with increasing distance from the wall and remains approximately constant between $x/D_{bed} = 0.2$ and 0.8 . On the other hand, as the fluidization velocity increases (i.e., $2.5u_{mf}$ and $3.5u_{mf}$), the solid velocity variances increase from the lowest values at walls and hit a maximum at the bed centre (i.e., $x/D_{bed} = 0.5$). These results are in accordance with the experimental data reported by Li et al. [4]

As shown in Figure 10c-d and Figure 11, the lateral solid velocity variance (i.e., $u^{\prime 2}$) has a pronounced maximum just above the distributor surface for all studied fluidization velocities. Further above the distributor, the lateral solid velocity variance remains approximately constant up to the regions close to the splashing zone. In contrary, the axial solid velocity variance increases and hits a maximum near the bed surface. This

rise in the axial solid velocity variance is sharper when higher fluidization velocity is applied.

Having compared the results depicted in Figure 6, Figure 10, and Figure 11, it can be concluded that higher solid velocity variances are predicted in bottom vortices for a small fluidization number of $1.5 u_{mf}$. In contrast, at higher fluidization velocities of $2.5 - 3.5 u_{mf}$, the top vortices have higher solids velocity fluctuations. The aforementioned conclusion suggests that only the bottom vortices play the central role in solids mixing at low fluidization number. It was also demonstrated that an increase in the excess gas velocity gives a rise in both axial and lateral solid mean velocity fluctuations. (See Appendix B for more detail)

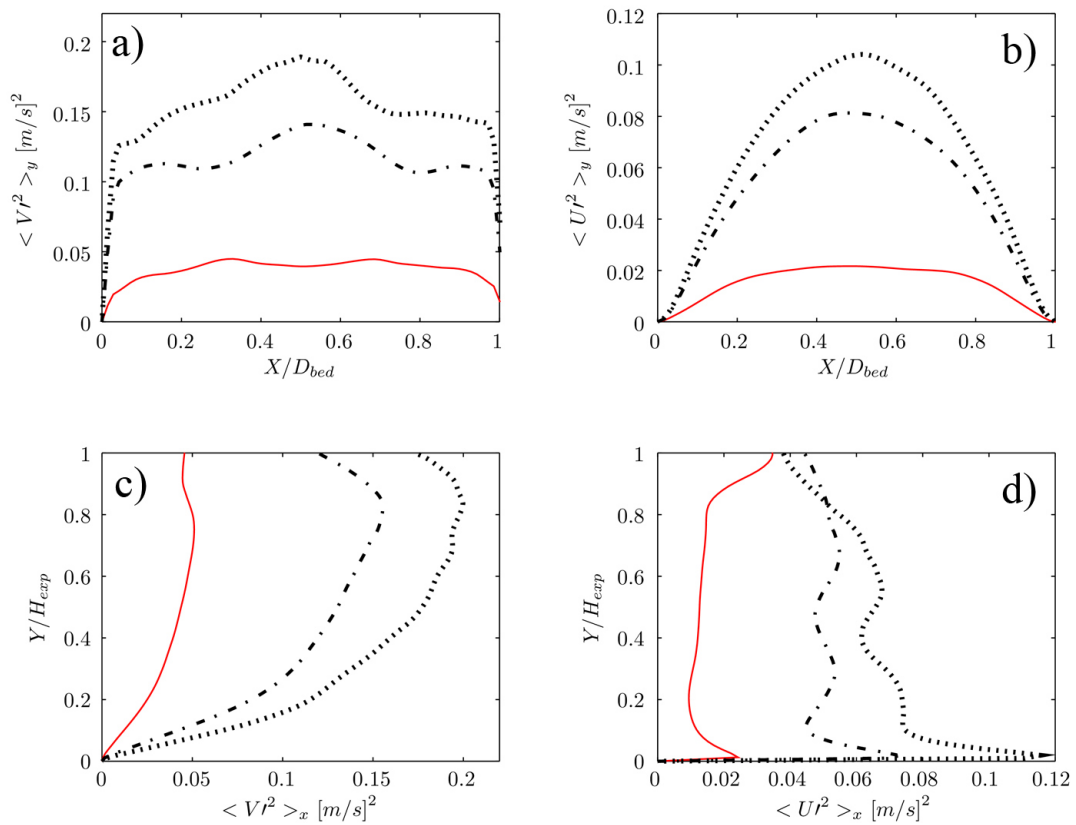


Figure 10. Distribution of the averaged solid mean velocity fluctuation in the fluidized bed: axially-averaged variance of a) axial velocity b) lateral velocity versus dimensionless lateral distance and laterally-averaged variance of c) axial velocity d) lateral velocity versus dimensionless axial distance for particle size of $485 [\mu\text{m}]$ and density of $2500 [\frac{\text{kg}}{\text{m}^3}]$ ($-1.5u_{mf}$; $-2.5u_{mf}$; \dots $3.5u_{mf}$)

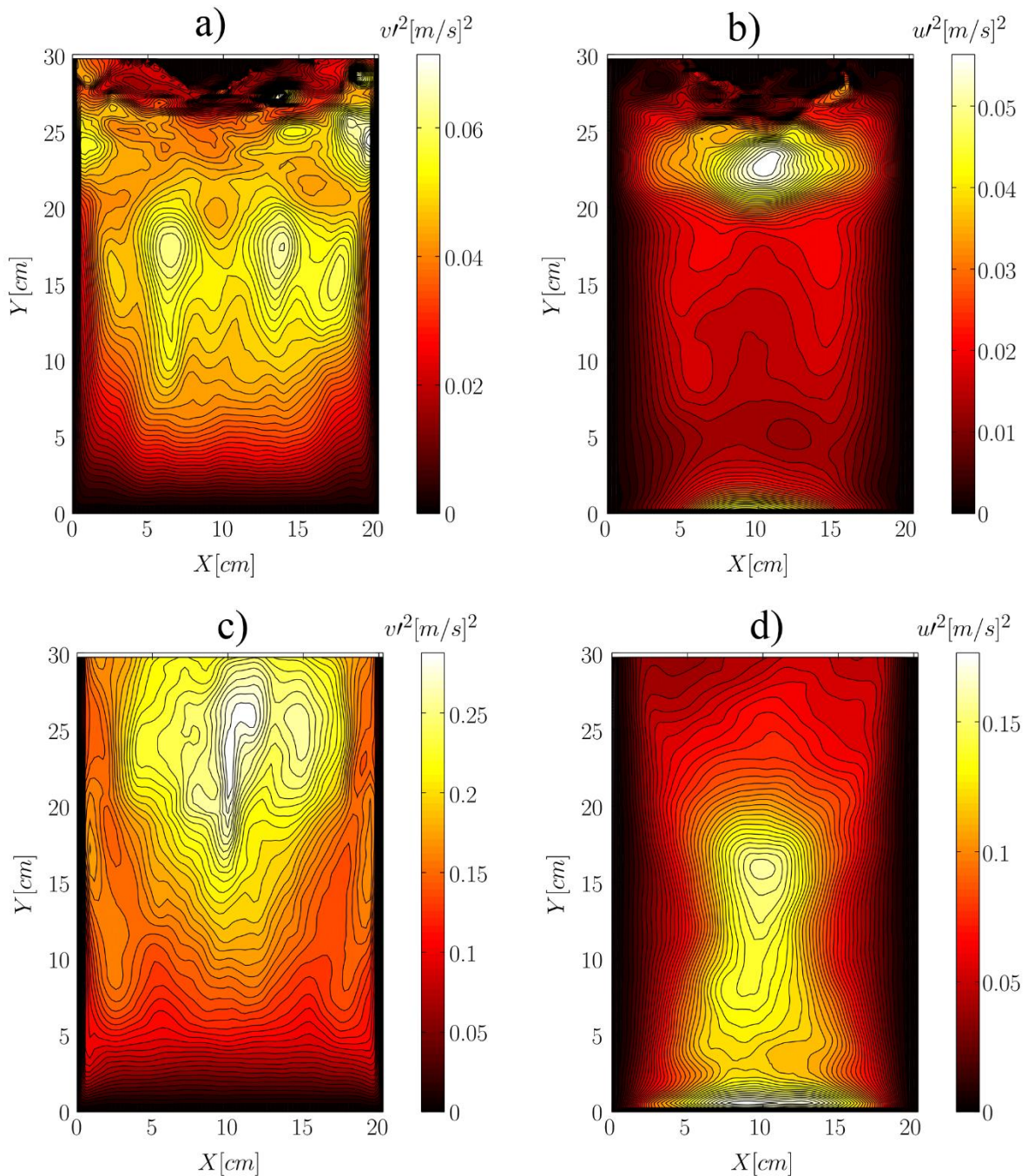


Figure 11. Contour plots of axial and lateral solid mean velocity fluctuation for the bed filled with particles of $2500 \frac{\text{kg}}{\text{m}^3}$ in density and at fluidization velocity of $1.5u_{mf}$ (top panels) and $3.5u_{mf}$ (bottom panels)

It is essential to correlate solid dispersion and diffusion to the particle properties, and fluidization velocity. The reason is since the quality of mixing is mainly governed by solid mean velocity fluctuations and granular temperature through solid dispersion

and diffusion respectively. To realize it, the particle volume-weighted average granular temperature is computed for each case as:

$$\langle \bar{\theta} \rangle = \frac{1}{\sum_{i=1}^{N_t} \varepsilon_{s_i}} \sum_{i=1}^{N_t} [\varepsilon_{s_i} \bar{\theta}] \quad (33)$$

Comparing the value of the solid mean velocity fluctuation (weighted based on the time-averaged solid volume fraction) in Figure 12 reveals that the axial solid mean velocity fluctuation outweighs the lateral one by a factor of 2 to 3. The same ratio was also reported by Natarajan et al. [24], who experimentally investigated solids velocity fluctuations in an FB. A similar finding has been reported by Luo et al. [25]. Also, the solid mean velocity fluctuations dominate the averaged granular temperature by 1 – 2 orders of magnitude. This finding shows that random particle motion (i.e., diffusion) is only marginally contributing to mixing compared to a bubble-induced solid motion, i.e., dispersion.

To lump the effect of particle size and density as well as the fluidization velocity, the domain-averaged solid mean velocity fluctuation and granular temperature were plotted versus the excess gas velocity in Figure 12. As easily discerned from this Figure, the axial solid mean velocity fluctuation constantly increases with an increase in the excess gas velocity, while the particle granular temperature depends not only on the excess gas velocity but also on the particle size. To put in more detail, at the same excess gas velocity, a larger particle size results in a larger granular temperature. This finding can be explained by the production of granular temperature by shear [56], which leads to a granular temperature scaling $\theta \propto d_s^2$.

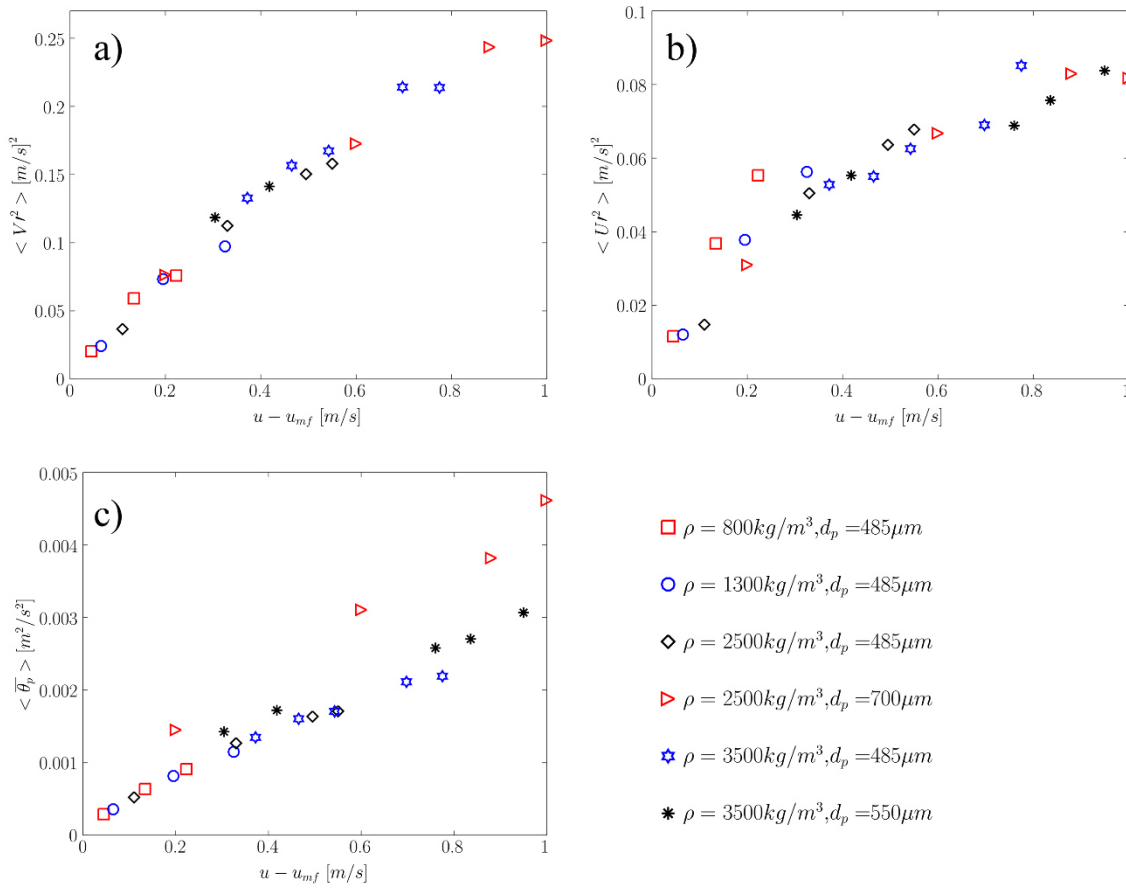


Figure 12. Variation of a) axial solid mean velocity fluctuation, b) lateral solid mean velocity fluctuation, and c) particle granular temperature as a function of particle density versus the excess gas velocity

Now it is beneficial to quantify the degree of mixing based on the solid dispersion coefficient and particle diffusivity and correlate them with suitable variables. To achieve this, the solid dispersion in k direction and diffusion coefficient can be calculated based on the solids mean velocity fluctuation and the granular temperature [56], respectively

$$C_{disp}^k = \frac{1 - \langle \bar{\varepsilon}_s \rangle}{f} \mathbf{v}_k'^2 \quad (34)$$

$$C_{diff} = \frac{d_s \sqrt{\pi \theta}}{8(1 + e_s) \langle \bar{\varepsilon}_s \rangle g_0(\langle \bar{\varepsilon}_s \rangle)} \quad (35)$$

Here g_0 and e_s are the radial distribution function and the particle-particle restitution coefficient, respectively. The parameter f denotes the bubble frequency, and can be estimated via [56]

$$f = \frac{1}{2\pi} \left(\frac{g}{H_0} \right)^{0.5} \left[\frac{(3 \langle \bar{\varepsilon}_s \rangle / (1 - \langle \bar{\varepsilon}_s \rangle) + 2) \langle \bar{\varepsilon}_s \rangle}{\varepsilon_{s0}} \right]^{0.5} \quad (36)$$

in which H_0 and ε_0 are the initial bed height and the initial voidage, respectively. It should be added that in Eqns.(34)-(36), $\langle \bar{\varepsilon}_s \rangle$ is the domain- time- average particle volume fraction in the bed. Using Eqns. (34)-(35), and the results of the CFD simulations, the solid dispersion and diffusivity were computed and are depicted in Figure 13. Furthermore, the contribution of convective particle transport relative to particle dispersion was quantified by calculating a dispersion Peclet Number as follows:

$$Pe = \frac{(u - u_{mf})D_h}{C_{disp}} \quad (37)$$

where D_h denotes the hydraulic diameter based on the beds cross section. As demonstrated by the simulation results in Figure 13a-b, the axial and lateral dispersion coefficients can be linearly correlated to the excess gas velocity. Substituting the hydraulic diameter of the studied fluidized bed in Equation (37), the axial and lateral Peclet numbers for the studied system can be calculated as

$$Pe^{ax} = 1.54 \quad (38)$$

$$Pe^{lat} = 3.92 \quad (39)$$

Besides, the particle diffusivity can be linearly correlated to the excess gas velocity multiplied with the particle diameter, as shown in Figure 13c. Equation (37) can be modified to calculate a diffusion Peclet number in case the particle diffusivity replaces the dispersion coefficient in the denominator of this equation, and the particle diameter replaces the hydraulic diameter. Consequently, a diffusion Peclet Number for our present set of simulations has the value of

$$Pe^{Diff} = 312.5 \quad (40)$$

It should be noted that the predicted solid diffusivity is four orders of magnitude smaller than the dispersion coefficient. Thus, the solid diffusivity contribution to the overall solids mixing process can be neglected compared with the one caused by coherent particle motion.

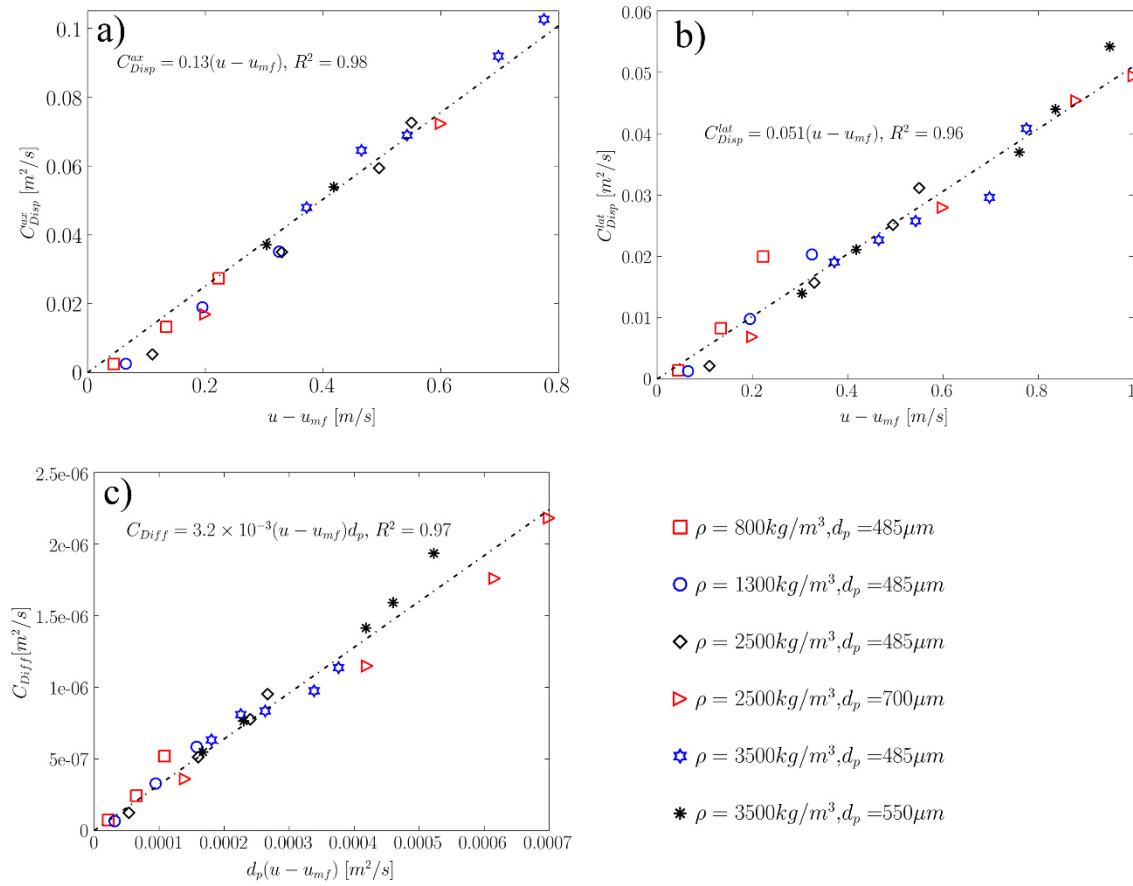


Figure 13. The dependency of a) axial and b) lateral dispersion, as well as c) the particle diffusion coefficients on particle properties and the excess gas velocity

3.3.5. Mixing Time Correlation

As explained in the previous section, the particle properties, and fluidization velocity significantly influence solid dispersion. In detail, a higher excess gas velocity induces a higher dispersion coefficient, which leads to faster solids mixing. Aiming at quantifying the mixing rate, a specific scalar quantity was set to a group of particles using a checkerboard pattern (with the size of $D_{bed}/2$) after the BFB has reached a pseudo steady-state condition. Afterward, the variation of this quantity was tracked in the bed by solving the scalar transport equation, as presented in Section 3.2.2. To calculate the characteristic mixing time, the transport equation for fluctuating solid scalar quantity should be considered. To derive such an equation, the local species concentration can be defined as the summation of a mean and fluctuating value

$$x_s = \bar{x}_s + \sigma_{x_s} \quad (41)$$

As reported by Müller [57] a characteristic time t_c for mixing of a scalar quantity can be calculated based on the temporal decay of the scalar quantity variance as follows:

$$\frac{\sigma_{x_s}}{\sigma_{x_{s_0}}} = e^{-t/t_c} \quad (42)$$

To calculate t_c , the predicted temporal decay of scalar variance was fitted to the exponential function in Eqn. 42. As shown in Figure 14, for a given particle size and density, a higher fluidization velocity results in a shorter mixing time, which can be attributed to a larger dispersion coefficient, and consequently a more efficient mixing in the fluidized bed.

We note in passing that the initialization of flow affects the mixing rate of a scalar quantity. To do so, a set of simulations were performed for the particle density of $2500 \text{ [kg/m}^3\text{]}$ and diameter of 485 [\mu m] at two different fluidization numbers (i.e., $u/u_{mf} = 1.5$ and 3.5). Two different strategies to color the particles were investigated: A) coloring the particles at rest immediately after particles were packed, and B) coloring the particles when the bed reached a pseudo steady state (flow) condition (i.e., when the profile of velocity variance does not change with time). According to the results reported in Table 4, the characteristic mixing time of strategy A are 20 and 45 percent smaller than the corresponding values of strategy B at a fluidization number of 1.5 and 3.5, respectively. Furthermore, in order to guarantee the independency of characteristic mixing time from the period during which the variance of the scalar was tracked, the mixing time was obtained by applying strategy B at initial different times (of course, after the pseudo steady state was reached). According to the results (not shown here), identical characteristic mixing times were predicted for these simulations. Thus, as long as the bed reaches a pseudo steady state, the mixing rate can be described to a good approximation with a single mixing time scale.

Table 4. The characteristic mixing time of a solids species depending on the coloring scenario: A) coloring at rest B) coloring after reaching the pseudo steady-state.

$\rho_s \text{ [}\frac{\text{kg}}{\text{m}^3}\text{]}$	$d_s \text{ [\mu m]}$	$u/u_{mf} \text{ [-]}$	$t_{c,A} \text{ [s]}$	$t_{c,B} \text{ [s]}$
2500	485	1.5	2.12	2.55
2500	485	3.5	0.74	1.06

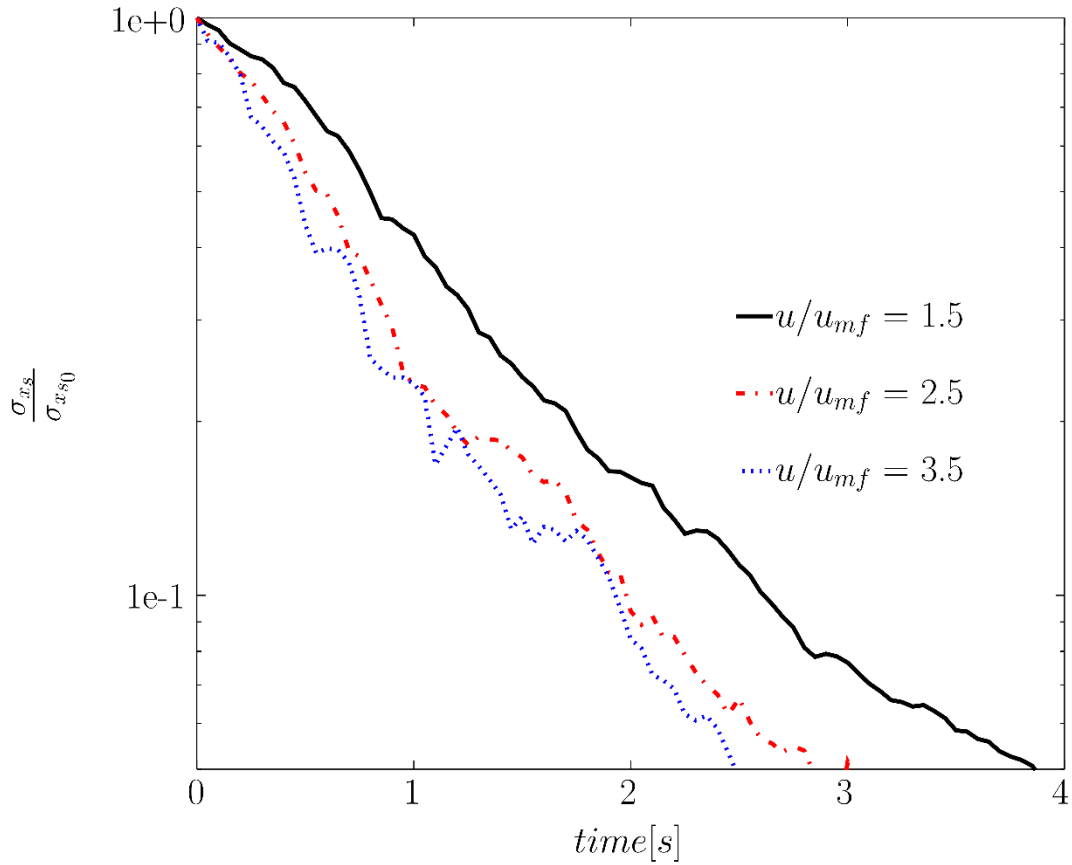


Figure 14. Concentration variance of species x versus time for different fluidization velocities for particles with a density of $2500 \frac{kg}{m^3}$.

Same as for the solid dispersion coefficients, the characteristic mixing time was calculated for various solid densities, and it was correlated to the most relevant parameters. As shown in Figure 15, a dimensionless mixing time $t_c^* = t_c C_{disp} / H_{exp}^2$ can be correlated to an excess velocity-based Froude Number defined as $N_{Fr} = \frac{u - u_{mf}}{\sqrt{g D_{bed}}}$ as:

$$t_c = 0.56 \frac{H_{exp}^2}{C_{disp}} N_{Fr}^{0.56} \quad (43)$$

It should be noted that the dispersion coefficient in the above equation (i.e., C_{disp}) has been calculated based on the fluctuation of the mean particle velocity, i.e., $v'^2 = \frac{1}{3} v_{ax}'^2 + \frac{2}{3} v_{lat}'^2$. These results are in line with the data for the solids dispersion coefficient (see

section 3.3.4), i.e., larger dispersion velocities result in a smaller mixing time when considering a fixed expanded bed height.

It should be noted that the effect of the bed geometry and bed aspect ratio on mixing time can be of interest for researchers, but have not been studied in our present contribution. This topic will be analyzed in our future publications.

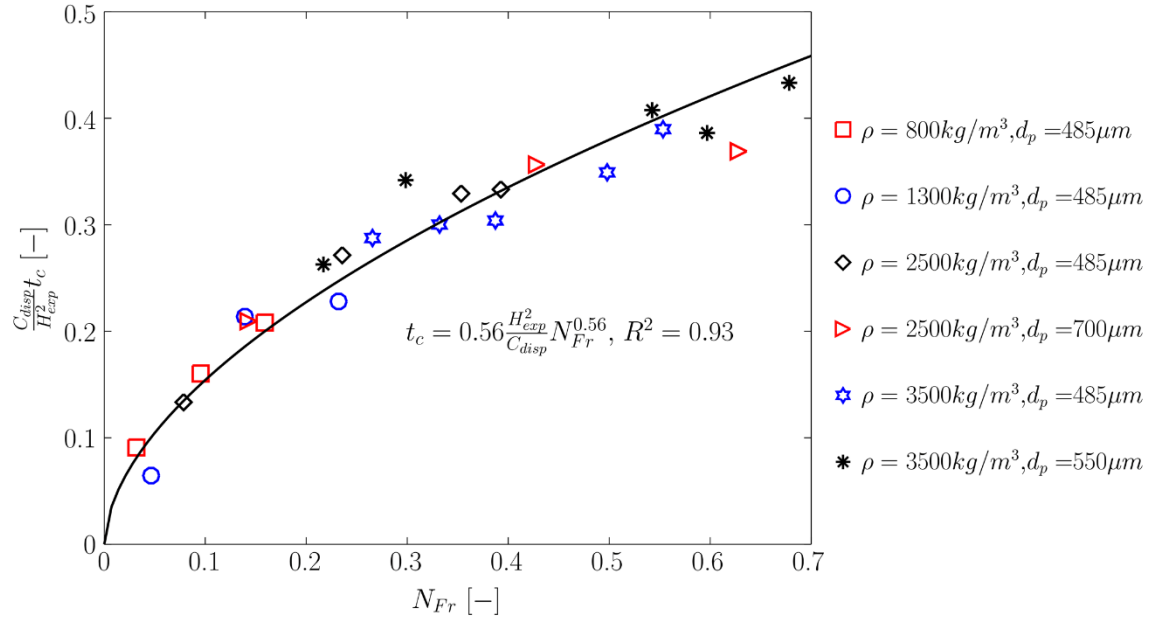


Figure 15. The characteristic time of particle mixing versus excess gas velocity for different particle densities and particle sizes

Bakshi et al. [53] proposed two correlations for i) the average positive circulation time (i.e., τ_{Cor}^+) and ii) the average circulation time (i.e., τ_{Cor}). Even though the definition of the circulation time is not identical to the characteristic mixing time presented in our present work, it is worth comparing these two time scales. To do so, the mixing time was calculated (using our present correlation) for the fluidized bed studied by Bakshi et al. [53]. As shown in Figure 16, the trend of our mixing time (i.e., t_c) follows the trend of τ_{Cor}^+ though the slope is smaller. If this circulation time is scaled with a factor of 1.4 (see the data for $\tau_{Cor}^{+scaled}$ in Figure 16), a maximum relative difference of 26% can be predicted in comparison with the characteristic mixing time.

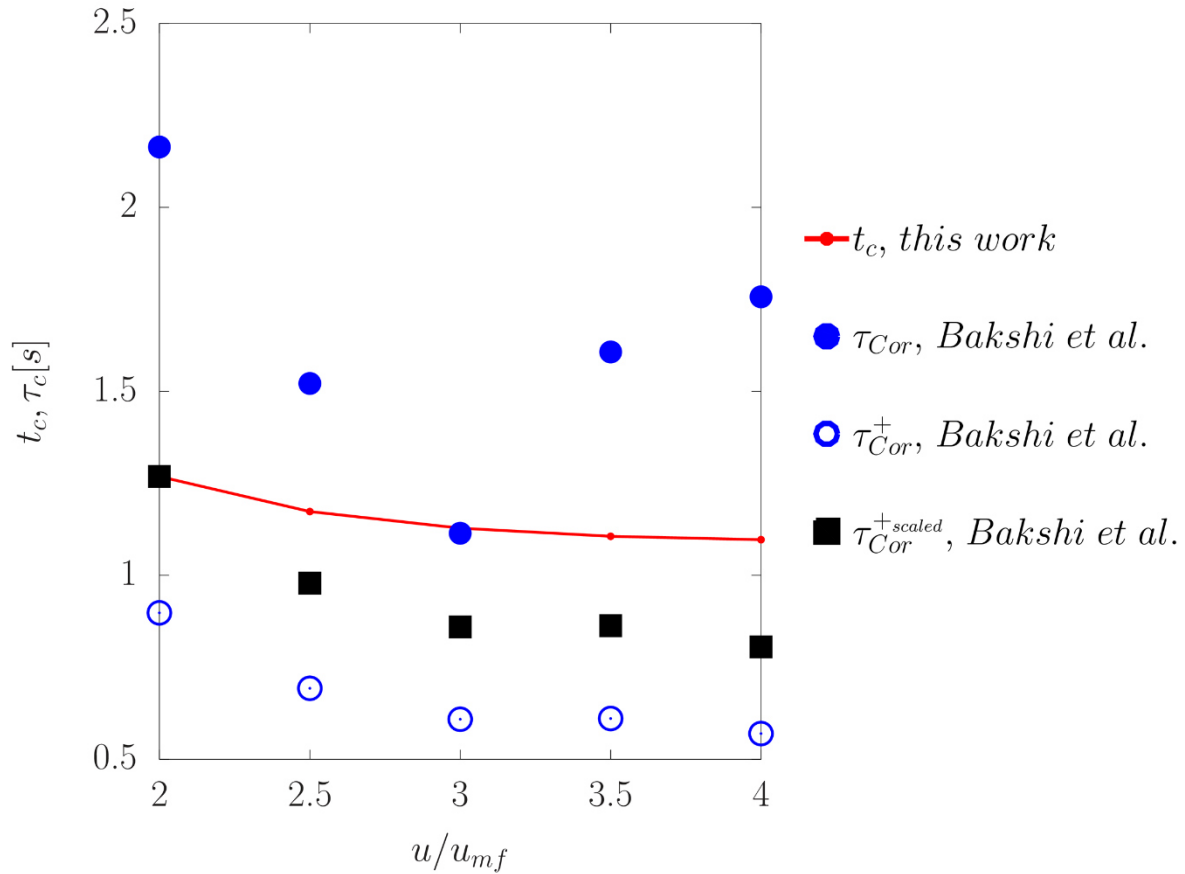


Figure 16. Comparison of the average circulation time proposed by Bakshi et al. [53] with the characteristic time of particle mixing presented in our current study.

3.3.6. Vortex-Specific Mixing Rates

To examine the effect of solid flow pattern on the mixing time, two sets of simulations were performed in which the initialization of the solid tracer was varied. Especially, particles were marked (i) in the top and (ii) in the bottom vortices after reaching a pseudo-steady state flow, as shown in Figure 17. The mixing time was then computed through the same procedure as described in Section 3.3.5.

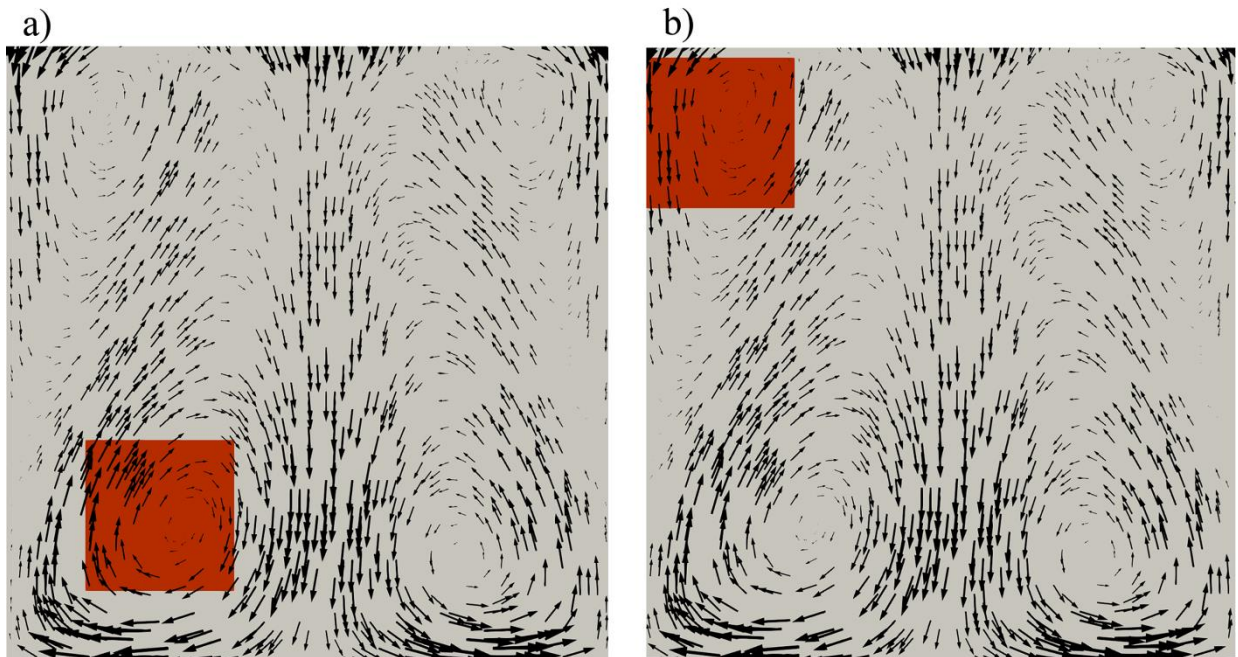


Figure 17. Illustration of coloring particles (red color) in the fluidized bed in a) the bottom vortex and, b) the top vortex

Comparing the mixing times for different injection points reveals that the fluidization velocity significantly affects the mixing time, as reported in Table 5. For example, at a fluidization velocity of $1.5u_{mf}$, mixing occurs more efficiently (i.e., is faster) in the bottom vortices. This is due to the larger size of this vortex. As the fluidization velocity increases, the difference of the mixing times becomes smaller between the top and bottom vortices. Another point discerned from this Table is the effect of particle density on the mixing time ratio. In detail, for a fluidization number of 2.5 and 3.5, an increase in the particle density reduces the mixing time for the top and the bottom vortices. In summary, the mixing time depends on the point at which the species is injected at low and moderate fluidization number. However, at high enough fluidization number, the solid dispersion is large enough to mix the solids efficiently regardless of the injection point.

Table 5. The characteristic time of species x dispersion injected at different vortices: 1) top (i.e., $t_{c,top}$) 2) bottom (i.e., $t_{c,bottom}$)

ρ_p [$\frac{\text{kg}}{\text{m}^3}$]	d_p [μm]	u/u_{mf} [-]	$t_{c,bottom}$ [s]	$t_{c,top}$ [s]
800	485	1.5	1.639	2.387
800	485	2.5	1.035	0.855
800	485	3.5	1.008	1.022
1300	485	1.5	1.017	1.076
1300	485	2.5	1.018	0.794
1300	485	3.5	0.746	0.737
2500	485	1.5	2.036	2.341
2500	485	2.5	0.918	0.814
2500	485	3.5	0.599	0.568

3.4. Conclusion

In the present study, the fluidization and mixing behavior of Geldart's B particle was numerically investigated in a BFB. Two-fluid model based on KTGF has been adopted to run the simulations. The range of particle diameter and density have been selected such that the entire range of Geldart's group classification B can be covered.

The grid sensitivity analysis proved that the optimum grid size strongly depends on particle properties, as well as fluidization velocity. This finding can be attributed to the size of the bubbles formed in the bed. It was also revealed that the solid flow pattern predicted for particles of Geldart's group B/D differs from the one observed for the particles with lower density and/or size: Specifically, four vortices are formed in the bed for Geldart B particles various fluidization velocities when considering the mean particle velocity distribution. In contrast, for the heavier particles approaching Geldart's group D, four vortices were predicted only at low fluidization velocities.

Interestingly, an increase of the fluidization velocity in case of group B/D particles results in the formation of two vortices. This conclusion reveals the significant contribution of particle density in the solid flow behavior in a fluidized bed, which was

not addressed in previous studies focusing on solid flow pattern [17,22]. Our finding is supported by the numerical results of Bakshi et al. [53], who studied the effect of particle density on the solid circulation time in the FB.

Solid dispersion and diffusion coefficients were obtained by analyzing the velocity variance of solid particles. The simulation results showed that the effect of particle properties (i.e., density and diameter) and fluidization velocity can be lumped to a single parameter, namely the excess gas velocity. Considering the diameter of the bed as the relevant characteristic, this led to a constant dispersion Peclet number of 3.92 and 1.54 for lateral and axial solid dispersion, respectively. In contrast, a particle diffusion-based Peclet number of 312 was calculated from our simulation data, indicating that mixing on a particle scale is convection dominated. We note in passing that solid dispersion and diffusion has been investigated in the open literature by various researchers [4,12,14,24–26]. Nonetheless, no concrete correlation has been presented in previous studies [13,23–25,32], a gap which is closed by our present work.

In our current study, the characteristic mixing time was computed assuming exponential decay of the variance of a scalar tracer adhering to the particles. The results of our simulations demonstrated that an adequately normalized mixing time can be successfully correlated to an excess velocity-based particle Froude Number for particles falling into Geldart's classification B. The proposed correlation can be readily used to calculate the mixing time without necessitating experimental measurements. In contrast, when using the correlation developed by Bakshi et al. [53] for the solids circulation time (which can be seen as a global mixing time), (i) the bubble diameter, (ii) momentum coefficients, as well as (iii) a correlation coefficient must be determined beforehand, which limits the application of this correlation. Besides, the static bed height was considered as a characteristic length for mixing, which does not agree with our finding (and the more natural idea) of using the expanded bed height.

Also, the effect of fluid bed initialization on the computed mixing rate has not been adequately addressed in previous studies [12,25,26]. As our present work demonstrated, particle mixing time can be over-predicted by up to 45% in case of evaluating particle mixing during FB start-up. This is because the bed has not reached

a pseudo-steady state condition. Clearly, in future work care has to be taken to consider data from a FB at pseudo-steady state, which imposes an additional limitation for experimental studies (i.e., initially colored particles cannot be used).

Finally, to link mixing quality to solid flow pattern, the characteristic mixing time was computed for situations in which particles are dispersed from (i) the top, and (ii) bottom vortices. It was revealed that at a gas inlet velocity of $1.5u_{mf}$, solids mixing is faster in the two bottom vortices. Interestingly, at higher fluidization velocities, a faster mixing was predicted for the top vortices. This finding hints to unused potentials when maximizing the performance of fluidized beds, e.g., by determining the optimal feed location of educts in an FB reactor as a function of the fluidization velocity.

3.5. Nomenclature

C_d	Drag coefficient;
C_{Diff}	Solid diffusivity coefficient; [m^2/s]
C_{Disp}^k	Solid dispersion coefficient in k direction; [m^2/s]
C_{Disp}^{ax}	Axial solid dispersion coefficient; [m^2/s]
C_{Disp}^{lat}	Lateral solid dispersion coefficient; [m^2/s]
D_{Bed}	Bed diameter; [m]
D_h	Hydraulic Bed diameter; [m]
\mathbf{D}_g	Rate of deformation tensor for phase for the gas phase; [s^{-1}]
\mathbf{D}_s	Rate of deformation tensor for phase for the solid phase; [s^{-1}]
d_s	Particle diameter; [m]
D_{gn}	Diffusion coefficient of n^{th} gas-phase species; [$kg/m \cdot s$]
D_{mn}	Diffusion coefficient of n^{th} solids-phase-m species-n; [$kg/m \cdot s$]
e_s	Coefficient of restitution for the particle-particle collisions
e_w	Coefficient of restitution for the particle-wall collisions
f	Bubble frequency; [Hz]
g	Acceleration due to gravity; [m/s^2]
g_0	Radial distribution function
H_{exp}	Expanded bed height; [m]
H_{bed}	Total bed height; [m]
H_0	Static bed height; [m]

\mathbf{I}_{gs}	Interphase momentum exchange force; [N/m^3]
J_s	Granular energy dissipation due to inelastic interaction; [m^2/s^3]
\mathbf{n}	Unit outward normal vector to the surface
$N_{\Delta t}$	Total number of time steps
N_{Fr}	Froude number
P_g	Pressure in the fluid phase; [Pa]
P_s^{fr}	Frictional pressure in the solid phase; [Pa]
P_s^{kc}	Collisional pressure in the solid phase; [Pa]
P_s	Solid pressure; [Pa]
Pe	Peclet number
Pe^{ax}	Peclet number in axial direction
Pe^{lat}	Peclet number in lateral direction
Pe^{Diff}	Diffusion Peclet number
\mathbf{q}	Pseudo-thermal energy (PTE) flux vector ; [kg/s^3]
Re_s	Solids phase particle Reynolds number
\mathbf{S}_s^{fr}	Frictional solid stress tensor; [Pa]
\mathbf{S}_s^{kc}	Kinetic and collisional solid stress tensor; [Pa]
\mathbf{T}_g	Gas phase shear stress tensor; [Pa]
t	Time; [s]
t_c	Characteristic mixing time; [s]
t_c^*	Dimensionless mixing time
$t_{c,top}$	Characteristic mixing time of species x injected at top vortices; [s]
$t_{c,bottom}$	Characteristic mixing time of species x injected at bottom vortices; [s]
u_{mf}	Minimum fluidization velocity; [m/s]
u	Superficial gas velocity; [m/s]
\mathbf{u}_g	Fluid-phase velocity vector; [m/s]
\mathbf{u}_s	Solid-phase velocity vector; [m/s]
\bar{u}_s	Dimensionless local slip velocity at the wall
\mathbf{u}_s^{sl}	Solid slip velocity at the wall; [m/s]
\mathbf{v}_{ij}	Instantaneous solid velocity in cell ij ; [m/s]
$\bar{\mathbf{v}}_{ij}$	Time-averaged solid velocity in cell ij ; [m/s]
$\mathbf{v}_{ij}'^2$	Solid mass-weighted velocity variance in cell ij ; [m^2/s^2]

v'^2	Solid mass-weighted velocity variance; [m^2/s^2]
$v'_{ax}{}^2$	Solid mass-weighted velocity variance in axial direction; [m^2/s^2]
$v'_{lat}{}^2$	Solid mass-weighted velocity variance in lateral direction; [m^2/s^2]
x_s	mass fraction of scalar quantity in the solid particle
\bar{x}_s	time-averaged species mass fraction in the solid phase

Greek Letters

α	A constant with value of 1.6; dimensionless
β_{gs}	Coefficient for the interphase exchange force; [kg/m^3s]
β_0	Tangential restitution coefficient
σ_{x_s}	Fluctuation of scalar quantity in the solid phase
ε_g	Volume fraction of the fluid phase (void fraction)
ε_g^*	Volume fraction of the fluid phase at minimum fluidization condition
ε_s^{mf}	Volume fraction of the solid phase at minimum fluidization condition
ε_s^{max}	Packed-bed (maximum) solids volume fraction
ε_s	Volume fraction of solids phase
ε_{sij}	Volume fraction of solids phase in cell ij
ε_{s0}	Initial solid volume fraction
η_s	Function of particle-particle restitution coefficient
η_w	Function of particle-wall restitution coefficient
θ	Granular temperature of solid phase; [m^2/s^2]
κ	Granular energy diffusion coefficient; [$kg/m \cdot s$]
λ_s^{kc}	solid bulk viscosity; [$Pa \cdot s$]
μ_g	Molecular viscosity of the fluid phase; [$Pa \cdot s$]
μ_s^{fr}	Frictional shear viscosity of the solid phase; [$Pa \cdot s$]
μ_s^{kc}	Collisional shear viscosity of the solid phase; [$Pa \cdot s$]
μ_w	coefficient of wall friction
σ_{x_s}	fluctuating species concentration
Π_s	Fluctuation exchange energy in granular energy equation; [$kg/m \cdot s^3$]
ρ_g	Microscopic (material) density of the fluid phase; [kg/m^3]
ρ_s	Microscopic (material) density of solids phase; [kg/m^3]
τ_s^{kc}	Wall shear stresses due to particle-wall collisions; [Pa]
τ_s^{fr}	Wall shear stresses due to frictional particle-wall contacts; [Pa]

φ Angle of internal friction, also used as a general scalar

Operators

$\langle M \rangle_x$ Laterally-averaged of M quantity weighted by solid volume fraction

$\langle M \rangle_y$ Axially-averaged of M quantity weighted by solid volume fraction

$\langle M \rangle$ Domain-averaged of M quantity weighted by solid volume fraction

\bar{M} Time averaged of M quantity

Acronyms

CFD Computational Fluid dynamics

DEM Discrete Element Method

KTGF Kinetic Theory of Granular Flow

MFIX Multiphase Flow with Interphase eXchange

TFM Two-Fluid Model

2D Two-Dimensional

3D Three-Dimensional

3.6. References

- [1] W.C. Yang, Handbook of Fluidization and Fluid-Particle Systems, Taylor & Francis, 2003.
- [2] D. Kunii, O. Levenspiel, H. Brenner, Fluidization Engineering, Elsevier Science, 1991.
- [3] P. Basu, Combustion and gasification in fluidized beds, CRC press, 2006.
- [4] Y. Li, J. Rong, K. Zhang, X. Fan, Impact of solid and gas flow patterns on solid mixing in bubbling fluidized beds, Chem. Eng. Res. Des. 132 (2018) 1037–1053. doi:10.1016/j.cherd.2017.12.014.
- [5] P. Salatino, R. Solimene, Mixing and segregation in fluidized bed thermochemical conversion of biomass, Powder Technol. 316 (2017) 29–40. doi:10.1016/j.powtec.2016.11.058.
- [6] M. Hemati, R. Cherif, K. Saleh, V. Pont, Fluidized bed coating and granulation: Influence of process-related variables and physicochemical properties on the growth kinetics, Powder Technol. 130 (2003) 18–34. doi:10.1016/S0032-5910(02)00221-8.

- [7] H.P. Cui, M. Strabel, D. Rusnell, H.T. Bi, K. Mansaray, J.R. Grace, C.J. Lim, C.A. McKnight, D. Bulbuc, Gas and solids mixing in a dynamically scaled fluid coker stripper, *Chem. Eng. Sci.* 61 (2006) 388–396. doi:10.1016/j.ces.2005.06.014.
- [8] S. Andersson, S. Radl, I.-H. Svenum, S.A. Shevlin, Z. Xiao Guo, S. Amini, Towards rigorous multiscale flow models of nanoparticle reactivity in chemical looping applications, *Catal. Today.* (2019). doi:10.1016/J.CATTOD.2019.06.024.
- [9] D. Liu, X. Chen, Lateral solids dispersion coefficient in large-scale fluidized beds, *Combust. Flame.* 157 (2010) 2116–2124. doi:10.1016/j.combustflame.2010.04.020.
- [10] L.M. Garcia-Gutierrez, A. Soria-Verdugo, U. Ruiz-Rivas, Optimization of the feeding ports location in a fluidized bed combustor based on Monte Carlo simulations of fuel particles motion, *Fuel.* 141 (2015) 82–92. doi:10.1016/j.fuel.2014.10.027.
- [11] L. Shen, M. Zhang, Y. Xu, Solids mixing in fluidized beds, *Powder Technol.* 48 (1993) 38. doi:10.1016/0026-0657(93)92818-P.
- [12] J. Sánchez-Prieto, F. Hernández-Jiménez, L.M. Garcia-Gutierrez, A. Soria-Verdugo, Experimental study on the characteristic mixing time of solids and its link with the lateral dispersion coefficient in bubbling fluidized beds, *Chem. Eng. J.* 307 (2017) 113–121. doi:10.1016/j.cej.2016.08.075.
- [13] M. Askarishahi, M.-S. Salehi, H.R. Godini, G. Wozny, CFD study on solids flow pattern and solids mixing characteristics in bubbling fluidized bed: Effect of fluidization velocity and bed aspect ratio, *Powder Technol.* 274 (2015). doi:10.1016/j.powtec.2015.01.025.
- [14] Y. Li, H. Fan, X. Fan, Identify of flow patterns in bubbling fluidization, *Chem. Eng. Sci.* 117 (2014) 455–464. doi:10.1016/j.ces.2014.07.012.
- [15] J.A. Laverman, X. Fan, A. Ingram, V.S.M. Annaland, D.J. Parker, J.P.K. Seville, J.A.M. Kuipers, Experimental study on the influence of bed material on the scaling of solids circulation patterns in 3D bubbling gas-solid fluidized beds of glass and polyethylene using positron emission particle tracking, *Powder Technol.* 224 (2012) 297–305. doi:10.1016/j.powtec.2012.03.011.

- [16] J.A. Laverman, I. Roghair, M. Van Sint Annaland, H. Kuipers, Investigation into the hydrodynamics of gas-solid fluidized beds using particle image velocimetry coupled with digital image analysis, *Can. J. Chem. Eng.* 86 (2008) 523–535. doi:10.1002/cjce.20054.
- [17] J.S. Lin, M.M. Chen, B.T. Chao, A novel radioactive particle tracking facility for measurement of solids motion in gas fluidized beds, *AIChE J.* 31 (1985) 465–473.
- [18] S.H. Hosseini, G. Ahmadi, R. Rahimi, M. Zivdar, M.N. Esfahany, CFD studies of solids hold-up distribution and circulation patterns in gas-solid fluidized beds, *Powder Technol.* 200 (2010) 202–215. doi:10.1016/j.powtec.2010.02.024.
- [19] M. Farzaneh, S. Sasic, A.E. Almstedt, F. Johnsson, D. Pallarès, A study of fuel particle movement in fluidized beds, *Ind. Eng. Chem. Res.* 52 (2013) 5791–5805. doi:10.1021/ie301515v.
- [20] N. Mostoufi, J. Chaouki, Local solid mixing in gas-solid fluidized beds, *Powder Technol.* 114 (2001) 23–31. doi:10.1016/S0032-5910(00)00258-8.
- [21] X. Fan, Z. Yang, D.J. Parker, B. Armstrong, Prediction of bubble behaviour in fluidised beds based on solid motion and flow structure, *Chem. Eng. J.* 140 (2008) 358–369.
- [22] X. Fan, Z. Yang, D.J. Parker, Impact of solid sizes on flow structure and particle motions in bubbling fluidization, *Powder Technol.* 206 (2011) 132–138.
- [23] M. Askarishahi, M.-S. Salehi, A. Molaei Dehkordi, Numerical investigation on the solid flow pattern in bubbling gas-solid fluidized beds: Effects of particle size and time averaging, *Powder Technol.* 264 (2014). doi:10.1016/j.powtec.2014.05.061.
- [24] V.V.R. Natarajan, M.L. Hunt, E.D. Taylor, Local measurements of velocity fluctuations and diffusion coefficients for a granular material flow, *J. Fluid Mech.* 304 (1995) 1–25. doi:10.1017/S0022112095004320.
- [25] K. Luo, F. Wu, S. Yang, J. Fan, CFD-DEM study of mixing and dispersion behaviors of solid phase in a bubbling fluidized bed, *Powder Technol.* 274 (2015) 482–493. doi:10.1016/j.powtec.2015.01.046.

- [26] S. Gorji-Kandi, S.M. Alavi-Amleshi, N. Mostoufi, A solids mixing rate correlation for small scale fluidized beds, *Particuology*. 21 (2015) 55–64. doi:10.1016/j.partic.2014.10.003.
- [27] N. Gui, X. Yang, J. Tu, S. Jiang, A generalized particle-to-wall collision model for non-spherical rigid particles, *Adv. Powder Technol.* 27 (2016) 154–163. doi:10.1016/j.appt.2015.12.002.
- [28] T. Oschmann, J. Hold, Numerical investigation of mixing and orientation of non-spherical particles in a model type fluidized bed, *Powder Technol.* 258 (2014) 304–323. doi:10.1016/j.powtec.2014.03.046.
- [29] F. Tian, M. Zhang, H. Fan, M. Gu, L. Wang, Y. Qi, Numerical study on microscopic mixing characteristics in fluidized beds via DEM, *Fuel Process. Technol.* 88 (2007) 187–198. doi:10.1016/j.fuproc.2006.04.006.
- [30] J.A. Medrano, M. Tasdemir, F. Gallucci, M. van Sint Annaland, On the internal solids circulation rates in freely-bubbling gas-solid fluidized beds, *Chem. Eng. Sci.* 172 (2017) 395–406. doi:10.1016/j.ces.2017.06.046.
- [31] Z. Wang, C. Zhang, R. Kang, X. Wei, F. Bin, T. Li, B. Li, Dispersion characteristics of dissimilar materials in a fluidized bed with unevenly distributed fluidizing air, *Powder Technol.* 319 (2017) 365–372. doi:10.1016/j.powtec.2017.07.017.
- [32] M. Banaei, N.G. Deen, M. van Sint Annaland, J.A.M. Kuipers, Particle mixing rates using the two-fluid model, *Particuology*. 36 (2018) 13–26. doi:10.1016/j.partic.2017.01.009.
- [33] M.J. Rhodes, X.S. Wang, M. Nguyen, P. Stewart, K. Li, Study of mixing in gas-solid fluidized beds using a DEM model, *Chem. Eng. Sci.* 56 (2001) 2859–2866.
- [34] M. Syamlal, *MFIX documentation numerical technique*, 1998. doi:10.2172/656644.
- [35] N. Xie, F. Battaglia, S. Pannala, Effects of using two- versus three-dimensional computational modeling of fluidized beds: Part I, hydrodynamics, *Powder Technol.* 182 (2008) 1–13. doi:https://doi.org/10.1016/j.powtec.2007.07.005.

- [36] N. Reuge, L. Cadoret, C. Coufort-Saudejaud, S. Pannala, M. Syamlal, B. Caussat, Multifluid Eulerian modeling of dense gas-solids fluidized bed hydrodynamics: Influence of the dissipation parameters, *Chem. Eng. Sci.* 63 (2008) 5540–5551. doi:10.1016/j.ces.2008.07.028.
- [37] T.B. Anderson, R. Jackson, Fluid Mechanical Description of Fluidized Beds. Equations of Motion, *Ind. Eng. Chem. Fundam.* 6 (1967) 527–539. doi:10.1021/i160024a007.
- [38] C.Y. Wen, Y.H. Yu, Mechanics of fluidization, in: *Chem. Eng. Prog., Symp. Ser.*, 1966: pp. 100–111.
- [39] S. Schneiderbauer, A. Aigner, S. Pirker, A comprehensive frictional-kinetic model for gas-particle flows: Analysis of fluidized and moving bed regimes, *Chem. Eng. Sci.* 80 (2012) 279–292. doi:10.1016/j.ces.2012.06.041.
- [40] B.G.M. van Wachem, J.C. Schouten, C.M. van den Bleek, R. Krishna, J.L. Sinclair, Comparative analysis of CFD models of dense gas–solid systems, *AIChE J.* 47 (2001) 1035–1051. doi:10.1002/aic.690470510.
- [41] S. Schneiderbauer, D. Schellander, A. Löderer, S. Pirker, Non-steady state boundary conditions for collisional granular flows at flat frictional moving walls, *Int. J. Multiph. Flow.* 43 (2012) 149–156. doi:10.1016/j.ijmultiphaseflow.2012.03.006.
- [42] M. Syamlal, W. Rogers, T.J. O'Brien, *MFIX documentation theory guide*, 1993. doi:10.2172/10145548.
- [43] K. Agrawal, P.N. Loezos, M. Syamlal, S. Sundaresan, The role of meso-scale structures in rapid gas–solid flows, *J. Fluid Mech.* 445 (2001) 151–185.
- [44] C.M. Hrenya, J.L. Sinclair, Effects of particle-phase turbulence in gas-solid flows, *AIChE J.* 43 (1997) 853–869.
- [45] C.K.K. Lun, S.B. Savage, D.J. Jeffrey, Kinetic theories for granular flow : inelastic particles in Couette flow and slightly inelastic particles in a general flowfield, *J. Fluid Mech.* 140 (1984).
- [46] D.L. Koch, Kinetic theory for a monodisperse gas–solid suspension, *Phys. Fluids A Fluid Dyn.* 2 (1990) 1711–1723.

- [47] S. Schneiderbauer, D. Schellander, A. Löderer, S. Pirker, Non-steady state boundary conditions for collisional granular flows at flat frictional moving walls, *Int. J. Multiph. Flow.* 43 (2012) 149–156. doi:10.1016/j.ijmultiphaseflow.2012.03.006.
- [48] S.S. Hsiau, M.L. Hunt, Granular thermal diffusion in flows of binary-sized mixtures, *Acta Mech.* 114 (1996) 121–137. doi:10.1007/BF01170399.
- [49] A. Bakshi, C. Altantzis, R.B. Bates, A.F. Ghoniem, Eulerian-Eulerian simulation of dense solid-gas cylindrical fluidized beds: Impact of wall boundary condition and drag model on fluidization, *Powder Technol.* 277 (2015) 47–62. doi:10.1016/j.powtec.2015.02.056.
- [50] A. Bakshi, C. Altantzis, L.R. Glicksman, A.F. Ghoniem, Gas-flow distribution in bubbling fluidized beds: CFD-based analysis and impact of operating conditions, *Powder Technol.* 316 (2017) 500–511. doi:10.1016/j.powtec.2017.01.005.
- [51] A. Bakshi, *Multiscale Continuum Simulations of Fluidization: Bubbles, Mixing Dynamics and Reactor Scaling*, 2017.
- [52] A. Bakshi, C. Altantzis, R.B. Bates, A.F. Ghoniem, Study of the effect of reactor scale on fluidization hydrodynamics using fine-grid CFD simulations based on the two-fluid model, *Powder Technol.* 299 (2016) 185–198. doi:10.1016/j.powtec.2016.05.029.
- [53] A. Bakshi, A.F. Ghoniem, C. Altantzis, Mixing dynamics in bubbling fluidized beds, *AIChE J.* 63 (2017) 4316–4328. doi:10.1002/aic.15801.
- [54] D. Geldart, J. Baeyens, The design of distributors for gas-fluidized beds, *Powder Technol.* 42 (1985) 67–78. doi:10.1016/0032-5910(85)80039-5.
- [55] T. Finch, Incremental calculation of weighted mean and variance, *Gen. Relativ. Gravit.* 39 (2009) 511–520. doi:10.1143/PTP.126.993.
- [56] J. Jung, D. Gidaspo, I.K. Gamwo, Measurement of Two Kinds of Granular Temperatures, Stresses, and Dispersion in Bubbling Beds, *Ind. Eng. Chem. Res.* 44 (2005) 1329–1341. doi:10.1021/ie0496838.

[57] W. Müller, Methoden und derzeitiger Kenntnisstand für Auslegungen beim Mischen von Feststoffen, Chemie Ing. Tech. 53 (1981) 831–844. doi:10.1002/cite.330531102.

3.7. Appendix A. Model Validation and Mesh Dependency

3.7.1. A.1 Validation

It is necessary to validate the numerical implementation of the boundary condition proposed by Schneiderbauer [1]. To do so, we simulated the experimental setup used by Buijtenen et al. [2] (See Figure A.1). The simulation setup has been reported in Table A.1. As shown in Figure A. 2, the time-averaged solid axial velocity (during 20 [s] of flow time) at two different heights are well-matched with the experimental value.

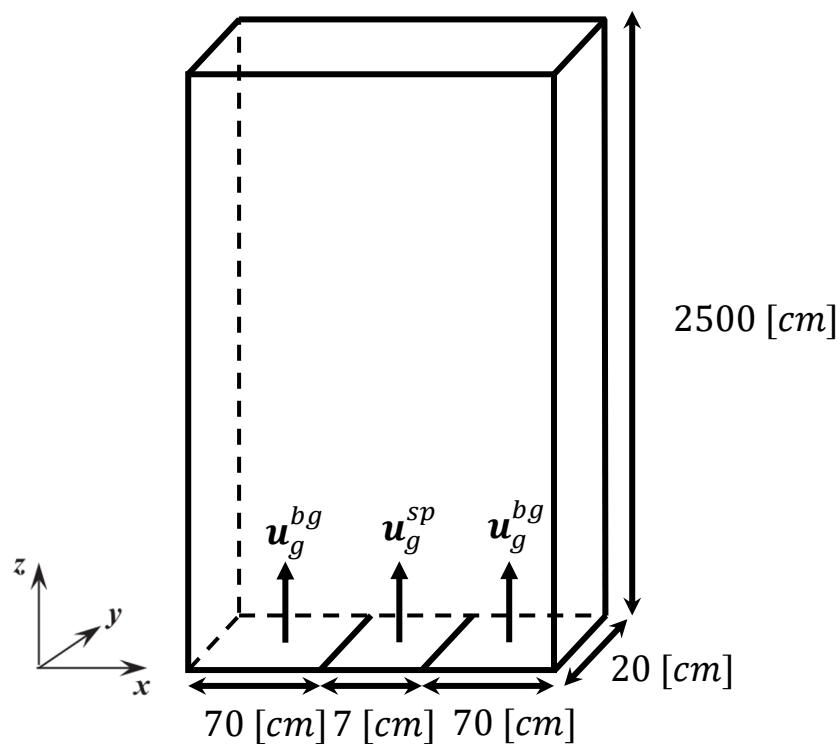


Figure A.1. The schematic view of the validation case based on experimental setup reported in [2]

Table A.1. The schematic view of the validation case based on experimental setup reported in [2]

Property	Value
L_{Bed}	1.47 [m]
H_{bed}	2.5 [m]
ρ_s	2500 [kg/m ³]
d_s	3 [mm]
ε_g^*	0.42
$\varepsilon_s^{\text{max}}$	0.6
φ	28.5°
e_s	0.9
e_w	0.9
β_0	0.4
μ_w	0.5
ρ_g	1.225 [kg/m ³]
μ_g	1.78×10^{-5} [Pa.s]
u_g^{bg}	2.4 [m/s]
u_g^{sp}	43.5 [m/s]

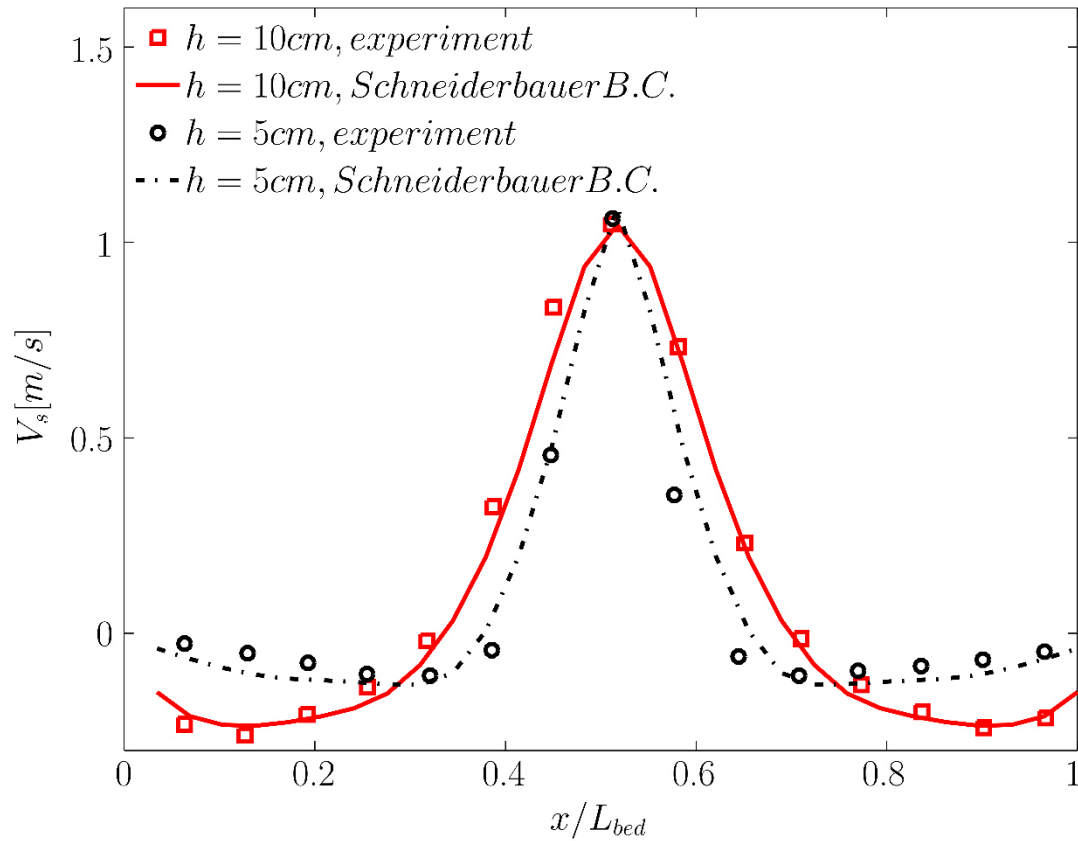


Figure A. 2. Validation of implemented boundary condition presented by Simon Schneiderbauer [3] based on the data reported by Buijtenen et al. [2] (maximum relative error of 30% for $h = 5[cm]$ and 10% for $h = 10[cm]$)

3.7.2. A.2 Grid Sensitivity Analysis:

To examine the independency of the solution from the grid size, a fluidized bed with D_{bed} of 0.2 [m] and H_{Bed} of 0.75 [m] and aspect ratio of 1 (same as the case in manuscript) was simulated at the fluidization velocity of $1.5u_{mf}$ for various particle densities (i.e., $\rho_p = 2500 [kg/m^3]$ and $800 [kg/m^3]$). As depicted in Figure A. 3 and Figure A. 4, the accuracy of time- laterally-averaged voidage distribution along the bed is not significantly improved upon refining the mesh to value smaller than $7d_p$ and $4d_p$ for particles with the densities of $2500 [kg/m^3]$ and $800 [kg/m^3]$ respectively. The same analysis has been performed for various cases with different particle densities and diameters. As reported in Table 2 in the main manuscript, the beds filled with larger and heavier particles need a coarser grid. This can be explained by the fact that utilization of particles featuring lower minimum fluidization velocities induces the

formation of smaller bubbles. Therefore, a finer mesh is required to capture such small bubbles and consequently to predict the voidage distribution in the fluidized bed accurately. This is also the case for the lower fluidization velocity. However, in this study, the optimum grid size for lower fluidization velocity was used for the entire range of fluidization velocity to be on a safe side.

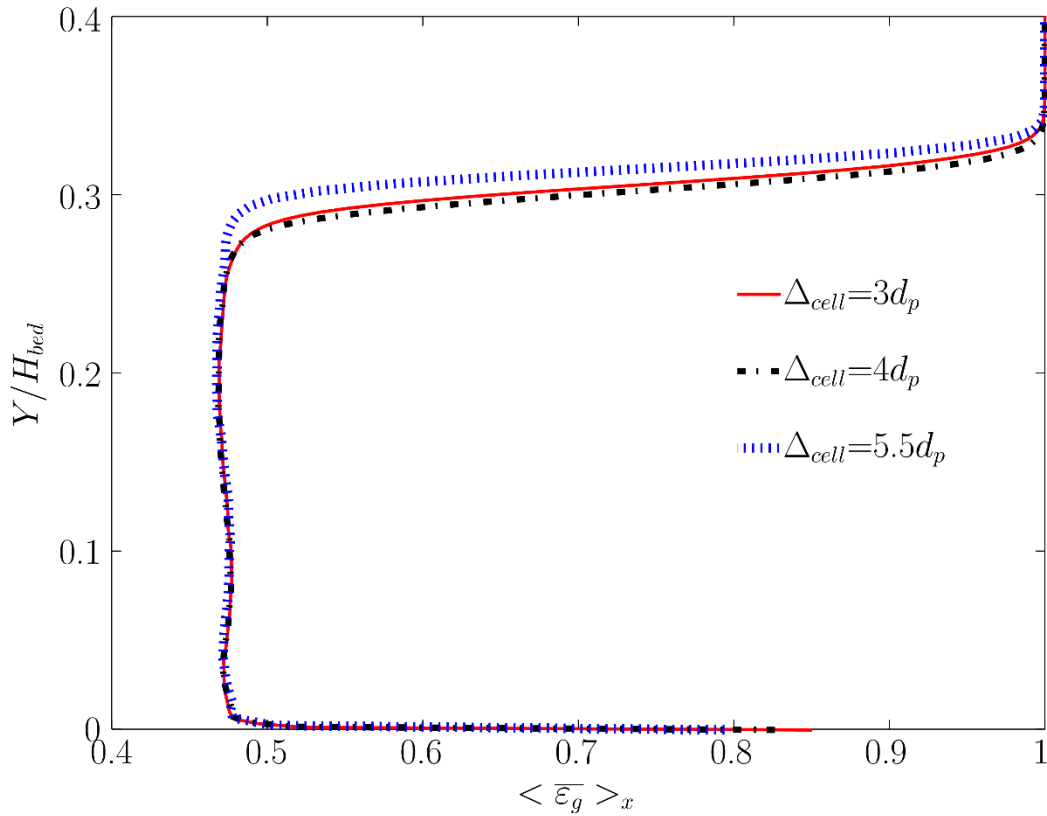


Figure A. 3. The dependency of the time- and laterally-averaged voidage on the grid size for the bed at $\frac{u}{u_{mf}} = 1.5$ and particles with $800 [kg/m^3]$ in density and $485 [\mu m]$ in diameter (maximum relative error 10% and 2% for $\Delta_{cell} = 5.5d_p$ and $\Delta_{cell} = 4d_p$ respectively in comparison with $\Delta_{cell} = 3d_p$)

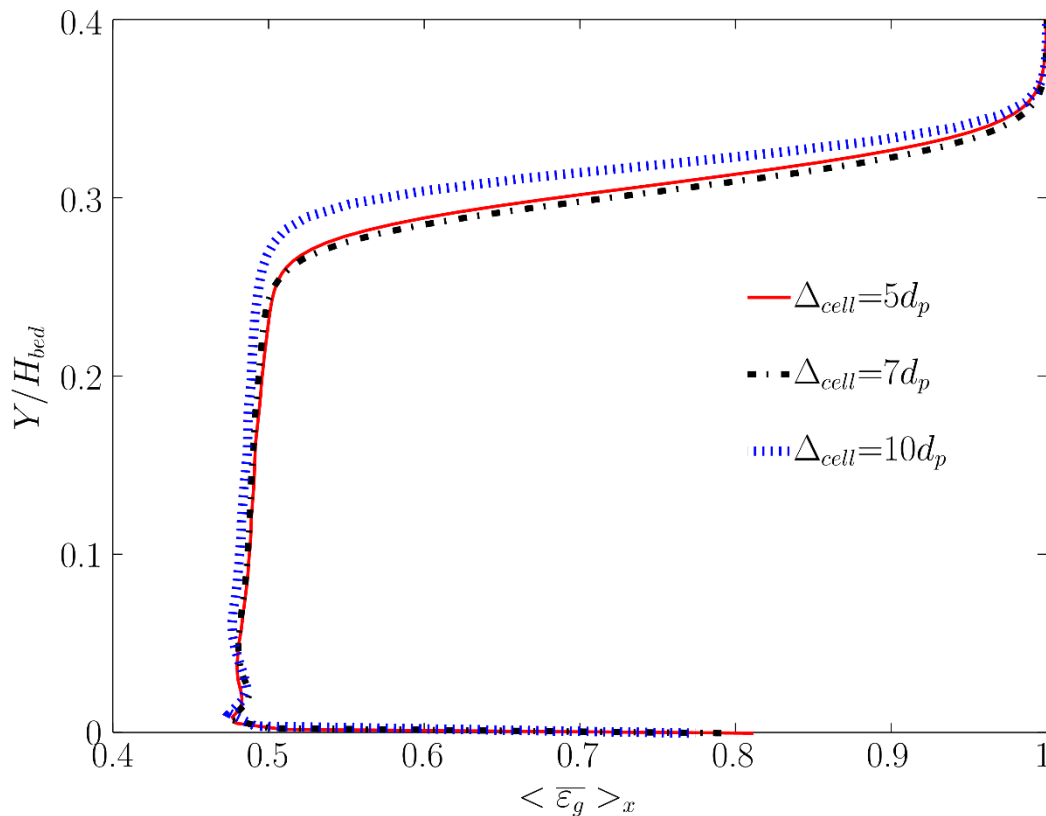


Figure A. 4. The dependency of the time- and laterally-averaged voidage on the grid size for the bed at $\frac{u}{u_{mf}} = 1.5$ and particles with $2500 [kg/m^3]$ in density and $485 [\mu m]$ in diameter (maximum relative error 10% and 2% for $\Delta_{cell} = 10d_p$ and $\Delta_{cell} = 7d_p$ respectively in comparison with $\Delta_{cell} = 5d_p$)

3.7.3. References

- [1] S. Schneiderbauer, D. Schellander, A. Löderer, S. Pirker, Non-steady state boundary conditions for collisional granular flows at flat frictional moving walls, *Int. J. Multiph. Flow.* 43 (2012) 149–156. doi:10.1016/j.ijmultiphaseflow.2012.03.006.
- [2] M.S. van Buijtenen, W.-J. van Dijk, N.G. Deen, J.A.M. Kuipers, T. Leadbeater, D.J. Parker, Numerical and experimental study on multiple-spout fluidized beds, *Chem. Eng. Sci.* 66 (2011) 2368–2376. doi:10.1016/j.ces.2011.02.055.
- [3] S. Schneiderbauer, A. Aigner, S. Pirker, A comprehensive frictional-kinetic model for gas-particle flows: Analysis of fluidized and moving bed regimes, *Chem. Eng. Sci.* 80 (2012) 279–292. doi:10.1016/j.ces.2012.06.041.

3.8. Appendix B. Solid Mean Velocity Fluctuation

To compute the dispersion coefficient, we need to quantify the locally-average particle velocity, which should be weighted by solid volume fraction. As it can be discerned from Figure B.1 to Figure B.3, an increase in the excess gas velocity leads to a rise in both axial and lateral solid mean velocity fluctuations for the studied range of particle density and diameter:

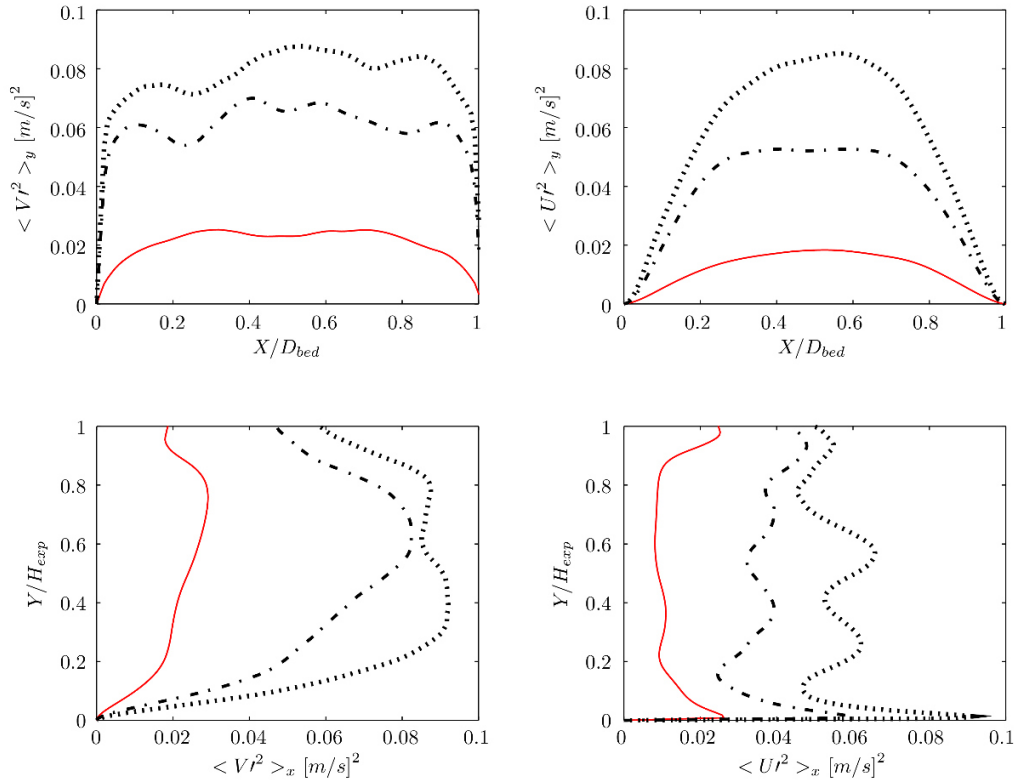


Figure B.1. Distribution of the averaged solid mean velocity fluctuation in the fluidized bed: axially-averaged variance of a) axial velocity b) lateral velocity versus dimensionless lateral distance and laterally-averaged variance of c) axial velocity d) lateral velocity versus dimensionless axial distance for particle size of $485[\mu m]$ and density of $800 \frac{kg}{m^3}$ ($-1.5u_{mf}$; $-2.5u_{mf}$; \dots $3.5u_{mf}$)

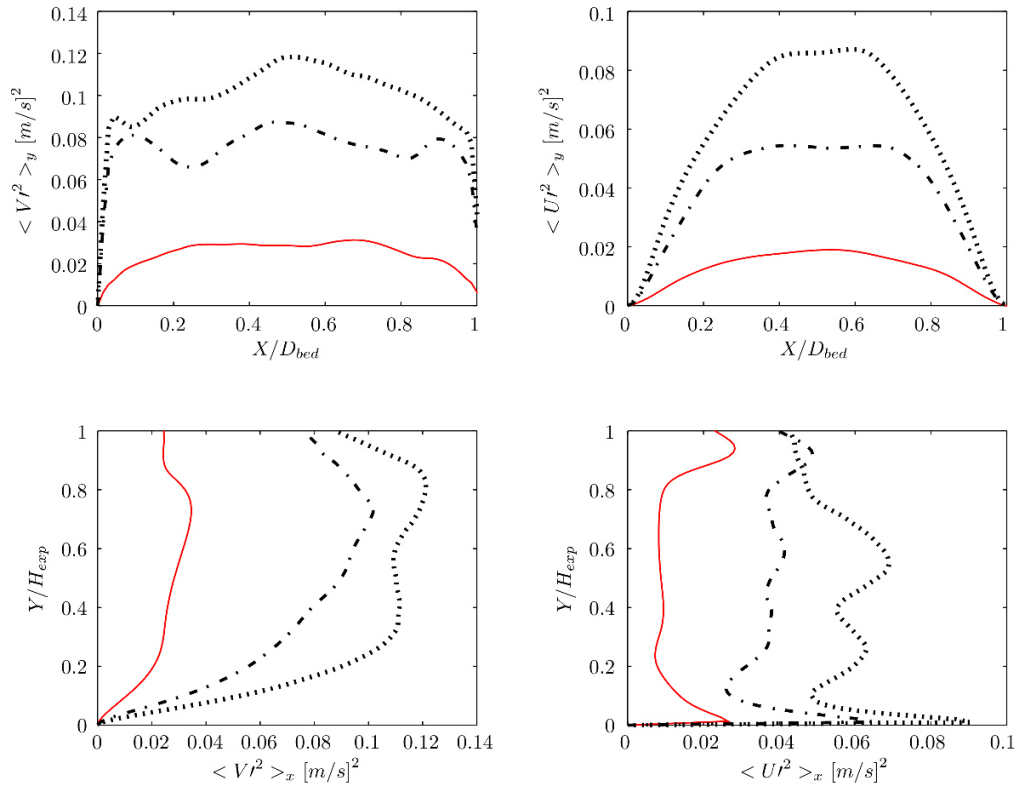


Figure B.2. Distribution of the averaged solid mean velocity fluctuation in the fluidized bed: axially-averaged variance of a) axial velocity b) lateral velocity versus dimensionless lateral distance and laterally-averaged variance of c) axial velocity d) lateral velocity versus dimensionless axial distance for particle size of $485 [\mu m]$ and density of $1300 [\frac{kg}{m^3}]$ ($-1.5u_{mf}$; $-2.5u_{mf}$; $3.5u_{mf}$)

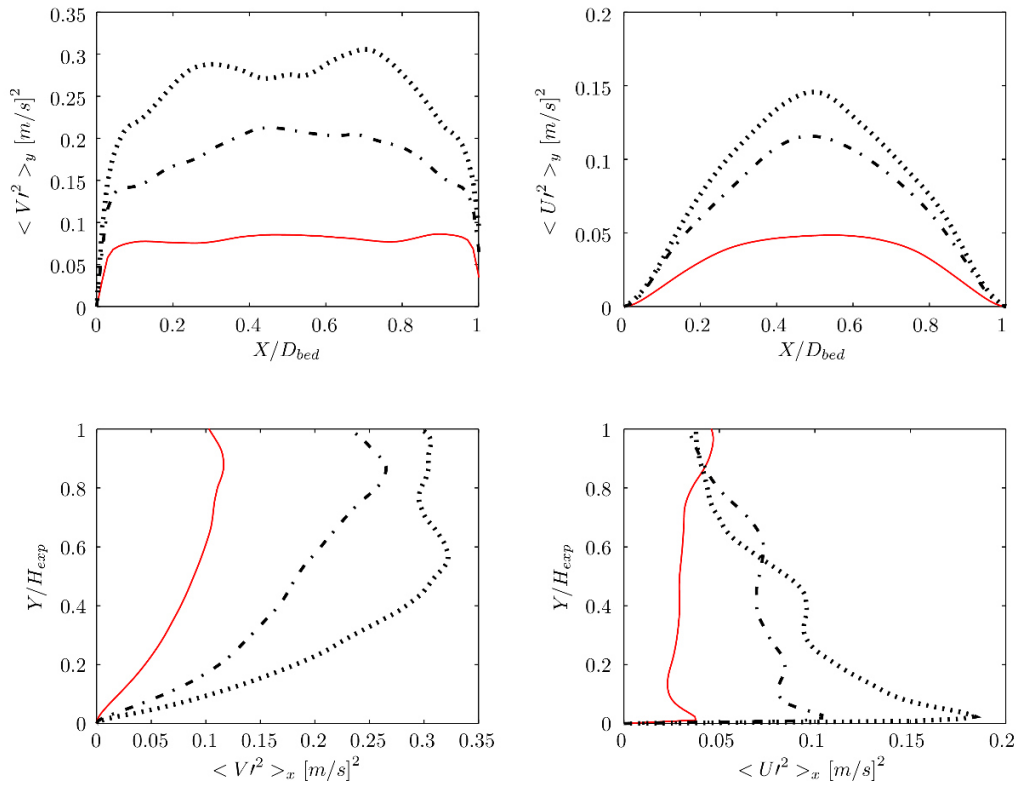


Figure B.3. Distribution of the averaged solid mean velocity fluctuation in the fluidized bed: axially-averaged variance of a) axial velocity b) lateral velocity versus dimensionless lateral distance and laterally-averaged variance of c) axial velocity d) lateral velocity versus dimensionless axial distance for particle size of $700[\mu m]$ and density of $2500[\frac{kg}{m^3}]$ ($-1.5u_{mf}$; $-2.5u_{mf}$; \dots $3.5u_{mf}$)

“Engineering or technology is all about using the power of science to make life better for people, to reduce cost, to improve comfort, to improve productivity.”

(N. R. Narayana Murthy)

4

CFD Simulation of Oxidative Coupling of Methane in Fluidized-Bed Reactors: A Detailed Analysis of Flow-Reaction Characteristics and Operating Conditions

In this section, the effect of operating condition and feed compositions is investigated in a reactive bubbling fluidized bed. The aim is to study the performance of oxidative coupling of methane reactor if a bubbling bed is used.

This article was published in *Industrial & Engineering Chemistry Research* 55, 2016, 1149-1163, DOI: 10.1021/acs.iecr.5b02433

Copyright is held by American Chemical Society, and all rights are reserved by this organization. Permission has been granted by American Chemical Society for including the following publication into the present thesis.

CFD Simulation of Oxidative Coupling of Methane in Fluidized-Bed Reactors: A Detailed Analysis of Flow-Reaction Characteristics and Operating Conditions

Mohammad-Sadegh Salehi,^{*,†} Maryam Askarishahi,[†] Hamid Reza Godini,^{*,†} Reinhard Schomäcker,[‡] and Günter Wozny[†]

[†]Chair of Process Dynamics and Operation, Berlin Institute of Technology, Strasse des 17. Juni 135, Sekr. KWT-9, D-10623 Berlin, Germany

[‡]Institute of Chemistry, Berlin Institute of Technology, Strasse des 17. Juni 124, D-10623 Berlin, Germany

ABSTRACT: The effect of operating conditions and feed characteristics on the performance of the oxidative coupling of methane (OCM) reactor was investigated numerically by analyzing the concentration of the reactants and products along the fluidized-bed reactor. Aimed at modeling such multiphase flow, a two-fluid model based on the kinetic theory of granular flow was applied. The impact of the kinetic model was conceptually investigated through investigation of the observed reaction pathways along the reactor under various feed dilutions. The overall predicted selectivity toward ethylene and ethane (C_2 -products) and methane conversion were in agreement with the experimental data. In detail, the results of simulations demonstrated that the fast acceleration of ethylene steam reforming at $T > 800$ °C results in C_2 selectivity peaking around $T = 800$ °C. However, an increase in pressure from 1 bar to 3 bar slightly decreases the C_2 selectivity. At identical space velocity, a decrease in CH_4/O_2 ratio improves the C_2 yield.

1. INTRODUCTION

Oxidative Coupling of Methane (OCM) is an attractive alternative process for direct ethylene production from methane-rich resources.¹ The OCM reactions are represented by the combination of several gas phase and catalyst surface reactions with a strong net exothermic behavior. This complicated system requires a detailed thermal-reaction analysis to control the operating temperature in the reactor section and improve its reaction performance in terms of ethylene yield and selectivity.² Therefore, it is believed that the reactor design along with developing a stable and selective catalyst are the two main challenging tasks for the OCM process. So far, the reported achieved ethylene yield under industrially relevant conditions has been limited to 20% and is still far from being industrially implemented not only due to its economic incompetence but also because of its operational challenges, especially in its reactor section. The last concern can be addressed via utilizing an OCM fluidized-bed reactor which offers a relatively smooth thermal performance. However, a detailed analysis of the fluid dynamic of the gas–solid reaction system is required to ensure an optimal design and efficient performance of the OCM fluidized-bed reactor. Here in this paper, such analysis is provided using the computational fluid dynamics (CFD) model.

In general, CFD models are economical and effective tools to investigate and optimize the thermal and reaction performances of the fluidized bed units. For instance, utilizing the CFD tools can provide fruitful information related to the formation of hot spots in an exothermic reaction environment such as OCM. Moreover, along with the experimental results extracted from various laboratory and pilot-scale plants, conducting the CFD studies provides valuable information for design and possible

scale-up tasks. This tool has been successfully applied for similar applications, and reviewing them here enables one to extract useful information, for instance, the reports carried out on natural gas combustion and methane activation systems, which are also exothermic reactions with similar characteristics as in the OCM system.

Krugger-Emden et al.¹ studied the transient behavior of the chemical-looping combustion (CLC) of methane in the riser and bubbling fluidized bed reactors using the two-fluid model (TFM). It can be concluded from their work that the simulated flow time should be long enough so that the predicted results can be compared with the experimental data. Deng et al.² utilized TFM-CFD simulation to investigate the performance of a chemical-looping combustion reactor where the effect of the gas flow rate and the bed temperature on the reactor performance have been highlighted.

Bougamra and Huilin³ performed a CFD simulation of the complete CLC process including the fuel reactor, air reactor, and loop seal. Their simulation results were in good agreement with the experimental data presented by Adánez et al.⁴ and show the importance of the distribution of oxygen and prolonging the residence time of carrier particles to improve the degree of reoxidation.

Quiceno et al.⁵ studied the catalytic partial oxidation of methane (CPOM) over a platinum gauze reactor numerically. Through their CFD simulation, gas-phase and surface reaction mechanisms were investigated, and the predicted results of their

Received: July 5, 2015

Revised: December 25, 2015

Accepted: January 12, 2016

Published: January 29, 2016

simulation were in good agreement with the experimental data reported by Reyniers et al.⁶ and De Smet et al.⁷ Through investigating various components' concentrations along the bed using CFD simulation, they predicted the contribution of various reactions in the CPOM reactor. They found that, for typical CPOM conditions, heterogeneous steps govern the overall reactor performance. The results of their simulation demonstrated that an increase in pressure and residence time signifies the effect of gas-phase reactions and ethane production. These are all the types of findings which can be looked into in other similar CFD simulation systems such as the OCM reactor as it will be discussed in the current paper. More valuable information can be found by reviewing other similar CFD simulations. For instance, Lindborg and Jakobsen⁸ studied the process of steam methane reforming in a bubbling fluidized bed using CFD simulation based on the TFM approach and kinetic theory of granular flow (KTGF). The predicted outlet concentrations of the components were in good agreement with the experimental results. However, implementing the 2D cylindrical frame does not allow the particles to cross the centerline, and consequently the predicted solid flow pattern shows some deviation from the experimental observations. In the performed CFD study of the OCM fluidized-bed reactor, however, investigating the effect of internal circulation of catalytic particles and spatial temperature variation on the reactor performance should be considered.

Loha et al.⁹ carried out three-dimensional numerical simulation of a bubbling fluidized bed biomass gasifier using the Lagrangian–Eulerian approach. They utilized the solid flow pattern and distribution of pressure as well as gas composition predicted by the CFD simulation to examine the contribution of homogeneous and heterogeneous reactions. The results of their simulation showed some deviation from the observed experimental values. Loha et al.⁹ attributed these discrepancies to the kinetic parameters used for heterogeneous reactions.

Open source simulations have also been used for such applications. For instance, Liu and Hinrichsen¹⁰ used OpenFOAM code for CFD simulation of the methanation reactor and successfully predicted the concentration of various components along the bed.

Various methodologies can be used for simulation of transport phenomena in a fluidized bed. One of the earliest approaches is phenomenological models, e.g., the two-phase model developed by various groups such as Kunii and Levenspiel¹¹ and Kato and Wen¹² uses some simplified assumptions, such as the steady state with a plug or a well-mixed flow in the emulsion phase. As a result, these simulations are limited to one dimension, and bed properties cannot be investigated in lateral directions. Additionally, the emulsion phase is assumed to flow at minimum fluidization velocity.¹³ Moreover, bed hydrodynamics in most of these models are mainly governed by the bubble size obtained through empirical correlations. However, these correlations have been developed for a single rising bubble, so its application is questionable for the fluidized bed in which bubbles are affected by the pressure field of other bubbles. In addition, these phenomenological models need to use correlations for predicting the mass transfer coefficient between the bubble and emulsion phases.

Through simulation of the rising single bubble, Patil et al.¹⁴ showed that the basic assumptions in the phenomenological models for derivation of the correlations used for predicting the mass transfer coefficients are not reliable. Therefore, application of a robust numerical method without these simplified

assumptions is required. This need can be met through application of computational fluid dynamics.

In spite of the phenomenological models and lumped formulation, in the finite volume CFD method, energy and mass balance equations are discretized considering all convection, diffusion, and source terms. Therefore, application of the simplified heat and mass transfer coefficient is not needed. Moreover, CFD simulation provides detailed information in every grid including temperature, concentration, and reaction rates profiles in axial and radial directions, which allows examination of the applied kinetic model and hot-spot formation in the studied system.

Considering the above studies, it can be concluded that a CFD simulation can be successfully utilized for investigating similar aspects of the catalytic–gas-phase conversion of methane also in the present study. Moreover, the limitations and the potentials highlighted in reviewing the above-mentioned similar CFD studies were also taken into consideration in the performed analysis in the present study. Therefore, the CFD simulation tool was efficiently employed to analyze the oxidative coupling of methane in a fluidized-bed reactor. In order to study the reactor performance, reaction pathways, and the contribution of various reactions, a Eulerian–Eulerian approach based on the kinetic theory of granular flow was used. The comprehensive description of kinetic theory of granular flow can be found in the book written by Gidaspow.¹⁵

2. MATHEMATICAL MODELING AND SIMULATION METHOD

The Eulerian–Eulerian approach was applied for simulating the multiphase flow case in the present study. In this approach, different phases are treated mathematically as interpenetrating continua.¹⁶ The corresponding model is usually known as the multifluid model (MFM) in the case of considering several particulate phases. Conservation equations were derived for each phase and linked by interphase momentum transfer coefficient and pressure. For calculation of solid phase properties, the kinetic theory of granular flow was used.

2.1. Governing and Constitutive Equations. CFD simulation of a fluidized-bed reactor in the 2D Cartesian coordinate system was performed to represent the 3D experimental setup. According to Xie et al.,¹⁷ the 2D Cartesian model can be used for describing the 3D cylindrical fluidized bed operation under bubbling conditions. In detail, in the flow restricted up to the bubbling regime, axial terms resulting from the drag forces are predominant, so lateral terms can be neglected. In other words, the bubbles' pressure field is not so high that it signifies the bubble motion and coalescence in the lateral direction. As a result, 2D Cartesian simulation could be reasonably validated by the experimental results obtained from a 3D cylindrical bed. On the other hand, at higher velocities where the bed flow shifts to the slugging and turbulent regime, these terms cannot be neglected, and therefore the 3D simulation seems necessary. Hydrodynamic models of gas–solid fluidized beds are based on the conservation of momentum and total mass. Continuity, energy, and momentum equations for reactive, nonisothermal, and transient flow for each phase were applied. The fractional-step method (FSM) was also used to decouple the reaction source terms. In detail, in this method, the convection/diffusion equations are first solved without chemical reaction source terms. Then, a coupled

Table 1. Governing Equations and Constitutive Relations

momentum conservation equations

$$\frac{\partial(\varepsilon_g \rho_g U_{gi})}{\partial t} + \frac{\partial}{\partial x_j}(\varepsilon_g \rho_g U_{gj} U_{gi}) = -\varepsilon_g \frac{\partial P_g}{\partial x_i} + \frac{\partial \tau_{gij}}{\partial x_j} - I_{gsi} + \varepsilon_g \rho_g g_i \quad (1)$$

$$\frac{\partial(\varepsilon_s \rho_s U_{si})}{\partial t} + \frac{\partial}{\partial x_j}(\varepsilon_s \rho_s U_{sj} U_{si}) = -\varepsilon_s \frac{\partial P_g}{\partial x_i} + \frac{\partial \tau_{sij}}{\partial x_j} + I_{gsi} + I_{lmi} + \varepsilon_s \rho_s g_i \quad (2)$$

interphase momentum transfer

$$I_{gsi} = \beta_{gs} (u_{gi} - u_{si}) \quad (3)$$

$$\beta_{gs} = \begin{cases} 150 C_d \frac{(1 - \varepsilon_g)^2}{\varepsilon_g (d_p)^2} \mu_g + 1.75 (1 - \varepsilon_g) \frac{\rho_g}{d_p} |u_g - u_s| & \text{for } \varepsilon_g \leq 0.8 \\ \frac{3}{4} C_d \frac{\varepsilon_g (1 - \varepsilon_g)}{d_p} \rho_g |u_g - u_s| \varepsilon_g^{-2.65} & \text{for } \varepsilon_g > 0.8 \end{cases} \quad (4)$$

$$C_d = \begin{cases} \frac{24}{\varepsilon_g Re_p} [1 + 0.15 (\varepsilon_g Re_p)^{0.687}] & \text{for } Re_p \leq 1000 \\ 0.44 & \text{for } Re_p > 1000 \end{cases} \quad (5)$$

$$Re_p = \frac{\rho_g |u_g - u_s| d_p}{\mu_g} \quad (6)$$

solid-phase stress tensor

$$\tau_{sij} = \left(-P_s + \eta \mu_b \frac{\partial U_{si}}{\partial x_i} \right) \delta_{ij} + 2 \mu_s S_{sij} \quad (7)$$

solid-phase shear rate

$$S_{sij} = \frac{1}{2} \left(\frac{\partial U_{si}}{\partial x_j} + \frac{\partial U_{sj}}{\partial x_i} \right) - \frac{1}{3} \frac{\partial U_{si}}{\partial x_i} \quad (8)$$

solid viscosity

$$\mu_s = \left(\frac{2 + \alpha}{3} \right) \left[\frac{\mu_s^*}{g_0 \eta (2 - \eta)} \left(1 + \frac{8}{5} g_0 \eta \varepsilon_s \right) \left(1 + \frac{8}{5} \eta (3\eta - 2) g_0 \varepsilon_s \right) + \frac{3}{5} \eta \mu_b \right] \quad (9)$$

$$\mu_s^* = \frac{\varepsilon_s \rho_s \Theta g_0 \mu}{\varepsilon_s \rho_s \Theta g_0 + \frac{2\beta\mu}{\varepsilon_s \rho_s}} \quad (10)$$

$$\mu = \frac{5}{96} \rho_s d_p \sqrt{\pi \Theta} \quad (11)$$

$$\mu_b = \frac{256}{5\pi} \mu \varepsilon_s g_0 \quad (12)$$

solid pressure

$$P_s = \varepsilon_s \rho_s \Theta [1 + 4\eta \varepsilon_s g_0] \quad (13)$$

$$\eta = \frac{1 + \varepsilon}{2} \quad (14)$$

transport equation for granular energy

$$\frac{3}{2} \left(\frac{\partial(\varepsilon_s \rho_s \Theta)}{\partial t} + \frac{\partial(\varepsilon_s \rho_s u_s \Theta)}{\partial x_j} \right) = \frac{\partial}{\partial x_i} \left(\kappa_s \frac{\partial \Theta}{\partial x_i} \right) + \tau_{sij} \frac{\partial U_{si}}{\partial x_j} + \Pi_s - \varepsilon_s \rho_s I_s \quad (15)$$

$$\kappa_s = \left(\frac{K_s^*}{g_0} \right) \left[\left(1 + \frac{12}{5} \eta \varepsilon_s g_0 \right) \left(1 + \frac{12}{5} \eta^2 (4\eta - 3) \varepsilon_s g_0 \right) + \frac{64}{25\pi} (41 - 33\eta) \eta^2 (\varepsilon_s g_0)^2 \right] \quad (16)$$

$$\kappa_s^* = \frac{\varepsilon_s \rho_s g_0 \Theta \kappa}{\varepsilon_s \rho_s g_0 \Theta + \frac{6\beta\kappa}{5\varepsilon_s \rho_s}} \quad (17)$$

$$\kappa = \frac{75 \rho_s d_p \sqrt{\pi \Theta}}{48 \eta (41 - 33\eta)} \quad (18)$$

Table 1. continued

transport equation for granular energy

$$\Pi_s = -3\beta\Theta + \frac{81\varepsilon_g \mu_g^2 |u_g - u_s|^2}{g_0 \rho_s^2 d_p^3 \sqrt{\pi\Theta}} \quad (19)$$

$$J_s = \frac{48}{\sqrt{\pi}} \eta(1-\eta) \frac{\varepsilon_s g_0}{d_p} \Theta^{3/2} \quad (20)$$

frictional force

$$\bar{\tau}_{s,f} = P_{s,f} \bar{I} + \mu_{s,f} [\nabla u_s + (\nabla u_s)^T] \quad (21)$$

$$\mu_s = \mu_{s,KTFG} + \mu_{s,f} \quad (22)$$

$$P_s = P_{s,KTFG} + P_{s,f} \quad (23)$$

$$\mu_{s,f} = \begin{cases} \min\left(\frac{P_s \sin(\varphi)}{2\sqrt{\bar{I}_{2D}}}, \mu_m^{\max}\right), & \text{for } \varepsilon_g < \varepsilon_g^* \\ 0, & \text{for } \varepsilon_g \geq \varepsilon_g^* \end{cases}$$

$$\mu_m^{\max} = 1000 \text{ Poise and } \varepsilon_g^* = 0.5 \text{ in the present study} \quad (24)$$

$$\bar{I}_{2D} = \frac{1}{6} \left[\left(\frac{\partial u_{s,x}}{\partial x} - \frac{\partial u_{s,y}}{\partial y} \right)^2 + \left(\frac{\partial u_{s,y}}{\partial y} - \frac{\partial u_{s,z}}{\partial z} \right)^2 + \left(\frac{\partial u_{s,z}}{\partial z} - \frac{\partial u_{s,x}}{\partial x} \right)^2 \right] \\ + \frac{1}{4} \left[\left(\frac{\partial u_{s,x}}{\partial y} + \frac{\partial u_{s,y}}{\partial x} \right)^2 + \left(\frac{\partial u_{s,y}}{\partial z} + \frac{\partial u_{s,z}}{\partial y} \right)^2 + \left(\frac{\partial u_{s,z}}{\partial x} + \frac{\partial u_{s,x}}{\partial z} \right)^2 \right] \quad (25)$$

$$P_{s,f} = Fr \frac{(\varepsilon_s - \varepsilon_{s,\min})^n}{(\varepsilon_{s,\max} - \varepsilon_s)^p} \\ Fr = 0.05, n = 2, \text{ and } p = 5 \quad (26)$$

thermal energy equations and constitutive equations

$$\varepsilon_g \rho_g C_{p,g} \left(\frac{\partial T_g}{\partial t} + \mathbf{u}_g \cdot \nabla T_g \right) \\ = -\nabla \cdot \mathbf{q}_g + \sum_{m=1}^M \gamma_{gm} (T_{sm} - T_g) - \Delta H_{rg} + \gamma_{Rm} (T_{Rm}^4 - T_{sm}^4) \quad (27)$$

$$\varepsilon_{sm} \rho_{sm} C_{p,sm} \left(\frac{\partial T_{sm}}{\partial t} + \mathbf{u}_{sm} \cdot \nabla T_{sm} \right) = -\nabla \cdot \mathbf{q}_{sm} + \gamma_{gm} (T_{sm} - T_g) + \gamma_{Rm} (T_{Rm}^4 - T_{sm}^4) \quad (28)$$

$$\mathbf{q}_g = -\varepsilon_g k_g \nabla T_g \quad (29)$$

$$\mathbf{q}_{sm} = -\varepsilon_{sm} k_{sm} \nabla T_{sm} \quad (30)$$

thermal conductivity of the solid phase

$$\frac{k_{sm}}{k_g} = \frac{\phi_k R_{km} + (1 - \phi_k) \lambda_{rm}}{\sqrt{1 - \varepsilon_g}} \quad (31)$$

$$\lambda_{rm} = -\frac{2}{(1 - b/R_{km})} \left[\frac{(1 - R_{km})b/R_{km}}{(1 - b/R_{km})^2} \ln(b/R_{km}) + \frac{b-1}{(1 - b/R_{km})} + \frac{b+1}{2} \right] \quad (32)$$

$$b = 1.25 \left(\frac{1 - \varepsilon_g}{\varepsilon_g} \right)^{10/9} \quad (33)$$

heat transfer coefficient

$$\gamma_{gm} = \frac{C_{p,g} R_{0m}}{\exp\left(\frac{C_{p,g} R_{0m}}{\gamma_{gm}^0}\right) - 1} \quad (34)$$

$$\gamma_{gm}^0 = \frac{6k_g \varepsilon_g N u_m}{d_{pm}^2} \quad (35)$$

$$N u_m = (7 - 10\varepsilon_g + 5\varepsilon_g^2) \cdot (1 + 0.7Re_p^{0.2} Pr^{1/3}) + (1.33 - 2.4\varepsilon_g + 1.2\varepsilon_g^2) R \\ \varepsilon_p^{0.7} Pr^{1/3} \quad (36)$$

Table 1. continued

transport equations for the species

$$\frac{\partial}{\partial t}(\epsilon_g \rho_g X_{gn}) + \nabla \cdot (\epsilon_g \rho_g X_{gn} \mathbf{u}_g) = \nabla \cdot D_{gn} \nabla X_{gn} + R_{gn} \quad (37)$$

set of ordinary differential equations is directly integrated to impose the chemical reactions effects.

A summary of governing equations and closure relations is given in Table 1. In detail, momentum conservation equations were derived for each phase, and the momentum equations have been linked by the interphase momentum transfer. The momentum exchange coefficient was calculated through Gidaspow's drag model.¹⁸

Since the reactions taking place in the OCM reactor are highly exothermic, and distribution of the reaction temperature plays an important role in the reaction rates, it is necessary to precisely address this nonisothermal system and solve the energy conservation equations for the gas and solid phases. Since the temperature difference between the reactor wall and the gas inlet is significant, a radiative heat transfer mechanism has been considered in the modeling.

The species transport inside the solid catalyst phase is not considered, so the equations of mass conservation were solved only for the gas components.

2.2. Simulation Conditions and Solution Method. In this section, the computational domain information, initial and boundary conditions used for simulations, and the numerical methods implemented to solve the set of governing equations are presented in detail.

2.2.1. Simulation Conditions. The numerical simulations in the current study have been performed in accordance with the experimental data reported by Mleczko et al.¹⁹ and Jašo.²⁰ Detailed simulation conditions are represented in Table 2.

Table 2. Physical Properties and Simulation Parameters Reported by Mleczko et al.¹⁹ (These Data Are Reported with Permission of Wiley) and Jašo²⁰

parameters	Mleczko et al. ¹⁹	Jašo ²⁰
bed geometry		
D_{Bed} (m)	0.07	0.04
H_T (m)	1.00	1.00
H_0 (m)	0.021	0.132
solid phase properties		
d_p (μm)	302.5	350
u_{mf} (m/s)	0.041	0.0145
φ (deg)	30.0	30.0
e	0.95	0.95
φ_s	0.5	0.5
e_w	1.0	1.0
gas phase properties		
ρ_g (kg/m^3)	1.225	1.225
μ_g	5.0×10^{-5}	1.79×10^{-5}

The mechanism of heterogeneous OCM reactions was presented through the kinetic model developed for the same catalyst, i.e., $\text{La}_2\text{O}_3/\text{CaO}$ catalyst, by Stansch et al.²¹ In order to consider the gas-phase reactions taking place in the OCM reactor, the kinetic models presented by Lane and Wolf²² as well as the one reported by Zanthoff and Baerns²³ were tested in this study showing no significant difference in predicting the OCM reactor performance. More detailed guidelines for testing

different mechanisms for OCM gas-phase and surface reactions will soon be reported separately. Therefore, only the simulation results using the Lane and Wolf²² model were presented in this paper. Detailed information about the kinetic models developed by Stansch et al.²¹ and Lane and Wolf²² is presented in Table 3. The kinetic parameters can be found in the original references.

Table 3. Heterogeneous Reactions: Kinetic Model Reported by Stansch et al.²¹

total oxidation of methane	$\text{CH}_4 + 2\text{O}_2 \rightarrow \text{CO}_2 + 2\text{H}_2\text{O}$
oxidative coupling of methane to ethane	$2\text{CH}_4 + 0.5\text{O}_2 \rightarrow \text{C}_2\text{H}_6 + \text{H}_2\text{O}$
partial oxidation of methane	$\text{CH}_4 + \text{O}_2 \rightarrow \text{CO} + \text{H}_2\text{O} + \text{H}_2$
oxidation of carbon monoxide	$\text{CO} + 0.5\text{O}_2 \rightarrow \text{CO}_2$
oxidative dehydrogenation of ethane	$\text{C}_2\text{H}_6 + 0.5\text{O}_2 \rightarrow \text{C}_2\text{H}_4 + \text{H}_2\text{O}$
oxidation of ethylene	$\text{C}_2\text{H}_4 + 2\text{O}_2 \rightarrow 2\text{CO} + 2\text{H}_2\text{O}$
thermal dehydrogenation of ethane	$\text{C}_2\text{H}_6 \rightarrow \text{C}_2\text{H}_4 + \text{H}_2$
steam reforming of ethylene	$\text{C}_2\text{H}_4 + 2\text{H}_2\text{O} \rightarrow 2\text{CO} + 4\text{H}_2$
conversion of carbon monoxide to carbon dioxide and vice versa by water-gas shift reactions	$\text{CO} + \text{H}_2\text{O} \rightarrow \text{CO}_2 + \text{H}_2$ $\text{CO}_2 + \text{H}_2 \rightarrow \text{CO} + \text{H}_2\text{O}$
homogeneous reactions: Lane and Wolf ²²	
$\text{CH}_4 + 2\text{O}_2 \rightarrow \text{CO}_2 + 2\text{H}_2\text{O}$	$2\text{CH}_4 + 0.5\text{O}_2 \rightarrow \text{C}_2\text{H}_6 + \text{H}_2\text{O}$
$\text{CH}_4 + 1.5\text{O}_2 \rightarrow \text{CO} + 2\text{H}_2\text{O}$	$2\text{CH}_4 + \text{O}_2 \rightarrow \text{C}_2\text{H}_4 + 2\text{H}_2\text{O}$

2.2.2. Numerical Simulation Method. The set of governing equations was solved using the finite volume method in a two-dimensional Cartesian frame. The modified SIMPLE algorithm for multiphase flow²⁴ was applied to consider the pressure–velocity coupling. For temporal discretization, the implicit backward Euler method was applied, and Superbee method was exploited for spatial discretization of convective terms. The maximum residual at convergence for continuity, momentum, concentration, and energy was set to 10^{-4} . The initial and maximum time steps were set to 10^{-4} and 10^{-3} s, respectively. The grid sizes used to resolve computational domain are 1 mm in radius and axial directions.

2.2.3. Initial and Boundary Conditions. The initial conditions for solid and gas phase velocity were set to zero. It was assumed that initially the reactor was filled with nitrogen.

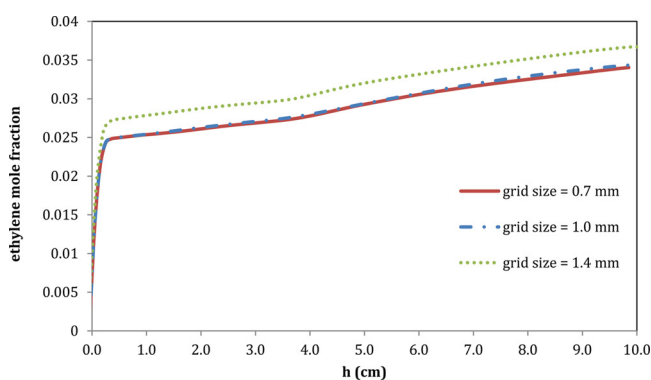
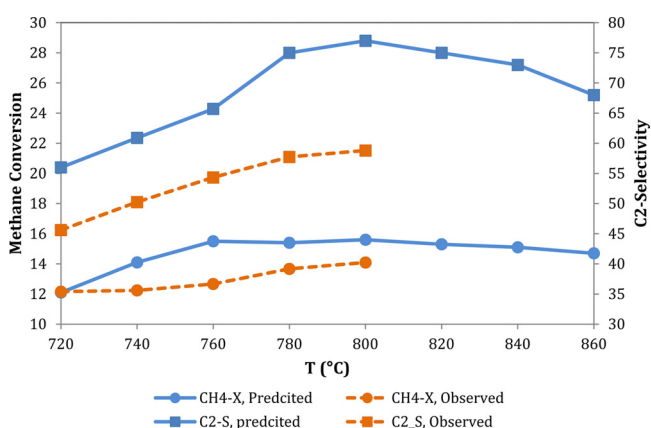
Turning to boundary conditions, uniform velocity-inlet boundary conditions were applied. At the top, the pressure-outlet boundary conditions were used. At the walls, no-slip boundary conditions were applied for the gas phase, while free-slip boundary conditions were used for the solid catalyst phase. It should be mentioned that the furnace temperature, i.e., wall temperature in this study, was considered as the operating temperature. A summary of initial and boundary conditions is reported in Table 4.

3. RESULTS AND DISCUSSIONS

3.1. Grid Sensitivity. In order to investigate the independence of the solution from the mesh size, several simulations were performed with a grid size of 0.7, 1, and 1.4 mm. As shown in Figure 1, upon refining the computational

Table 4. Initial and Boundary Conditions for the Present Simulation

parameter	Mleczo et al. ¹⁹	Jašo ²⁰
initial condition		
gas velocity (m/s)	0	0
solid velocity (m/s)	0	0
gas volume fraction	0.4	0.35
mole fraction of N ₂	1.0	1.0
mole fraction of CH ₄	0.0	0.0
mole fraction of O ₂	0.0	0.0
gas temperature (K)	993.15–1113.15	998.15–1123.15
inlet boundary condition		
velocity inlet (cm[STP]/s)	16.4–102.5	6.1
gas volume fraction	1.0	1.0
mole fraction of N ₂	0.34	0.7–0.76
mole fraction of CH ₄	0.6	0.2
mole fraction of O ₂	0.06	0.04–0.1
gas temperature (K)	673.15	673.15
outlet boundary condition		
outlet pressure	wall	atmospheric
wall boundary condition		
gas phase	no slip	no slip
temperature	993.15–1113.15	998.15–1123.15

**Figure 1.** Predicted values of ethylene mole fraction along the bed for various grid sizes.**Figure 2.** Effect of temperature on methane conversion and C₂ selectivity and comparing the predicted results with the values reported by Mleczo et al.¹⁹ (these data reported with the permission from ref 19, copyright 1996 Wiley).

domain to values smaller than 1 mm, the accuracy of the solution will not be improved, while deviation can be observed

for a coarse grid size of 1.4 mm. As a result, a value of 1 mm was adopted to achieve high accuracy and low computational cost.

3.2. Effect of Operating Conditions. Aimed at achieving the desired values of the C₂ yield (ethylene and ethane) via securing a certain level of methane conversion for highly selective conversion, in this section the effects of operating and applied temperature and pressure on the reactor performance are investigated. It should be noted that in all cases C₂ selectivity and methane conversion have been calculated at the bed outlet.

3.2.1. Operating Temperature. The effect of operating temperature on the predicted values of methane conversion and C₂ selectivity is depicted in Figure 2. Showing a maximum deviation of 22% for methane conversion and 30% for the C₂ selectivity, the predicted values are in good agreement with the experimental data reported by Mleczo et al.¹⁹ The predicted trends for methane conversion and C₂ selectivity are similar to the observed ones. In detail, the predicted values for methane conversion are in good agreement with the experimental data reported by Mleczo et al.,¹⁹ while larger deviation was predicted for C₂ selectivity.

These results can be explained via comparing the predicted and the observed components' concentration profiles along the bed. As can be discerned from Figure 2, a sharper decrease in oxygen concentration, which is in favor of selective reaction, results in overprediction of C₂ selectivity. Apart from this, underprediction of CO concentration and a sharper increase in ethylene concentration reveals the underestimation of the consumption rate of C₂H₄ in the ethylene oxidation reaction, due to a lower predicted oxygen concentration, as well as steam reforming reaction in Stansch's kinetic model. Therefore, according to the simulation results, the C₂H₄ concentration is higher inside the area of the dense bed. Consequently, a higher value for C₂ selectivity will be predicted.

As shown in this figure, methane conversion and C₂ selectivity hit a maximum value at about $T = 800$ °C. The same trend is also reported by Jašo²⁰ and Pannek and Mleczo²⁵ for a wide range of Gas Hourly Space Velocity (GHSV), methane-to-oxygen ratio, and particle size in their experimental study. This trend can be explained by analyzing the observed changes in the components' mole fraction along the bed under different applied temperatures. As shown in Figure 3a, even though the amount of ethane produced at the bed inlet section under $T = 860$ °C is approximately similar to its value at $T = 800$ °C, the consumption rate for this component increases dramatically along the bed in comparison to lower temperatures. On one side, according to the Stansch's kinetic model and parameters,²¹ it is expected that the ethane dehydrogenation reaction is intensified under higher operating temperatures. On the other side, as seen in Figure 3b, lower concentration was predicted for ethylene at $T = 860$ °C along the catalytic bed. Therefore, the produced ethylene should have been consumed in the nonselective reactions. Considering the reactions in Stansch's kinetic model,²¹ it can be concluded that by increasing the temperature to a value higher than $T = 800$ °C, the reaction rate for ethylene steam reforming should have been also accelerated. These conclusions are supported by the observed remarkable increase in hydrogen concentration along the dense bed at temperatures higher than 800 °C, as depicted in Figure 3c, which is due to the highest stoichiometric coefficient for hydrogen in ethylene steam reforming reaction. Moreover, at $T = 860$ °C, the difference between the predicted trend for the mole fraction of carbon monoxide along the bed

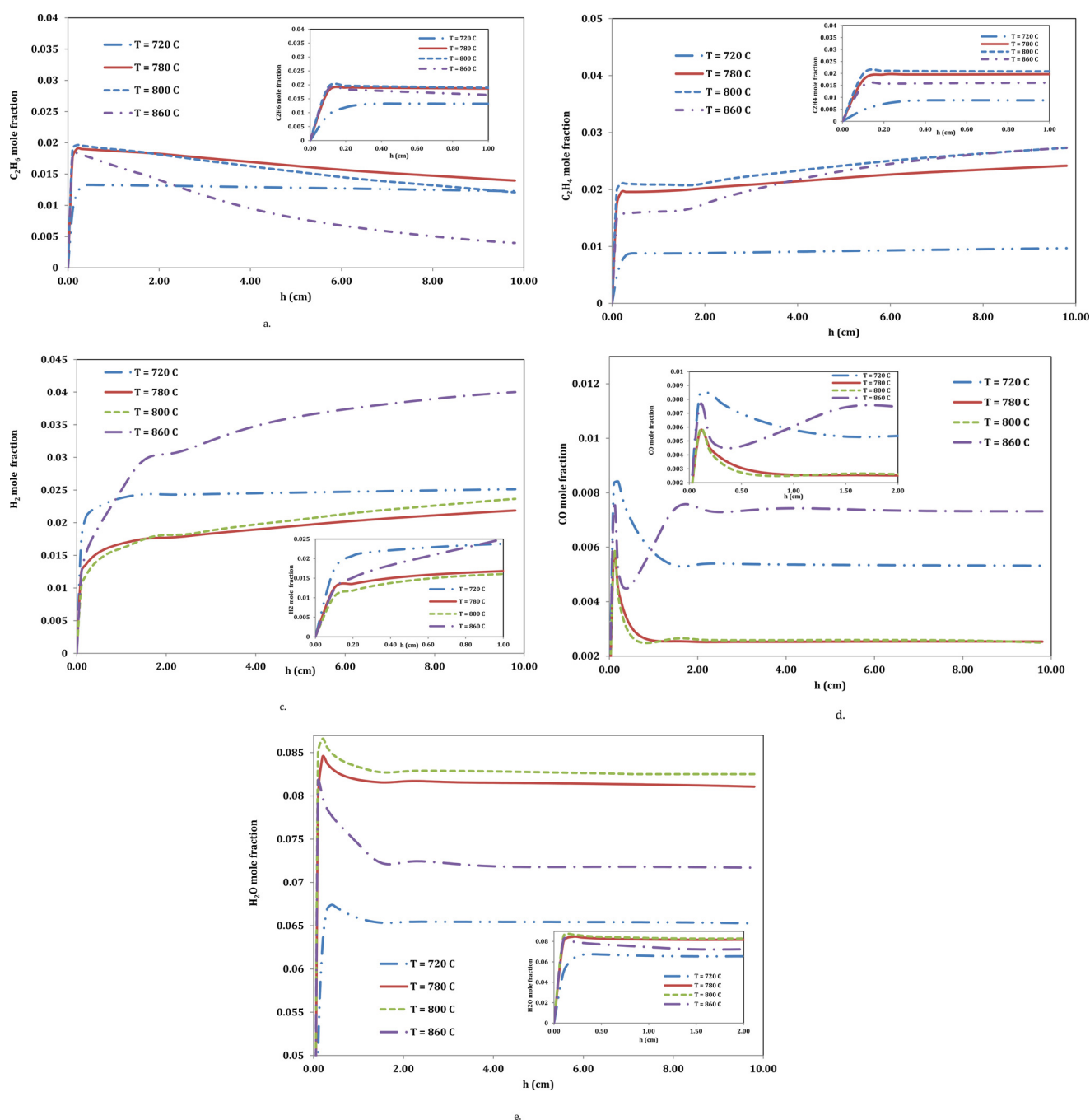


Figure 3. Variation of concentrations of (a) C_2H_6 , (b) C_2H_4 , (c) H_2 , (d) CO, and (e) H_2O along the bed with temperature.

and its predicted trend under other temperatures proves the acceleration of steam reforming of ethylene. As shown in Figures 3d,e, at $T = 860\text{ }^\circ\text{C}$, CO concentration soars after a significant decrease at the bed inlet, while H_2O concentration drops dramatically. This demonstrates the high rate of the ethylene steam reforming reaction. Apart from this, this can be directly concluded as the ethylene steam reforming has the highest activation energy in the selected kinetic model, which reflects the highest sensitivity to temperature.

3.2.2. Pressure. The effect of pressure on the reactor performance is very important. In possible industrial applications of the OCM process, at least a few bars of operating pressure is needed to ensure the continual flow of the gas streams. Higher pressures might be required for possible

integration with other reactors and processes. The effect of operating pressure was examined at a CH_4/O_2 ratio of 10 and a GHSV of 1815 1/h. Results of the simulation predicted that an increase in pressure results in decreasing the C_2 selectivity and, in certain ranges, also the methane conversion, as shown in Figure 4.

Moreover, as discerned from Figure 5a–d, at a pressure of 1 bar, the ethylene concentration is significantly higher than its value at 3 bar, while carbon monoxide has a lower concentration under 1 bar of pressure. The height at which oxygen concentration reaches a zero value is in accordance with the height at which the slope of change in the ethylene and carbon monoxide concentrations significantly reduces. These changes in concentrations can be attributed to the acceleration

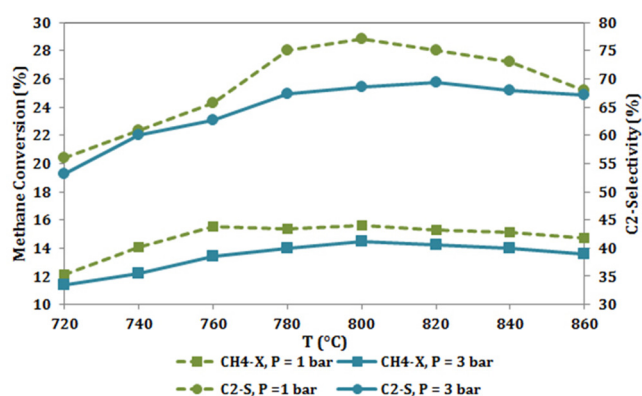


Figure 4. Effect of pressure on methane conversion (CH₄-X) and C₂ selectivity (C₂-S).

of oxidation of the ethylene reaction. This change in CO concentration cannot stem from partial oxidation of methane and ethylene steam reforming since the rate of these two reactions does not change considerably due to the slight change in the hydrogen concentration.

The effect of pressure on the reactor performance was also numerically investigated at various CH₄/O₂ ratios as shown in Figure 6.

It can be easily discerned that upon applying a CH₄/O₂ ratio of less than 8, increasing the operating pressure from 1 to 3 bar reduces the selectivity while increasing the methane conversion. However, a greater increase in the pressure comes along with less significant change in the reactor performance in terms of methane conversion and C₂ selectivity. Despite the fact that

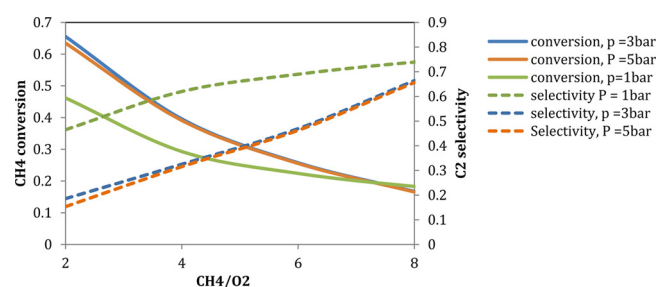


Figure 6. Effect of pressure on methane conversion and C₂ selectivity at various CH₄/O₂ ratios.

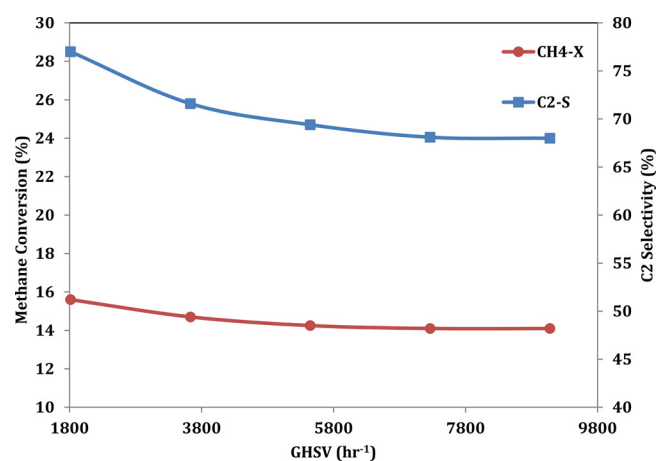


Figure 7. Dependency of methane conversion and C₂ selectivity on gas hourly space velocity.

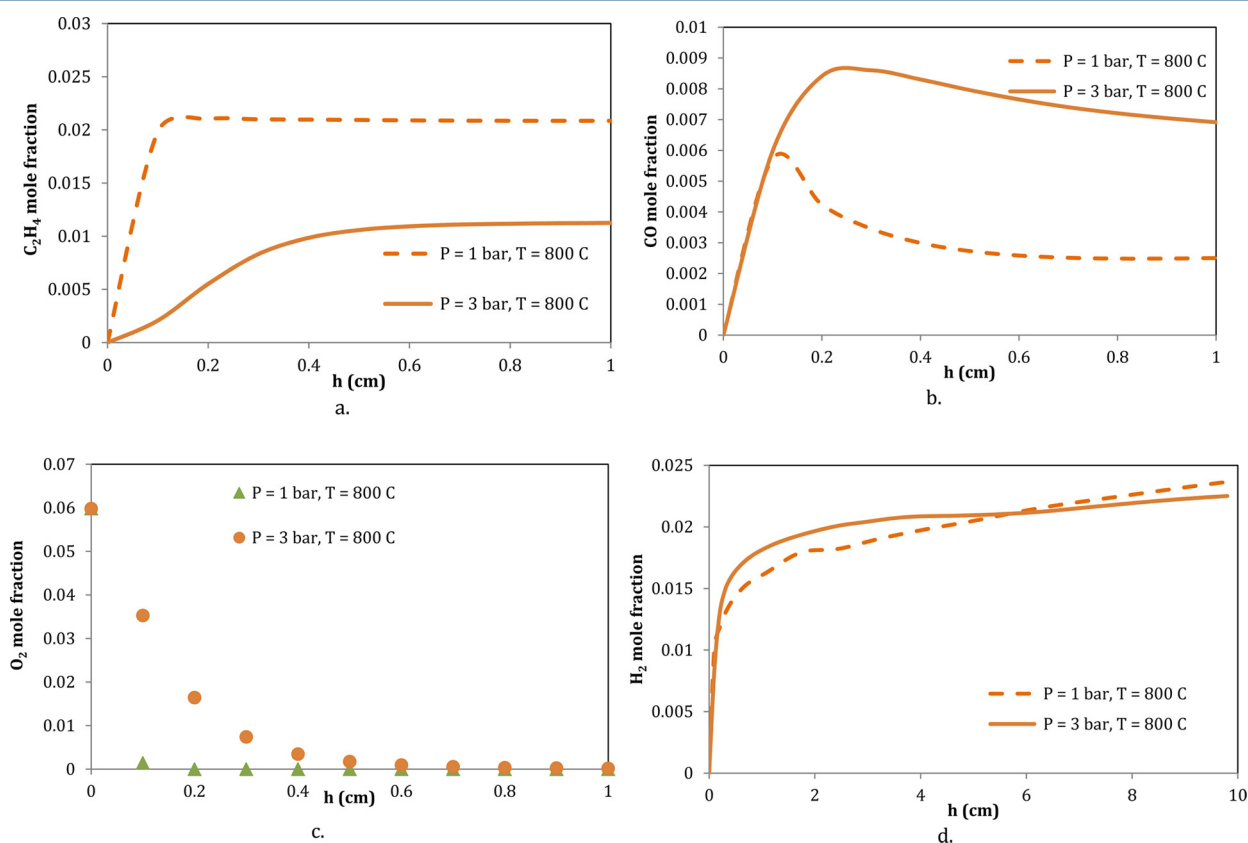


Figure 5. Variation of (a) C₂H₄, (b) CO, (c) O₂, and (d) H₂ along the bed with pressure.

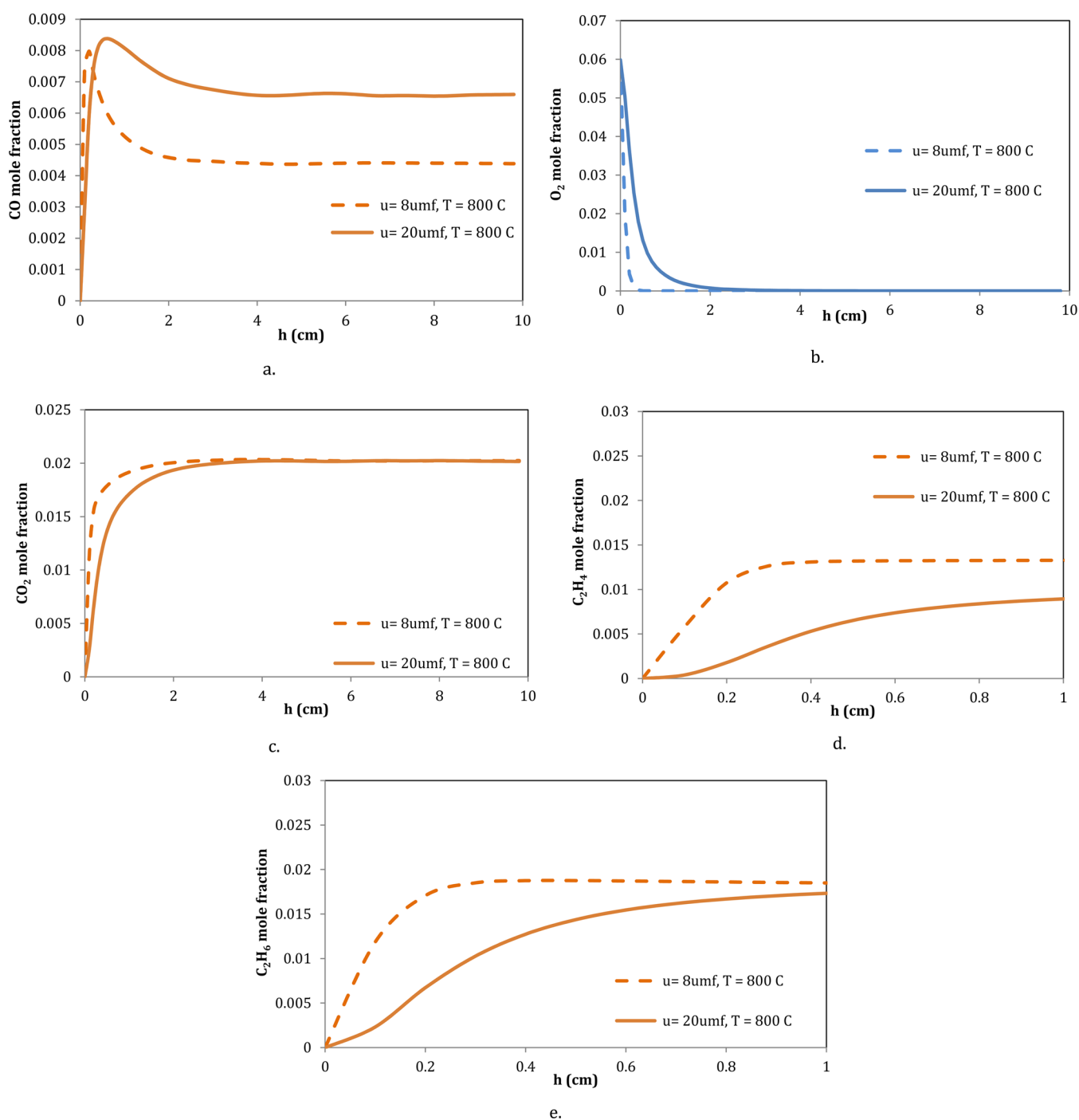


Figure 8. Variation of (a) CO, (b) O_2 , (c) CO_2 , (d) C_2H_4 , and (e) C_2H_6 along the bed with a change in GHSV.

operating at higher pressure significantly emboldens the gas phase reactions, generally the effect of the gas-phase reactions is marginal in comparison to the catalytic reactions for the entire studied range of operating pressure.

It should be mentioned that not predicting the expected trend in which methane conversion increases in higher pressures is because of the implemented kinetic model, which is too fast. The oxygen conversion will be completed very fast, even at a lower operating pressure, and as a result, changing the contact time in such simulations plays a marginal role in methane conversion. This fact can be also seen in the dependency of the reactor performance on the feed dilution. Since p_{O_2} and p_{CH_4} under a total pressure of 5 bar does not fall

into the range at which Stansch's kinetic model is valid, there is some uncertainty for the predicted results at a total pressure of 5 bar.

3.3. Effect of Feed Characteristics. In this section, the effects of variation of volumetric feed flow rate and the inlet partial pressure of the reactants on the C_2 selectivity and methane conversion are examined.

3.3.1. Gas Hourly Space Velocity. The variations of predicted C_2 selectivity and methane conversion with GHSV at $T = 800\text{ °C}$ and $P = 1$ bar are demonstrated in Figure 7.

As discerned from this figure, the decrease in GHSV gives a rise in C_2 selectivity and methane conversion. This finding can be explained through analyzing the components' mole fraction

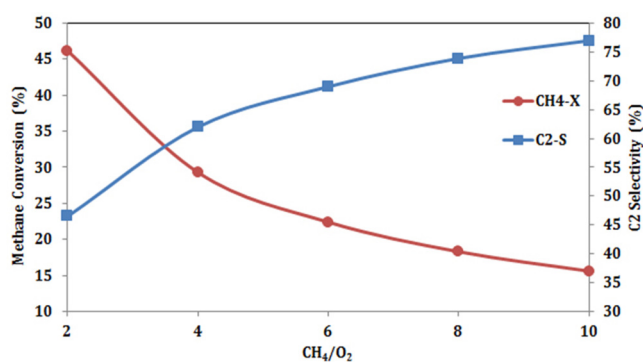


Figure 9. Effect of methane to oxygen ratio on methane conversion and C₂ selectivity.

along the bed. As shown in Figure 8, CO is produced in partial oxidation of methane, ethylene oxidation, and ethylene steam reforming. This component is consumed in the water–gas shift reaction and in the oxidation of carbon monoxide. It can be concluded that at higher velocity and near the bed inlet, CO is mainly produced through partial oxidation of methane, and the contribution of ethylene oxidation and steam reforming reactions is marginal because the amount of ethane and ethylene below a height of 3 mm is low. At higher distances, due to the increase in ethane and ethylene concentration, CO can be produced via ethylene steam reforming and ethylene oxidation as well. However, at lower velocity, all of these reactions contribute comparably.

Considering the trends in Figure 7, the observed change in methane conversion with velocity is marginal, whereas the observed change in C₂ selectivity is more significant. This shows that the nonselective reactions occur to a greater extent

in higher velocity. This finding can be also observed in the concentration profile of ethane and ethylene. At higher velocities, ethane is converted to ethylene at a lower rate.

Considering CO and CO₂ concentration profiles along the bed, it can be concluded that the position at which CO concentration hits a peak is approximately in accordance with the position in which the slope of CO₂ concentration decreases, and eventually its concentration reaches a plateau where oxygen is completely consumed. This proves that the rate of carbon monoxide oxidation increases dramatically due to the fact that this reaction is not oxygen-demanding. This leads to a decrease in CO concentration up to the position at which oxygen is completely consumed.

The drop for CO concentration after hitting a peak is more significant for the lower GHSV due to the fact that at higher GHSV, the decrease in CO concentration due to the water–gas shift reaction may be compensated with the CO produced in ethylene oxidation, which is low-oxygen-demanding, and consequently it may be accelerated when oxygen concentration is low. The acceleration of this nonselective reaction also results in a selectivity drop.

Regarding methane conversion dependency, the ratio of CH₄/O₂ is identical at the bed inlet for both GHSVs. Comparing the components' concentration profiles along the bed at both velocities reveals that the distribution of the oxygen concentration along the bed is more uniform at higher velocities. As a result, oxygen will be consumed in both selective and nonselective reactions respectively near the inlet and outlet of the reactor. However, at lower velocities, oxygen concentration drops significantly near the bed inlet and less oxygen remains to reach the bed outlet, and therefore the nonselective reactions are suppressed which require a greater amount of oxygen in comparison to the selective reactions.

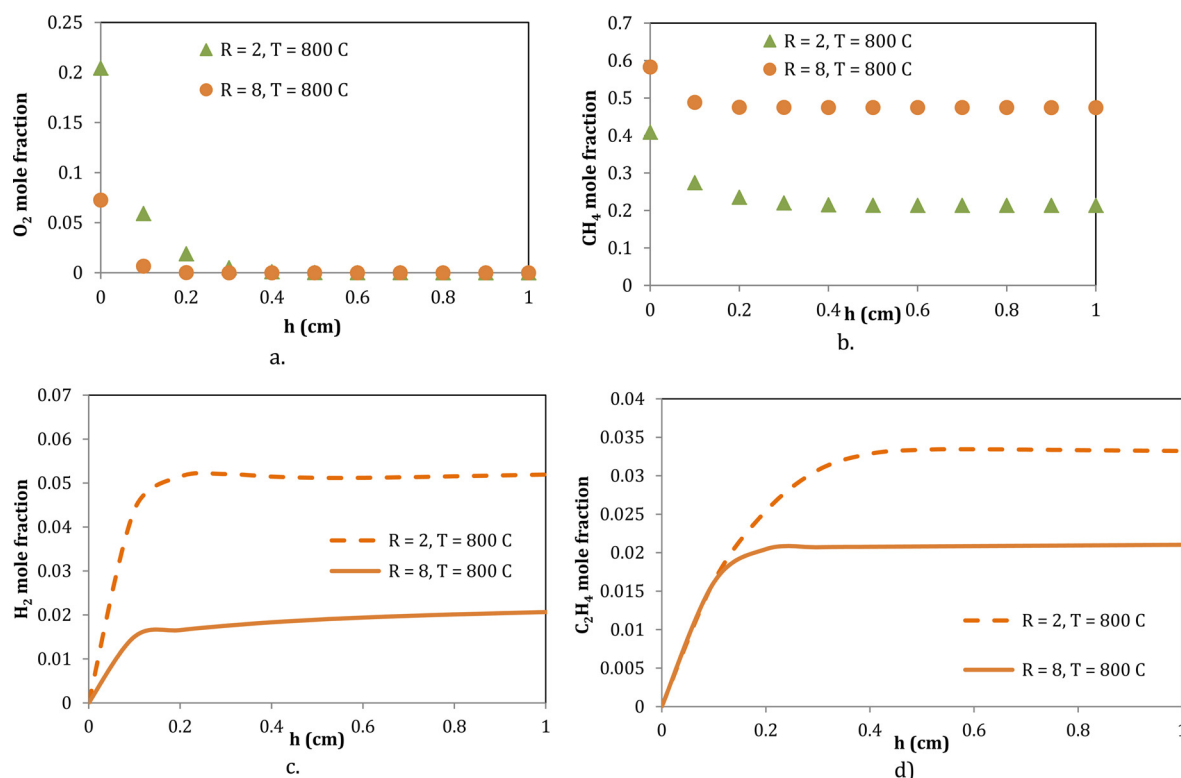


Figure 10. Variation of concentration of (a) O₂, (b) CH₄, (c) H₂, (d) C₂H₄ along the bed with change in CH₄/O₂ ratio.

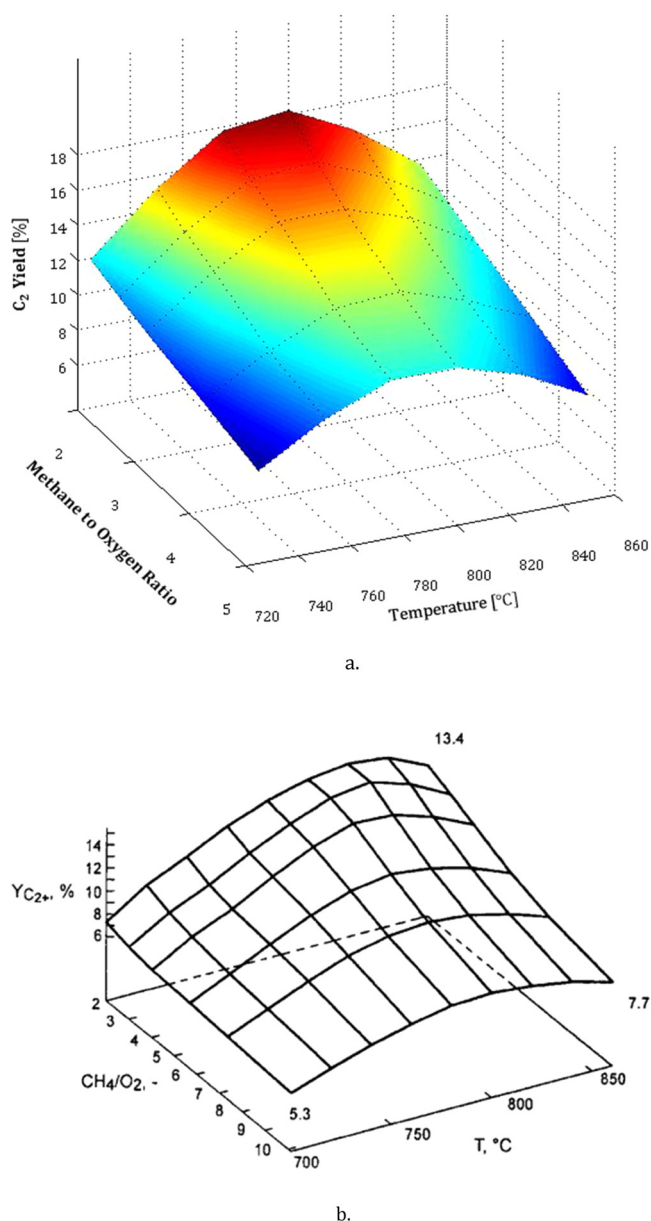


Figure 11. Effect of temperature and methane-to-oxygen ratio on C₂ yield (a) obtained in the present study and (b) reported by Pannek and Mleczko²⁵ (reproduced with permission from ref 25, copyright 1996 Elsevier) for the same catalyst but under different conditions ($d_p = 120 \mu\text{m}$, $u/u_{mf} = 20$).

3.3.2. Methane to Oxygen Ratio. The dependency of OCM fluidized-bed reactor performance on the value of the CH₄/O₂ ratio was investigated at $T = 800 \text{ }^\circ\text{C}$, $P = 1 \text{ bar}$, and $\text{GHSV} = 18151 \text{ h}^{-1}$ as illustrated in Figure 9. Increasing the CH₄/O₂ ratio gives a rise in C₂ selectivity, while it reduces methane conversion. This is a typical behavior for the OCM reaction, and such a trend enables a selection of the range of CH₄/O₂ ratio so that, for a high level of selectivity, enough methane conversion can be secured.

This dependency on the methane-to-oxygen ratio can be explained by reviewing the components' concentration profiles along the bed. As shown in Figure 10, the ratio of methane to oxygen soars along the bed for all studied ratios (for the ratios higher than 2) due to the fact that oxygen concentration drops dramatically along the bed, while methane concentration does

not undergo such a significant change. Moreover, at a low CH₄/O₂ ratio, near the bed inlet, the mole fractions of H₂, H₂O, CO₂, and CO products increase far more significantly in comparison to their rising trends at a high ratio of methane to oxygen. This can be attributed to the acceleration of nonselective reactions, which stems from the difference in the apparent reaction order with respect to oxygen for the selective and nonselective steps.²¹

At a low ratio of CH₄/O₂, near the bed inlet, the rate of nonselective reactions will increase. By increasing the vertical distance from the distributor, oxygen concentration drops, the availability of oxygen for nonselective reaction decreases, and consequently the rates of selective reactions simultaneously rise. In this case, methane will be consumed at both selective and nonselective reactions. On the other hand, when methane is present abundantly, methane reacts to a greater extent at selective reactions. The predicted profile for ethane concentration near the inlet proves this claim. This is shown in Figure 10d, where ethylene concentration is identical for both ratios up to $h = 0.1 \text{ cm}$. At higher positions, ethylene concentration increases along the bed for the oxygen-rich feed because at this vertical distance, the oxygen concentration levels off, and consequently oxidative dehydrogenation of ethylene, which is a low-oxygen-demanding reaction, will be accelerated. All these observations are in agreement with the fact that a lower oxygen level, either because of a higher methane presence or inert dilution, is in favor of selective OCM reactions.

3.4. Sensitivity Analysis. The sensitivity of reactor performance on the temperature and methane-to-oxygen ratio is shown in Figure 11a. According to this figure, an increase in the methane-to-oxygen ratio gives a rise in C₂ yield in the entire studied range of temperatures. Furthermore, the temperature at which C₂ yield hits a peak does not significantly change with an increase in methane-to-oxygen ratio in the entire studied range. A similar trend has been also reported by Pannek and Mleczko²⁵ for the same catalyst but under different operating conditions, as shown in Figure 11b. This figure is of main importance in terms of reactor engineering, as it provides valuable information with regard to the desired range of operating conditions to secure an optimum value of C₂ yield. From this figure, it can also be concluded that the CFD simulation can successfully predict the overall performance of the OCM reactor.

3.5. Evaluation of the Kinetic Model. As mentioned in previous sections, upon using Stansch's kinetic model for heterogeneous reactions, the effect of gas-phase reactions was marginal. It was also observed that in comparison to the catalytic reactions, the gas-phase reactions occur so slowly that increasing the pressure does not bring about any change in contribution of gas-phase reactions. Considering these findings, Stansch's kinetic model seems to be very fast, and re-evaluation of this kinetic model seems to be necessary in this regard.

Moreover, aimed at completing this evaluation, the concentration of various components along the bed was compared with the experimental data reported by Mleczko et al.¹⁹ As can be discerned in Figure 12a, due to the implemented fast Stansch's kinetic model, the simulation results predicted that the oxygen will be completely consumed shortly after entering the reactor, so the oxygen is not available to be bypassed through the bubble phase. However, in the experimental investigation based on the La₂O₃/CaO catalyst, this might be the case and have a marginal effect on the reactor performance, especially in higher gas velocities. It might be

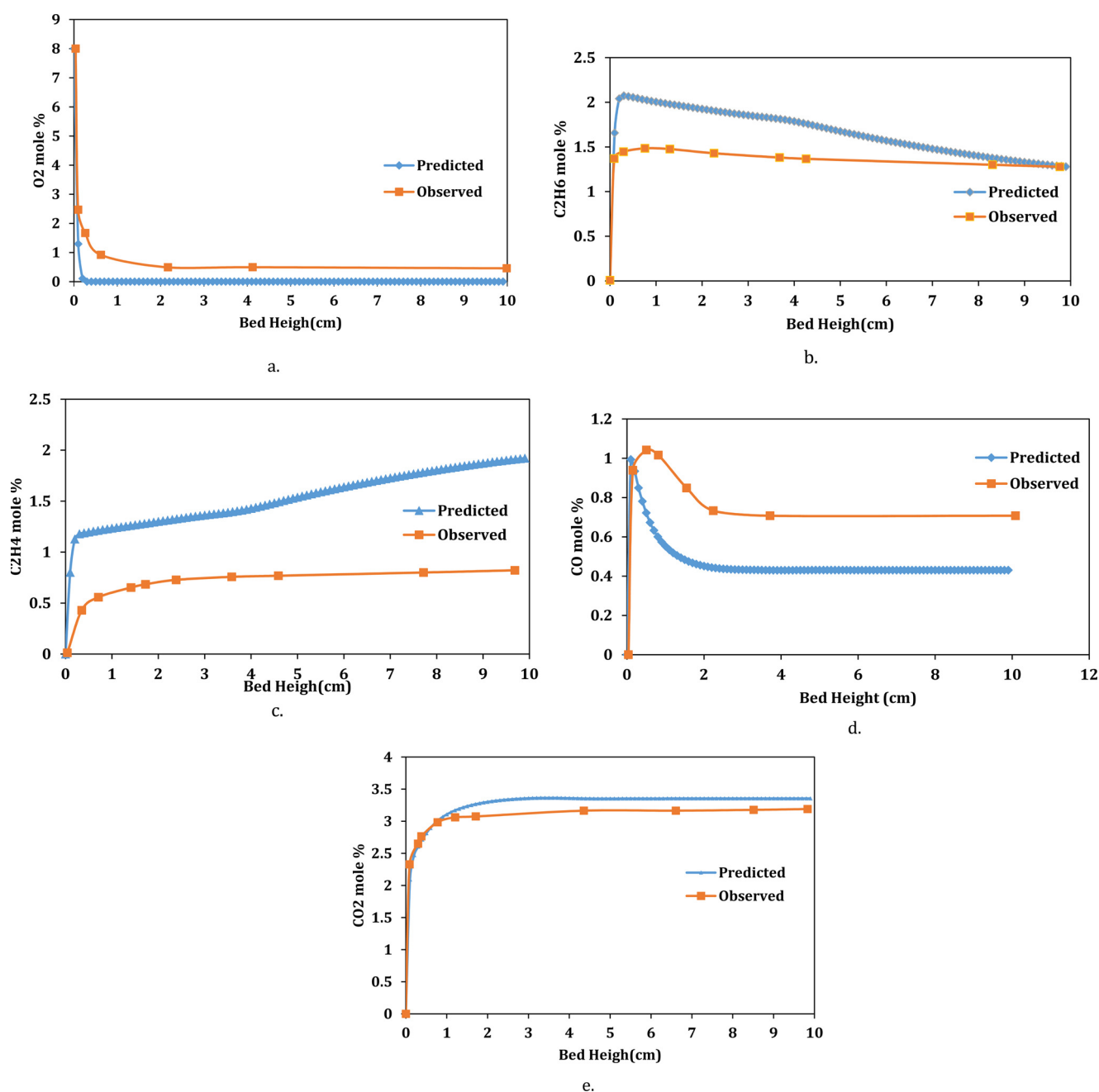


Figure 12. Comparison of the predicted mole fraction of (a) O₂, (b) C₂H₆, (c) C₂H₄, (d) CO, (e) CO₂ along the bed with the experimental data reported by Mleczko et al.¹⁹

quite different behavior, however, for some other OCM catalysts under some other sets of operating conditions. For instance, in the Li/MgO catalyst and to some extent in the Mn–Na₂WO₄/SiO₂ catalyst, the gas bypass via bubbles might result in the combustion of products and a significant reduction of the selectivity.

As another support for claiming that this kinetic model is very fast, the effect of feed dilution with nitrogen was also examined in this study, and as can be easily seen from Figure 13, diluting the feed with 34% nitrogen does not change the reactor performance in terms of C₂ selectivity and methane conversion. This is not in accordance with the general experimental observations in OCM reactors.

The implemented kinetic model and in fact all available OCM kinetic models yet have to be further developed to clearly

reflect the real contribution of the reactions in producing the carbon oxide components in the gas and over the catalyst. Here in this manuscript, the emphasis is to extract valuable information from the available kinetic models if they are utilized in their limited range of validity and if their limitations are considered in the reactor analysis.

Considering the concentrations' profiles along the bed, it can be concluded that application of a set of short fluidized-bed reactors for the OCM process is conceptually feasible. However, in terms of reactor design, extra reactor height is necessary for securing enough methane conversion and oxygen conversion, achieving the desired yield and avoiding the safety issues. A well designed cyclic short contact reactor can be a promising reactor concept for OCM.

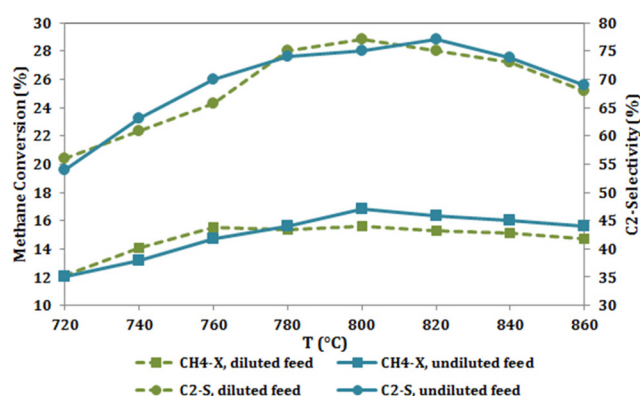


Figure 13. Effect of feed dilution on the reactor performance indicators.

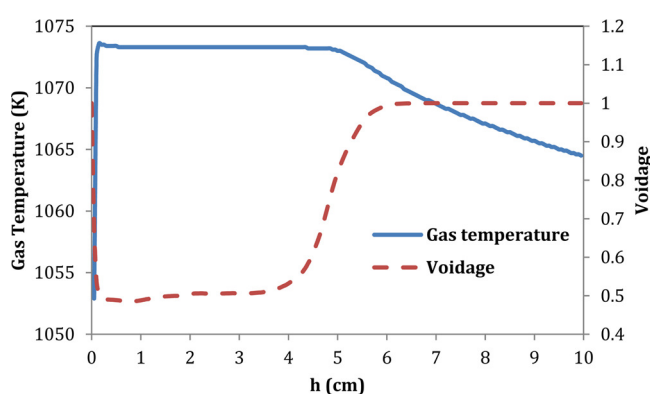


Figure 14. Time-averaged gas volume fraction and temperature profile along the bed.

3.6. Effect of Bed Hydrodynamic on Reactor Performance. One of the striking features of a fluidized bed is its high rate of heat and mass transfer due to the bubble motion and particle mixing. Since most of the reactions occurring in an OCM reactor are highly exothermic, fluidized bed hydrodynamics play an important role for handling the thermal behavior of such a system. The variation of gas volume fraction and the gas temperature along the bed is depicted in Figure 14. As can be easily discerned from this figure, in the dense bed, the

Table 5. Effect of Restitution Coefficient on Predicted Reactor Performance

restitution coefficient	C ₂ selectivity	methane conversion
0.75	0.6221	0.1279
0.80	0.6225	0.1281
0.90	0.6224	0.1279
0.95	0.6223	0.1281

gas volume fraction is less than 0.52, and near the freeboard where bubble bursting occurs, its value increases dramatically to 1. This figure reveals that the temperature profile is approximately uniform along the dense bed, while the gas temperature decreases rapidly in the freeboard due to the endothermic reaction of thermal dehydrogenation of ethylene, which occurs in the gas phase. This trend has been also reported by Mleczko et al.¹⁹

Moreover, the effect of restitution coefficient on the reactor performance was investigated. As shown in Table 5, C₂ selectivity and methane conversion are hardly affected by the restitution coefficient in the applied range of 0.75–0.95.

4. CONCLUSION

A two-fluid model based on the kinetic theory of granular flow was successfully applied in order to investigate the effect of operating conditions, contact time, and partial pressure of reactants on the performance of oxidative coupling of the methane reactor. The kinetic model developed by Stansch et al.²¹ was implemented to represent the heterogeneous reactions occurring in this reactor. The general predicted selectivity toward C₂ products and methane conversion were in agreement with the experimental data with a maximum deviation of 30% and 22%, respectively. The dependency of the reactor performance on the operating conditions and the feed characteristic was thoroughly investigated through the change in components' mole fraction along the bed. Furthermore, a slight decrease in methane conversion and C₂ selectivity by increase in pressure from 1 bar to 3 bar at various temperatures can be attributed to the acceleration of ethylene oxidation reaction at higher pressure. Moreover, C₂ selectivity and methane conversion dropped upon increasing the GHSV due to acceleration of ethylene oxidation at a lower contact time.

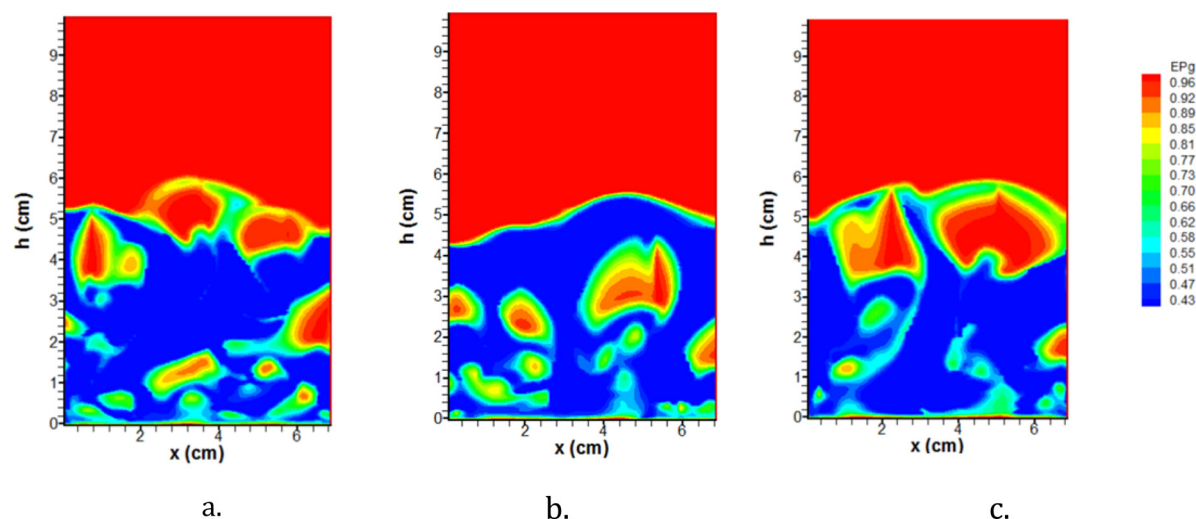


Figure 15. Gas volume fraction contour plot in the bed at (a) 1 s, (b) 1.5 s, (c) 2 s.

The validity of Stansch's kinetic model²¹ was also examined through analyzing the reaction pathways and the contributions of different reactions on the concentration profiles of all species along the reactor. It was concluded that this kinetic model represents a set of too fast reactions, and further study is needed to address the uncertainties related to the source of each product species as well as their rates of productions.

AUTHOR INFORMATION

Corresponding Authors

*E-mail: sdgh19@gmail.com.

*Tel.: +49 30 31421619. Fax: +49 30 31426915. E-mail: hamid.r.godini@tu-berlin.de.

Notes

The authors declare no competing financial interest.

ACKNOWLEDGMENTS

The authors gratefully acknowledge the financial support from the cluster of excellence within the framework of "Unifying Concepts in Catalysis" coordinated by the Technische Universität Berlin and funded by the German Research Foundation—Deutsche Forschungsgesellschaft.

NOMENCLATURE AND ABBREVIATIONS

CFD = Computational Fluid Dynamics
 CLC = Chemical-Looping Combustion
 CPOM = catalytic partial oxidation of methane
 FBR = Fluidized-Bed Reactor
 KTGF = kinetic theory of granular flow
 OCM = Oxidative Coupling of Methane
 OpenFOAM = Open source Field Operation And Manipulation
 SIMPLE = Semi-Implicit Method for Pressure-Linked Equations
 TFM = Two-Fluid Model
 UniCat = "Unifying Concepts in Catalysis" (a research group in Berlin)

Symbols

C_d = drag coefficient
 $C_{p,sm}$ = specific heat of the fluid phase, J/kg·K
 $C_{p,g}$ = specific heat of the m th solid phase, J/kg·K
 d_p = diameter of the particles, m
 D_{Bed} = bed diameter, m
 D_{gij} = rate of strain tensor, fluid phase, S^{-1}
 D_{sij} = rate of strain tensor, solid phase, s^{-1}
 D_{gn} = diffusion coefficient of n th gas-phase species, $kg/m \cdot s$
 e = coefficient of restitution for the collisions in solid phases
 e_w = coefficient of restitution for the collisions between solid particles and wall
 g_i = acceleration due to gravity, m/s^2
 g_0 = radial distribution function at contact
 H_f = bed height at fluidization condition, m
 ΔH_{rg} = heat of reaction in the fluid phase, $J/m^3 \cdot K$
 H_T = total bed height, m
 H_0 = static bed height, m
 i, j = indices to identify vector and tensor components; summation convention is used only for these indices
 I_{gsi} = interphase momentum exchange force, N/m^3
 J_s = granular energy transfer, m^2/s^3
 k_g = fluid-phase conductivity, $J/m \cdot K \cdot s$
 k_{sm} = m th solid phase conductivity, $J/m \cdot K \cdot s$

m = index of the m th solids phase, " $m = 0$ " indicates fluid phase

n = constant in the friction model reported by Johnson et al.¹⁸

Nu_m = Nusselt number

P_g = pressure in the fluid phase, Pa

$P_{s,f}$ = frictional pressure in the solid phase, Pa

P_s = solid pressure, Pa

Pr = Prandtl number

q_g = fluid-phase conductive heat flux, $J/m^2 \cdot s$

q_{sm} = m th solid phase conductive heat flux, $J/m^2 \cdot s$

R_{gm} = rate of transfer of mass from m th phase to k th phase, k or $m = 0$ indicates fluid phase, $kg/m^2 \cdot s$

R_{gn} = rate of production of the n th chemical species in the fluid phase, $kg/m^3 \cdot s$

R_{km} = ratio of solids to fluid conductivity

Re_p = solids phase particle Reynolds number

S_{gij} = gas phase shear rate, s^{-1}

S_{sij} = solid phase shear rate, s^{-1}

t = time, s

T_g = thermodynamic temperature of the fluid phase, K

T_{sm} = Thermodynamic temperature of the solids phase m , K

u_{mf} = minimum fluidization velocity, m/s

u_0 = superficial gas velocity, m/s

U_{gi} = fluid-phase velocity vector, m/s

U_{si} = solid-phase velocity vector, m/s

x_i = i th coordinate direction, m

X_{gn} = mass fraction of the n th chemical species in the fluid phase

Greek Letters

α = a constant with value of 1.6, dimensionless

γ_{gm} = fluid–solids heat transfer coefficient corrected for interphase mass transfer; $J/m^3 \cdot K \cdot s$

β_{gs} = coefficient for the interphase force between the fluid phase and the solid phase, $kg/m^3 \cdot s$

δ_{ij} = Kronecker delta function

ϵ_g^g = volume fraction of the fluid phase (void fraction)

ϵ_g^* = volume fraction of the fluid phase in minimum fluidization conditions

$\epsilon_{s,max}$ = packed-bed (maximum) solids volume fraction

ϵ_s = volume fraction of solids phase

η = function of restitution coefficient

Θ = granular temperature of solid phase, m^2/s^2

κ_s = granular energy diffusion coefficient, $kg/m \cdot s$

λ_{rm} = solid conductivity function

μ_g = molecular viscosity of the fluid phase, $kg/m \cdot s$

μ_{sf} = frictional shear viscosity of the solid phase, $kg/m \cdot s$

Π_s = exchange force in granular energy equation, $kg/m \cdot s^3$

ρ_g = microscopic (material) density of the fluid phase, kg/m^3

ρ_s = microscopic (material) density of the m th solids phase, kg/m^3

τ_{gij} = fluid-phase stress tensor, Pa

τ_{sij} = solids phase m stress tensor, Pa

$\bar{\tau}_{s,f}$ = solid phase frictional stress tensor, Pa

φ = angle of internal friction, also used as general scalar

φ_s = specular coefficient

φ_k = contact area fraction in solids conductivity model

REFERENCES

- (1) Kruggel-Emden, H.; Rickelt, S.; Stepanek, F.; Munjiza, A. Development and testing of an interconnected multiphase CFD-model for chemical looping combustion. *Chem. Eng. Sci.* **2010**, *65*, 4732–4745.

- (2) Deng, Z.; Xiao, R.; Jin, B.; Song, Q. Numerical simulation of chemical looping combustion process with CaSO₄ oxygen carrier. *Int. J. Greenhouse Gas Control* **2009**, *3*, 368–375.
- (3) Bougamra, A.; Huilin, L. Modeling of chemical looping combustion of methane using a Ni-based oxygen carrier. *Energy Fuels* **2014**, *28*, 3420–3429.
- (4) Adánez, J.; Dueso, C.; de Diego, L. F.; García-Labiano, F.; Gayán, P.; Abad, A. Methane combustion in a 500 Wth chemical-looping combustion system using an impregnated Ni-based oxygen carrier. *Energy Fuels* **2008**, *23*, 130–142.
- (5) Quiceno, R.; Deutschmann, O.; Warnatz, J.; Pérez-Ramírez, J. Rational modeling of the CPO of methane over platinum gauze: Elementary gas-phase and surface mechanisms coupled with flow simulations. *Catal. Today* **2007**, *119*, 311–316.
- (6) Reyniers, M.-F.; de Smet, C. R.; Menon, P. G.; Marin, G. B. Catalytic partial oxidation. part i. catalytic processes to convert methane: Partial or total oxidation. *CATTECH* **2002**, *6*, 140–149.
- (7) De Smet, C.; De Croon, M.; Berger, R.; Marin, G.; Schouten, J. An experimental reactor to study the intrinsic kinetics of catalytic partial oxidation of methane in the presence of heat-transport limitations. *Appl. Catal., A* **1999**, *187*, 33–48.
- (8) Lindborg, H.; Jakobsen, H. A. Sorption enhanced steam methane reforming process performance and bubbling fluidized bed reactor design analysis by use of a two-fluid model. *Ind. Eng. Chem. Res.* **2008**, *48*, 1332–1342.
- (9) Loha, C.; Chattopadhyay, H.; Chatterjee, P. K. Three dimensional kinetic modeling of fluidized bed biomass gasification. *Chem. Eng. Sci.* **2014**, *109*, 53–64.
- (10) Liu, Y.; Hinrichsen, O. CFD Simulation of Hydrodynamics and Methanation Reactions in a Fluidized-Bed Reactor for the Production of Synthetic Natural Gas. *Ind. Eng. Chem. Res.* **2014**, *53*, 9348–9356.
- (11) Kunii, D.; Levenspiel, O. *Fluidization Engineering*; John Wiley: New York, 1969.
- (12) Kato, K.; Wen, C. Bubble assemblage model for fluidized bed catalytic reactors. *Chem. Eng. Sci.* **1969**, *24*, 1351–1369.
- (13) Yang, W.-C. *Handbook of Fluidization and Fluid-Particle Systems*; CRC Press: Boca Raton, FL, 2003.
- (14) Patil, D. J.; van Sint Annaland, M.; Kuipers, J., Gas dispersion and bubble-to-emulsion phase mass exchange in a gas-solid bubbling fluidized bed: a computational and experimental study. *Int. J. Chem. React. Eng.* **2003**, *1*, DOI: [10.2202/1542-6580.1049](https://doi.org/10.2202/1542-6580.1049).
- (15) Gidaspow, D. *Multiphase Flow and Fluidization: Continuum and Kinetic Theory Descriptions*; Academic Press: 1994.
- (16) Anderson, T. B.; Jackson, R. Fluid Mechanical Description of Fluidized Beds. Equations of Motion. *Ind. Eng. Chem. Fundam.* **1967**, *6*, 527–539.
- (17) Xie, N.; Battaglia, F.; Pannala, S. Effects of using two- versus three-dimensional computational modeling of fluidized beds: Part I: hydrodynamics. *Powder Technol.* **2008**, *182*, 1–13.
- (18) Gidaspow, D.; Bezburuah, R.; Ding, J. *Hydrodynamics of Circulating Fluidized Beds: Kinetic Theory Approach*; Illinois Inst. of Tech.: Chicago, IL, 1991.
- (19) Mleczko, L.; Pannek, U.; Rothaemel, M.; Baerns, M. Oxidative coupling of methane over a La₂O₃/CaO catalyst. Optimization of reaction conditions in a bubbling fluidized-bed reactor. *Can. J. Chem. Eng.* **1996**, *74*, 279–287.
- (20) Jašo, S. *Modeling and Design of the Fluidized Bed Reactor for the Oxidative Coupling of Methane*; Universitätsbibliothek der Technischen Universität: Berlin, 2012.
- (21) Stansch, Z.; Mleczko, L.; Baerns, M. Comprehensive Kinetics of Oxidative Coupling of Methane over the La₂O₃/CaO Catalyst. *Ind. Eng. Chem. Res.* **1997**, *36*, 2568–2579.
- (22) Lane, G. S.; Wolf, E. E. Methane utilization by oxidative coupling: I. A study of reactions in the gas phase during the cofeeding of methane and oxygen. *J. Catal.* **1988**, *113*, 144–163.
- (23) Zanthoff, H.; Baerns, M. Oxidative coupling of methane in the gas phase. Kinetic simulation and experimental verification. *Ind. Eng. Chem. Res.* **1990**, *29*, 2–10.
- (24) Patankar, S. *Numerical Heat Transfer and Fluid Flow*; CRC Press: Boca Raton, FL, 1980.
- (25) Pannek, U.; Mleczko, L. Comprehensive model of oxidative coupling of methane in a fluidized-bed reactor. *Chem. Eng. Sci.* **1996**, *51*, 3575–3590.

“The science of today is the technology of tomorrow.”

(Edward Teller)

5

Sustainable Process Design for Oxidative Coupling of Methane (OCM): Comprehensive Reactor Engineering via Computational Fluid Dynamics (CFD) Analysis of OCM Packed-Bed Membrane Reactors

In this section, the effect of feed dosing on oxidative coupling of methane reactor is investigated through applying computational fluid dynamics. In detail, a CFD code is developed and used to expand the border of reaction engineering knowledge in the performance of OCM reactors through thermal-reaction analysis.

This article was published in *Industrial & Engineering Chemistry Research* 55, 2016, 3287–3299, DOI: 10.1021/acs.iecr.5b03292

Copyright is held by American Chemical Society, and all rights are reserved by this organization. Permission has been granted by American Chemical Society for including the following publication and its appendix into the present thesis.

Sustainable Process Design for Oxidative Coupling of Methane (OCM): Comprehensive Reactor Engineering via Computational Fluid Dynamics (CFD) Analysis of OCM Packed-Bed Membrane Reactors

Mohammad-Sadeqh Salehi,^{*,†} Maryam Askarishahi,[†] Hamid Reza Godini,^{*,†} Oliver Görke,[‡] and Günter Wozny[†]

[†]Chair of Process Dynamics and Operation, Berlin Institute of Technology, Strasse des 17. Juni 135, Sekr. KWT-9, D-10623 Berlin, Germany

[‡]Department of Ceramic Materials, Institute for Material Science and Technologies, Berlin Institute of Technology, Hardenbergstrasse 40, D-10623 Berlin, Germany

Supporting Information

ABSTRACT: The oxidative coupling of methane (OCM) reaction system was investigated in a packed-bed membrane reactor (PBMR) numerically via a comprehensive computational fluid dynamics (CFD) study. In this context, the complete set of momentum, mass, and energy balances were solved through finite-volume method in cylindrical coordinate system. The fractional-step method was utilized to decouple the reaction source terms from the convection-diffusion terms. The general observed trends for variation of the components' concentrations along the bed were successfully explained by analyzing the rate of reactions. In this study, the effect of membrane thermal conductivity, and oxygen permeation were also examined which can affect the OCM reactor and process performance significantly. Finally, the dynamics behavior of the system was studied and by following the reaction rates and the shift of reactions along the catalytic-bed and with time, the reaction mechanisms were discerned. The results of the performed CFD simulation can be used as a baseline for a possible optimization approach for OCM reactor performance improvement.

1. INTRODUCTION

In order to develop alternative technologies for ethylene production that are more sustainable and economically promising simultaneously, a great effort is still needed. According to Cavani,¹ margins exist not only for the improvement of the processes currently in use, but also for rethinking the chemical productions through innovative approaches. Oxidation catalyzes generally are playing a leading role in the ambitious project of more sustainable industrial chemistry.^{1,2} In fact, oxidation processes are among the reactions with the greatest potential for being further improved; in recent years, this has led to the development of a series of highly efficient processes.^{1,2}

Ethylene as an important raw material for downstream petrochemical industries can be produced via methane catalytic oxidation as well as cracking processes. In conventional processes such as steam thermal cracking, ethane or heavier hydrocarbons are used as the feedstock to produce ethylene and the process consumes high rate of energy. On the other hand, since methane oxidative coupling represents an exothermic set of reactions, its generated heat and energy can be utilized in other processes. Therefore, substituting the highly endothermic cracking processes with the methane oxidative coupling process can address both energy and chemical productions. Apart from this, utilization of natural gas instead of oil and implementation of the new technologies and catalysts in catalytic oxidation reactors have been suggested to improve the economic aspects of those conventional chemical production processes.² Here, the sustainability potential of

the oxidative coupling of methane (OCM) process³ can be specifically highlighted.

Sustainability of the feedstock is an important parameter that must be considered. In comparison to the oil-based feedstocks, methane is more sustainable feed due to the low cost, lower carbon footprint (i.e., CO₂ emission), and the possibility for being supplied from various sustainable resources. In detail, apart from the methane available in the major sources such as natural gas and coal, it can be also produced through biogas,⁴ fermentation of organic matter,⁴ and the methane hydrates stored at the ocean floor.⁵

Despite all these favorable factors, methane is still underutilized as a feedstock for chemical production, because of a lack of sustainable strategies for its selective oxidation,⁶ particularly in the OCM process, because of low yield,¹ stemmed from the production of carbon dioxide and carbon monoxide in the total and partial oxidation of methane. Besides, according to Tang et al.⁷ and Mitsudome et al.,⁸ the main challenges related to OCM are low yield, catalyst deactivation at high temperature, and bad economics. They suggested that Mn/Na₂WO₄-SiO₂ and La₂O₃-CaO can provide the highest

Special Issue: Sustainable Manufacturing

Received: September 4, 2015

Revised: January 23, 2016

Accepted: January 25, 2016

Published: January 25, 2016

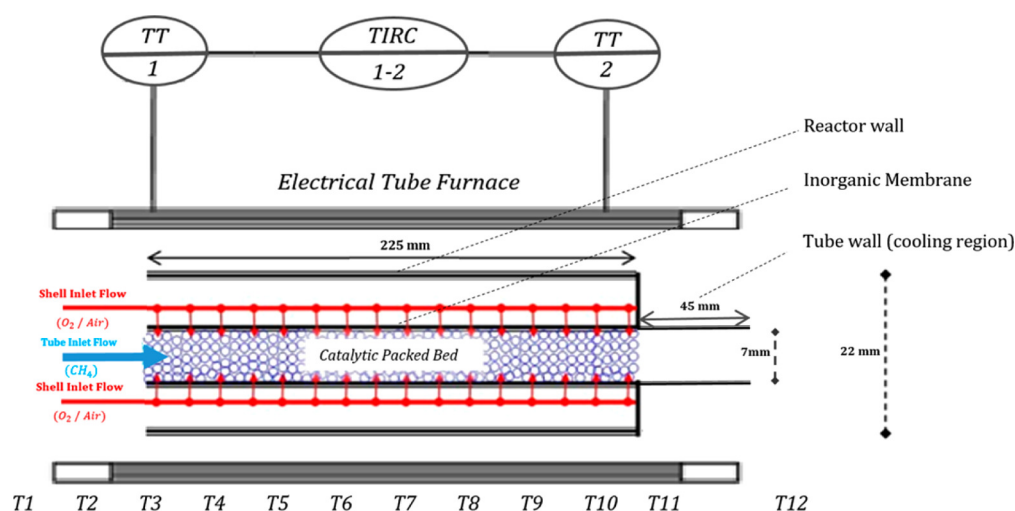


Figure 1. Schematic representation of OCM packed-bed membrane reactor concept in its dimensions utilized in the modeling and experimentations in this research.

performance, in terms of C_2 -products selectivity and yield, while providing relatively stable catalytic performance.

In addition to the limitation in conversion and yield, selective separation of the desired products from undesired ones as well as the unreacted methane is of crucial importance in this process, which can be achieved via integrating the OCM process with other processes such as methane reforming, ethylene oligomerization, and oxygenate synthesis, as reported by Kumar et al.⁹

Utilizing alternative reactor configurations and feeding policies of reactants is a factor that can contribute to the development of a more sustainable chemical industry, especially for the catalytic selective oxidation processes.¹ Specifically for the OCM process, various reactor concepts such as fluidized-bed reactors, packed-bed reactors, and membrane-assisted reactors have been suggested and tested.^{10,11} Lu et al.^{12,13} reported that, upon using membrane reactor and helium as a diluent, the selectivity and yield of the desired products (ethylene and ethane: C_2) increase by 30% and 10%, respectively. Several studies^{3,14} proved that, by adjustment of oxygen-to-methane ratio, reactor performance can be improved, in terms of C_2 yield. Therefore, application of membrane that allows adjustment of the local oxygen-to-methane ratio along the catalytic packed bed may improve the reactor performance. For instance, Lu et al.¹³ investigated a cross-flow reactor with six feeding pattern, and concluded that multipoint feeding increases the C_2 yield.

Considering above discussion and aimed at developing more sustainable process, the numerical study of the OCM reactor is necessary to understand the reactor performance. Such understanding can be employed to improve the performance of the reactor, in terms of increasing the selectivity and yield, which will be addressed in detail in future studies. Various methodologies can be used for simulation of the reactive multiphase flow. In the phenomenological models and lumped formulation, the radial distribution of the heat and component concentration, as well as the thermal resistance of the membrane, are neglected, which can affect the accuracy of the solution, as proved by various studies in the literature. For instance, utilizing a two-dimensional (2D) simulation of a multichannel membrane reactor for steam reforming of methane, Vigneault et al.¹⁵ proved that the driving forces for

the thermal conduction in the axial and lateral directions are of the same order at the wall separating the combustion channel. Moreover, Marín et al.¹⁶ demonstrated the importance of the radial distribution for methane steam reforming process and water–gas-shift reactions in a fixed-bed and hydrogen permselective membrane reactor.

Rattananon et al.¹⁷ developed a 2D model for packed bed with various policies for oxygen and methane feeding under isothermal conditions. They claimed that when methane is fed as the main flow and oxygen is fed as the side flow, better reactor performance can be predicted. However, because of the exothermicity of the reaction, temperature distribution influence on reactor performance should be investigated and, consequently, it is necessary to consider nonisothermal conditions.

CFD simulations take more details of the system into analysis, and, therefore, can predict the effects of the variation of parameters in the system more accurately. Such a model is needed to ensure achieving the best reactor performance, along with a safe operation. For instance, Quiceno et al.¹⁸ carried out a simulation on catalytic partial oxidation of methane. They investigated the gas-phase reaction and surface reaction mechanism and predicted that increasing the residence time and the total pressure resulted in the formation of ethane from the oxidative coupling reaction and carbon dioxide and water from the total combustion of methane.

In comparison to the lumped formulation, in the finite volume method, energy and mass balance equations are discretized considering all convection, diffusion, and source terms, even in the membrane section. Therefore, there is no need to estimate the simplified mass- and heat-transfer coefficient across the shell side, membrane, and the tube side. As a result, less possible errors can be expected and the accordingly performed analysis will be more precise. Moreover, CFD simulation allows analyzing the interaction of the thermal aspects and reaction aspects in a control volume and thereby, track the impact of the applied kinetic model and hot-spot formation locally.

Significant efforts in both theoretical and experimental research activities are still required to understand the efficient mechanism through which the OCM reactor performance can be improved and to come up with an efficient innovative

Table 1. Equations Used in the Simulations

equation	No.
Gas-Phase Continuity	
$\frac{\partial(\varepsilon_g \rho_g)}{\partial t} + \frac{\partial}{\partial x_i}(\varepsilon_g \rho_g U_{gi}) = 0$	T1
Gas-Phase Momentum	
$\frac{\partial(\varepsilon_g \rho_g U_{gi})}{\partial t} + \frac{\partial}{\partial x_j}(\varepsilon_g \rho_g U_{gi} U_{gj}) = -\varepsilon_g \frac{\partial P_g}{\partial x_i} + \frac{\partial \tau_{gij}}{\partial x_j} - I_{gsi} + \nabla P_{\text{membrane}} + \varepsilon_g \rho_g g_i$	T2
Gas-Phase Stress Tensor	
$\tau_{gij} = 2\mu_g S_{gij}$	T3
$S_{gij} = \frac{1}{2} \left(\frac{\partial U_{gi}}{\partial x_j} + \frac{\partial U_{gj}}{\partial x_i} \right) - \frac{1}{3} \left(\frac{\partial U_{gi}}{\partial x_i} \right) \delta_{ij}$	T4
Interphase Momentum Transfer Coefficient²⁵	
$I_{gsi} = \beta_{gs} (u_{gi} - u_{si})$	T5
$\beta_{gs} = 150 C_d \frac{(1 - \varepsilon_g)^2}{\varepsilon_g (d_p)^2} \mu_g + 1.75 (1 - \varepsilon_g) \frac{\rho_g}{d_p} \mathbf{u}_g - \mathbf{u}_s $	T6
Gas Energy Balance	
$\begin{aligned} \varepsilon_g \rho_g C_{Pg} \left(\frac{\partial T_g}{\partial t} + \mathbf{u}_g \cdot \nabla T_g \right) \\ = -\nabla \cdot \mathbf{q}_g + \sum_{m=1}^M \gamma_{gm} (T_{sm} - T_g) - \Delta H_{rg} + \gamma_{Rg} (T_{Rg}^4 - T_g^4) \end{aligned}$	T7
Gas Conduction	
$\mathbf{q}_g = -k_g \nabla T_g$	T8
Gas-Solids Heat-Transfer Coefficient	
$\gamma_{gm} = \frac{C_{Pg} R_{0m}}{\exp\left(\frac{C_{Pg} R_{0m}}{\gamma_{gm}^0}\right) - 1}$	T9
$\gamma_{gm}^0 = \frac{6k_g \varepsilon_g Nu_m}{d_{pm}^2}$	
$\begin{aligned} Nu_m = (7 - 10\varepsilon_g + 5\varepsilon_g^2)(1 + 0.7Re_p^{0.2}Pr^{1/3}) \\ + (1.33 - 2.4\varepsilon_g + 1.2\varepsilon_g^2)Re_p^{0.7}Pr^{1/3} \end{aligned}$	
Solid Energy Balance	
$\begin{aligned} \varepsilon_{sm} \rho_{sm} C_{Psm} \left(\frac{\partial T_{sm}}{\partial t} \right) = -\nabla \cdot \mathbf{q}_{sm} + \sum_{m=1}^M \gamma_{gm} (T_{sm} - T_g) - \Delta H_{rsm} \\ + \gamma_{Rsm} (T_{Rsm}^4 - T_{sm}^4) \end{aligned}$	T10
Solid Conduction	
$\mathbf{q}_{sm} = -k_{sm} \nabla T_{sm}$	T11
$k_{sm} = [\varphi_k R_{km} + (1 - \varphi_k) L_{Rsm}] \left(\frac{k_g}{\sqrt{1 - \varepsilon_g}} \right)$	
$B = 1.25 \frac{(1 - \varepsilon_g)^{10/9}}{\varepsilon_g}$	
$R_{km} = \frac{k_s}{k_g}$	
$B_R = \frac{B}{R_{km}}$	
$L_{Rsm} = -\left(\frac{2}{1 - B_R} \right) \left[\frac{R_{km} - 1}{(1 - B_R)^2} B_R \ln B_R + \frac{B - 1}{1 - B_R} + \frac{B + 1}{2} \right]$	
$\varphi_k = 7.26 \times 10^{-3}$	

Table 1. continued

equation	No.
Gas Species Balance	
$\frac{\partial}{\partial t}(\epsilon_g \rho_g X_{gn}) + \nabla \cdot (\epsilon_g \rho_g X_{gn} \mathbf{u}_g) = \nabla \cdot D_{gn} \nabla X_{gn} + R_{gn}$	T12
Pressure Drop across the Membrane	
$\nabla p_{\text{membrane}} = - \left(\frac{\mu_g}{C_1} \right) \mathbf{u}_g$	T13

alternative reactor configuration for this application. Aimed at achieving this goal, CFD simulation was developed in the present study to expand the available knowledge, especially in thermal-reaction analysis of the OCM reactor, to operate the reactor with a more selective and productive manner and therefore makes this process more sustainable. In detail, the main objective of the present study is to perform a numerical investigation of the OCM reaction performance in a packed-bed membrane reactor to establish the baseline performance of the reactor, which can be used for detailed parametric study and optimization for improving the potential and sustainability of this process in subsequent studies.

2. MATHEMATICAL MODELING

2.1. Governing and Constitutive Equations. CFD simulation of a packed-bed membrane reactor in 2D cylindrical coordinate system has been performed using MFIX open-source code.¹⁹ The geometry of the studied system is shown in Figure 1, where the locations of the external electrical heater and the thermocouples have been depicted. This information is important for analyzing and controlling the thermal performance of the OCM reactor as will be discussed in details by reviewing the steady and dynamic behaviors of the OCM reactor performance in this study.

Eulerian–Eulerian approach was applied in the present study to model a multiphase flow system. In this approach, the phases are mathematically represented as interpenetrating continua.²¹ Interphase momentum transfer coefficient was considered to include the drag force exerted by the solid phase on the gas phase. The implemented governing and constitutive equations have been shown in Table 1. Further details regarding the models and constitutive equations can be found in the Supporting Information.

2.2. Simulation Conditions and Solution Method.

2.2.1. Simulation Conditions. The numerical simulations in the current study have been performed in accordance with the experimental data reported by Godini.³ Detailed simulation conditions are summarized in Table 2.

Kinetic models reported by Stansch et al.²⁰ was used for quantifying the rates of the OCM reactions as reported in Table 3. Comprehensive information about the reaction rate equations can be found elsewhere.²⁰

2.2.2. Numerical Simulation Method. The set of governing equations was solved using the finite volume method in a 2D cylindrical frame. The modified SIMPLE algorithm for multiphase flow²⁴ was applied to consider the pressure–velocity coupling. For temporal discretization, implicit backward Euler method was applied and Superbee method²¹ was exploited for spatial discretization of convective terms. Maximum residuals on the convergence for continuity, momentum, concentration, and energy were set to 10^{-4} . Initial and maximum time steps were set to 10^{-4} and 10^{-3} s,

Table 2. Physical Properties and Simulation Parameters

parameter	value
Bed Geometry	
D_{shell}	22 mm
H_T	370 mm
H_0	225 mm
D_T	7 mm
Membrane Properties	
length	225 mm
thickness	1.5 mm
permeability	$1.5\text{--}6 \text{ cm}^3 \text{ cm}^{-2} \text{ min}^{-1} \text{ bar}^{-1}$
Solid Phase Properties	
$\rho_{s,\text{catalyst}}$	400 kg/m^3
$\rho_{s,\text{inert}}$	1400 kg/m^3
d_p	$350 \mu\text{m}$
ϵ_g	0.35

respectively. The grid sizes used to resolve the computational domain were 0.5 mm and 1 mm in radius and axial directions, respectively. (See the Supporting Information for details.)

2.2.3. Initial and Boundary Conditions. The initial conditions for the solid- and gas-phase velocity were set to zero. It was assumed that the tube side was initially filled with nitrogen and in the shell side, nitrogen and oxygen presented in the same mole fractions as in the shell side inlet feed stream.

Turning to the boundary conditions, velocity-inlet boundary condition was specified in the simulation. At the top, the pressure-outlet boundary condition was used for the tube side, while for the shell side dead-end wall boundary condition was considered. At the shell side, wall which is surrounded by the oven, no-slip boundary condition was applied for the gas phase and the temperature was set to constant value of 970 K. This is the value of the oven temperature set in the experimentations. According to the experimental observation, during the cooling process and using water in the cooling jacket wall, as shown in Figure 1, the temperature decreases to 893 K, on average, and wall temperature variation in the cooling region was <10 K. Therefore, the average value of 893 K was used for wall temperature in cooling region, i.e., $h = 22\text{--}27$ cm in the simulation for simplification. The summary of the initial and boundary conditions have been reported in Table 4.

3. RESULTS AND DISCUSSION

Generally speaking, the study of CFD reaction engineering allows one to predict the effects of operating and structural parameters on the reactor outlet products' composition, even beyond the limitations that exist for analyzing such effects in the experimentation.

The results of this CFD simulation should be analyzed in consideration of the following facts:

- Considering the dosing feeding policy in PBMR and the characteristics of the implemented kinetic, oxygen is available

Table 3. Representing Set of OCM Reactions

reaction	equation	reaction heat	No.
total oxidation of methane	$\text{CH}_4 + 2\text{O}_2 \rightarrow \text{CO}_2 + 2\text{H}_2\text{O}$	-802.2	R-1
oxidative coupling of methane	$2\text{CH}_4 + 0.5\text{O}_2 \rightarrow \text{C}_2\text{H}_6 + \text{H}_2\text{O}$	-176.8	R-2
partial oxidation of methane	$\text{CH}_4 + \text{O}_2 \rightarrow \text{CO} + \text{H}_2\text{O} + \text{H}_2$	-227.5	R-3
oxidation of carbon monoxide	$\text{CO} + 0.5\text{O}_2 \rightarrow \text{CO}_2$	-282.98	R-4
oxidative dehydrogenation of ethane	$\text{C}_2\text{H}_6 + 0.5\text{O}_2 \rightarrow \text{C}_2\text{H}_4 + \text{H}_2\text{O}$	-104.86	R-5
oxidation of ethylene	$\text{C}_2\text{H}_4 + 2\text{O}_2 \rightarrow 2\text{CO} + 2\text{H}_2\text{O}$	-755.92	R-6
thermal dehydrogenation of ethane	$\text{C}_2\text{H}_6 \rightarrow \text{C}_2\text{H}_4 + \text{H}_2$	+136.96	R-7
steam reforming of ethylene	$\text{C}_2\text{H}_4 + 2\text{H}_2\text{O} \rightarrow 2\text{CO} + 4\text{H}_2$	+210.31	R-8
conversion of carbon monoxide to carbon dioxide and vice versa by water-gas shift reaction	$\text{CO} + \text{H}_2\text{O} \rightarrow \text{CO}_2 + \text{H}_2$	-41.17	R-9
	$\text{CO}_2 + \text{H}_2 \rightarrow \text{CO} + \text{H}_2\text{O}$	+41.17	R-10

Table 4. Initial and Boundary Conditions for the Present Simulation

parameter	shell	tube
Initial Condition		
gas velocity	0 m/s	0 m/s
solid velocity	0 m/s	0 m/s
gas volume fraction	0.35	0.35
mole fraction of N_2	0.58	1.0
mole fraction of CH_4	0.0	0.0
mole fraction of O_2	0.42	0.0
gas temperature	827.15 K	827.15 K
Inlet Boundary Condition		
volumetric flow	2.58 $\text{cm}^3[\text{STP}]/\text{s}$	4.2 $\text{cm}^3[\text{STP}]/\text{s}$
gas volume fraction	0.35	0.35
mole fraction of N_2	0.58	0.48
mole fraction of CH_4	0.0	0.52
mole fraction of O_2	0.42	0.0
gas temperature	827.15 K	857.15 K
Outlet Boundary Condition		
outlet pressure	wall	atmospheric
Wall Boundary Condition		
gas phase	no slip	no slip
temperature	packed bed section (970 K) cooling section (893 K)	adiabatic

all along the PBMR, and, as a result, the oxidative catalytic and gas-phase reactions will always be present.

• The net energy balance of the OCM reactions is highly exothermic and by gradual conversion of reactants, the operating temperature continually increases until the temperature gradient between the reaction temperature and the temperature in the external surrounding environment becomes high enough to emit the excess generated heat. Approaching the end of the reactor, methane and oxygen (in reactors with co-feeding structure) are progressively consumed and the operating temperature decreases. Therefore, the reactor wall temperature is a very important parameter to be tuned in experiments.

Reactor performance is usually referenced in terms of the conversion of the main reactant and the selectivity of valuable products. Therefore, for the OCM process, the methane conversion, predicted yield of C_2 products (ethylene and ethane), and C_2 selectivity, as the performance indicators of the OCM reaction, are calculated using eqs 1–3:

methane conversion:

$$X_{\text{CH}_4} = \frac{n_{\text{CH}_4}^{\text{inlet}} - n_{\text{CH}_4}^{\text{outlet}}}{n_{\text{CH}_4}^{\text{inlet}}} \quad (1)$$

yield of C_2 products:

$$Y_{\text{C}_2} = \frac{2 \times (n_{\text{C}_2\text{H}_6} + n_{\text{C}_2\text{H}_4})}{n_{\text{CH}_4}^{\text{inlet}}} \quad (2)$$

C_2 selectivity:

$$S_{\text{C}_2} = \frac{Y_{\text{C}_2}}{X_{\text{CH}_4}} = \frac{2 \times (n_{\text{C}_2\text{H}_6} + n_{\text{C}_2\text{H}_4})}{n_{\text{CH}_4}^{\text{inlet}} - n_{\text{CH}_4}^{\text{outlet}}} \quad (3)$$

In these equations, n is the molar flow rate of the gaseous species, and X , Y , and S represent the methane conversion, yield, and selectivity, respectively.

3.1. Diffusion and Thermal Characteristics. **3.1.1. Oxygen Permeation (Quantitative Analysis and Pattern).** Considering the practical possibility for tailoring the membrane permeability,²² the effect of oxygen permeation on the PBMR performance was investigated. As shown in Figure 1, in the dead-end PBMR structure, all shell-side gas passes through the membrane but in different proportions along the membrane, depending on the membrane permeation. However, it was experimentally observed that working in the membrane permeation in the range of 1.5–6 $\text{cm}^3/(\text{cm}^2 \text{ min bar})$ provides the best performance in this PBMR structure.^{3,22} Therefore, this range of permeation was numerically investigated.

As shown in Table 5, the predicted methane conversion and C_2 selectivity changed marginally by increasing the permeation from 1.5 $\text{cm}^3/(\text{cm}^2 \text{ min bar})$ to 6 $\text{cm}^3/(\text{cm}^2 \text{ min bar})$. As a result, the mean value for this range was chosen in the simulation.

3.1.2. Thermal Conductivity of the Membrane and Radial Heat Transfer. Radial heat transfer generally and the thermal conductivity of the membrane specifically have significant effect on the thermal reaction performance of the PBMR system. The value of the membrane conductivity was calculated based on the measured conductivity of the membrane material (Al_2O_3), as shown in eq 4.

$$K_{\text{mem}} = \varepsilon_g K_g + (1 - \varepsilon_g) K_{\text{Al}_2\text{O}_3} \quad (4)$$

This is important to highlight that choosing a proper value for this parameter in the modeling of an OCM membrane

Table 5. Comparison of Selectivity, Yield, and Conversion for Various Membrane Permeability at $t = 180$ s and $t = 552$ s

	$P_m = 1.5$ cm ³ /(cm ² min bar)		$P_m = 6$ cm ³ /(cm ² min bar)	
	$t = 552$ s	$t = 180$ s	$t = 552$ s	$t = 180$ s
selectivity	0.625	0.464	0.631	0.464
conversion	0.495	0.335	0.497	0.337
yield	0.309	0.155	0.314	0.157
C ₂ H ₄ selectivity	0.514	0.301	0.520	0.302
C ₂ H ₆ selectivity	0.111	0.163	0.111	0.162
C ₂ H ₄ yield	0.255	0.101	0.257	0.102
C ₂ H ₆ yield	0.055	0.054	0.055	0.055

reactor is very important. Looking at the predicted values of the C₂ selectivity and C₂ yield, as typically shown in Table 6, it can

Table 6. Comparison of Selectivity, Yield, and Conversion for Various Membrane Conductivities

K_m	selectivity	C ₂ yield
$K_{Al_2O_3}$	0.46	0.155
$0.5K_s$	0.53	0.20
$0.1K_s$	0.52	0.18

be concluded that choosing a lower values for the membrane conductivity may lead to (1) a higher reaction temperature peak, and (2) an overprediction of the C₂ selectivity and C₂ yield. To explain this, it should be considered that the majority of the reactions occurring in the OCM process are highly exothermic and less membrane conductivity means that the generated heat of reactions cannot be easily removed from the tube side through the membrane. Therefore, the reaction temperature rises. On the other side, since methane oxidative coupling reactions are strongly dependent on the temperature,

the rise of temperature significantly accelerates the rate of coupling reactions, in comparison to that of other reactions. Moreover, near the membrane, temperature hits a peak since most of the reactions occur there and the rate of highly O₂-demanding reaction being also highly exothermic is faster near the membrane because of the fact that oxygen is available more than the value required in accordance with stoichiometric value.

Similar to the trends observed in Table 6, the experimentally measured temperature trajectories in Figure 2 reflect the limitations of the heat transfer in the OCM packed-bed membrane reactor, as well as the difficulty of temperature control in this system and its effect on the fluctuation of temperature and, consequently, the reaction performance. Following these experimentally observed dynamic trends showed that the highest C₂-yield was obtained when the local temperature, measured by some of the thermocouples, follow an ascending trend.

3.2. Analyzing the Predicted Reactor Performance through Reaction Pathway. 3.2.1. Predicted Results in Transient and Steady States (180 and 552 s).

Table 7. Comparing the Selectivity, Yield, and Methane Conversion between the Simulation and Experimental Data

	Predicted Value		observed experimental value
	$t = 552$ s	$t = 180$ s	
selectivity	0.63	0.46	0.6
conversion	0.50	0.34	0.26
yield	0.31	0.16	0.2
C ₂ H ₄ selectivity	0.52	0.3	0.51
C ₂ H ₆ selectivity	0.11	0.16	0.09
C ₂ H ₄ yield	0.26	0.1	0.17
C ₂ H ₆ yield	0.06	0.05	0.03

values of the selectivity, conversion, and yield obtained through the simulation are compared with their corresponding

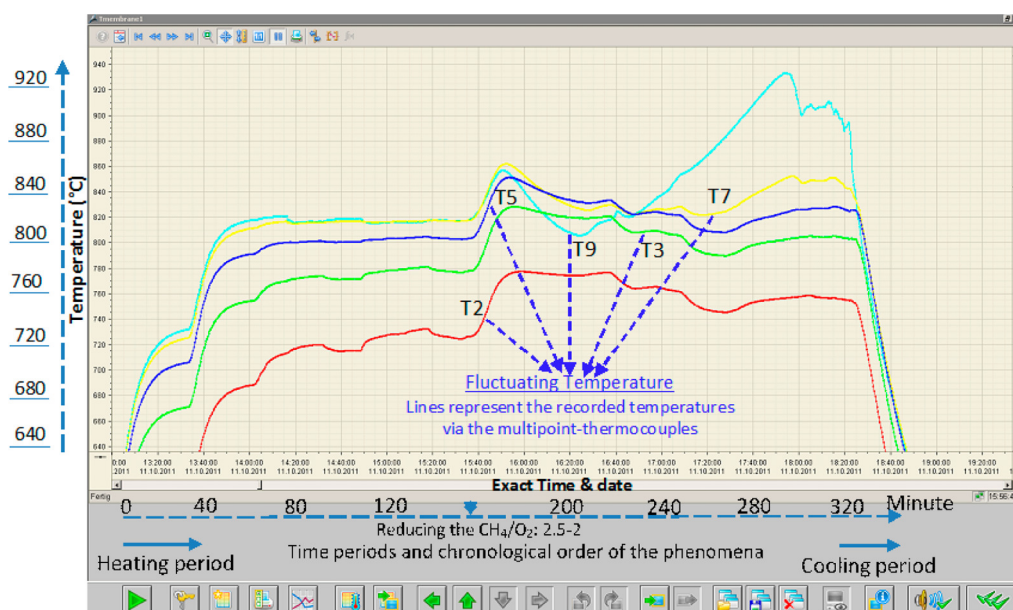


Figure 2. Transient thermal-reaction behavior of the OCM membrane reactor to be addressed via proper thermal-reaction engineering. The locations of the thermocouple are addressed as following and their position have been shown in Figure 1: T2, thermocouple 2 is located 2 cm before the beginning of the catalytic bed; T3, thermocouple 3 is located in the beginning of the catalytic bed; T5, thermocouple 5 is located 4 cm into the catalytic bed; T7, thermocouple 7 is located 8 cm into the catalytic bed; and T9, thermocouple 9 is located 12 cm into the catalytic bed.

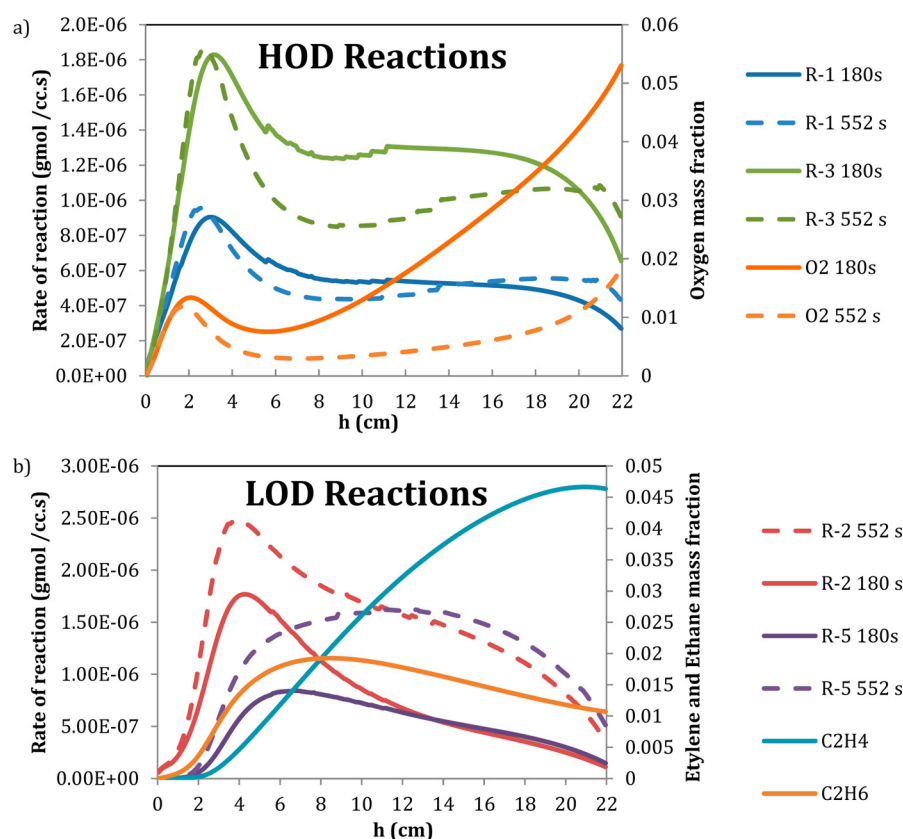


Figure 3. Variation of reaction rates in accordance with oxygen mass fraction along the bed at $t = 180$ s and $t = 552$ s.

experimental data. At $t = 552$ s, the predicted values for the C_2 selectivity are in good agreement with the observed experimental data, while the predicted conversion is almost twice that of the observed one. This difference can be attributed to the assumption that implemented kinetic model is accurate only for prediction of the steady-state selectivity. The reason is that usually the experimental data on the selectivity are used for fitting the parameters in the kinetic development stage. The difference may be attributed to the fact that the time required to establish the steady-state behavior in the OCM reaction system is longer than the times spent on extracting the experimental data utilized for kinetic development. In order to explain the deviation of the predicted methane conversion from the observed experimental one, as shown in Table 7, the experimental data have been compared with the predicted value at $t = 180$ s, which is approximately the time when the reaction shift occurs and deviation of the predicted methane conversion from their experimentally observed values sharply increases. In fact, under the conditions reached at this time, a decrease in the oxygen concentration is in favor of the selective reactions. According to the stoichiometry coefficient of methane in the kinetic model developed by Stansch et al.,²⁰ these selective reactions, which includes oxidative coupling of methane and ethane oxidative dehydrogenation, requires higher amount of methane and are lowly oxygen-demanding (LOD) in comparison to the nonselective reaction, which are highly oxygen-demanding (HOD), followed by higher conversion of this components. Therefore, overprediction of methane conversion can be explained as a consequence of using this kinetic model.

3.2.2. Concentration, Reaction Rate, and Reaction Heat along the Bed. In Figures 3–5, variations of the reaction rates

and the generated reaction heats, as well as the oxygen mass fraction along the bed, have been shown at $t = 180$ s and $t = 522$ s. Since, in this process, most of the reactions, especially the total oxidation of methane (reaction R-1 in Table 3) are highly exothermic, all reactions rates increase due to temperature soar. Strongly dependent on the bed temperature, at $h = 2$ cm, the rate of methane oxidative coupling (reaction R2) outweighs that of the total oxidation reactions. Since the heat of reaction of the total oxidation of methane (reaction R1) is much higher than the heat of coupling reaction (OCM) ($\Delta H_{TOM} = 4.56 \Delta H_{OCM}$), the generated heat due to the reactions hits a peak at slightly higher position ($h = 3.7$ cm). This is because of the thermal and mass-transfer restrictions. At $h = 2$ cm, because of the observed increase in the reaction rates, oxygen consumption begins to grow, so a local maximum for oxygen concentration can be observed at this height. At $h = 3$ cm, rate of HOD reactions such as total and partial oxidation of methane meet a maximum.

Reduction in the oxygen concentration results in the contributions of LOD reactions such as oxidative coupling of methane (reaction R-2 in Table 3) and oxidative dehydrogenation of ethane (reaction R-5 in Table 3) occurring at higher rates. Since these LOD reactions are not as highly exothermic as HOD ones, the total heat generated—and, consequently, the reactor temperature—decreases. As a result, the temperature and, accordingly, the reaction rates decrease and the inferiority of the HOD reactions results in less oxygen consumption and its concentration plummets at $h \approx 5.7$ cm. Because of the thermal and mass-transfer restrictions, hot-spot temperature is observed at a higher position (i.e., $h = 6.8$ cm). The rate of LOD reactions also reaches its maximum value at $h = 4.4$ cm.

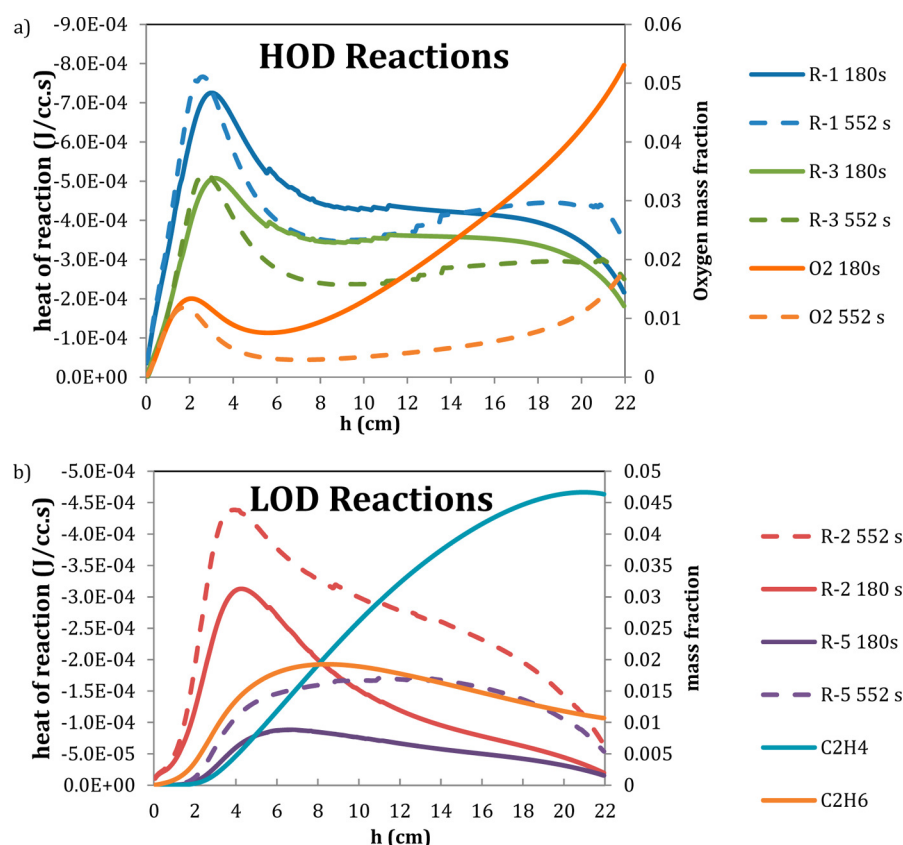


Figure 4. Variation of reaction heats for (a) HOD and (b) LOD reactions, in accordance with the mass fraction of ethane and ethylene along the bed at $t = 180$ s and $t = 552$ s.

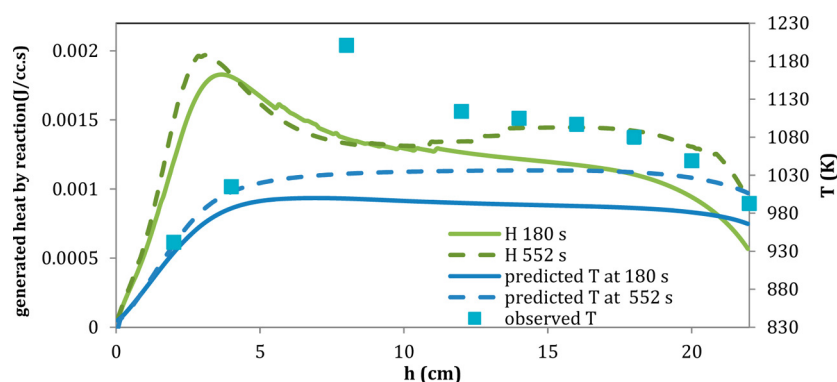


Figure 5. Variation of temperature and total generated heat along the bed at various times.

As shown in Figure 3a, at the axial position where $h < h_{\max O_2}$ at identical height, the oxygen concentration does not undergo significant change for both flow times. Similar trend can be also observed for HOD reactions rates. This proved that these reactions are strongly affected by the oxygen concentration. On the other hand, the rates of LOD reactions increase with time due to the temperature growth, which shows that these reactions are highly dependent on the reactor temperature.

Concentration profiles for selective products (i.e., ethane and ethylene) along the bed have been shown in Figure 3b. As it can be discerned from this figure, after a small distance from the reactor inlet, the ethane mole fraction rises significantly, followed by a gradual decrease up to the reactor outlet. This can be explained by the fact that, upon rising along the reactor, the ethane consumption rate in the dehydrogenation reaction

(reaction R-5 in Table 3) is higher than its production rate in the OCM reaction (reaction R-2 in Table 3), so the ethylene concentration increases sharply.

3.2.3. Temperature Profile. In Figure 4, the predicted temperature profiles were compared with the experimental data. At $t = 180$ s, hot-spot temperature can be observed, while at $t = 552$ s, temperature reaches a plateau. This can be explained by the fact that at $t = 180$ s, as shown in Figures 3 and 4, after hitting a peak, the rates of more exothermic reactions, including the total and partial oxidation of methane, as well as oxidation of carbon monoxide, decrease sharply along the bed and then remain approximately constant up to $h = 20$ cm. Other less exothermic reactions including the OCM (reaction R-1) and ODE (reaction R-5) decline marginally after reaching the maximum value. These variations in the generated heats of

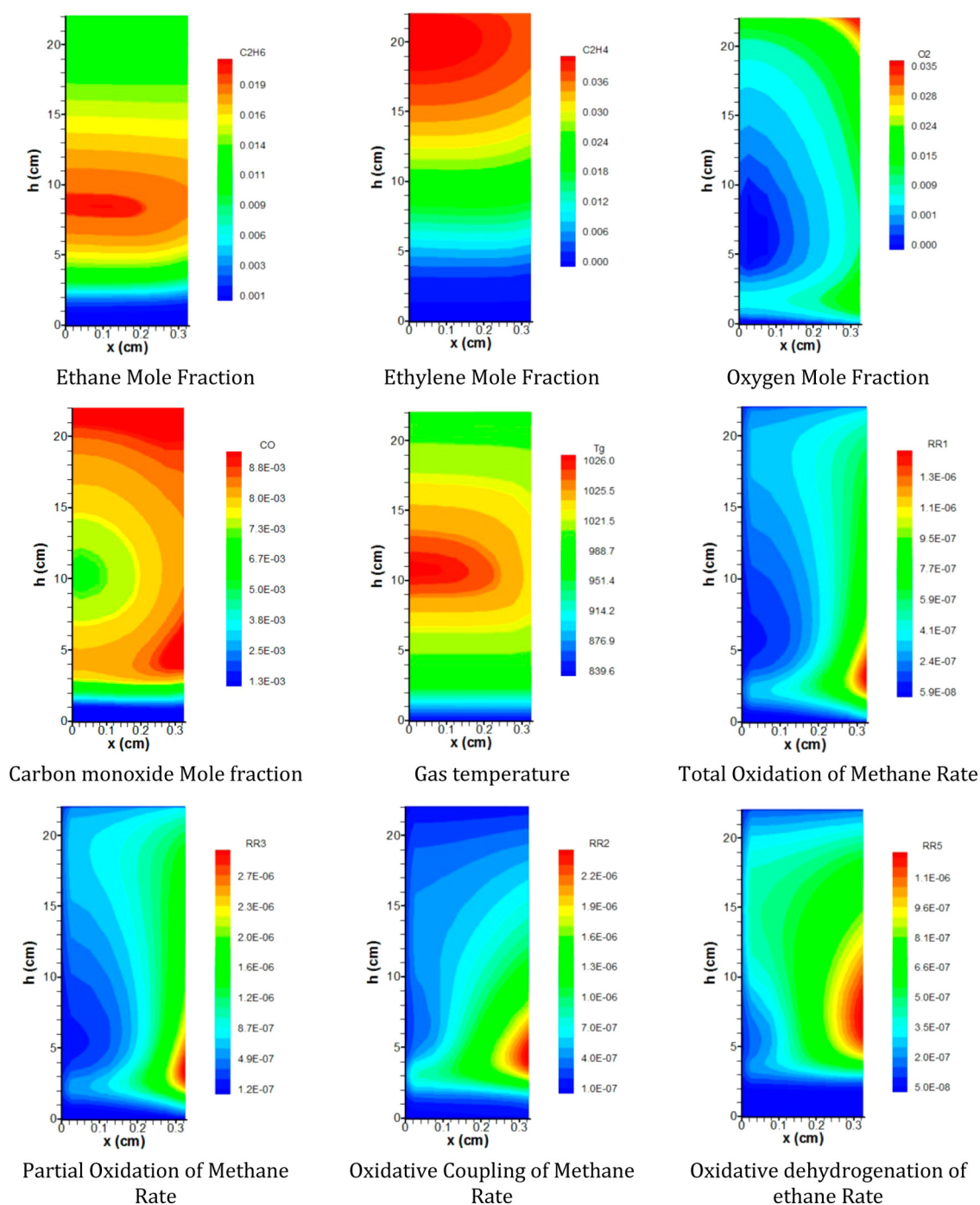


Figure 6. Contour plots for temperature, component mole fraction, and reaction rates; $x = 0$ represents the symmetric axis and $x = 0.35$ corresponds to the membrane interface with the tube side.

reactions enhance the hot-spot temperature. On the other hand, at $t = 552$ s, the heat generated by more exothermic reactions increases to a small extent after plummeting. The less exothermic reactions in this case decrease more marginally, in comparison to $t = 180$ s. As a consequence, the reactor temperature levels off at $h = 5.8$ cm.

Moreover, there is another fact that can explain this trend. When gas enters in the beginning of the reactor, where the wall temperature is higher than the reactor temperature, heat is transferred from the shell side to the tube side until reaching the point where the gas temperature reaches the wall temperature due to the generated heat of reaction. This

happens up to $h = 3.3$ cm, where the maximum heat generated by the reactions is released, as shown in Figure 5. At higher positions, the direction of heat transfer is reversed. Since the shell wall acts like a cooling boundary, the temperature increases up to $h = 5$ cm, where a heat balance between the generated reactions heat and the heat removed by the shell wall is achieved. The lag due to the membrane thermal resistance and the solid particles conductivity delays the effect of change in the heat-transfer direction up to the point at which temperature gradient between the tube side and the shell wall becomes significant. At higher position, since the wall temperature and the generated reaction heat are constant, the

gas temperature remains virtually constant along the bed at $t = 552$ s. However, at $t = 180$ s, since the generated heat of reactions decreases along the bed after plunging, and since the wall temperature is constant along the bed, the predicted temperature profile follows a trend similar to that observed for the heat of reaction.

Regarding the temperature profile along the bed, at $h = 20$ cm, the temperature suddenly decreases since a cooling jacket is located right after the reactor aimed at fast cooling the gas that is leaving the reactor and stopping the reactions. This sudden decline in temperature leads to a fast reduction in the rates and heats of reactions.

Comparison of the predicted temperature profile with the observed one proves the agreement between them. In the 5 cm length along the bed, some deviation can be observed, which is associated with the local hot-spot formation, because the general temperature profile can be successfully predicted. The criterion that Stansch et al.²⁰ used for steady-state conditions is constancy of oxygen concentration. However, considering Figure 7 (presented later in this work), it can be observed that oxygen concentration in the bed outlet changes very slowly after 300 s. Considering the stoichiometry coefficient for selective reactions in Stansch's²⁰ kinetic model, a lower amount of oxygen was required to produce ethane and ethylene. As a result, a justification for deviation of the predicted results from the observed results may be the conditions at which kinetic model has been developed.

3.2.4. Contour Plots and Analysis of Thermal Reaction Fluid Flow. Contour plots for temperature, the mole fraction of various components, and the reaction rates have been shown in Figure 6. As it can be discerned from this figure, the temperature gradient in the radial direction cannot be easily seen, because the reactor diameter, in comparison to the bed height, is very small. Since the methane concentration, not shown here, exceeds its stoichiometric value, its concentration gradient is not significant in the radial direction and its consumption rate is limited by the oxygen availability in the reactor.

On the other side, since oxygen enters the tube side radially through the membrane and most of the reactions in the OCM reactor are oxygen-intensive, radial gradient of oxygen mole fraction is sharp. As shown in Figure 6, ethylene mole fraction increases along the bed. Because of the fact that the ethylene production reaction (i.e., oxidative dehydrogenation of ethane) is an LOD reaction and a higher amount of ethane is observed far from the membrane wall at $h = 5$ cm to $h = 15$ cm, a sufficient amount of ethane and oxygen is present to produce ethylene. Consequently, ethylene concentration is slightly higher at central region of the tube in comparison to other regions. In this region, selective reactions (i.e., reactions R-2 and R-5 in Table 3) performed well and these reactions are not considered to be as highly exothermic as nonselective reactions, and therefore, the temperature does not increase sharply. Regarding H₂O mole fraction, its concentration is lower near the membrane, because this component is produced in several reactions, most important of which are OCM and ODE (reactions R-2 and R-5), both of which being LOD reactions. As discerned from the figure, CO mole fraction is lower in the central region of the tube at intermediate height. Its radial gradient is also more considerable than the axial one. This can be explained by the fact that carbon monoxide is mainly produced in reaction R-3, and is mainly consumed in the CO oxidation reaction. Since reaction R-3 is an HOD reaction and

reaction R-5 is an LOD reaction, the CO consumption rate is higher at the central region, where lower oxygen concentration is present, while its production rate is higher near the membrane, where oxygen exists in more than the stoichiometric value required in this region.

3.3. Dynamic Behavior. **3.3.1. Applied and Operating Temperature and Pressure.** In order to investigate the dynamic behavior of the reactor, the laterally averaged temperature and pressure of the reactor in the bed outlet was calculated. The reactor temperature in the bed outlet increases as time elapses, since most of the reactions occurring in the OCM reaction set are highly exothermic. The reactor pressure also slightly increases as time passes.

3.3.2. Reaction Mechanisms, Concentrations, and Heat. In Figure 7, variation of laterally averaged mole fraction of various

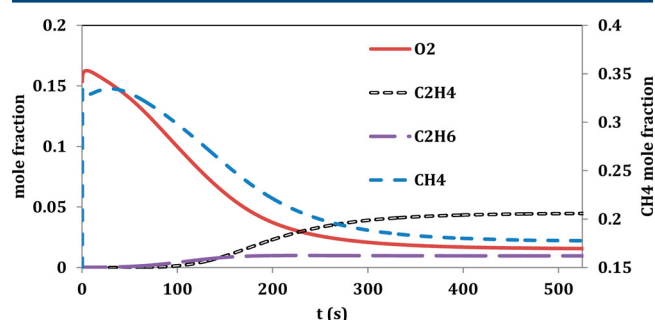


Figure 7. Dynamic behavior of the reactor, in terms of component mole fractions.

components in the bed outlet against the time as well as the values of C₂ selectivity, C₂ yield, and methane conversion have been shown. In order to reach the steady-state conditions, simulation was required to continue for 552 s as the heat distribution is not performed fast in the packed bed. Besides, since OCM reactions occur in the tube side, while furnaces are located at the shell wall, membrane thermal resistance and the solid particles filling the shell side prevent the heat from reaching the tube side readily. As it can be seen from these figures, oxygen mass fraction decreases more rapidly than the methane fraction, because of the fact that the reactions occurring in the OCM process are in high demand for oxygen. Comparing the consumption rates of these two components proves this fact, as shown in Table 8. Another point discerned

Table 8. Comparing the Consumption Rate of the Methane and Oxygen at Various Simulation Times

t (s)	Reaction Rate ($\times 10^6$ gmol/(cm ³ s))		
	RR _{CH₄}	RR _{O₂}	RR _{O₂} /RR _{CH₄}
180	3.30	3.61	1.10
552	4.45	5.88	1.32

from Figure 7 is that the ethane concentration increases slightly after $t = 150$ s, while the ethylene concentration increases sharply. This can be explained by comparing the reaction rate for the OCM and ODE (reactions R-2 and R-5) at various times. In fact, as time elapses, ODE reaction rate increases more significantly in comparison to the OCM one. Hence, ethane that is produced by the OCM reaction is converted to ethylene rapidly.

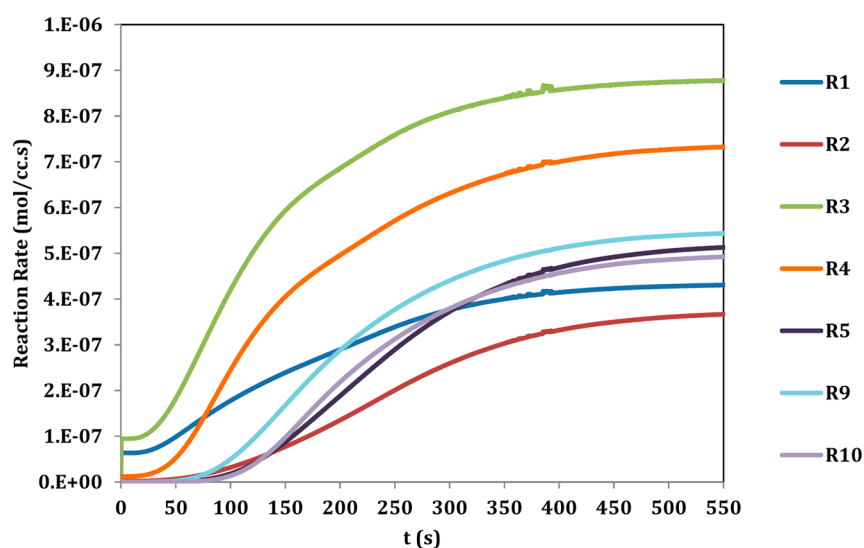


Figure 8. Dynamic behavior in terms of reaction rates.

Considering the reaction rates, as shown in Figure 8, as time passes, the reaction rate of the reaction R-1 loses its significance to greater extent in comparison to other reactions, which favors ethylene production. Since this reaction is the most exothermic reaction in the OCM process, decrease in its rate causes the reactor temperature and consequently the reactor pressure to go up with larger slope.

The information obtained from CFD simulation can be used to understand the OCM process, with the objective of improving the reactor performance and, consequently, the sustainability of such a process. Such information should be also taken into consideration to design the process downstream. For instance, using carbon dioxide as a diluent in the OCM reactor, and even simultaneously as a reactant in an integrated OCM-reforming dual membrane reactor,²³ not only allows one to control the operating temperature there, but also in combination with an appropriate adsorption unit in the OCM process downstream. In fact, it can lead to a carbon-dioxide-free process. The detailed design and experimental operation of various downstream units and process scenario structures have been analyzed as a support for the sustainable development of the OCM process.^{14,24}

Considering the discussion presented in this section, it can be concluded that the application of the packed-bed membrane reactor can improve the sustainability of OCM reactor in terms of improving the C_2 selectivity and C_2 yield to reach more than 70% and 25%, respectively, by addressing the thermal aspects of the design and tailoring the dimensions of the OCM reactor. In detail, considering the oxygen stoichiometry coefficient in the applied kinetic model, selective reactions are LOD, while the nonselective reactions are HOD. As a result, the fine distribution of oxygen through the membrane can be favorable for selective reactions, and hence nonselective reactions have less chance to occur. On the other hand, in conventional packed-bed reactor structure, oxygen and methane contact in the bed inlet, which results in higher consumption rate of the oxygen in the total and partial methane oxidation reactions. However, the amount of the produced carbon dioxide is not negligible in this process. With the objective of reducing CO_2 emissions, this component can be used as a reactant for other reactors through heat and mass reactor integration in the form of dual-membrane reactor structure for instance and the

preliminary study shows that utilizing such reactor structure can lead to $\sim 60\%$ less CO_2 emission in the outlet. Therefore, CFD simulation-assisted design of such reactor structures can be a step forward toward sustainability of the OCM process.

4. CONCLUSION

With the objective of developing a more sustainable process, CFD simulation of oxidative coupling of methane in packed-bed membrane reactor as a promising alternative configuration reactor was performed. Kinetic model developed by Stansch et al.²⁰ was implemented to represent the heterogeneous reactions occurring in this reactor. The effect of membrane specifications including conductivity and permeation was examined. Through investigation of predicted reaction rates and implemented kinetic model, the predicted components' concentration profiles were successfully analyzed. The reactor performance in terms of methane conversion and C_2 selectivity was compared with experimental data. The predicted C_2 selectivity under steady-state conditions was in good agreement with experimental data, while an overprediction of methane conversion was observed. Through investigation of dynamic behavior of the reactor, this deviation from experimental data can be attributed to reaction shift that occurred in dynamic behavior, and the conditions under which the kinetic model was developed.

It should be noted that the improvement of the OCM reactor performance and, accordingly, the sustainability of the OCM process, has not been completely corroborated by the performed simulations in this study. Therefore, there is a need for comprehensive detailed analysis of the effect of each structural and operating parameters using the simulation tool developed in this work. In detail, the presented OCM reactor analysis in this research can be used as a baseline for improving the performance of the OCM reactor and accordingly the sustainability of the OCM process through sustainable product design performance via

- establishing a selective performance and reducing the CO_2 production in an OCM reactor;
- utilizing the heat and materials via an integrated reactor such as dual-membrane reactor and the integrated process to reduce the process scale net CO_2 emission

(this also allows controlling the temperature profile along the reactor in accordance with the evolution of the reaction pathways along the bed);

- (c) utilizing an efficient downstream unit such as adsorption in an integrated process structure, which leads to a reduction of operating and fixed costs; and
- (d) focusing on one section of the reactor and not performing a process-wide mini-plant analysis, for example, can lead to ignoring some of those potentials and shortcomings in the conclusions.

■ ASSOCIATED CONTENT

■ Supporting Information

The Supporting Information is available free of charge on the ACS Publications website at DOI: 10.1021/acs.iecr.5b03292.

Supplementary data associated with this article include constitutive equations for the heat-transfer equation and grid sensitivity analysis (PDF)

■ AUTHOR INFORMATION

■ Corresponding Authors

*E-mail: sadegh.salehi1987@gmail.com (M.-S. Salehi).

*Tel.: +49 30 31421619. Fax: +49 30 31426915. E-mail: hamid.r.godini@tu-berlin.de (H. R. Godini).

■ Notes

The authors declare no competing financial interest.

■ ACKNOWLEDGMENTS

The authors gratefully acknowledge the financial support from the cluster of excellence within the framework of “Unifying Concepts in Catalysis” coordinated by the Technische Universität Berlin and funded by the German Research Foundation—Deutsche Forschungsgemeinschaft.

■ NOMENCLATURE

■ Abbreviations

CFD = computational fluid dynamics
 CLC = chemical-looping combustion
 CPOM = catalytic partial oxidation of methane
 C_2 = ethane + ethylene
 HOD = highly oxygen-demanding reaction
 LOD = lowly oxygen-demanding reaction
 KTGf = kinetic theory of granular flow
 OCM = oxidative coupling of methane
 OpenFOAM = open source field operation and manipulation
 PBMR = packed bed membrane reactor
 SIMPLE = semi-implicit method for pressure-linked equations
 TFM = two-fluid model
 TOM = total oxidation of methane

■ Variables

C_d = drag coefficient
 C_{psm} = specific heat of the fluid phase (J/(kg K))
 C_{pg} = specific heat of the m th solid phase (J/(kg K))
 C_1 = inertial resistance (m^2)
 d_p = diameter of the particles (m)
 D_{gn} = diffusion coefficient of n th gas-phase species (kg/(m s))
 D_{shell} = shell diameter (m)
 D_T = tube diameter (m)
 g_i = acceleration due to gravity (m/s^2)

h = reactor length (m)

ΔH_{rg} = heat of reaction in the fluid phase (J/(m³ s))

ΔH_{rsm} = heat of reaction of the m th component in the solid phase (J/(m³ s))

H_T = total bed height (m)

H_0 = catalytic bed height (m)

i, j = indices used to identify vector and tensor components; summation convention is used only for these indices

I_{gsi} = interphase momentum exchange force (N/m³)

K_s = thermal conductivity of the solid body (J/(m K s))

$K_{Al_2O_3}$ = thermal conductivity of alumina material (J/(m K s))

K_{mem} = thermal conductivity of membrane (J/(m K s))

K_g = fluid-phase conductivity (J/(m K s))

k_{sm} = m th solid phase conductivity (J/(m K s))

m = index of the m th solids phase ($m = 0$ indicates fluid phase)

Nu_m = Nusselt number

P_g = pressure in the fluid phase (Pa)

Pr = prandtl number

q_g = fluid-phase conductive heat flux (J/(m² s))

q_{sm} = m th solid phase conductive heat flux (J/(m² s))

R_{gn} = rate of production of the n th chemical species in the fluid phase (kg/(m³ s))

R_{km} = ratio of solids to fluid conductivity

Re_p = solids phase particle Reynolds number

S = selectivity

Sg_{ij} = gas phase shear rate (s^{-1})

t = time (s)

T_g = thermodynamic temperature of the fluid phase (K)

T_{sm} = thermodynamic temperature of the solids phase m (K)

u_0 = superficial gas velocity (m/s)

U_{gi} = fluid-phase velocity vector (m/s)

u_s = solid-phase velocity vector (m/s)

x_i = i th coordinate direction (m)

X_{gn} = mass fraction of the n th chemical species in the fluid phase

X = conversion

Y = yield

■ Greek Letters

α = constant ($\alpha = 1.6$)

γ_{gm} = fluid–solids heat-transfer coefficient corrected for interphase mass transfer (J/(m³ K s))

β_{gs} = coefficient for the interphase force between the fluid phase and the solid phase (kg/(m³ s))

δ_{ij} = Kronecker Delta function

ε_g = volume fraction of the fluid phase (void fraction)

ε_s = volume fraction of solids phase

κ_s = granular energy diffusion coefficient (kg/(m s))

λ_{rm} = solid conductivity function

μ_g = molecular viscosity of the fluid phase (kg/(m s))

ρ_g = microscopic (material) density of the fluid phase (kg/m³)

ρ_s = microscopic (material) density of the m th solids phase (kg/m³)

τ_{gij} = fluid-phase stress tensor (Pa)

φ = Angle of internal friction, also used as general scalar

ϕ_k = contact area fraction in solids conductivity model

■ REFERENCES

- (1) Cavani, F. Catalytic selective oxidation: The forefront in the challenge for a more sustainable chemical industry. *Catal. Today* **2010**, *157*, 8–15.

- (2) Cavani, F. Catalytic selective oxidation faces the sustainability challenge: turning points, objectives reached, old approaches revisited and solutions still requiring further investigation. *J. Chem. Technol. Biotechnol.* **2010**, *85*, 1175–1183.
- (3) Godini, H. R. *Analysis of Individual and Integrated Packed-Bed Membrane Reactors for Oxidative Coupling of Methane*; TU Berlin: Berlin, 2014.
- (4) Chynoweth, D. P.; Owens, J. M.; Legrand, R. Renewable methane from anaerobic digestion of biomass. *Renewable Energy* **2001**, *22*, 1–8.
- (5) Stringer, J.; Horton, L. *Basic Research Needs to Assure a Secure Energy Future*; Oak Ridge National Laboratory: Oak Ridge, TN, 2003; pp A-97–A-101.
- (6) Hermans, I.; Spier, E. S.; Neuenschwander, U.; Turrà, N.; Baiker, A. Selective oxidation catalysis: opportunities and challenges. *Top. Catal.* **2009**, *52*, 1162–1174.
- (7) Tang, Q.; Wang, Y.; Liang, J.; Wang, P.; Zhang, Q.; Wan, H. Co²⁺-exchanged faujasite zeolites as efficient heterogeneous catalysts for epoxidation of styrene with molecular oxygen. *Chem. Commun.* **2004**, 440–441.
- (8) Mitsudome, T.; Nosaka, N.; Mori, K.; Mizugaki, T.; Ebitani, K.; Kaneda, K. Liquid-phase epoxidation of alkenes using molecular oxygen catalyzed by vanadium cation-exchanged montmorillonite. *Chem. Lett.* **2005**, *34*, 1626–1627.
- (9) Kumar, P.; Thybaut, J.; Marin, G. Oxidative coupling of methane followed by oligomerization to liquids (OCMOL). Presented at the *1st International Workshop of the European Nanoporous Materials Institute of Excellence Nanostructured Materials for Sorption, Separation and Catalysis*; European Nanoporous Materials Institute of Excellence (ENMIX), 2010.
- (10) Fini, T.; Patz, C.; Wentzel, R. *Oxidative Coupling of Methane to Ethylene*; University of Pennsylvania: Philadelphia, PA, 2014.
- (11) Stuenkel, S.; Godini, H. R.; Repke, J.-U.; Wozny, G. Simultaneous Synthesis of the Downstream Process and the Reactor Concept for the Oxidative Coupling of Methane (OCM). *Comput.-Aided Chem. Eng.* **2009**, *27*, 975–980.
- (12) Lu, Y.; Dixon, A. G.; Moser, W. R.; Ma, Y. H. Analysis and optimization of cross-flow reactors with staged feed policies— isothermal operation with parallel-series, irreversible reaction systems. *Chem. Eng. Sci.* **1997**, *52*, 1349–1363.
- (13) Lu, Y.; Dixon, A. G.; Moser, W. R.; Hua Ma, Y. Oxidative coupling of methane in a modified γ -alumina membrane reactor. *Chem. Eng. Sci.* **2000**, *55*, 4901–4912.
- (14) Godini, H. R.; Xiao, S.; Jašo, S.; Stünkel, S.; Salerno, D.; Son, N. X.; Song, S.; Wozny, G. Techno-economic analysis of integrating the methane oxidative coupling and methane reforming processes. *Fuel Process. Technol.* **2013**, *106*, 684–694.
- (15) Vigneault, A.; Elnashaie, S. S.; Grace, J. R. Simulation of a compact multichannel membrane reactor for the production of pure hydrogen via steam methane reforming. *Chem. Eng. Technol.* **2012**, *35*, 1520–1533.
- (16) Marín, P.; Patiño, Y.; Díez, F. V.; Ordóñez, S. Modelling of hydrogen perm-selective membrane reactors for catalytic methane steam reforming. *Int. J. Hydrogen Energy* **2012**, *37*, 18433.
- (17) Rattananon, N.; Assabumrungrat, S.; Arpornwichanop, A.; Putivisutisak, S.; Wiyaratn, W. Analysis of an Oxidative Coupling of Methane (OCM) Reactor: Multi Point Feeding Policy. Presented at the *TIChE International Conference*, Thailand, 2011.
- (18) Quiceno, R.; Pérez-Ramírez, J.; Warnatz, J.; Deutschmann, O. Modeling the high-temperature catalytic partial oxidation of methane over platinum gauze: Detailed gas-phase and surface chemistries coupled with 3D flow field simulations. *Appl. Catal., A* **2006**, *303*, 166–176.
- (19) Syamlal, M.; Rogers, W.; O'Brien, T. J. *MFLX Documentation*; U.S. Department of Energy, Federal Energy Technology Center, Morgantown, WV, 1993.
- (20) Stansch, Z.; Mleczko, L.; Baerns, M. Comprehensive kinetics of oxidative coupling of methane over the La₂O₃/CaO catalyst. *Ind. Eng. Chem. Res.* **1997**, *36*, 2568–2579.
- (21) Syamlal, M. *MFLX Documentation: Numerical Technique*, EG and G Technical Report; DE-AC21-95MC31346, 1998. Available at <https://mfix.netl.doe.gov/documentation/numerics.pdf>, 1998.
- (22) Godini, H.; Gili, A.; Görke, O.; Simon, U.; Hou, K.; Wozny, G. Performance Analysis of a Porous Packed Bed Membrane Reactor for Oxidative Coupling of Methane: Structural and Operational Characteristics. *Energy Fuels* **2014**, *28*, 877–890.
- (23) Godini, H.; Xiao, S.; Kim, M.; Görke, O.; Song, S.; Wozny, G. Dual-membrane reactor for methane oxidative coupling and dry methane reforming: Reactor integration and process intensification. *Chem. Eng. Process.* **2013**, *74*, 153–164.
- (24) Nghiem, X. S. *Ethylene production by oxidative coupling of Methane: new process flow diagram based on adsorptive separation*. Dissertation, Technische Universität Berlin, Berlin, 2014.
- (25) Ergun, S.; Orning, A. A. Fluid flow through randomly packed columns and fluidized beds. *Ind. Eng. Chem.* **1949**, *41*, 1179–1184.

Supporting Information

Sustainable process design for oxidative coupling of methane (OCM): Comprehensive reactor engineering via CFD analysis of OCM packed-bed membrane reactors

Mohammad-Sadegh Salehi*¹, Maryam Askarishahi¹, Hamid-Reza Godini*¹, Oliver Goerke², Günter Wozny¹

*¹ Chair of Process Dynamics and Operation, Berlin Institute of Technology, Strasse des 17. Juni 135,
Skr. KWT-9, D-10623 Berlin, Germany*

*² Department of ceramic materials, Institute for material science and technologies, Berlin Institute of
Technology, Hardenbergstrasse 40, D-10623 Berlin, Germany*

*Corresponding author: Mohammad-Sadegh Salehi. E-mail address: sadegh.salehi1987@gmail.com

*Corresponding author: Hamid Reza Godini. E-mail address: hamid.r.godini@tu-berlin.de Tel: +49 30 31421619. Fax: +49 30 31426915

Constitutive Equations for Heat Transfer Equation and Grid Sensitivity Analysis

Thermal energy equations and constitutive equations

Since the reactions taking place in the OCM reactor are highly exothermic, and distribution of the reaction temperature plays an important role in the reaction rates, it is necessary to precisely address this non-isothermal system and solve the energy conservation equations for the gas and solid phases which are given respectively as followings:

$$\varepsilon_g \rho_g C_{Pg} \left(\frac{\partial T_g}{\partial t} + \mathbf{u}_g \cdot \nabla T_g \right) = -\nabla \cdot \mathbf{q}_g + \sum_{m=1}^M \gamma_{gm} (T_{sm} - T_g) - \Delta H_{rg} + \gamma_{Rm} (T_{Rm}^4 - T_{sm}^4) \quad (1)$$

$$\varepsilon_{sm} \rho_{sm} C_{Psm} \left(\frac{\partial T_{sm}}{\partial t} + \mathbf{u}_{sm} \cdot \nabla T_{sm} \right) = -\nabla \cdot \mathbf{q}_{sm} + \gamma_{gm} (T_{sm} - T_g) + \gamma_{Rm} (T_{Rm}^4 - T_{sm}^4) \quad (2)$$

Where $\nabla \cdot \mathbf{q}_g$ and $\nabla \cdot \mathbf{q}_{sm}$ denote the conductive heat fluxes for the gas and solid phases respectively and have been calculated as followings:

$$\mathbf{q}_g = -\varepsilon_g k_g \nabla T_g \quad (3)$$

$$\mathbf{q}_{sm} = -\varepsilon_{sm} k_{sm} \nabla T_{sm} \quad (4)$$

Thermal conductivity of the solid phase can be calculated according to Bauer and Schlunder¹ as in equation 5.

$$\frac{k_{sm}}{k_g} = \frac{\phi_k R_{km} + (1 - \phi_k) \lambda_{rm}}{\sqrt{1 - \varepsilon_g}} \quad (5)$$

Where constant ϕ_k is the contact area fraction which equals to 7.2×10^{-3} . λ_{rm} is the solids conductivity function defined by equation 6.

$$\lambda_{rm} = -\frac{2}{(1 - b/R_{km})} \left[\frac{(1 - R_{km}) b/R_{km}}{(1 - b/R_{km})^2} \ln(b/R_{km}) + \frac{b - 1}{(1 - b/R_{km})} + \frac{b + 1}{2} \right] \quad (6)$$

where

$$(7)$$

The term $\gamma_{gm} (T_{sm} - T_g)$ in the conservation equation of thermal energy is convective heat transfer between the gas and the m^{th} solid phase. The heat transfer coefficient is given by Bird, et al.²

$$\gamma_{gm} = \frac{C_{pg}R_{0m}}{\exp\left(\frac{C_{pg}R_{0m}}{\gamma_{gm}^0}\right) - 1} \quad (8)$$

Where the heat transfer coefficient is related to Nusselt number as reported in equation 9.

$$\gamma_{gm}^0 = \frac{6k_g\varepsilon_g Nu_m}{d_{pm}^2} \quad (9)$$

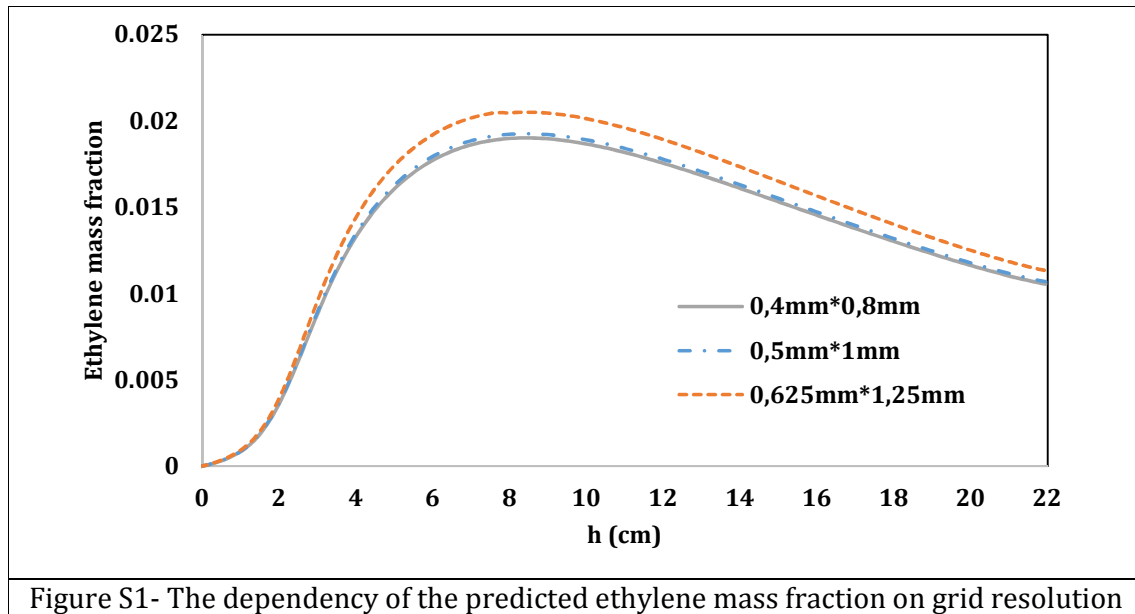
Nusselt number for individual particles of m^{th} solid phase is given by the correlation presented by Gunn ³.

$$Nu_m = (7 - 10\varepsilon_g + 5\varepsilon_g^2) \cdot (1 + 0.7Re_p^{0.2}Pr^{1/3}) + (1.33 - 2.4\varepsilon_g + 1.2\varepsilon_g^2)Re_p^{0.7}Pr^{1/3} \quad (10)$$

Prandtl number is defined as $\frac{C_{pg}\mu_g}{k_g}$. This correlation is applicable for a porosity range of 0.35-1.0 and a Reynolds number up to 10^5 . ³

Grid Sensitivity Study

In order to investigate the independency of solution from the mesh size, several simulations were performed with the grid size of $0.4 \text{ mm} \times 0.8 \text{ mm}$, $0.5 \text{ mm} \times 1 \text{ mm}$ and $0.625 \text{ mm} \times 1.25 \text{ mm}$. As shown in Figure 1, upon refining the computational domain to the values smaller than $0.5 \text{ mm} \times 1 \text{ mm}$, the accuracy of the predicted ethylene mass fraction will not be improved, while deviation can be observed for the coarse grid size of $0.625 \text{ mm} \times 1.25 \text{ mm}$. As a result, the value of $0.5 \text{ mm} \times 1 \text{ mm}$ was adopted to achieve high accuracy and low computational cost.



References

- (1) Bauer, R.; Schlunder, E., Effective Radial Thermal-Conductivity of Packings in Gas-Flow. 2. Thermal-Conductivity of Packing Fraction without Gas-Flow. *Int. Chem. Eng.* **1978**, 18, 189-204.
- (2) Bird, R.; Stewart, W.; Lightfoot, E., Transport Phenomena (revised second ed.) John Wiley & Sons. *New York* **2007**.
- (3) Gunn, D., Transfer of heat or mass to particles in fixed and fluidised beds. *Int. J. Heat Mass Transfer* **1978**, 21, 467-476.

“We're always, by the way, in fundamental physics, always trying to investigate those things in which we don't understand the conclusions. After we've checked them enough, we're okay.”

(Richard P. Feynman)

6

Conclusion and Outlook

Here, we summarize the key findings of each chapter, which are outlined in a structure based on the goals defined in chapter 1. Afterwards, several ideas for future work are listed in the outlook section.

6.1 Conclusion

The present thesis aims at the simulation of transport phenomena in reactive gas-solid systems with a focus on oxidative coupling of methane (OCM) process. This goal was realized by developing validated and verified platforms for simulation. To do so, we derived an analytical solution to verify an Euler-Lagrange approach (Goal I). Moreover, a Euler-Euler approach was employed to study transport phenomena in fluidized beds and packed bed reactors (Goal II, III, and IV). To be more specific, initially, an analytical solution was derived based on Laplace transformations. Afterward, this analytical solution was used to verify the heat exchange between fluid and particles in the presence of a constant heat source. Subsequently, the validity of the developed CFD-DEM platform (i.e., CFDEM^{®1} and LIGGGHTS^{®2}) was evaluated (Goal I). In the next step, aimed at improving the reduced-order model for mass transfer in a fluidized bed, solid mixing was quantified. Subsequently, a set of correlations was developed for a number of mixing metrics; namely, i) axial solid dispersion coefficients; ii) lateral solid dispersion coefficients; and iii) solid diffusivity (Goal II). Besides, a correlation was proposed to evaluate the characteristic mixing time in fluidized beds based on the operating conditions and the solid particle properties (Goal II). These correlations can benefit reaction engineers to evaluate the mixing time, and compare it with the reaction time for a more efficient reactor design and its optimization.

In the next step, a TFM-based platform (i.e., MFiX) was extended to evaluate the performance of a fluidized bed reactor for an OCM process. This was done by evaluation of reactor performance in terms of selectivity towards C_2 -product (ethane and ethylene) and CH_4 conversion for a wide range of operating conditions (Goal III). Finally, the MFiX platform was extended to simulate packed bed membrane reactors for the OCM process. In detail, the TFM approach was employed to analyze the reactor performance via reaction pathway analysis (Goal IV) as suggested by Schwach et al.³. This method can be advantageous to investigate the effect of reactant dosing (e.g., oxygen in OCM reactors) on the thermal and chemical performance of the reactor, e.g., hotspot formation and selectivity towards the desired products. In the following sections, the results of research studies performed to realize these goals, as delineated in Chapter 1, will be briefly described to draw general conclusions.

6.1.1 Goal I: Verification of Simulation Platform

An analytical solution was derived for the thermal transport in fluid-solid flows, including a constant heat source or heat sink. In detail, our analytical solution enables one to calculate the temporal distribution of temperature along a packed bed. Such an analytical solution can benefit researchers to examine the reliability of their simulation. Specifically, this solution can be helpful in cases experimental validation may be faced with several challenges. For instance, Patil et al.⁴ adjusted the wall heat transfer coefficient to fit their CFD-DEM simulation with the experiments. Such difficulties stem from contribution of various mechanisms of heat transfer, which cannot be readily isolated.

The correctness of the proposed exact solution was examined in two ways: namely, i) comparison with the exact solution proposed by Schumann⁵ for heat transfer without heat source; and ii) comparison with the numerical prediction of MATLAB[®] code by solving the governing equations using a “PDEPE” solver. It was demonstrated that our analytical solution can reproduce the data predicted by the Schumann solution⁵. Our analytical solution speeds up the calculation about 100 times compared to a numerical computation with MATLAB[®].

In the next step, the proposed exact solution was utilized to examine the validity of the fluid-solid heat transfer implemented in the CFDEM^{®1} code. It was demonstrated that the developed code can successfully predict the heat exchange between fluid and solid phases with and without a constant thermal heat source. However, systematic deviations are primarily observed near the inlet region, which can be attributed to the Lagrangian-Eulerian mapping of the void fraction. Such a deviation will be amplified upon increasing the heating rate from the heat source. The reason is that the implemented correlation of heat transfer proposed by Deen et al.⁶ in the CFDEM^{®1} code is highly sensitive to the local solid volume fraction. Likewise, Askarishahi et al.⁷ demonstrated that in the case of large voidage gradients, EL approaches show higher deviations for the total drag force compared to the EE approach. This finding motivates researchers to improve the particle volume mapping used in an EL approach, e.g., in the CFDEM^{®1} code.

Finally, a map was proposed to check the validity of Schumann's solution⁵ as it is extensively used by many researchers in the literature, even for cases with heat source. The proposed map clearly shows that the bed length is the most critical parameter which affects the validity of Schumann's solution⁵.

The analytical and numerical solutions presented in the literature for these applications are limited to very simple cases. For instance, very recently, Wang et al.⁸ presented an analytical solution for a flow of fluid over a single particle to evaluate the reliability of their CFD-DEM results. However, the heat transfer coefficient in a fluidized bed is highly governed by the presence of other particles (i.e., the solid volume fraction).

In another study, Sutkar et al.⁹ used the analytical solution proposed by Anzelius¹⁰ for fluid-particle heat exchange in a wet fluidized bed. However, the contribution of heat transfer due to particle drying needs to be accounted for as well. As demonstrated in the present thesis, marginalizing the contribution of a heat source or sink in gas-particle flow can influence the accuracy of solution. This effect becomes dominant when the volumetric heat source is comparable to the volumetric heat transfer rate (i.e., heat transfer coefficient times specific exchange area).

Consequently, when an analytical solution is derived for a system, all involved phenomena should be accounted for which are relevant in the targeted use case. It should be noted that due to the transient nature of fluidized beds and the non-linearity of the Navier-Stokes equation, the derivation of general analytical solution for such a system is infeasible. Therefore, we limited our case to the packed bed with volumetric heat source or sink.

6.1.2 Goal II: Importance of solid mixing and the degree of uniformity

We employed an EE approach based on the two-fluid model (TFM) to study the degree of mixing of Geldart B particles. To do so, the quality of mixing was evaluated based on solid flow pattern, solid dispersion, and diffusion, as well as on mixing time. The results of our simulations showed that in the bed filled with Geldart B particles, four vortices are formed in the studied range of fluidization velocity (i.e., $1.5 - 3.5u_{mf}$). However, for the heavier and larger particles approaching Geldart D (i.e., Geldart BD) a different

pattern is observed at high fluidization velocity. Specifically, the two bottom vortices disappear at lower fluidization velocity compared to one for Geldart B particles. This behavior demonstrates the significant contribution of particle density in the solid flow pattern, which was not addressed in previous studies of Lin et al.¹¹ and Fan et al.¹². In detail, the focus of previous studies was mainly on the influence of fluidization velocity^{11,13,14}, bed aspect ratio¹³⁻¹⁵, and particle diameter^{12,16} in a limited range. However, as revealed in the present contribution, solid flow pattern is highly influenced by particle density as well, especially the velocity at which bottom vortices disappear.

Another important finding is the effect of particle density and fluidization velocity on the grid size required for the simulation. In detail, as our grid dependency study revealed that a finer mesh is required for lighter particles processed at lower fluidization velocity to capture the formed bubbles. This finding demonstrated that grid size should be carefully adopted especially for light particles and at a velocity close to the minimum fluidization velocity. However, Wang et al.¹⁷ claimed that the grid size of 2 – 4 times particle diameter is enough to capture flow structures regardless of fluidization velocity. Nonetheless, the effect of particle density beside fluidization velocity should be accounted for. What is more, for lighter particles a significantly longer simulation time is required to reach a pseudo-steady state condition. This is due to a lower bubbling frequency in the bed.

To quantify the degree of mixing, the velocity variances of solid particles have been used to compute the solid dispersion rate. Similarly, solid granular temperature was used to compute the solid diffusivity. According to the results of TFM simulations, it is beneficial to lump the effect of superficial velocity and solid properties in an excess gas velocity. This allows to collapse the computed dispersion coefficients on a straight line for both lateral and axial mixing. Nonetheless, the particle diffusion coefficient should be correlated to another parameter: solid diffusivity is a linear function of particle diameter times excess gas velocity. Also, it was found that the dispersion coefficient outweighs the diffusion coefficient by approximately four orders of magnitude.

What is more, the characteristic mixing time was computed for the studied range of operating conditions. It was proven that the normalized mixing characteristic time can

be successfully correlated to an excess velocity-based particle Froude Number (See Figure 1). One of the main advantages of the present correlation is that it enables one to directly predict the mixing time without extensive experimentation. In contrast, the correlation presented by Bakshi et al.¹⁸ features several adjustable parameters which require experimental data. In another study, Gorgi-Kandi et al.¹⁹ presented a correlation using dimensional analysis. However, they did not exclude the effect of bed initialization. The same approach was also adopted in various other studies in literature¹⁹⁻²². Nonetheless, the results of our simulations demonstrated that mixing time can be over-predicted by 50% if mixing time is measured immediately after the bed fluidization is initiated. Therefore, it is essential to study the mixing time when the bed reaches pseudo-steady state (see Chapter 3).

It should be mentioned that the mixing of particles in larger beds can be different from the one in smaller beds. For example, Bakshi et al.^{23,24} reported that in larger fluidized beds, smaller bubbles are formed and the mixing is more efficient than in a smaller bed. The reason is that the effect of wall friction in small fluidized beds becomes dominant. Hence, it is crucial to test the validity of the developed models for larger FBs and to extend them - if it is needed - in future.

Eventually, a set of simulations have been performed to inspect the relation of solid flow pattern and mixing time by marking particles in a specific vortex. In detail, particles in a particular region in the top or bottom vortices have been marked with a scalar quantity. The simulation results demonstrated that bottom vortices contribute more in solid mixing if fluidized bed operates at the lowest studied fluidization velocity, i.e., $1.5u_{mf}$. In contrast, as fluidization velocity increases, the upper vortices play a significant role in the solid mixing. In other words, mixing is faster in larger vortices. This finding can practically help engineers to design side-feeding ports in FBs more effectively. Previous studies on solid flow pattern¹²⁻¹⁶ did not evaluate the applicability of a solid circulation map for industrial practice with respect to the feeding policy. The present study suggests that such an evaluation should be reconsidered.

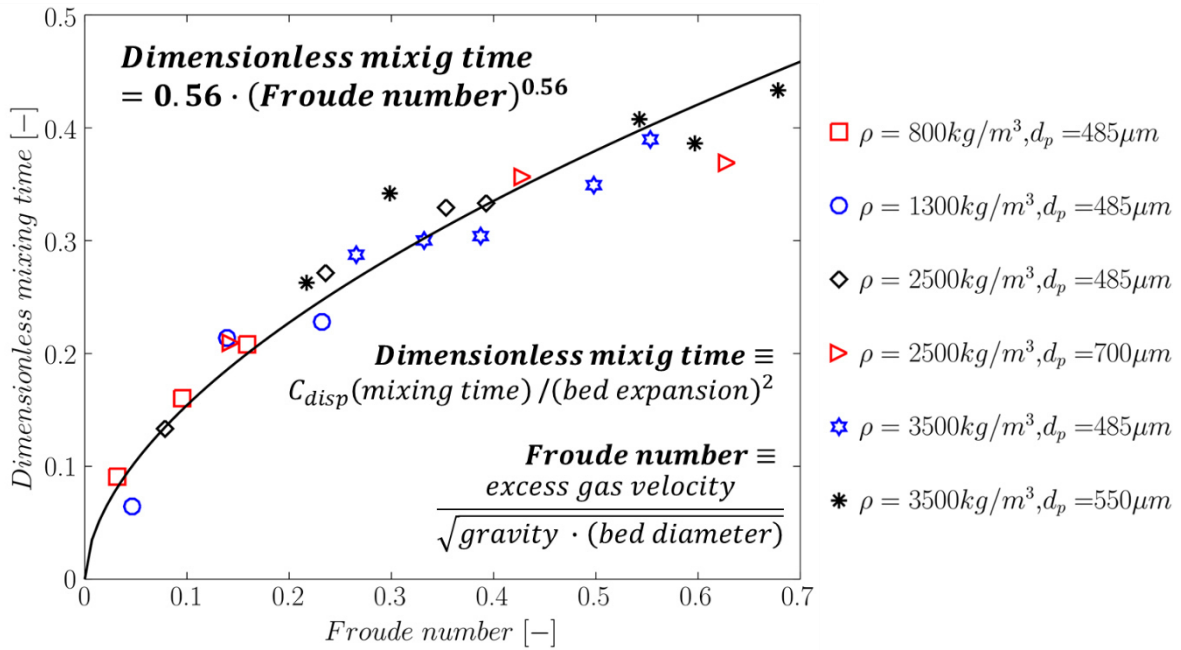


Figure 1. The characteristic time of particle mixing versus excess gas velocity for different particle densities and particle sizes (ρ indicates the particle density and d_p stands for particle diameter)

6.1.3 Goal III: Validated CFD Platform to Analyze OCM Process in Fluidized-Bed Reactors

Aimed at obtaining a deep understanding of the OCM process in FBs, a TFM-based platform (MFiX opensource code) was employed. Accurately, the objective was evaluating the contribution of desired and undesired reactions to the thermal and chemical performance of the OCM fluidized bed reactors. It should be noted that the present study is the first comprehensive study dealing with CFD simulation of OCM in FBs. The studies available in the literature^{25–28} focus mainly on fixed bed reactors and a single catalyst pellet. For instance, Zhang et al.^{25,26} simulated a single operating point of the OCM process in a packed bed. However, the performance of the OCM reactor highly depends on the oxygen dosing as reported by Jaso et al.²⁹. Therefore, evaluating a wider range of operating conditions seems to be essential, as conducted in the present study. Specifically, the effect of operating temperature, pressure, and feed methane-to-oxygen ratio and fluidization velocity was investigated.

In summary, the simulation results demonstrated that:

- i. For CH_4/O_2 ratios of smaller than eight, a rise in the operating pressure from 1 [bar] to 3 [bar] slightly reduces the selectivity towards C_2 -product while increases the conversion of methane. A further increase in pressure marginally influences reactor performance.
- ii. A higher fluidization velocity (i.e., gas hourly space velocity) drops the methane conversion due to (a) bypassing of the reactants via bubbles, and (b) acceleration of the ethylene oxidation reaction at a lower contact time.
- iii. An increase of the methane-to-oxygen ratio leads to a rise in C_2 -selectivity, while this reduces the methane conversion. This observation can be attributed to the availability of methane for low-oxygen-demanding reactions. This consequence finally leads to a rise in C_2 -yield.
- iv. An optimum temperature was predicted in such a way that C_2 -yield is maximized.

Furthermore, the validity of the kinetic model developed by Stansch et al.³⁰ was investigated. To do so, a detailed analysis of reaction pathways and concentration profiles was performed based on the experimental data reported by Pannek et al.³¹. It was revealed that the reaction rates presented in the kinetic model of Stansch et al.³⁰ seem to be fast compared to the ones observed in the experiments for various reasons. First, the pressure does not affect the contribution of the gas-phase reactions, which demonstrated that oxygen is mainly consumed in heterogeneous reactions. Second, the rate of consumption of oxygen along the bed is much higher in the simulation compared to the experiment. This finding supports our claim that the reaction rates should be slowed down in the Stansch kinetics³⁰ in order to match the experimental data. Very recently, Karakaya et al.³² claimed that the Stansch model fails to predict the local concentration in the reactor accurately. Therefore, revisiting the kinetic model seems essential for further reactor studies as also suggested by Kee et al.³³. Karakaya et al.³² proposed that methane activation through CH_3° radicals should be accounted in the kinetic model. It is worth noting that even though Stansch's model³⁰ over-predicts C_2 -selectivity, CH_4 conversion can be accurately predicted (maximum deviation of 7%).

Finally, a sensitivity analysis has been performed to specify the optimum scenario in which the C_2 -yield is maximized. To do so, the performance of the FB reactor was analyzed for various operating conditions (e.g., CH_4/O_2 ratio and operating temperature). According to this analysis, the maximum C_2 -yield was predicted at a temperature of around $800\text{ }^\circ\text{C}$. This finding is consistent with the experimental data of Pannek et al.³¹ for the CH_4/O_2 ratio of 2 – 5 and the recent data reported by Cruellas et al.^{34,35}. In detail, Cruellas et al.^{34,35} developed a 1D model which predicts the maximum C_2 -yield for the temperature range of $830\text{ }^\circ\text{C}$ – $870\text{ }^\circ\text{C}$. However, Pirro et al.²⁸ reported that maximum C_2 -yield for temperature below $650\text{ }^\circ\text{C}$ in an adiabatic fixed bed reactor.

Our results of simulation also showed that the maximum C_2 -yield is marginally influenced by the methane-to-oxygen ratio in the temperature range of $730\text{ }^\circ\text{C}$ – $850\text{ }^\circ\text{C}$. The recent results of Cruellas et al.^{34,35} support this finding. They also reported that the maximum C_2 -yield can be obtained at the CH_4/O_2 ratio of 1.5 at a constant operating temperature. This observation is also in accordance with our prediction.

6.1.4 Goal IV: performance analysis of a packed bed membrane reactor for an OCM Process and the kinetic model

As explained before, applying fluidized beds for OCM process results in a fast consumption of oxygen and consequently low C_2 -selectivity (i.e., 18%). This was also supported by the experimental data of Zohour et al.³⁶. Therefore, a packed bed membrane reactor can be a suitable alternative to improve the reactant dosing (for instance O_2) and to avoid bubble bypassing. Consequently, in the next step, the performance of a packed membrane reactor was investigated numerically and experimentally. The results of TFM simulation demonstrated that a fine distribution of oxygen over the membrane is in favor of oxidative coupling of methane. Consequently, our results showed that the application of PBMR can increase the C_2 -yield (i.e., 25%) compared to conventional reactors. This is in accordance with the data recently reported in the literature^{35,37,38}. Specifically, the C_2 -yield achieved in the present study (i.e., 25%) is slightly higher than the value observed by Aseem et al.³⁸ (C_2 -yield of 23.6%). Furthermore, the predicted C_2 -selectivity is in a good agreement with the

experimental data (with a deviation of 5%). However, the predicted methane conversion deviates from the observed one.

Finally, one should be honest about the accuracy of the model implemented to predict species concentration and temperature profiles. According to the simulation results in Chapter 4 and 5, a more reliable kinetic model should be implemented for OCM systems. Unfortunately, no better kinetic model than the Stansch model³⁰ is currently available in the open literature as also reported by several researchers^{33,39,40}.

6.2 Outlook

As mentioned before, some challenges remain in developing a novel OCM process from inception to industrial applications. Therefore, reaction engineering alongside developing new catalysts should be considered while a novel reactor equipped with new catalysts is designed for such purposes. Hence, there is still enormous room available for further developments, which can be summarized as follows:

- Extending the analytical solution developed for heat transfer with thermal source in a packed bed⁴¹ (see Chapter 2) by accounting for dispersion effects inherent to all fluid-solid flows
- Extending the correlations developed for solid dispersion, diffusivity and characteristic mixing time (see chapter 3) by considering the effect of bed geometry. Similarly, correlations for mixing metrics should be extended to cover cohesive particles as well. The closures recently provided by Gu et al.⁴² could be exploited for this purpose.
- Investigating polydisperse gas-particle systems with a focus on improving the proposed correlations in chapter 3 for solid mixing.
- Developing a new closure for reaction kinetics for oxidative coupling of methane which is catalyst-specific as also report by Kee et al.³³.
- Analyzing new reactor configuration with different membranes module for oxygen dosing, for example, using porous and dense membranes.
- Application of filtered models by developing the required closures for simulation of industrial-scale reactors (e.g., see the work of Schneiderbauer⁴³, Radl et al.^{44,45} or Cloete et al.⁴⁶). In detail, filtered models are based on averaging

over the micro and meso scales for flow, mass, and heat transfer. The results of such studies can be formulated in the form of filtering correlations which are applicable for macro-scale structure simulations. Up to now, several researchers proposed several “filtered models, primarily for drag and stress⁴⁷. Recently, Agrawal et al.⁴⁸ showed that similar methodology can be applied for heat and mass transfer simulations. However, most studies are limited to fully periodic boundaries. Therefore, there are open research topics in this field for the improvement of filtered correlations for real industrial application. Ultimately, such rigorous filtered models would allow simulating large-scale reactors with a lower computational cost without significantly deteriorating the accuracy of the results.

6.3 Abbreviations

CFD	Computational Fluid Dynamics
CFDEM®	Computational Fluid Dynamics-discrete Element Method (software)
DEM	Discrete Element Method
EE	Euler-Euler (Model)
EL	Euler-Lagrange (Model)
FB	Fluidized Bed
LIGGGHTS®	LAMMPS improved for General Granular and Granular Heat transfer Simulations (software)
MATLAB®	MATrix LABoratory (software)
MFIX	Multiphase Flow with Interphase eXchanges (software)
PBMR	Packed Bed Membrane Reactor
OCM	Oxidative Coupling of Methane
TFM	Two-Fluid Model

Latin Symbols

d_p particle diameter; [μm]

Greek Letters

ρ Microscopic (material) density of the solid phase; [kg/m^3]

6.4 References

1. Goniva, C., Kloss, C., Deen, N. G., Kuipers, J. A. M. & Pirker, S. Influence of rolling friction on single spout fluidized bed simulation. *Particuology* **10**, 582–591 (2012).
2. Kloss, C., Goniva, C., Hager, A., Amberger, S. & Pirker, S. Models, algorithms and validation for opensource DEM and CFD–DEM. *Prog. Comput. Fluid Dyn. an Int. J.* **12**, 140–152 (2012).
3. Schwach, P., Pan, X. & Bao, X. Direct conversion of methane to value-added chemicals over heterogeneous catalysts: challenges and prospects. *Chem. Rev.* **117**, 8497–8520 (2017).
4. Patil, A. V, Peters, E., Sutkar, V. S., Deen, N. G. & Kuipers, J. A. M. A study of heat transfer in fluidized beds using an integrated DIA/PIV/IR technique. *Chem. Eng. J.* **259**, 90–106 (2015).
5. Schumann, T. E. W. Heat transfer: A liquid flowing through a porous prism. *J. Franklin Inst.* **208**, 405–416 (1929).
6. Deen, N. G. & Kuipers, J. A. M. Direct Numerical Simulation (DNS) of mass, momentum and heat transfer in dense fluid-particle systems. *Curr. Opin. Chem. Eng.* **5**, 84–89 (2014).
7. Askarishahi, M., Salehi, M. S. & Radl, S. Voidage correction algorithm for unresolved Euler–Lagrange simulations. *Comput. Part. Mech.* **5**, 607–625 (2018).
8. Wang, S., Luo, K., Hu, C., Lin, J. & Fan, J. CFD-DEM simulation of heat transfer in fluidized beds: Model verification, validation, and application. *Chem. Eng. Sci.* **197**, 280–295 (2019).
9. Sutkar, V. S. *et al.* CFD-DEM model for coupled heat and mass transfer in a spout fluidized bed with liquid injection. *Chem. Eng. J.* **288**, 185–197 (2016).
10. Anzelius, A. Über erwärmung vermittelt durchströmender medien. *ZAMM-Journal Appl. Math. Mech. für Angew. Math. und Mech.* **6**, 291–294 (1926).
11. Lin, J. S., Chen, M. M. & Chao, B. T. A novel radioactive particle tracking facility for measurement of solids motion in gas fluidized beds. *AIChEJ.* **31**, 465–473 (1985).
12. Fan, X., Yang, Z. & Parker, D. J. Impact of solid sizes on flow structure and particle motions in bubbling fluidization. *Powder Technol.* **206**, 132–138 (2011).
13. Laverman, J. A. *et al.* Experimental study on the influence of bed material on the scaling of solids circulation patterns in 3D bubbling gas-solid fluidized beds of glass and polyethylene using positron emission particle tracking. *Powder Technol.* **224**, 297–305 (2012).
14. Askarishahi, M., Salehi, M.-S., Godini, H. R. & Wozny, G. CFD study on solids flow pattern and solids mixing characteristics in bubbling fluidized bed: Effect of fluidization velocity and bed aspect ratio. *Powder Technol.* **274**, 379–392 (2015).
15. Laverman, J. A., Roghair, I., Van Sint Annaland, M. & Kuipers, H. Investigation into the hydrodynamics of gas-solid fluidized beds using particle image velocimetry

- coupled with digital image analysis. *Can. J. Chem. Eng.* **86**, 523–535 (2008).
16. Askarishahi, M., Salehi, M.-S. & Molaei Dehkordi, A. Numerical investigation on the solid flow pattern in bubbling gas-solid fluidized beds: Effects of particle size and time averaging. *Powder Technol.* **264**, 466–476 (2014).
 17. Wang, J., van der Hoef, M. A. & Kuipers, J. A. M. Why the two-fluid model fails to predict the bed expansion characteristics of Geldart A particles in gas-fluidized beds: A tentative answer. *Chem. Eng. Sci.* **64**, 622–625 (2009).
 18. Bakshi, A., Ghoniem, A. F. & Altantzis, C. Mixing dynamics in bubbling fluidized beds. *AIChE J.* **63**, 4316–4328 (2017).
 19. Gorji-Kandi, S., Alavi-Amleshi, S. M. & Mostoufi, N. A solids mixing rate correlation for small scale fluidized beds. *Particuology* **21**, 55–64 (2015).
 20. Wang, Z. *et al.* Dispersion characteristics of dissimilar materials in a fluidized bed with unevenly distributed fluidizing air. *Powder Technol.* **319**, 365–372 (2017).
 21. Luo, K., Wu, F., Yang, S. & Fan, J. CFD-DEM study of mixing and dispersion behaviors of solid phase in a bubbling fluidized bed. *Powder Technol.* **274**, 482–493 (2015).
 22. Mostoufi, N. & Chaouki, J. Local solid mixing in gas-solid fluidized beds. *Powder Technol.* **114**, 23–31 (2001).
 23. Bakshi, A. Multiscale Continuum Simulations of Fluidization: Bubbles, Mixing Dynamics and Reactor Scaling. *Massachusetts Inst. Technol.* (2017).
 24. Bakshi, A., Altantzis, C., Bates, R. B. & Ghoniem, A. F. Study of the effect of reactor scale on fluidization hydrodynamics using fine-grid CFD simulations based on the two-fluid model. *Powder Technol.* **299**, 185–198 (2016).
 25. Zhang, Z., Guo, Z. & Ji, S. Numerical simulation of packed-bed reactor for oxidative coupling of methane. *J. Energy Chem.* **24**, 23–30 (2015).
 26. Zhang, Z., Guo, Z. & Ji, S. Numerical simulation of fixed bed reactor for oxidative coupling of methane over monolithic catalyst. *Chinese J. Chem. Eng.* **23**, 1627–1633 (2015).
 27. Vandewalle, L. A., Van de Vijver, R., Van Geem, K. M. & Marin, G. B. The role of mass and heat transfer in the design of novel reactors for oxidative coupling of methane. *Chem. Eng. Sci.* **198**, 268–289 (2019).
 28. Pirro, L., Obradović, A., Vandegehuchte, B. D., Marin, G. B. & Thybaut, J. W. Model-Based Catalyst Selection for the Oxidative Coupling of Methane in an Adiabatic Fixed-Bed Reactor. *Ind. Eng. Chem. Res.* **57**, 16295–16307 (2018).
 29. Jašo, S., Arellano-Garcia, H. & Wozny, G. Oxidative coupling of methane in a fluidized bed reactor: Influence of feeding policy, hydrodynamics, and reactor geometry. *Chem. Eng. J.* **171**, 255–271 (2011).
 30. Stansch, Z., Mleczko, L. & Baerns, M. Comprehensive kinetics of oxidative coupling of methane over the La₂O₃/CaO catalyst. *Ind. Eng. Chem. Res.* **36**, 2568–2579 (1997).

31. Pannek, U. & Mleczko, L. Comprehensive model of oxidative coupling of methane in a fluidized-bed reactor. *Chem. Eng. Sci.* **51**, 3575–3590 (1996).
32. Karakaya, C., Zhu, H., Loebick, C., Weissman, J. G. & Kee, R. J. A detailed reaction mechanism for oxidative coupling of methane over Mn/Na₂WO₄/SiO₂ catalyst for non-isothermal conditions. *Catal. Today* **312**, 10–22 (2018).
33. Kee, R. J., Karakaya, C. & Zhu, H. Process intensification in the catalytic conversion of natural gas to fuels and chemicals. *Proc. Combust. Inst.* **36**, 51–76 (2017).
34. Cruellas, A., Bakker, J. J., van Sint Annaland, M., Medrano, J. A. & Gallucci, F. Techno-economic analysis of oxidative coupling of methane: Current state of the art and future perspectives. *Energy Convers. Manag.* **198**, 111789 (2019).
35. Cruellas, A., Melchiori, T., Gallucci, F. & van Sint Annaland, M. Advanced reactor concepts for oxidative coupling of methane. *Catal. Rev. - Sci. Eng.* **59**, 234–294 (2017).
36. Zohour, B., Noon, D. & Senkan, S. Spatial Concentration and Temperature Profiles in Dual-Packed-Bed Catalytic Reactors: Oxidative Coupling of Methane. *ChemCatChem* **6**, 2815–2820 (2014).
37. Farrell, B. L., Igenegbai, V. O. & Linic, S. A Viewpoint on Direct Methane Conversion to Ethane and Ethylene Using Oxidative Coupling on Solid Catalysts. *ACS Catal.* **6**, 4340–4346 (2016).
38. Aseem, A. & Harold, M. P. C₂ yield enhancement during oxidative coupling of methane in a nonpermselective porous membrane reactor. *Chem. Eng. Sci.* **175**, 199–207 (2018).
39. Godini, H. R. *et al.* Techno-economic analysis of integrating the methane oxidative coupling and methane reforming processes. *Fuel Process. Technol.* **106**, 684–694 (2013).
40. Jašo, S., Godini, H. R., Arellano-Garcia, H. & Wozny, G. Oxidative coupling of methane: reactor performance and operating conditions. in *Computer Aided Chemical Engineering* **28**, 781–786 (Elsevier, 2010).
41. Salehi, M.-S., Askarishahi, M. & Radl, S. Analytical solution for thermal transport in packed beds with volumetric heat source. *Chem. Eng. J.* **316**, (2017).
42. Gu, Y., Ozel, A., Kolehmainen, J. & Sundaresan, S. Computationally generated constitutive models for particle phase rheology in gas-fluidized suspensions. 318–349 (2019). doi:10.1017/jfm.2018.856
43. Schneiderbauer, S. A spatially-averaged two-fluid model for dense large-scale gas-solid flows. *AIChE J.* **63**, 3544–3562 (2017).
44. Radl, S. & Sundaresan, S. A drag model for filtered Euler–Lagrange simulations of clustered gas–particle suspensions. *Chem. Eng. Sci.* **117**, 416–425 (2014).
45. Radl, S. *et al.* Closure Development for Multi-Scale Fluidized Bed Reactor Models: A Case Study. in *28 European Symposium on Computer Aided Process Engineering* (eds. Friedl, A., Klemeš, J. J., Radl, S., Varbanov, P. S. & Wallek, T. B. T.-C. A. C. E.) **43**, 247–252 (Elsevier, 2018).

46. Cloete, J. H., Cloete, S., Radl, S. & Amini, S. On the choice of closure complexity in anisotropic drag closures for filtered Two Fluid Models. *Chem. Eng. Sci.* **207**, 379–396 (2019).
47. Cloete, J. H. Development of Anisotropic Filtered Two Fluid Model Closures. (NTNU, 2018).
48. Agrawal, K., Holloway, W., Milioli, C. C., Milioli, F. E. & Sundaresan, S. Filtered models for scalar transport in gas–particle flows. *Chem. Eng. Sci.* **95**, 291–300 (2013).